2013-07-17

Performance Mapping of a Thrust Augmenting Ejector in Transition for Short Take-Off and Vertical Landing Aircraft

Francisco Martinez
University of Miami, francisco.martinez7889@gmail.com

UNIVERSITY OF MIAMI

PERFORMANCE MAPPING OF A THRUST AUGMENTING EJECTOR IN TRANSITION FOR SHORT TAKE-OFF AND VERTICAL LANDING AIRCRAFT

By

Francisco Martinez

A THESIS

Submitted to the faculty

of the University of Miami

in partial fulfillment of the requirements for

the degree of Master in Science

Coral Gables, Florida

August 2013

UNIVERSITY OF MIAMI

A thesis submitted in partial fulfillment of

the requirements for the degree of

Master of Science

PERFORMANCE MAPPING OF A THRUST AUGMENTING EJECTOR IN TRANSITION FOR SHORT TAKE-OFF AND VERTICAL LANDING AIRCRAFT

Francisco Martinez

Approved:

_____ Amir Rahmani, Ph.D. Assistant Professor Mechanical & Aerospace Engineering	_____ M. Brian Blake, Ph.D. Dean of the Graduate School
_____ Weiyong Gu, Ph.D. Professor Mechanical & Aerospace Engineering	_____ Ali Ghahremaninezhad, Ph.D. Assistant Professor Civil, Architectural and Environmental Engineering

MARTINEZ, FRANCISCO (M.S., Mechanical Engineering)

Performance Mapping of a Thrust Augmenting Ejector in Transition for Short Take-Off and Vertical Landing Aircraft. (August 2013)

Abstract of a thesis at the University of Miami.

Thesis supervised by Professor Amir Rahmani.
No. of pages in text. (134)

Previous research has shown the potential for a thrust augmenting ejector to be used as an alternative to the swivel nozzle for short take-off and vertical landing (STOVL) aircrafts. Previous designs for integrating a thrust augmenting ejector failed to make the transition from hovering to wing-borne flight and back to hovering or were not fully tested.

Therefore, the two main objectives of this research are: (1) to obtain a numerical solution for the performance of a thrust augmenting ejector in transition and (2) to verify if an ejector with enough thrust could be integrated into the wing and enable the aircraft to go through transition from hovering to wing-borne flight and back to hovering. The numerical solution for the ejector's performance was obtained by running multiple CFD simulations in ANSYS FLUENT for different speeds and ejector deflection angles. Our research demonstrated that the performance of an ejector wing registered an augmented thrust increase of up to 25 percent lower speeds than Mach 0.25. Similarly, the ejector performed well during transition at take-off and landing speeds; therefore, the feasibility of a thrust augmenting ejector proving to be an improvement to the swivel nozzle for Short Take-Off and Vertical Landing aircraft is high.

Acknowledgement

I would like to give special thanks to Dr. Paul Bevilaqua for his continuous guidance, support, and mentoring, and for giving me the chance and privilege of working with him. Without him, none of this would have been possible.

I would like to thank Dr. Amir Rahmani and my friends at the R.I.S.E. lab for allowing me to work alongside of them, and for helping and supporting me during this research.

I would also like to thank my family and friends, especially my parents and Sugey Ronquillo, for their continuous moral support and driving me forward to achieve my goals during times of hardship. Without their counsel and wisdom, I would not have been able to complete this thesis.

"If I have seen further, it is only because I have stood on the shoulders of giants." –Isaac Newton

Table of Contents

List of Figures

List of Tables

Nomenclature

A= Area (m^2)

B= substitution variable for the one dimensional analysis, dimensionless

CFD= Computational Fluid Dynamics

c_p= 1004.5, specific heat for air, (J/(kg*K))

I= turbulence intensity

K= substitution variable for the one dimensional analysis, dimensionless

L = substitution variable for the one dimensional analysis, dimensionless

M, Ma= Mach Number

P= Pressure (Pa)

P_t= Total/Stagnation Pressure (Pa)

R= 287, individual gas constant for air (J/(kg*K))

STOL= Short Take-Off and Landing

STOVL= Short Take-Off and Vertical Landing

T= Temperature (K)

T_t= Total/Stagnation Temperature (K)

U= velocity (m/s)

U_*= isentropic velocity (m/s)

VSTOL= Vertical Short Take-Off and Landing

γ= 1.4, specific heat ratio for air

ε= turbulent dissipation rate (m^2/s^3)

κ= turbulent kinetic energy (m^2/s^2)

ρ= density, ($kg/m^{3)}$

ρ_t= Total/Stagnation density , (kg/m^3)

Φ= Thrust Augmentation Ratio

Chapter 1: Introduction and Theoretical Analysis

The concept for short take-off and vertical landing (STOVL) aircrafts has been around since the days of World War II. During this time period, scientists tried numerous experiments and aircraft configuration in order to make the aircraft land vertically or reduce the runway needed for take-off. These configurations included rocket-powered aircraft and early designs of rocket and jet powered aircraft. During the decades after WWII, jet propulsion technology advanced sufficiently to provide viable solutions for STOVL aircraft. A clear example of this is the Hawker P.1127, which, like its successor the Harrier Jet, uses a certain number of swivel nozzles to decrease the distance needed for take-off and was able to land vertically. ("Swivel nozzle" referred to a nozzle that can rotate in the vertical or horizontal direction, thus providing thrust vectoring for the aircraft.) The drawback for the swivel nozzle system is the need for a large turbofan/turbojet engine in order to take off in a short distance or land vertically; so the engine will be sized for take-off instead of being sized for cruising.

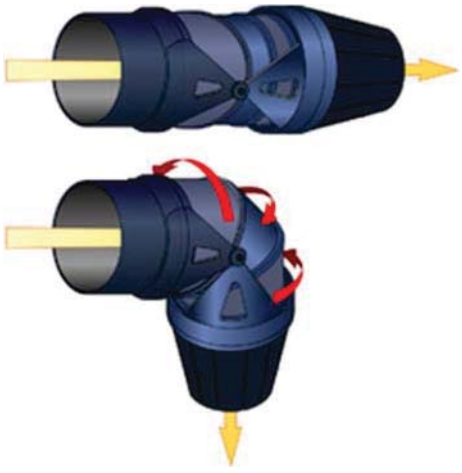

Figure 1: Simple Swivel Nozzle Configuration

Scientists also investigated another viable solution, the thrust augmenting ejector nozzle, a mechanically simple device in which a primary high speed jet is used to accelerate or pump a secondary flow by means of entrainment. A simple ejector consists of a nozzle and duct that directs a jet stream through the duct. The entrainment by the jet pumps a secondary, larger mass flow of air taken from the surrounding atmosphere through the duct, causing a suction force to form in the lip of the duct. This causes the ejector to function as a ducted fan, increasing the thrust of the jet [1]. Diverting the engine exhaust or bleeding air from the bypass of a turbofan can dramatically increase the thrust of an engine by as much 30 to 50 percent.

The thrust augmenting ejector is less efficient than a fan in terms of energy output compared to energy input [2]. However, the ejector utilizes the kinetic energy of the exhaust jet that otherwise would be dissipated or wasted, in order to increase the thrust output of the propulsion system. The measure of the thrust augmentation performance can be defined by the thrust augmentation ratio Φ.

$$\Phi = \int \frac{\rho U^2 dy}{m_0 U_*} \tag{1}$$

The augmentation ratio is the ratio of the mixed flow thrust divided by the isentropic thrust that would be obtained by expanding the primary jet to match atmospheric conditions.

The augmentation ratio could be simplified using basic formulation of a jet engine.

$$\Phi = \frac{\dot{m}_e(u_e - u_\infty)}{\dot{m}_o U_*} \tag{2}$$

Where U_* is

$$U_* = \left(\frac{2\gamma}{\gamma-1}\left(\frac{P_{to}}{\rho_{to}} - \frac{P_\infty}{\rho_\infty}\right)\right)^{\frac{1}{2}} \quad (3)$$

This can be simplified by using the Perfect Gas Law Equation:

$$U_* = \left(2c_p(T_{to} - T_\infty)\right)^{\frac{1}{2}} \quad (4)$$

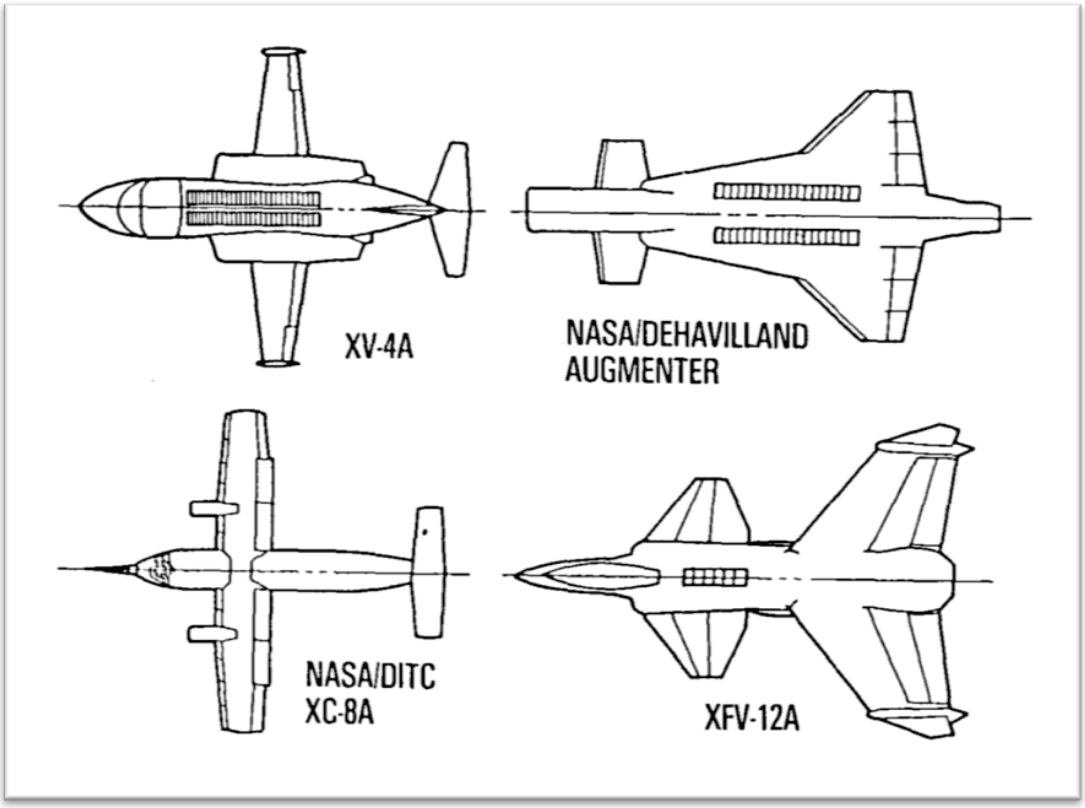

Figure 2: Prototype Aircrafts with Thrust Augmenting Ejectors [1]

Prototype aircrafts were built to incorporate the thrust augmenting ejectors in their design for VSTOL and STOVL purposes. These aircrafts can be separated into two main designs: thrust augmenting ejectors incorporated in the fuselage and thrust augmenting

ejectors integrated in the wing. The earliest design was the Lockheed XV4-A, which incorporated the ejectors into two longitudinal bays, one on each side of the fuselage. The XV4-A produced enough thrust augmentation to hover and demonstrated that ground effects during hovering would not stall the ejector or the engine. However, the aircraft could not transition from hovering to wing-borne flight. As the aircraft accelerated for take-off, it induced a ram drag and an associated pitching

Figure 3: Lockheed XV4-A Hummingbird Prototype Aircraft

moment on the aircraft. This caused instability in the aircraft, since the ejector couldn't create enough augmentation to counter the pitching moment and lift the aircraft at the same time, which ultimately caused the aircraft to crash. Similarly, the General Dynamics E-7, another fuselage-mounted ejector design, could produce enough augmentation to hover; but as the aircraft began to accelerate, the ram drag caused the aircraft to pitch up. In order to control the pitching moment, the vectoring nozzle had to remain vectored down, thus leaving the aircraft stuck in hover mode. Another fuselage designed ejector aircraft was the DeHavilland/NASA wind tunnel model, which was not actually meant to fly; rather it was designed for testing in NASA. This aircraft provided enough thrust

augmentation for both lift and pitching control, but suffered from the large ram drag which made acceleration difficult.

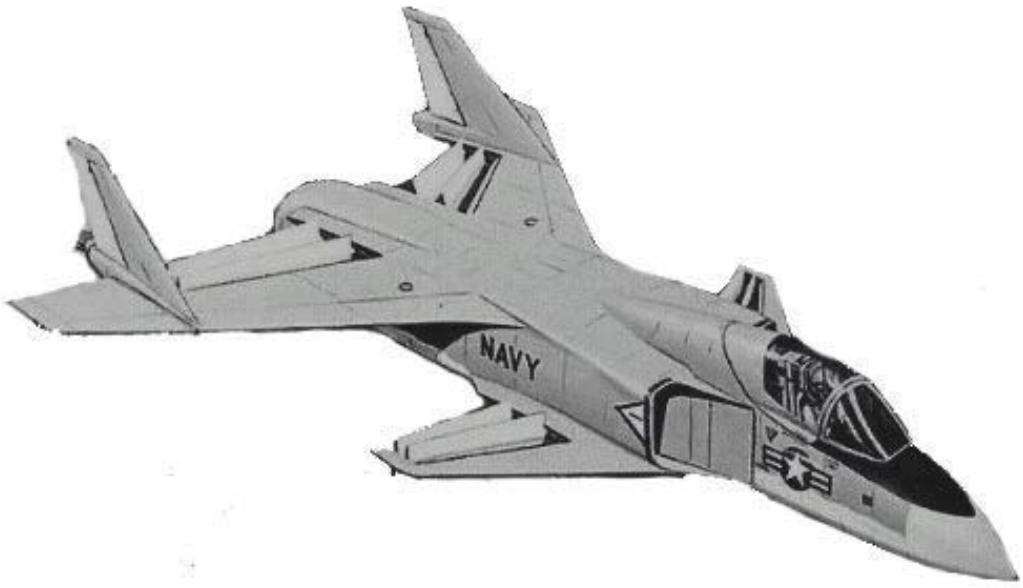

Figure 4: Rockwell XFV-12A Prototype Aircraft

The XC8-A aircraft was a STOL research prototype, which integrated the ejector flaps into two span-wise bays at the trailing edge of the wing. This aircraft was a Buffalo DHC-5 transport aircraft modified by DeHavilland and Boeing for research. The thrust augmentation of the ejectors gave the XC8-A great success as a STOL aircraft. The wing integrated ejector reduced the stall speed of the aircraft by almost 40% and the take-off distance by 25% [1]. Although the XC8-A was not designed to hover, the good STOL performance showed the advantages of integrating the ejector system into the wing. Similarly, the Rockwell XFV-12A incorporated span-wise ejectors into the wing and canard to obtain VSTOL performance. The aircraft was tested at NASA for hovering

performance; however the aircraft fail to produce enough vertical lift to hover due to poor deflection of the primary jet into the ejector duct. This was fixed by putting turning vanes into the nozzle. However the XFV-12A project was cancelled before any more testing could be done.

After evaluating both ejector designs, the wing-integrated ejector design proves superior for a STOVL mission. The fuselage-mounted ejector could not transition into wing-borne flight and had significant control problems due to large ram drag, whereas the wing-integrated design proved that it had good STOL properties as shown by the XC8-A. Although the XFV-12A could not produce enough lift to hover, the aircraft was never tested in transition for STOVL purposes. Since the XC8-A performed well as a STOL aircraft and the XFV-12A was never tested in transition, the wing integrated ejector design was chosen for this research. This configuration has the potential for good performance during transition into wing-borne flight. Furthermore, this configuration could also take advantage of the jet flap effect caused by putting the jet exhaust on top of the wing.

Williams, Butler and Wood [7] described the jet flap as an extension of slot blowing over the trailing edge flaps for boundary layer control that uses much higher quantities of air to increase the effective chord of the flap to produce super-circulation on the wing. The main idea of the concept is to use the exhaust gases of a jet engine to generate significant favorable lift on the wing with minimum propulsive thrust reduction. The term 'jet flap' implies that the exhaust gases are directed to leave the wing's trailing edge as a plane jet at an angle to the free stream velocity. This creates an asymmetrical flow pattern which generates circulation on the airfoil; this is somewhat similar to having large

trailing-edge flap. The lift from the vertical component of the jet momentum is increased several times by the pressure lift generated on the wing surface, while the thrust lies between the horizontal component and the full jet momentum.

1-D Ideal solution for Ejector performance

A method of analysis is needed in order to understand the behavior of a thrust augmenting ejector. However, the flow in an ejector is highly turbulent, thus making a functional model for predicting performance very complex and impractical. Bevilaqua [1] described a quasi-one dimensional approach suggested by von Karman to simplify the model of the system. This method showed reasonable results at low inlet area ratios when the 1-D parallel flow assumption was valid; however, this method cannot be used to simulated deflection angles. Furthermore, this method does not include losses such as incomplete mixing, pressure losses, or flow separation. Nevertheless, this method can be used to understand the behavior of an ejector. This model is based on a simple ejector that consists of a duct and a nozzle that directs a jet through the duct.

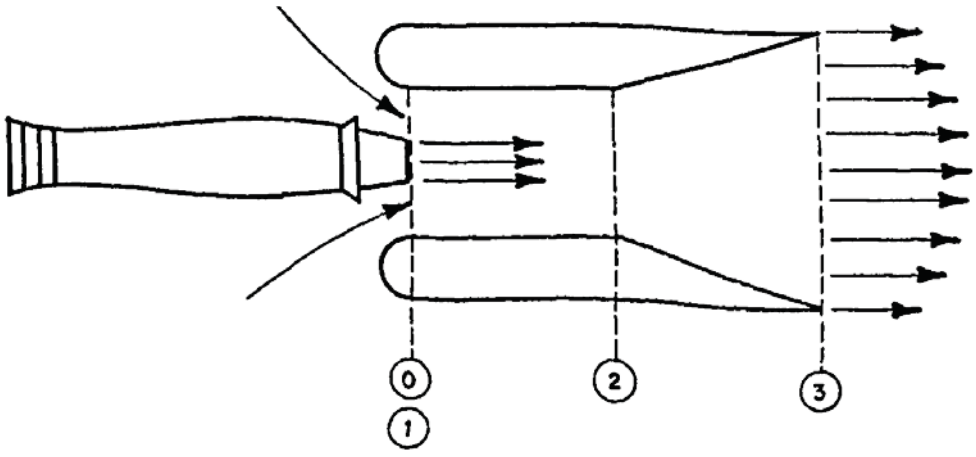

Figure 5: Simple Thrust Augmenting Ejector Configuration [1]

To calculate the thrust augmentation ratio, the velocity, pressure, temperature, area ratios, and density values in the primary, secondary, and mixed flows were needed. The equations that govern the mixed flow are the mass, momentum, energy conservation equations, and the ideal gas law, or equation of state. For the inlets and diffuser flows, the isentropic relation equations are used. This will create an indeterminate system of 14 equations and 20 unknowns. For the following equations, the subscript 0, 1, and 2 refer to the primary, secondary, and mixed stream flows respectively. To further simplify the analysis, the velocity profile is assumed to be uniform in each cross section of the ejector; thus the pressure profile is assumed to be constant.

The conservation of mass equation for the ejector is:

$$\rho_0 U_0 A_0 + \rho_1 U_1 A_1 = \rho_2 U_2 A_2 \tag{5}$$

The conservation of momentum equation is:

$$(P_0 + \rho_0 U_0^2) A_0 + (P_1 + \rho_1 U_1^2) A_1 = (P_2 + \rho_2 U_2^2) A_2 \tag{6}$$

The conservation of energy equation is:

$$\rho_0 U_0 A_0 \left(c_p T_0 + \frac{U_0^2}{2}\right) + \rho_1 U_1 A_1 \left(c_p T_1 + \frac{U_1^2}{2}\right) = \rho_2 U_2 A_2 (c_p T_2 + \frac{U_2^2}{2}) \tag{7}$$

The ideal gas law equation or state equation for each stream with i=0, 1, 2 is:

$$P_i = R \rho_i T_i \tag{8, 9, 10}$$

The primary and secondary flow streams are assumed to enter the ejector isentropically from the nozzle and secondary inlets respectively. Furthermore, the flow, once mixed, is

assumed to exhaust isentropically through the nozzle or diffuser. Thus, the energy conservation equation for a frictionless, adiabatic flow is:

$$c_P T_{ti} = c_p T_i + \frac{U_i^2}{2} \quad (11, 12, 13)$$

Also the Second Law of Thermodynamics applies to the inlets and exhaust for each stream (i=0, 1, 2) is:

$$\frac{T_i}{T_{ti}} = \left(\frac{P_i}{P_{ti}}\right)^{\frac{\gamma-1}{\gamma}} \quad (14, 15, 16)$$

In order to simulate mixing in the ejector, the static pressure of both, the secondary inlet and the jet nozzle exit have to expand to the same value as they enter of the mixing section of the ejector, thus:

$$P_0 = P_1 \quad (17)$$

Also, it is assumed that the exhaust mixed flow will expand or compress to atmospheric pressure; thus:

$$P_2 = P_\infty \quad (18)$$

In this analysis, the ejector geometry is determined by specifying the area ratio of the mixing section to the inlet (A_2/A_0) and the exit diffuser to the mixing section (A_3/A_2). The analysis is performed for a constant area duct, so that A_3 equals A_2. Also, the total pressure and total temperature for the secondary and primary inlet are known or specified in the problem. The secondary flow's total pressure and temperature are determined by:

$$P_{t\infty} = P_{t1} = P_{\infty}\left(1 + \frac{\gamma-1}{2}M_{\infty}^2\right)^{\frac{\gamma}{\gamma-1}} \quad (19)$$

$$T_{t\infty} = T_{t1} = T_{\infty}\left(1 + \frac{\gamma-1}{2}M_{\infty}^2\right) \quad (20)$$

A pressure ratio (P_{to}/P_{t1}) and temperature ratio (T_{t0}/T_{t1}) are used to specify the total pressure and temperature in the primary flow. Now the system is reduced to 14 equations and 14 unknowns which can be solved.

The solution of this system of equations is found by successive substitution until one equation with one unknown remains.

The systematic solution of the equations can start with equations 8, 9, and 10 and by solving each equation for density.

$$\rho_i = \frac{P_i}{RT_i} \quad (21)$$

Similarly, equations 11, 12, and 13 can be solved for the velocities at each stage.

$$U_i = \left(2c_p(T_{ti} - T_i)\right)^{\frac{1}{2}} \quad (22)$$

These variables and equations 17 and 18 can be inputted into the conservation of momentum equation.

$$\left(P_0 + \frac{\left(2c_p(T_{t0}-T_0)\right)P_0}{RT_0}\right) + \frac{A_1}{A_0}\left(P_0 + \frac{\left(2c_p(T_{t1}-T_1)\right)P_0}{RT_1}\right) = \frac{A_5}{A_0}\left(P_{\infty} + \frac{\left(2c_p(T_{t2}-T_2)\right)P_{\infty}}{RT_2}\right) \quad (23)$$

Using equations 14, 15, and 16, the temperatures can be solved in terms of the remaining variables.

$$T_i = T_{ti}\left(\frac{P_i}{P_{ti}}\right)^{\frac{\gamma-1}{\gamma}} \tag{24}$$

Substituting the temperatures in the momentum equation yields:

$$\left(P_0 + \frac{\left(2c_p\left(\left(\frac{P_{t0}}{P_0}\right)^{\frac{\gamma-1}{\gamma}} - 1\right)\right)P_0}{R}\right) + \frac{A_1}{A_0}\left(P_0 + \frac{\left(2c_p\left(\left(\frac{P_{t1}}{P_0}\right)^{\frac{\gamma-1}{\gamma}} - 1\right)\right)P_0}{R}\right)$$
$$= \frac{A_5}{A_0}\left(P_\infty + \frac{\left(2c_p\left(\left(\frac{P_{t2}}{P_\infty}\right)^{\frac{\gamma-1}{\gamma}} - 1\right)\right)P_\infty}{R}\right) \tag{25}$$

Since the only two unknown variables in this equation are P_0 and P_{t2}, one can be solved in terms of the other,

$$P_{t2} = P_\infty L^{\left(\frac{\gamma}{\gamma-1}\right)} \tag{26}$$

where L is:

$$L = \left\{ \frac{A_0}{A_5} \left[\frac{P_0}{P_\infty} \frac{R}{2c_p} + \frac{P_0}{P_\infty} \left(\left(\frac{P_{t0}}{P_0} \right)^{\frac{\gamma}{\gamma-1}} - 1 \right) + \frac{A_1}{A_0} \left(\frac{P_0}{P_\infty} \frac{R}{2c_p} + \frac{P_0}{P_\infty} \left(\left(\frac{P_{t1}}{P_0} \right)^{\frac{\gamma}{\gamma-1}} - 1 \right) \right) \right] - \frac{R}{2c_p} + 1 \right\} \tag{27}$$

Similarly, the variables for velocity, density, temperature, and equations 17 and 18 can be substituted into the conservation of energy equation. The left-hand side was substituted with the variable K for shorthand notation, since it is only a function of P_0 and specified parameters.

$$K = P_0 \left(\frac{P_{t0}}{P_0} \right)^{\frac{\gamma-1}{\gamma}} \left(2c_p T_{t0} \left(1 - \left(\frac{P_0}{P_{t0}} \right)^{\frac{\gamma-1}{\gamma}} \right) \right)^{\frac{1}{2}} + \frac{A_1}{A_0} P_0 \left(\frac{P_{t1}}{P_0} \right)^{\frac{\gamma-1}{\gamma}} \left(2c_p T_{t1} \left(1 - \left(\frac{P_0}{P_{t1}} \right)^{\frac{\gamma-1}{\gamma}} \right) \right)^{\frac{1}{2}} \tag{28}$$

The right-hand side of the energy conservation equation becomes:

$$RHS = \frac{A_5}{A_0} P_\infty \left(\frac{P_{t2}}{P_\infty} \right)^{\frac{\gamma-1}{\gamma}} \left(2c_p T_{t2} \left(1 - \left(\frac{P_\infty}{P_{t2}} \right)^{\frac{\gamma-1}{\gamma}} \right) \right)^{\frac{1}{2}} \tag{29}$$

Substituting the solution for P_{t2} into the RHS of the equation yields:

$$RHS = \frac{A_5}{A_0} P_\infty \left(2c_p T_{t2} (L^2 - L) \right)^{\frac{1}{2}} \tag{30}$$

Only two unknown variable remain in the equation, T_{t2} and P_0. Solving for T_{t2} yields:

$$T_{t2} = \frac{K^2}{\left(\frac{A_5}{A_0} P_\infty \right)^2 * \left(2c_p (L^2 - L) \right)} \tag{31}$$

Next, the velocities, temperature, densities, and equations 17 and 18 can be substituted into the conservation of mass equation. The left-hand side of the conservation of mass will be substituted with the variable B for shorthand notation. The left-hand side of the equation yields:

$$B = \frac{P_0}{T_{t0}} \left(\frac{P_{t0}}{P_0}\right)^{\frac{\gamma-1}{\gamma}} \left(2c_p T_{t0}\left(1-\left(\frac{P_0}{P_{t0}}\right)^{\frac{\gamma-1}{\gamma}}\right)\right)^{\frac{1}{2}} + \frac{A_1}{A_0}\frac{P_0}{T_{t1}} \left(\frac{P_{t1}}{P_0}\right)^{\frac{\gamma-1}{\gamma}} \left(2c_p T_{t1}\left(1-\left(\frac{P_0}{P_{t1}}\right)^{\frac{\gamma-1}{\gamma}}\right)\right)^{\frac{1}{2}} \tag{32}$$

The right-hand side of equation 5 becomes:

$$RHS = \frac{A_5}{A_0}\frac{P_\infty}{T_{t2}} \left(\frac{P_{t2}}{P_\infty}\right)^{\frac{\gamma-1}{\gamma}} \left(2c_p T_{t2}\left(1-\left(\frac{P_\infty}{P_{t2}}\right)^{\frac{\gamma-1}{\gamma}}\right)\right)^{\frac{1}{2}} \tag{33}$$

Substituting T_{t2} and P_{t2} will yield:

$$RHS = \left(\frac{A_5}{A_0}P_\infty\right)^2 \left(\frac{2c_p\left(L^2-L\right)}{K}\right) \tag{34}$$

Finally, the system of equation has been reduced to a single equation with a single unknown:

$$\left(\frac{A_5}{A_0}P_\infty\right)^2 \left(\frac{2c_p\left(L^2-L\right)}{K} - B = 0\right. \tag{35}$$

with L, K, and B defined in equations 27, 28, and 32.

The solution is obtained using an iterative process. There are multiple possible solutions that satisfy the three conservation laws and the Second Law of Thermodynamics;

however the solution with the greatest entropy is the one that correctly describes the behavior of the flow.

This method of solving the system of equations is very efficient, since it provides a closed-form solution. A different method for solving the system of equations was considered that used a matrix iteration algorithm to solve the system of equation. However that method was much more computationally intensive than the method presented here which only requires the iteration of one variable to solve the system of equations. Furthermore, since the method only iterates a single variable to calculate the solution, the numerical accuracy increases.

This model, under the assumption of complete mixing without fluid losses, reveals that increasing the inlet area ratio dramatically increases the thrust augmentation ratio. Under this assumption, an infinite inlet area ratio will produce an infinite augmentation ratio. In reality, increasing the inlet area ratio will increase the augmentation until ratio it reaches a peak and then the augmentation ratio will decrease, as shown in Margason and Bevilaqua [2].

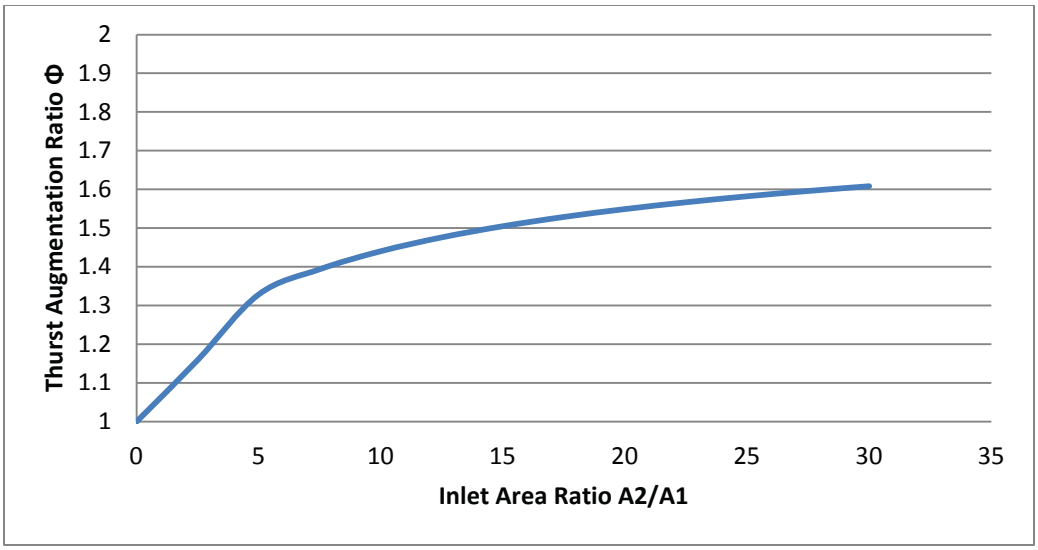

Figure 6: Thrust Augmentation for an ideal ejector.

The solutions predicted for the simple ejector configuration are shown in the Figure 7 for A_2/A_0 =5 and A_3/A_2=1. The graph shows the trend of the ejector performance as the aircraft accelerates. The ejector performance starts with a high augmentation ratio but exponentially decreases as the aircraft starts to accelerate. The solution was compared to Bevilaqua [1] for validation. Both solutions follow the same trend of increased performance at very low speeds, but dramatically decrease as the speed of the aircraft increases. Although the results from this model are encouraging, as stated before these results are ideal at best and do not contain viscous and pressure losses that happen in a real ejector. This model also assumes complete mixing, which depending on the ejector configuration is very improbable. Furthermore, the 1-D analysis cannot perform a deflection angle analysis since that would require a 2-D model. Hence, the 1-D analysis has the limitation of not predicting a decrease or increase in performance due to a deflection angle.

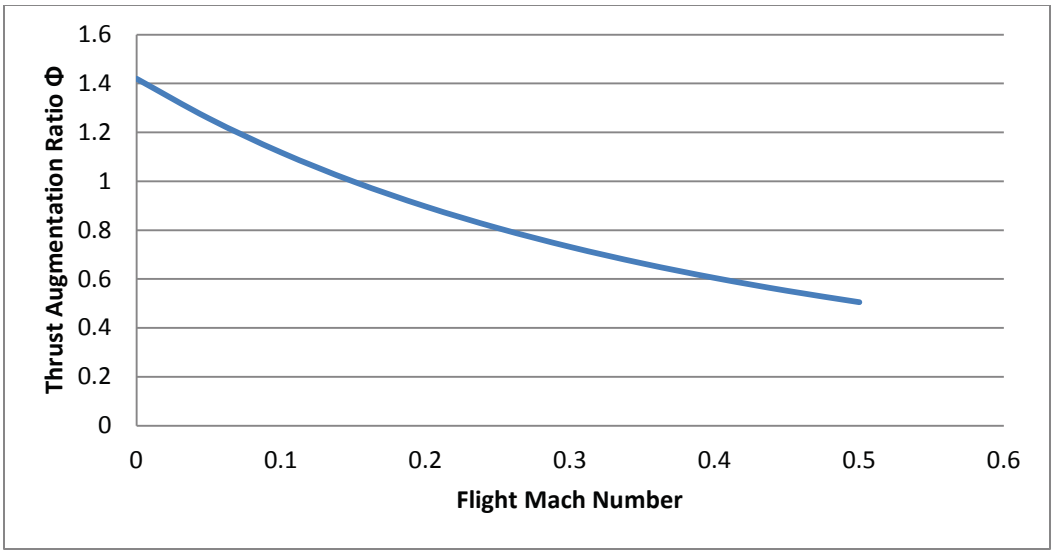

Figure 7: Ejector Performance solution for one dimensional model

Chapter 2: Numerical Procedure and Approach

The main objective of this research is to obtain a numerical solution for the performance of a thrust augmenting ejector in transition. To obtain the numerical solution for the ejector, a Computational Fluid Dynamics or CFD software is needed to simulate the flow in the ejector. The software used in this research is ANSYS FLUENT v14. This software has been proven to be reliable over the last decade making it an industry standard. Furthermore, ANSYS FLUENT provides a diversity of density-based and pressure-based solvers, each with different solving schemes for the Navier Stokes equations. The research used a two-equation turbulent model with the coupled pressure-based solver for the numerical analysis because it provided a robust and stable convergence, while requiring less computational time needed than the density-based solver.

For the simulations, there are design choices to be made in order to calculate the solution. The first is the operating condition for the system to be design at. Since the objective of the system is to be used for STOVL, then it will be operating close to the ground; thus the atmospheric conditions used are for standard sea level. As discussed in the previous chapter, the area ratios for the inlet and the diffuser area have to be specified for solution and geometric purposes. The inlet area ratio (A_2/A_0) is specified to be 5 while the diffuser area ratio (A_3/A_2) is specified to be 1.2. Finally, the total pressure ratio (P_{t0}/P_{t1}) and total temperature ratio (T_{t0}/T_{t1}) are specified to be 1.5 and 1.10 respectively. A higher pressure ratio gave a better performance; however any total pressure ratio higher than 1.5 would have compressibility problems and possible shockwaves inside the ejector. To avoid discontinuities in the flow, these values where chosen.

The ejector geometry used in this research consists of two flaps and a center body nozzle. The lower flap is integrated into a wing to exploit the jet flap effect caused by this configuration. The wing section of the ejector is a modified NACA 0012 symmetric airfoil. The ejector flap shroud is the same as the NACA 0012 airfoil shroud but scaled down. The inner mixing section of the ejector has an angle deflection of 3 degrees to progressively increase the diffuser area without any flow separation. The nozzle shroud center point is the origin for the Cartesian axis system. The nozzle exit is 0.02856 meter wide and the initial mixing area (A2) of 0.1428 meter wide. The exit area of the ejector has a width of 0.174 meter. The wing including the lower flap is approximately 1.06 meter long. The ejector flaps are 0.3858 meter long and 0.07138 meter wide, with an effective mixing length of approximately 0.3 meter long.

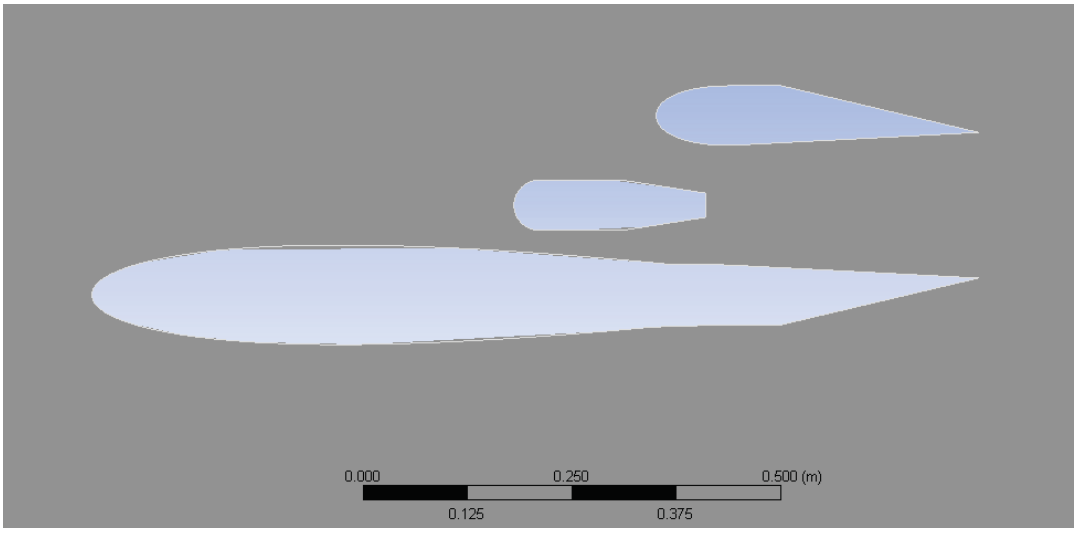

Figure 8: Geometry for a wing integrate thrust augmenting ejector

The ejector system will rotate around a hinge point locate in the lower flap. The lower flap will deflect down in the same manner of a normal control surface. The upper flap and nozzle will also rotate around this hinge point as demonstrated in Figure 9. Since

both flaps rotate around the same hinge point, both flaps remain parallel, providing an effective duct to guide the flow.

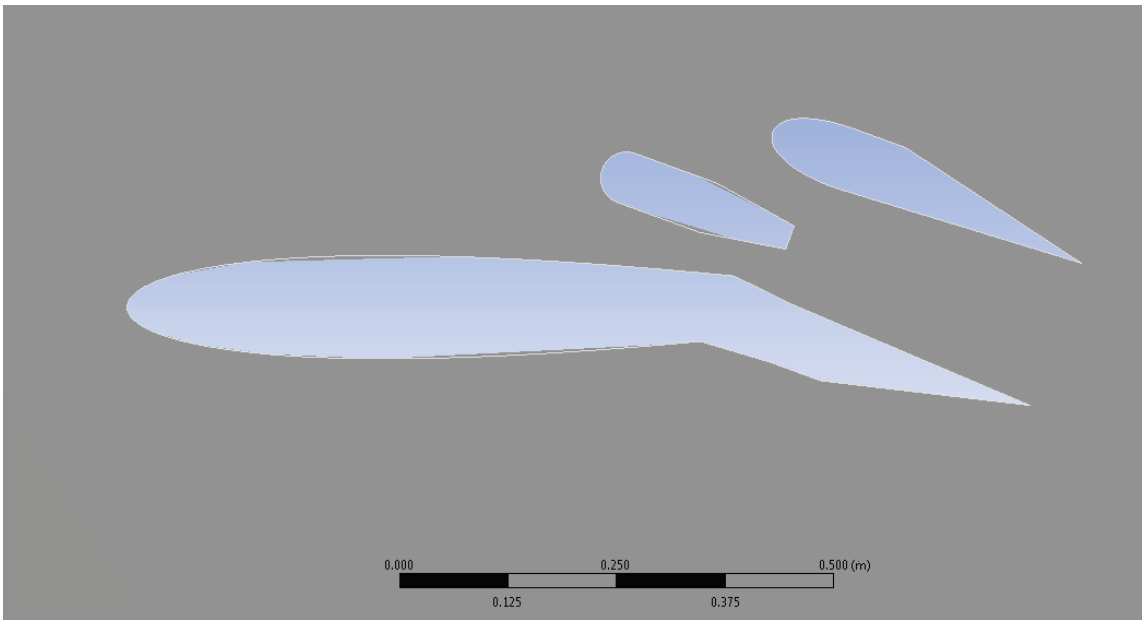

Figure 9: Ejector geometry at 20°

A two dimensional computational domain was generated for the ejector system and the surrounding flow region. The mesh type chosen was a triangular unstructured mesh. The origin of the coordinate system is the midpoint of the nozzle shroud. Since this is an asymmetrical configuration, the domain includes the entire ejector system. The domain size is 8 meter long to the left of the ejector and 16 meter to the right of the ejector. The height of the domain is 16 meter in total, divided in half by the Y line at the origin (y=0).

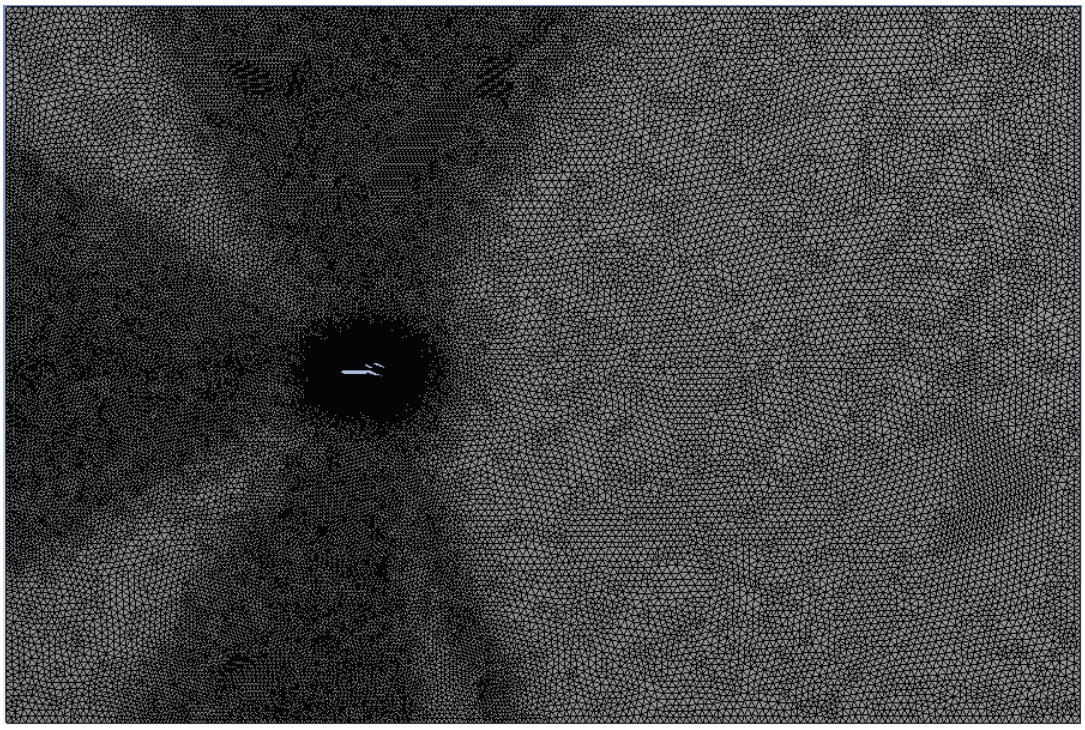

Figure 10: Entire Grid for the computational domain

The average computational domain for all the simulations was approximately 1.65 million triangular cells. The domain was tightly clustered around the edges of the ejector and the space between the ejector flaps. The minimum cell size around the edges was .0001 meter with a low cell growth rate of 1.05.

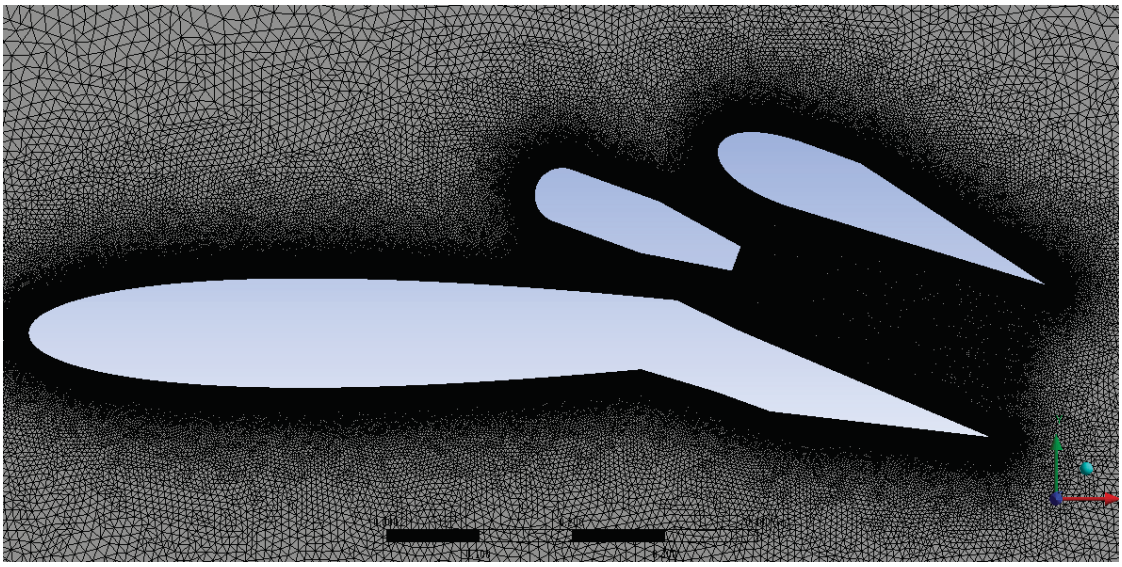

Figure 11: Grid near the ejector surfaces.

For this research, different domain sizes and configurations were tested to obtain the best balance of computational speed and accuracy. The first domain size was a combination of a semicircle and half-rectangle with a total length of 18 meter. The second configuration was a rectangular domain 18 meter long in total and 12 meter wide with the ejector in the center of the rectangular domain. The third configuration was a scaled up version of the second domain, 24 meter long by 16 meter wide with the ejector still in the center. The fourth configuration was the same as the third configuration but the ejector was skewed to the left, instead of being in the domain center. The fifth domain was a scaled up version of the fourth configuration, 30 meter by 20 meter. The fourth configuration was chosen, since it provided better accuracy than the previous configurations and no significant loss of accuracy, less than 1%, when compare to the fifth configuration.

Furthermore, the computational time needed was 200% less than that needed by the larger domain of the fifth configuration.

The turbulence model used in this research is the Realizable two-equation κ-ε turbulence model. This turbulence model is very common in CFD software for calculating Navier Stokes equations. The turbulence constants were left as the ANSYS FLUENT defaults for smoother convergence, and instead the turbulence was specified at the nozzle exit. The turbulence intensity was determined empirically by running different test run simulations with different initial turbulent kinetic energy (κ) values at the nozzle exit. The result with the best performance, the highest thrust augmentation ratio, and a good mixing at the ejector walls at the exit was found using the correlation of:

$$\kappa = 0.1 * U_0^2 \quad (36)$$

Using the equation from Tu, Yeoh [5]:

$$\kappa_{inlet} = \frac{3}{2}(U_{inlet}^2 I^2) \quad (37)$$

Using the two previous equations, the turbulence intensity, *I*, for the nozzle exit (which acts as an inlet in the CFD simulation) was 25% in order to simulate enhanced entrainment of a hyper mixing nozzle [10]. At this intensity level, the mixing caused by entrainment started to reach the ejector duct walls at the exit of the diffuser. This is a higher number in comparison to the numbers of Margason[2] who used 20% turbulence intensity; however this value is only specified at the nozzle exit. The flow turbulence is dissipated around the duct, which lowers the overall turbulence intensity of the mixed flow to well under 20%.

For the simulation, the coupled pressure-based solver was chosen for its robust convergence and computational time efficiency. For the momentum, continuity, and energy schemes a second-order upwind scheme was used, and for the turbulence scalar quantities a first-order upwind scheme was used with a convergence criterion of 1e-6 for all variables.

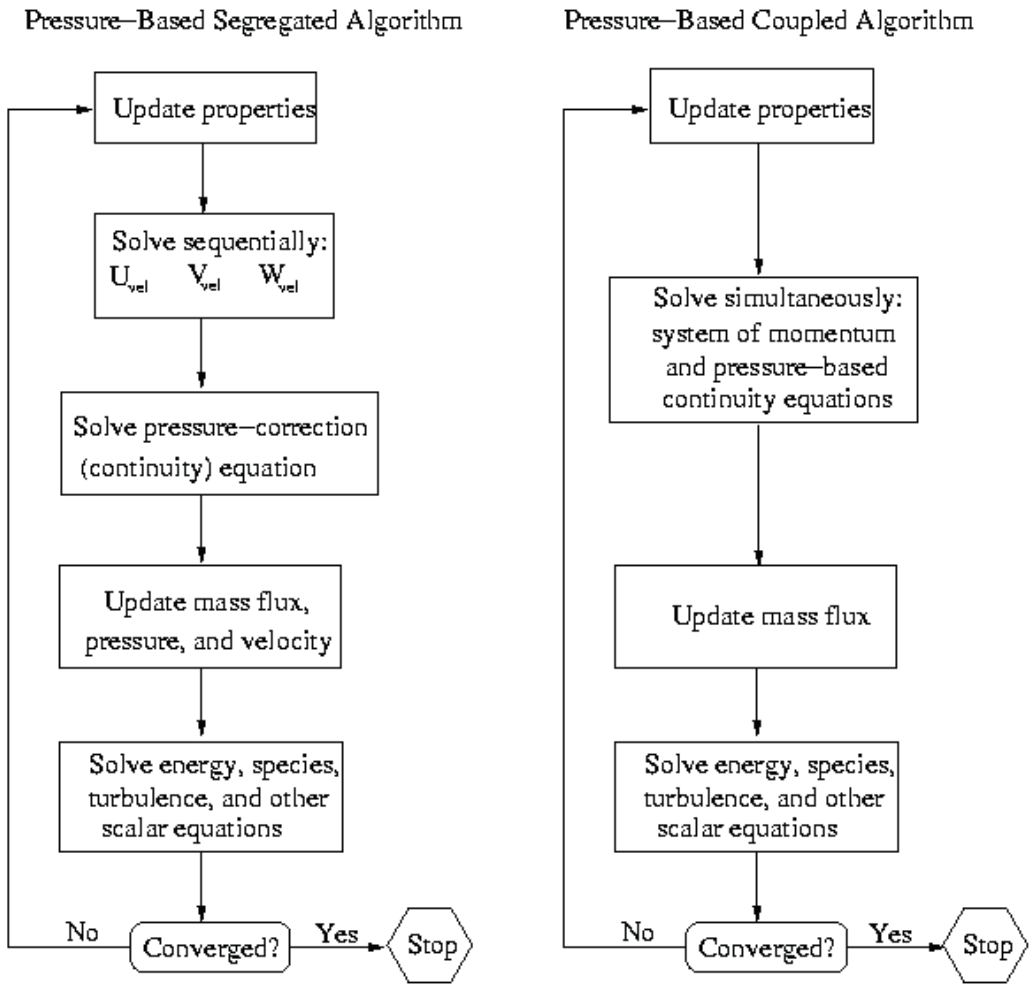

Figure 12: ANSYS FLUENT solution algorithm for Pressure Based Solver

For the boundary condition in FLUENT, the free stream flow velocity and the static temperature were specified at the upstream boundary of the computational domain. The

turbulence for the velocity inlet was left with the default values, since the atmospheric conditions are assumed to have little to no turbulence. The nozzle exit was specified as a pressure inlet, in which the total pressure, total temperature, and an initial value for static pressure are specified. The total pressure and temperature are user inputs, much like the theoretical model. However, the static pressure value is a function of the ejector entrance, so the initial condition given must be a similar value to the converged solution. The initial value inputted was taken from the 1-D analysis shown in the previous chapter. The end of the computational domain was specified as a pressure outlet, and it was left with the default settings. The fluid flow (air) was specified as an ideal gas, meaning density is not constant in the simulation.

The performance of the ejector in transition was obtained by running multiple CFD simulations, each with the ejector configuration deflected at a different angle. Each different deflection angle will be run at different Mach numbers to create a trend of how the ejector performance changes at that specific deflection angle as the speed of the aircraft increases. The deflection angles to be studied in this research were 0°, 12°, 20° to 60° in increments of 8°, and a final data point at 90°. Each deflection angle, with the exception of 12° and 90°, were tested at Mach numbers from 0.01 to 0.5 to understand the performance limitations of the ejector system. This Mach number range was specified because the design parameter for this ejector system is take-off and landing, where the velocities hardly past Mach 0.3. Mach 0.5 was added to demonstrate the effect of the ejector after take-off if the ejector was left operating.

The thrust augmentation ratio was calculated using Simpson's Rule to integrate the densities, velocities, and pressures at the ejector exit. Furthermore, Simpson's Rule is

also used to numerically calculate the mass flow rate at the primary nozzle exit. The thrust augmentation formula for the numerical solution includes a pressure term to account for under-compression or over-compression. Hence the formula becomes:

$$\Phi = (\int [\rho_3 U_3 (U_3 - U_\infty) + (P_3 - P_\infty)] dy_3)/(U_* \int U_0 \rho_0 dy_0) \quad (38)$$

The data values for the 20 points needed for each of numerical integration was taken from the solution using the Probe tool in the CFD-Post program.

Similarly, Simpson's Rule is used to integrate the pressure around the ejector's surfaces to determine the overall Lift to Thrust Ratio of the ejector system.

At a deflected angle, the thrust is vectored at an angle from the horizontal free-stream, and thus thrust calculation becomes a vector analysis problem. However, the assumption of horizontal thrust recovery was made to calculate the thrust augmentation ratio at the deflected angles. Spence's assumption[16] of horizontal thrust recovery postulates that for a jet flap in an ideal flow, the total jet thrust would always be recovered as a horizontal force regardless of the initial deflection angle, since the jet will ultimately be turned in the direction of the free-stream. In Bevilaqua, Schum, and Woan[3], the predicted thrust recovery is as high as 90% for a deflection angle of 70° and almost total for small angles. Thus, the assumption of horizontal thrust recovery was reasonable in this case; since a jet flap effect was caused by the ejector flap and the horizontal thrust was recovered downstream.

Chapter 3: Results & Discussion

The main approach of the research was to utilize a numerical solution for the performance of a thrust augmenting ejector in transition. As shown in Chapter 1, the thrust augmentation started with a high ratio but decreased as the aircraft began to accelerate. This trend was caused by a large increase in ram drag that decreased the suction at the inlet. So instead of the air being sucked in by entrainment, the forward speed was ramming the air into the ejector. Another similar explanation is that as the free stream velocities became larger than the entrainment velocities; hence the jet entrainment effect on the flow field became negligible. Similarly, as the airplane forward speed increased, so did the energy of the atmospheric flow. Since the flow was already partly energized, the amount of energy originally imparted by the ejector decreased. So basically, as $U_{atmosphere}$ approaches U_{exit} the energy or thrust augmentation imparted by the system goes to zero. However, this trend was only valid at a horizontal configuration with neither pressure nor flow separation losses.

Figure 13 and Figure 14 depict the performance trends of the ejector at different deflection angles for a real fluid. The trend displayed on Figures 13 & 14 demonstrates a decreased in performance as the deflection angle of the ejector increases.

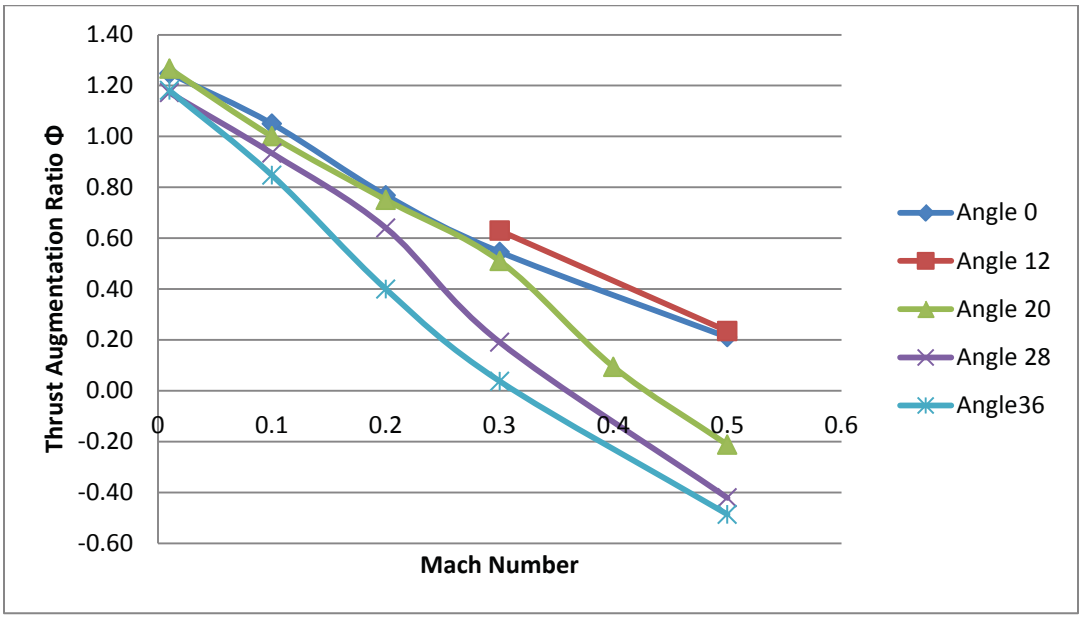

Figure 13: Performance Mapping of Ejector for deflection angles 0 to 36 degrees.

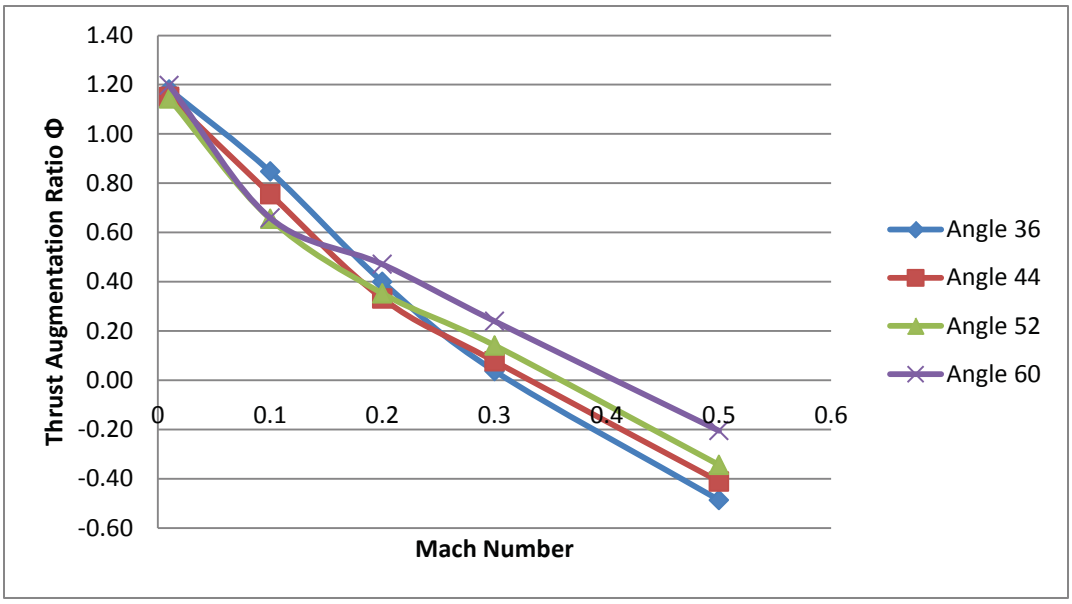

Figure 14: Performance Mapping of Ejector for deflection angles 36 to 60 degrees.

Table 1: Thrust Augmentation Ratio Results for the Numerical Simulations.

Angle	Mach Number .01	Mach Number .1	Mach Number .2	Mach Number .3	Mach Number .5
0	1.25	1.05	0.77	0.55	0.21
12				0.63	0.23
20	1.27	1.00	0.75	0.51	-0.21
28	1.17	0.93	0.64	0.19	-0.42
36	1.18	0.85	0.40	0.04	-0.49
44	1.15	0.76	0.33	0.08	-0.41
52	1.14	0.65	0.35	0.14	-0.34
60	1.20	0.66	0.47	0.24	-0.21
90	1.11				

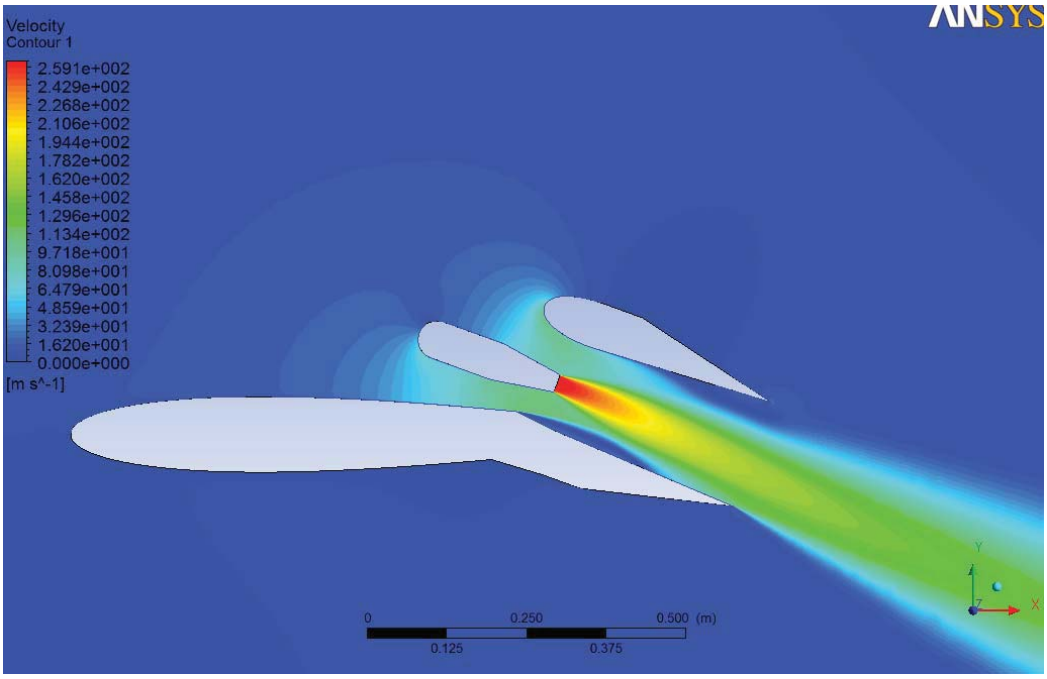

Figure 15: Velocity Contour at deflection angle 20 degrees and Mach number 0.01

The trend in Figure 13 can be explained using Figures 15 to 19 as reference. The trend depicts a decrease in performance as the velocity increases, which is due to ram drag as previously stated. In Figure 15, the ejector is producing a suction force caused by entrainment, which is reduced as the velocity increases as shown in Figures 16 and 17. Figures 18 and 19 show the ejector at high speed; where the entrainment effect on the field can no longer be observe and the flow is being rammed into the ejector by the forward speed; hence the loss of performance that was described by the analytical method. However, the trend values are lower than the analytical method predicted. The main reasons are boundary layer separation in the lower ejector wall, Figure 18, and pressure losses not predicted by the one dimensional analysis. As the deflection angle increased, the lower wall flow separation increases, and hence performance suffers. At higher speeds, the separation worsens and the trend shows an inflection point when

separation occurs on the lower wall. Similarly, the other deflection angles shown in Figure 13 behave in the same manner.

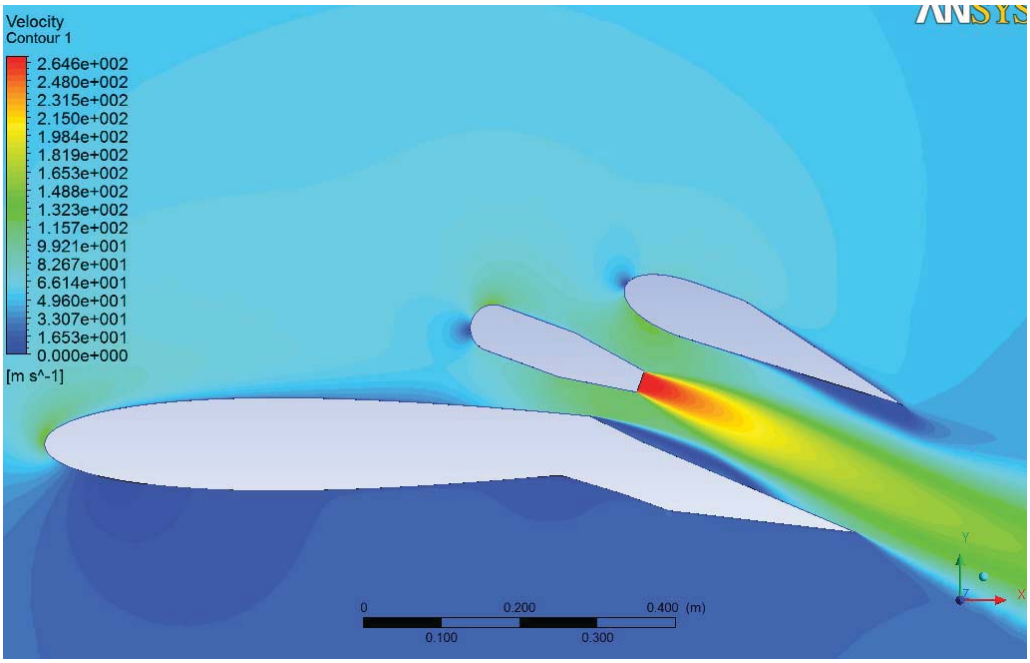

Figure 16: Velocity Contour at deflection angle 20 degrees and Mach number 0.1

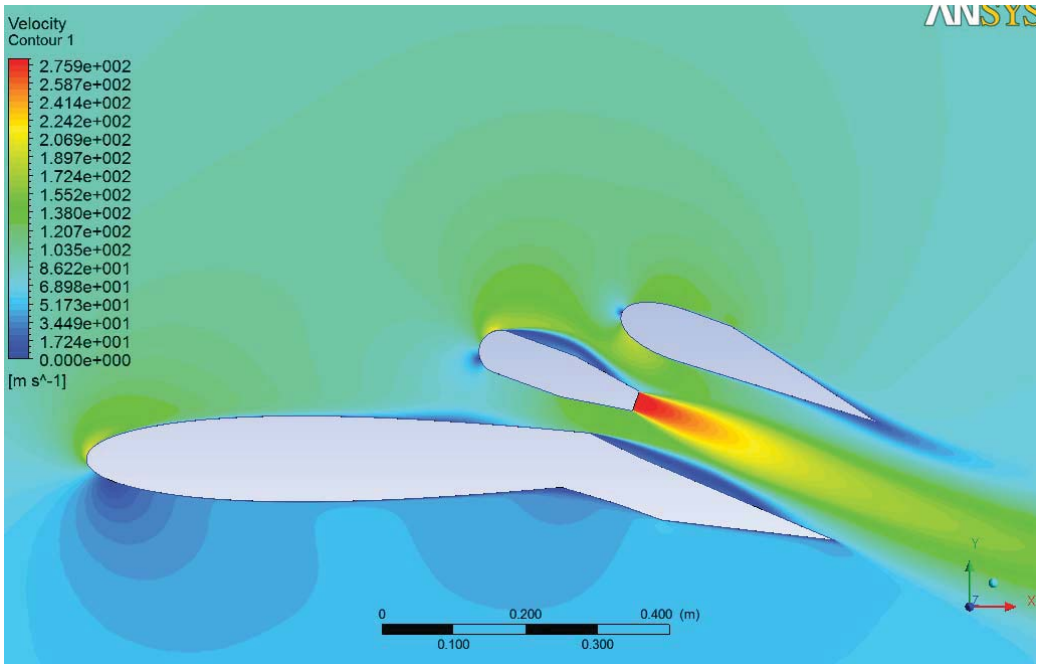

Figure 17: Velocity Contour at deflection angle 20 degrees and Mach number 0.2

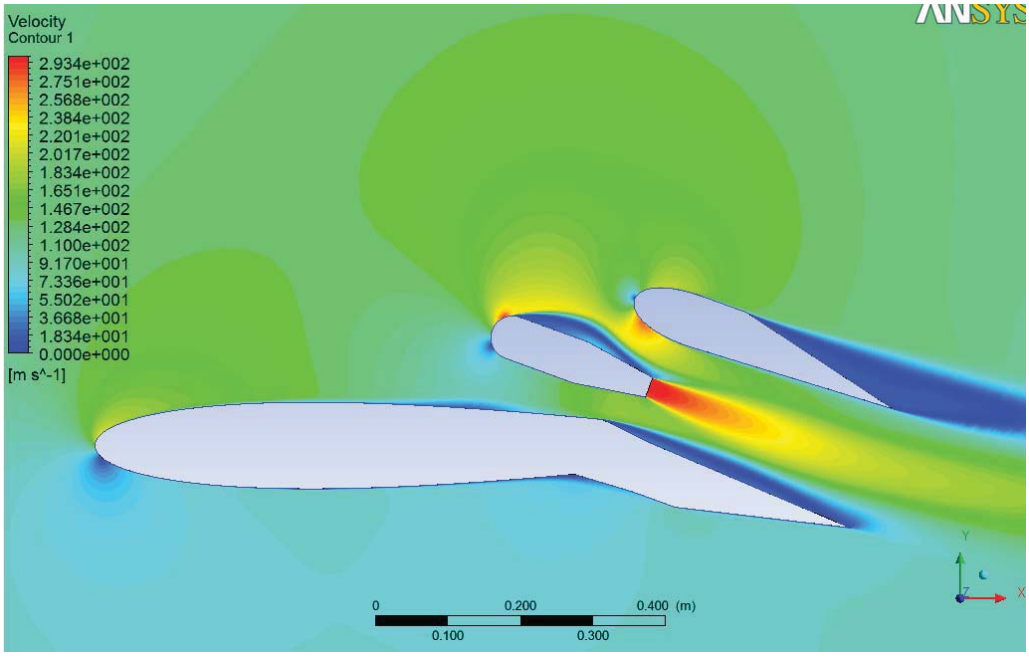

Figure 18: Velocity Contour at deflection angle 20 degrees and Mach number 0.3

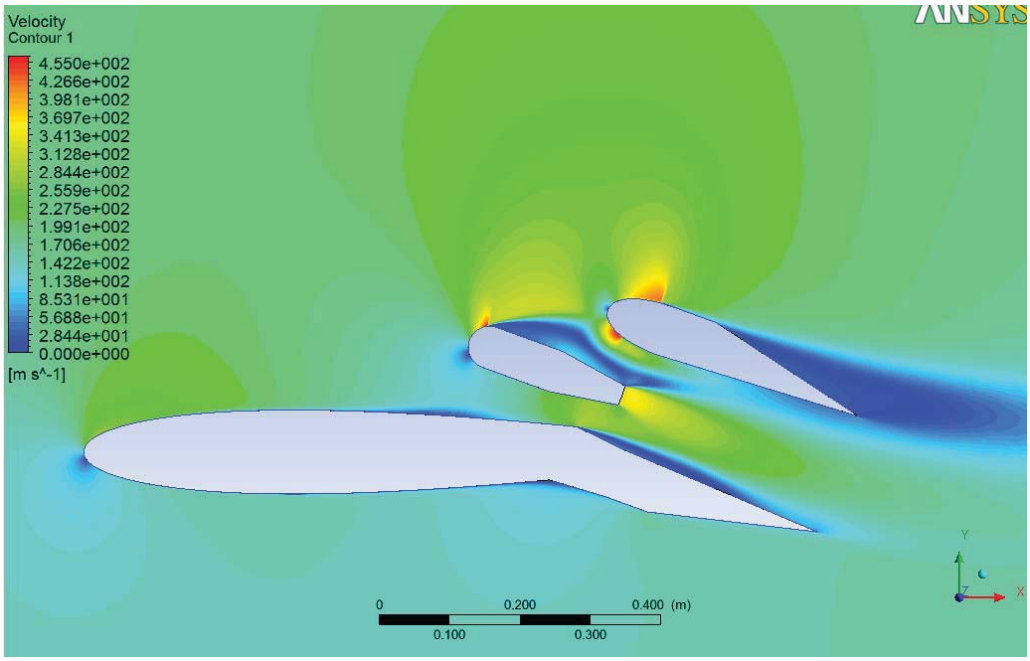

Figure 19: Velocity Contour at deflection angle 20 degrees and Mach number 0.5

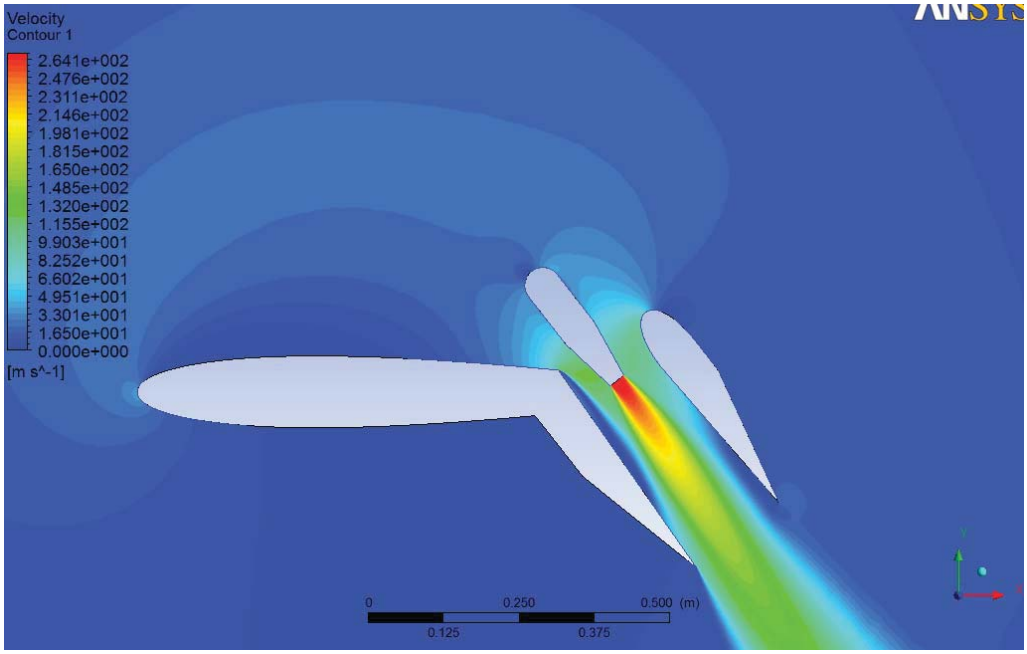

Figure 20: Velocity Contour at deflection angle 52 degrees and Mach number 0.01

The trends in Figure 14 can be explained by using Figures 20 to 24 for reference. These trends follow the same principle as the 1-D analysis, where the ram drag decreased the ejector performance by reducing the entrainment effect on the flow field. The trends in Figure 14 show an inflection point as the flow accelerates. The inflection point was caused by flow impingement on the upper wall of the ejector duct and flow separation from the lower wall as the forward speed accelerated, as shown in Figures 21 and 22. This effect appeared at lower speeds for higher deflection angles, as shown in Figure 19. There is an improvement as the velocity accelerates, reducing impingement and separation as shown in Figure 24; however, it is small when compared to the ram drag losses. The other angles on Figure 14 behave similarly.

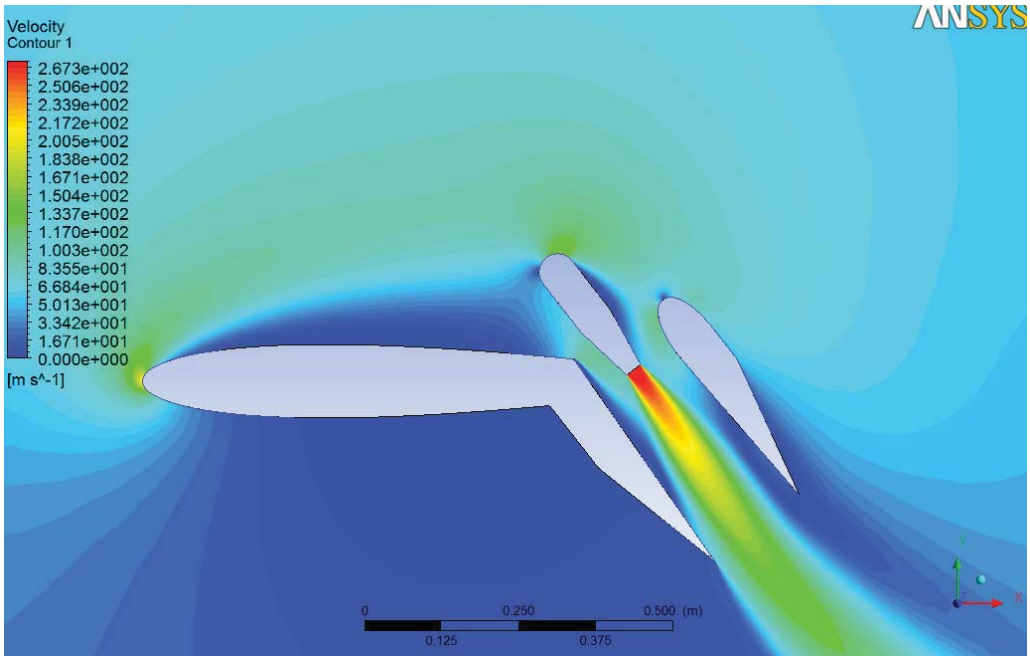

Figure 21: Velocity Contour at deflection angle 52 degrees and Mach number 0.1

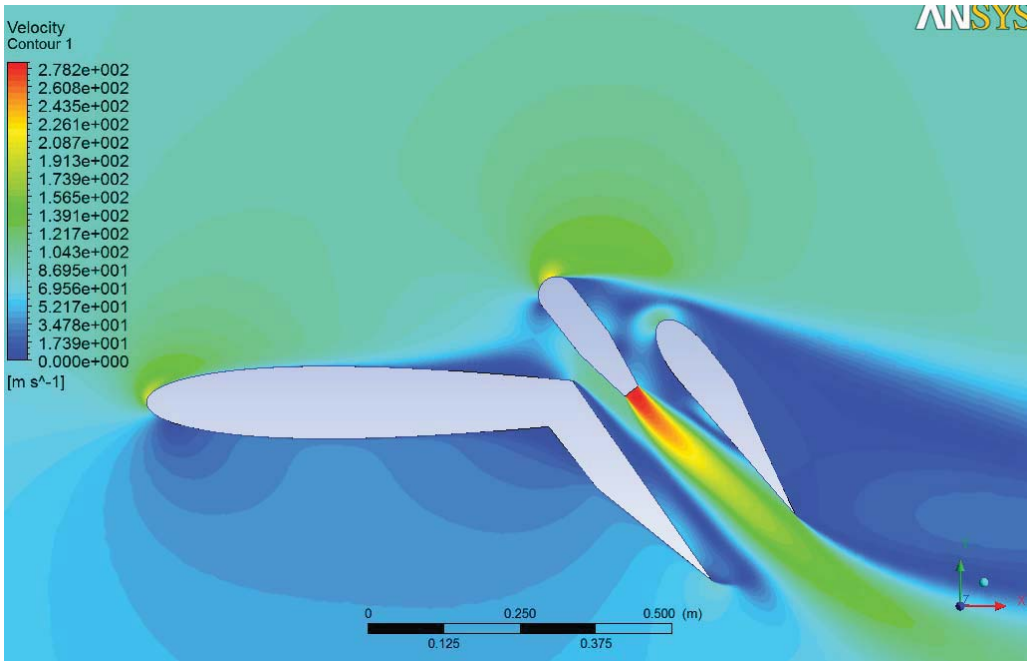

Figure 22: Velocity Contour at deflection angle 52 degrees and Mach number 0.2

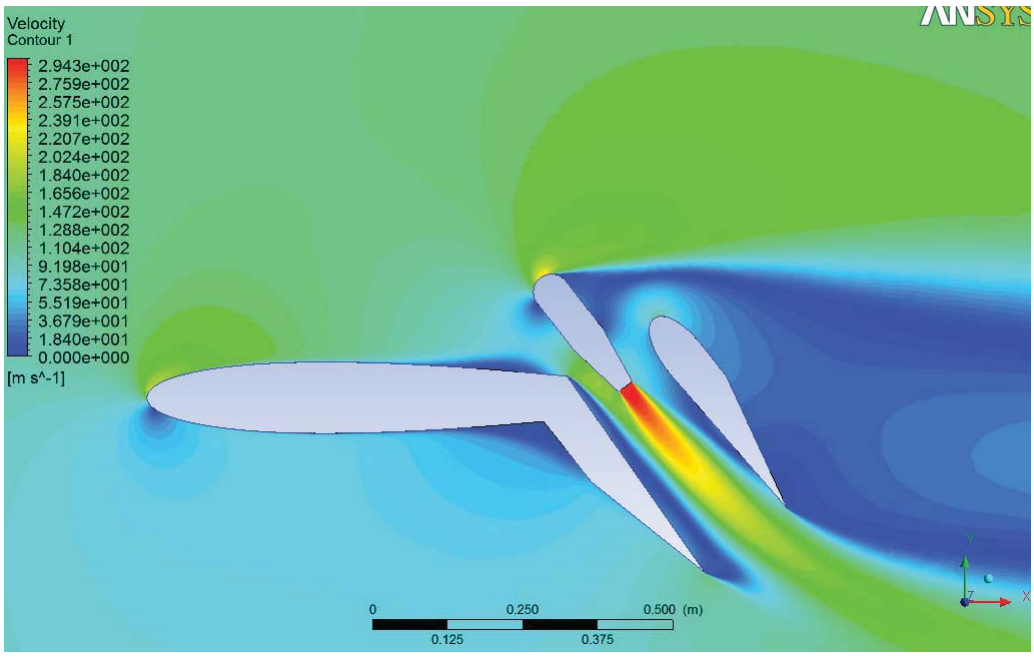

Figure 23: Velocity Contour at deflection angle 52 degrees and Mach number 0.3

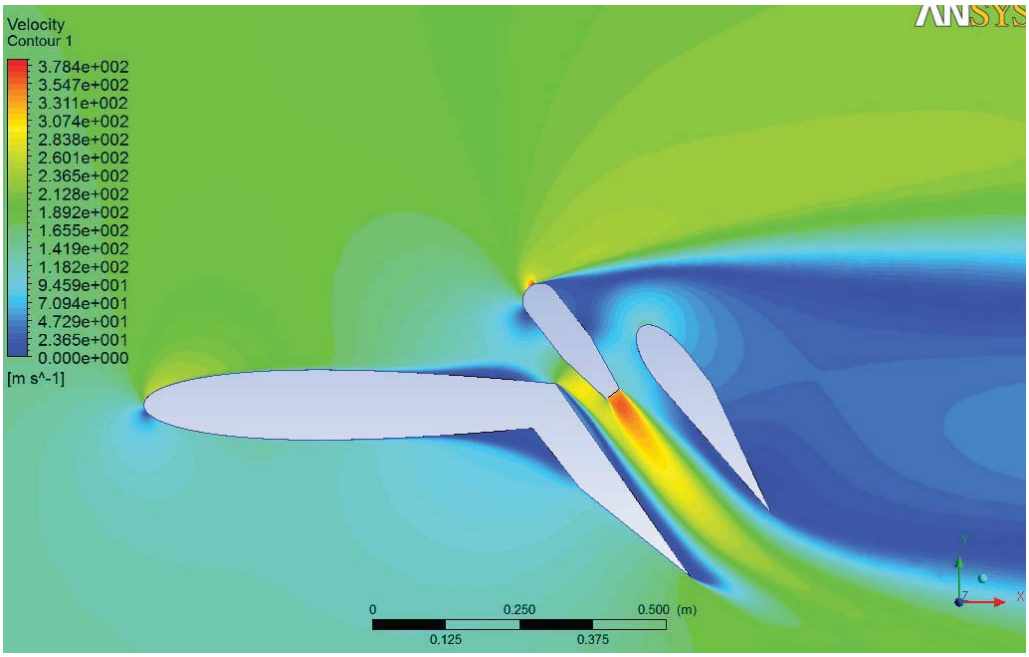

Figure 24: Velocity Contour at deflection angle 52 degrees and Mach number 0.5

The thrust augmenting ejector produces significant thrust augmentation at very low speeds, which is ideal for take-off and landing. However, the overall performance of the ejector seems to be limited to Mach numbers lower than 0.25, since the performance of the ejector quickly decreases at higher speeds. As explain before, the ejector ceases to function after Mach 0.3, since the ejector stops functioning as a jet pump. The entrainment effect of the flow field is overwhelmed by a large ram drag, which causes the thrust augmentation to decrease. Furthermore, a large flow separation at high deflection angles and heavy pressure losses occur in the ejector at high Mach numbers. The ejector configuration should be turned off after Mach 0.25 to avoid these disadvantages. At this speed, the wing produces enough lift to support the aircraft weight and become wing-

borne. After the ejector is turned off, it is folded into a single wing, thus avoiding any drag effects, as shown in Figure 25.

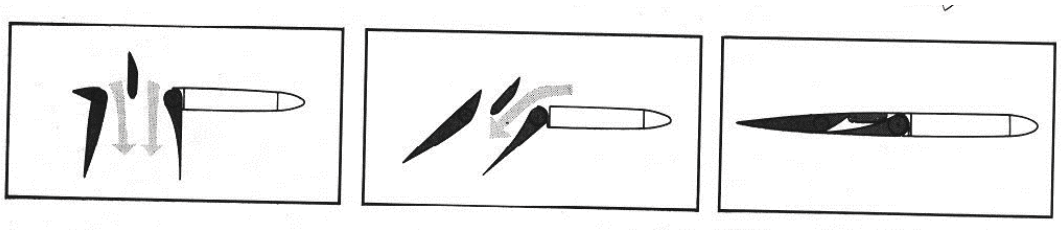

Figure 25: Wing-integrated ejector assembly for a XFV-12A prototype aircraft during and after operation. Provided by AVSIG.com[18]

Table 2: Lift results for the Wing-integrated Ejector configuration at Ma=0.1

	Angle 0	**Angle 20**	**Angle 28**	**Angle 36**	**Angle 44**	**Angle 52**	**Angle 60**
Total Lift (N)	1751.8	2520.8	3437.4	4522.3	4132.9	3664.5	4263.4
Lift toThrust Ratio	0.75	1.13	1.65	2.39	2.42	2.45	2.87

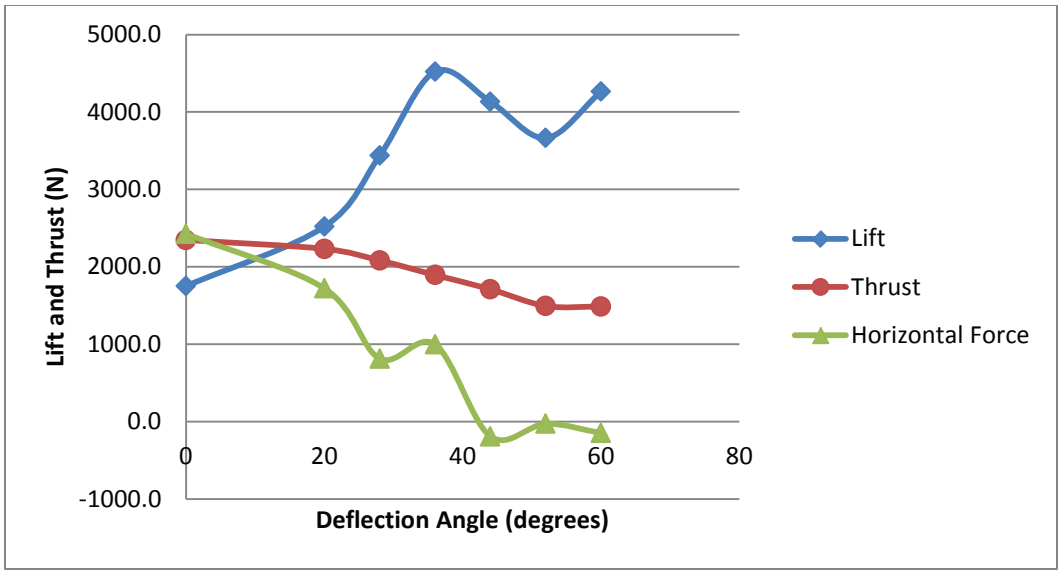

Figure 26: Forces produce by Ejector configuration at Ma=0.1.

Table 2 and Figure 26 depict the lift produce by the ejector wing configuration at Mach 0.1. The lift produced by the ejector peaks at the deflection angle of 36° before decreasing at 44° and 52°. This explanation for this main peak is that at higher angles, the lift vector is rotated back producing drag instead of lift. This effect was shown by the net horizontal force line decrease in Figure 21. However, by the deflection angle of 60°, the vertical component of the ejector thrust adds to the wing lift, increasing the total lift and producing the secondary peak. A 36° angle is the perfect balance for the amount of lift produce by flap deflection and the amount of surface area producing upward lift. Furthermore, the thrust continuously decreases as the as the deflection angle increases. This decrease in thrust is turned into lift by the thrust vectoring of the ejector.

After examining these results, the feasibility for this ejector configuration as STOVL instrument is definitely possible. The thrust is increased for the low speeds at which most aircraft take-off. The lift under the wing is significant, which allows the aircraft to have a

lower stall speed and a shorter take-off distance. The thrust augmentation ratio at near zero speeds is approximately 1.20 for most of the deflection angles; hence the aircraft could hover at these angles. As the aircraft accelerates forward, the pilot should decrease the deflection angle in order to maintain a high augmentation ratio and assure a smooth transition toward wing borne flight. Furthermore, as the pilot vectors the ejector towards 0 degrees and accelerate towards wing borne flight, the flow stays attached at the highest Mach numbers and smallest angles. After the aircraft is airborne, the pilot can turn off the ejector in order to avoid the drag effects caused during high speeds. Similarly for landing, the pilot could vector the ejector towards high deflection angles, where the separation drag will slow the aircraft down. This will allow the aircraft to land vertically, since as the aircraft slows down the thrust augmentation increases. This method of landing could reduce the need for arrested gear in aircraft carriers or the need for a breaking turn to reduce the aircraft speed. Furthermore, many landing accidents are caused by stalling the aircraft during the breaking turn. Since the aircraft can land vertically without the need for a breaking turn, the overall safety aircraft would be improved.

Chapter 4: Improvements & Recommendations

After evaluating the results and understanding the flow limitations of the design, two possible improvements over the original design were tested individually. In the first design, the nozzle was deflected to a lesser angle than the deflection angle of the ejector. This improvement was aimed to reduce the flow separation in the nozzle body and to improve the pumping effect through the inlets. The second design consisted of adding wall jets to the ejector wall near the entrance of the duct. In this design, the thrust for this design was split between the primary nozzle jet and the wall jets. The primary nozzle had half the original nozzle area and each wall jet had a quarter of the original nozzle area, so that the inlet area ratio was not changed. This improvement was aimed to reduce the flow separation in the ejector duct walls by energizing the boundary layer of the ejector diffuser walls. These improvements were tested on the ejector configuration at a deflection angle of 36° and compared to the original ejector configuration as a control parameter.

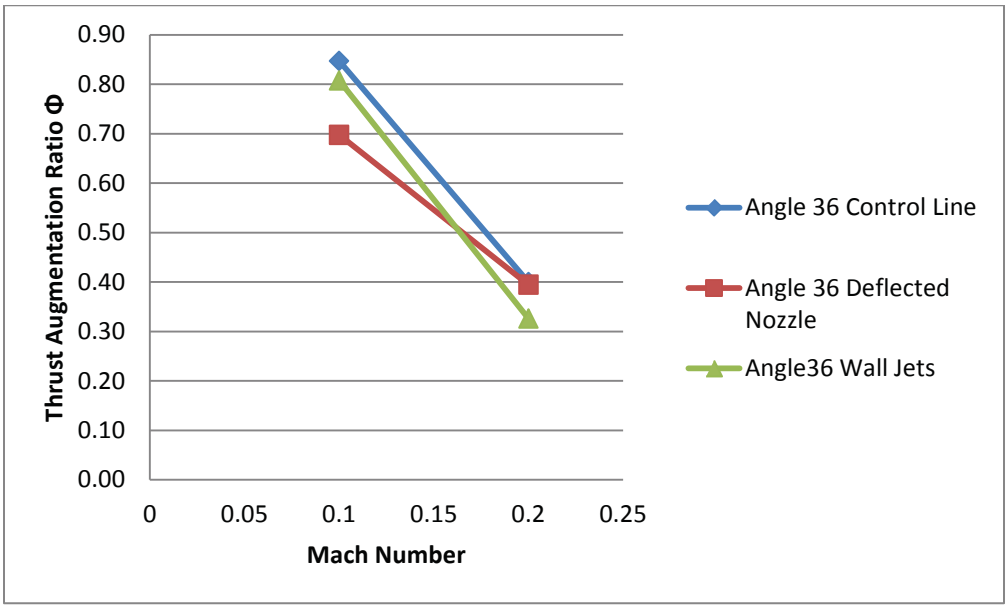

Figure 27: Thrust Augmentation Ratio trend for possible improved designs

Figure 27 shows that the possible improved designs performed slightly below the control configuration. The trends showed the wall jet configuration with a much steeper angle than the deflected nozzle. However, these results are mixed, since neither of the designs proved to be superior to the other.

Table3: Thrust Augmentation Ratio for possible improved designs at Mach 0.1 and 0.2

Configuration	Mach Number .1	Mach Number .2
Angle 36 Control Test	0.85	0.40
Angle 36 Deflected Nozzle	0.70	0.39
Angle 36 Wall Jets	0.81	0.33

Figures 28 and 29 demonstrate that the deflected configuration improved the upper inlet flow; however, this configuration had a detached flow on the lower wall of the ejector and heavy impingement of the upper ejector wall. This caused the ejector performance to decrease. There might be an intermediate position where the impingement and flow separation would be minimize, but such critical alignment between nozzle and ejector would be highly impractical in an aircraft system, and so this approach was not investigated further as part of this study.

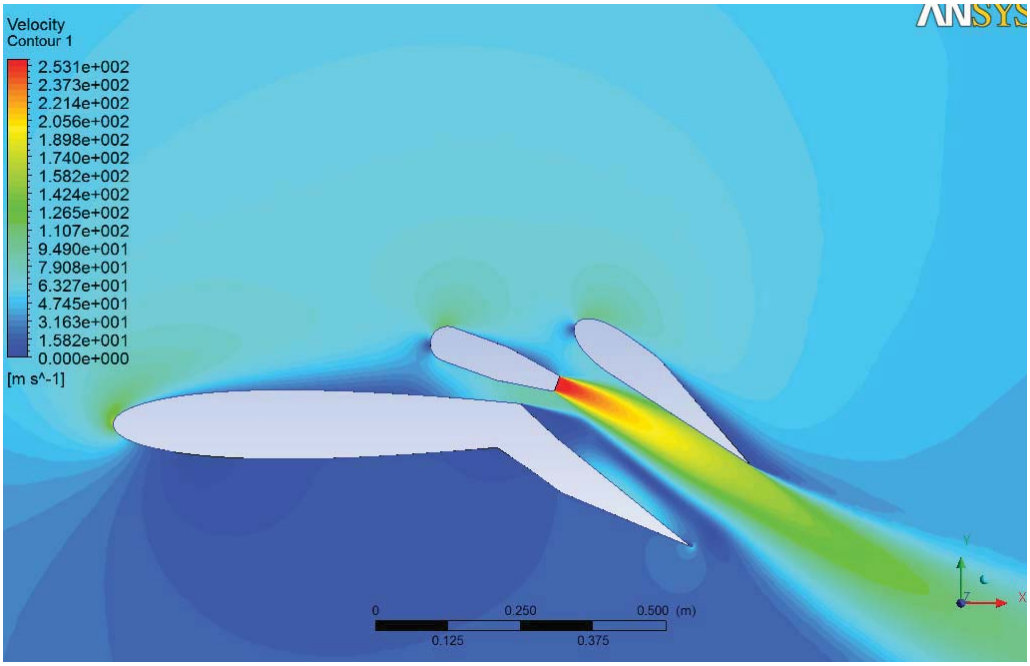

Figure 28: Velocity Contour for Deflected Nozzle Configuration at Mach 0.1

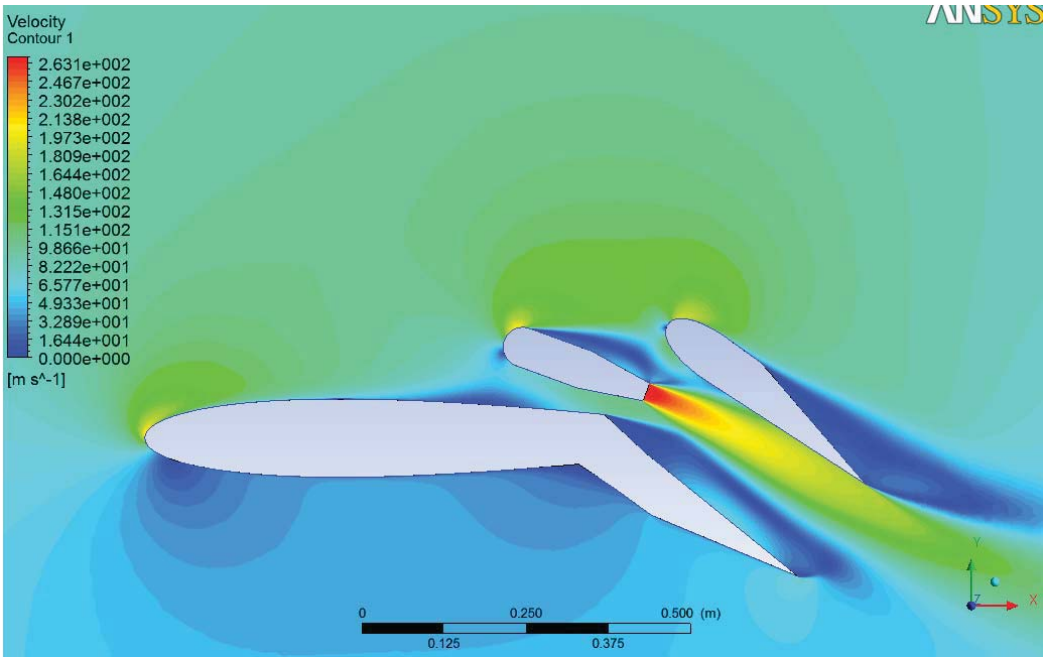

Figure 29: Velocity Contour for Deflected Nozzle Configuration at Mach 0.2

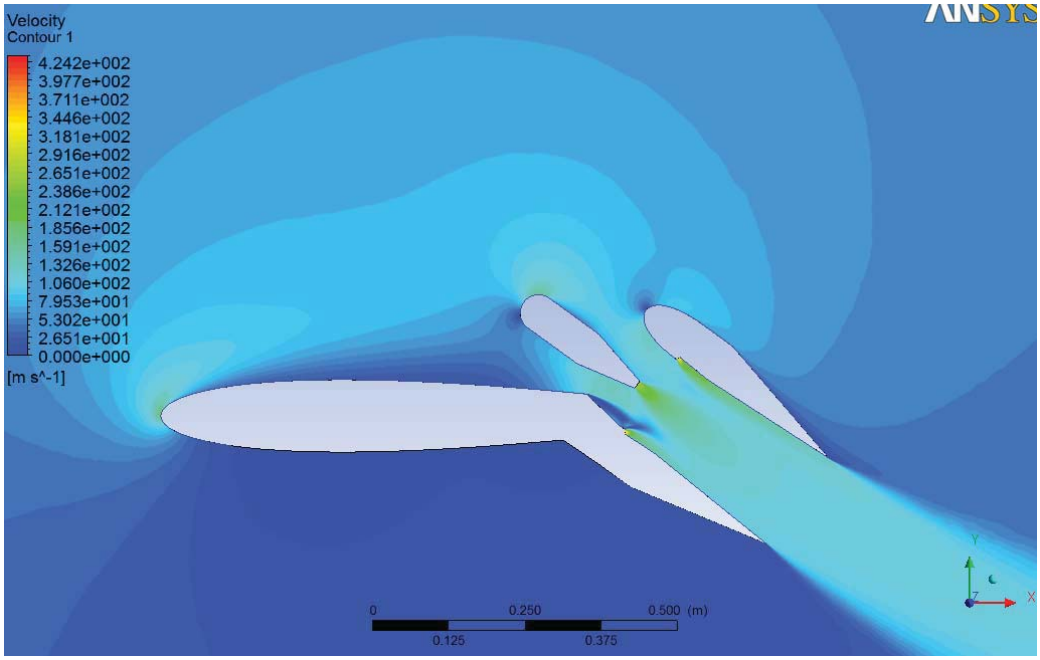

Figure 30: Velocity Contour for Wall Jets Configuration at Mach 0.1

Figures 30 and 31 show the wall jet configuration greatly improving mixing and eliminating flow separation inside the ejector duct. This configuration is more practical

than the deflected nozzle design, and could be implemented on the ejector. However, the configuration with wall jets has higher frictional losses than the configurations without wall jets and this reduces the thrust augmentation ratio as shown in Table 3 and Figure 27. Nevertheless, the Wall Jets can produce greater thrust augmentation at larger diffuser angles and/or larger inlet area ratios by providing better flow mixing and avoiding flow separation as shown by Margason [2].

Finally, this study analyzed only one inlet area ratio. Increasing the inlet area ratio improved the thrust augmentation ratio as demonstrated in Margason and Bevilaqua [2]. This might decrease the compressibility losses on the ejector and delay the critical Mach number of the system. Furthermore, rotating the flaps outward to increase the diffuser area might also ease the compressibility effects on the ejector. These solutions should warrant further studies for improving the ejector performance.

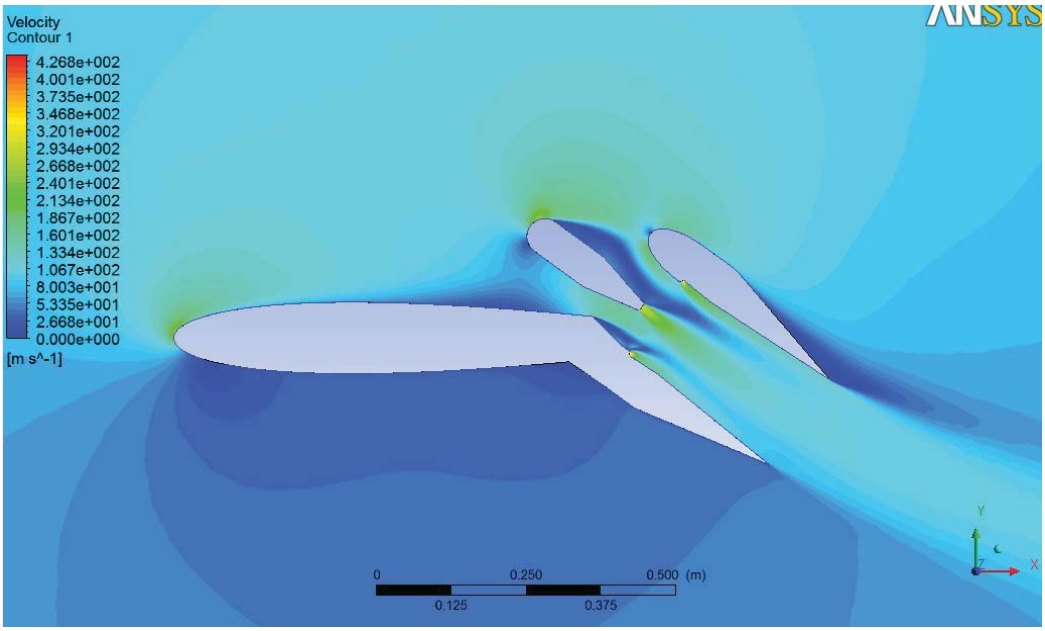

Figure 31: Velocity Contour for Wall Jets Configuration at Mach 0.2

Chapter 5: Results Summary

1. An ejector with enough thrust to hover could be integrated on a wing and would produce enough thrust augmentation to make the transition from hovering to wing-borne flight and back to hovering.
2. The Thrust Augmenting Ejector with an inlet area ratio of 5 in this study does not work for Mach numbers greater than 0.25, since the free-stream velocity becomes larger than the entrainment velocities; hence the jet entrainment effect on the flow field becomes negligible.
3. Thrust Augmenting Ejector produces reasonable results for Mach numbers less than 0.25; hence the aircraft can take-off and land as a STOVL aircraft at these speeds.
4. Thrust Augmentation decreases as the deflection angle increases due to flow separation and impingement on the ejector duct walls, and pressures losses.
5. The ejector should be placed at the trailing edge of the wing to obtain a favorable jet flap effect on the wing lift.
6. The ejector wing configuration produces a considerable amount of lift and high lift-to-thrust ratio.
7. The feasibility of a thrust augmenting ejector as an improvement to the swivel nozzle for STOVL aircraft is high, since the ejector performs well during transition at take-off and landing speeds ($M \leq 0.25$).

References

1] Bevilaqua, P., "Advances in Ejector Thrust Augmentation," SAE Technical Paper 872322, 1987, doi:10.4271/872322.

2] Margason, Richard, and Paul M. Bevilaqua. "Design of Thrust Augmenting Ejectors for Short Take Off and Vertical Landing Aircraft." *AIAA* (2011): n. pag. Print.

3] Bevilaqua, Paul, E. F. Schum, and C. J. Woan. "Progress Towards a Theory of Jet Flap Thrust Recovery." *AIAA* (1983): n. pag. Print.

4] Hill, Philip G., and Carl R. Peterson. *Mechanics and Thermodynamics of Propulsion*. Reading, MA: Addison-Wesley, 1992. Print.

5] Tu, Jiyuan, Guan Heng Yeoh, and Chaoqun Liu. *Computational Fluid Dynamics: A Practical Approach*. Amsterdam: Elsevier Butterworth-Heinemann, 2013. Print.

6] Bevilaqua, Paul, Richard Margason, and Charles Gaharan. "Jet Entrainment Theory for Vertical Takeoff and Landing Aircraft Suckdown." *AIAA Journal* 48.2 (2010): 330-39. Print.

7] Williams, J., S. F. Butler, and M. N. Wood. "The Aerodynamics of Jet Flaps." *ARC R&M* 3304 (1961): n. pag. Print.

8] Lund, T. S., L. Roberts, and D. A. Tavella. "Thrust Augmentor Inlet Optimization." *Journal of Propulsion and Power* 2.3 (1986): 253-58. Print

9] Cochrane, J. A., D. W. Riddle, M. D. Shovlin, and V. C. Stevens. "Selected Results from the Quiet Short-haul Research Aircraft Flight Research Program." *Journal of Aircraft* 19.12 (1982): 1076-082. Print.

10] Bevilaqua, Paul M. "Analytic Description of Hypermixing and Test of an Improved Nozzle." *Journal of Aircraft* 13.1 (1976): 43-48. Print.

11] Bevilaqua, Paul M. "Lifting Surface Theory for Thrust-Augmenting Ejectors." *AIAA Journal* 16.5 (1978): 475-81. Print.

12] Bevilaqua, P. M. "Some Observations on the Mechanism of Entrainment." *AIAA Journal* 15.8 (1977): 1194-196. Print.

13] Bevilaqua, P. M., and P. S. Lykoudis. "Mechanism of Entrainment in Turbulent Wakes." *AIAA Journal* 9.8 (1971): 1657-659. PrintHeiser, W. H. "Ejector Thrust Augmentation." *Journal of Propulsion and Power* 26.6 (2010): 1325-330. Print.

14] Seiler, M. R., and E. F. Schum. "Analytical and Experimental Investigation of Diffusers for VSTOL Thrust-Augmenting Ejectors." *Journal of Aircraft* 16.10 (1979): 643-44. Print.

15] Anderson, John David. *Fundamentals of Aerodynamics*. Boston: McGraw-Hill, 2007. Print.

16] Spence, D. A. "The Lift Coefficient of a Thin, Jet-Flapped Wing." *Proceedings of the Royal Society A: Mathematical, Physical and Engineering Sciences* 238.1212 (1956): 46-68. Print.

17] "AVSIG Aviation Forum." *AVSIG Aviation Forum*. N.p., n.d. Web. June 19, 2013.

Appendix A: Pressure Contours

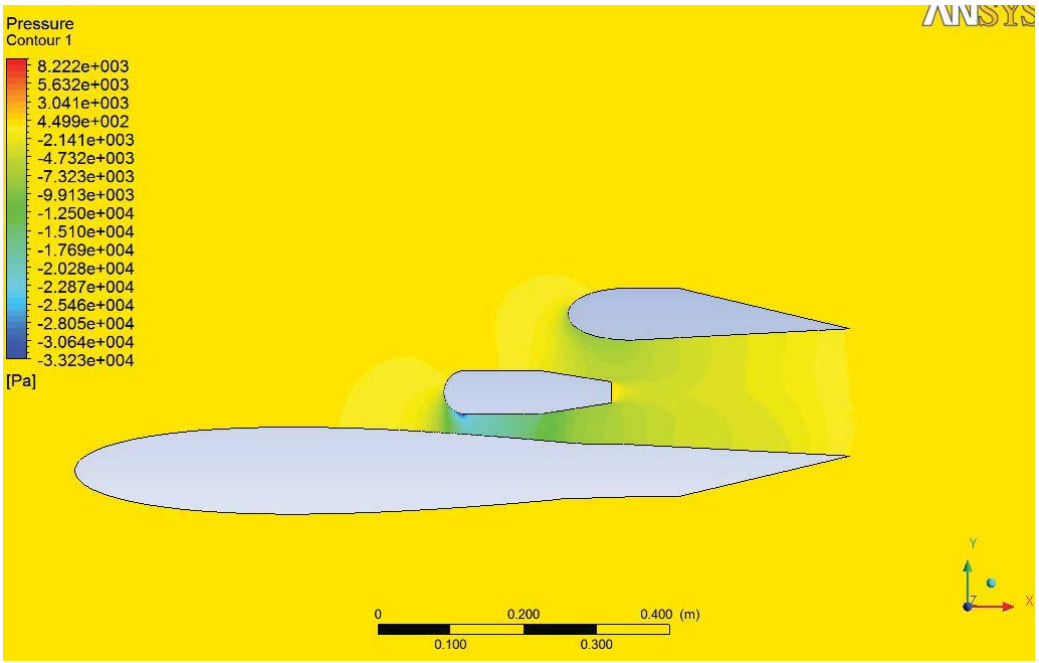

Pressure Contour: Angle 0 Mach =0.01

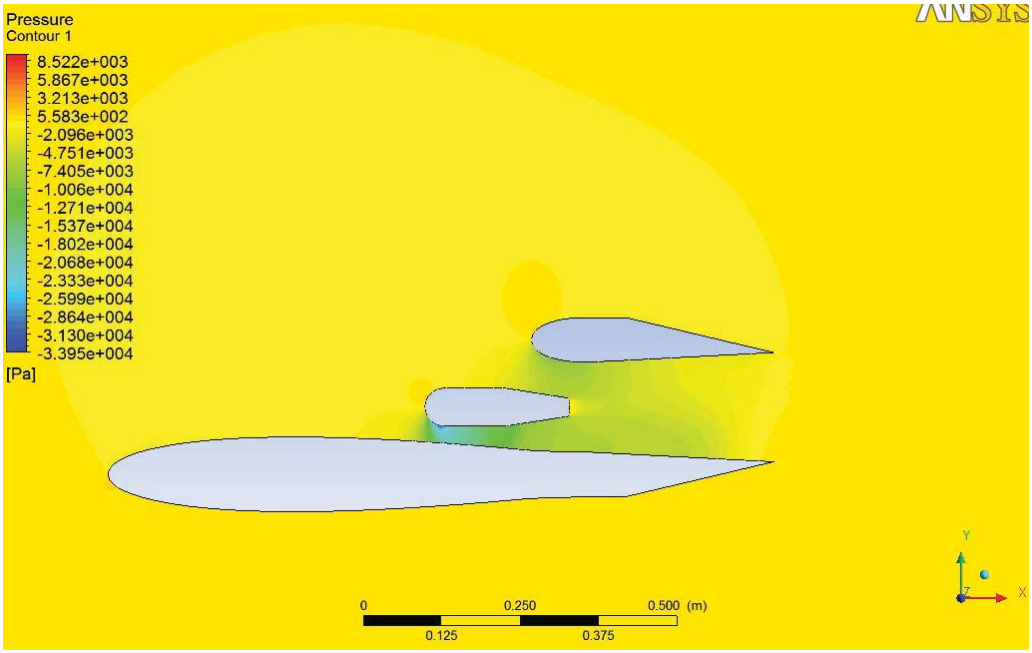

Pressure Contour: Angle 0 Mach =0.1

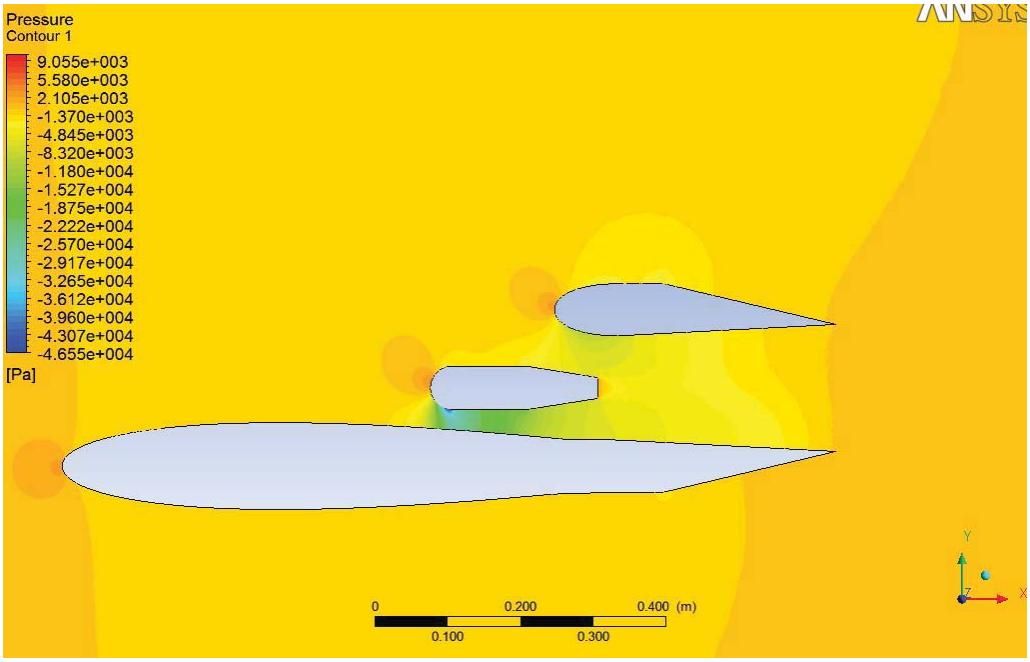

Pressure Contour: Angle 0 Mach =0.2

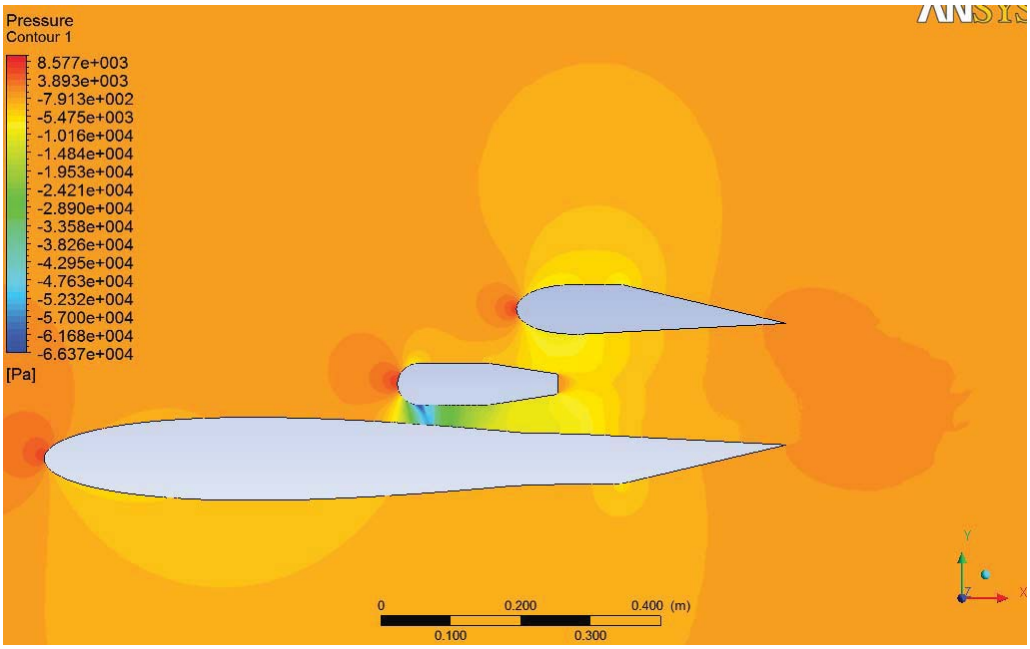

Pressure Contour: Angle 0 Mach =0.3

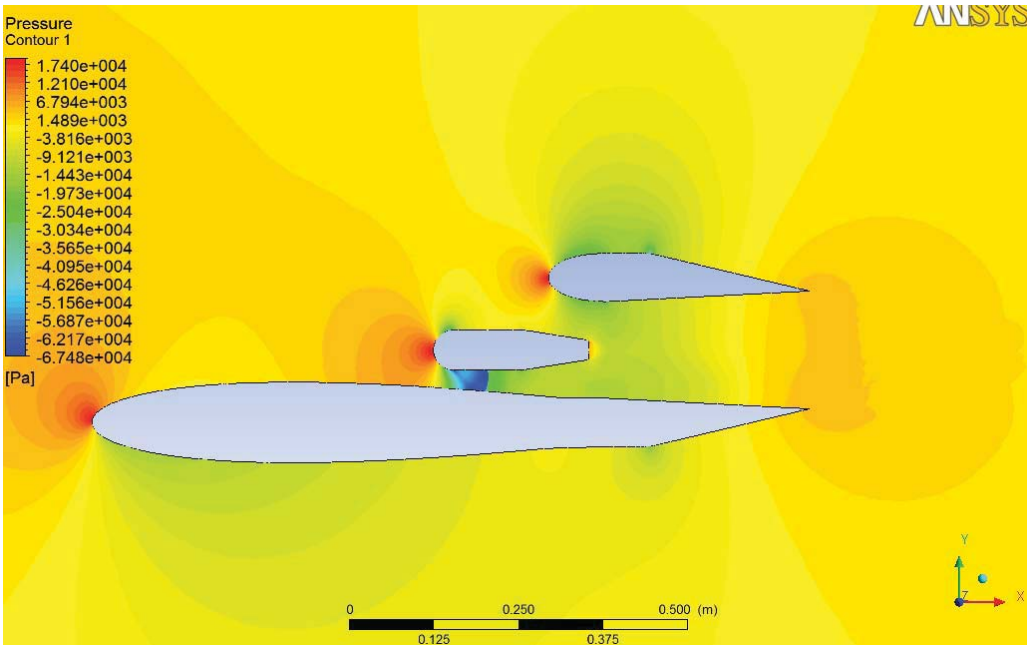

Pressure Contour: Angle 0 Mach =0.5

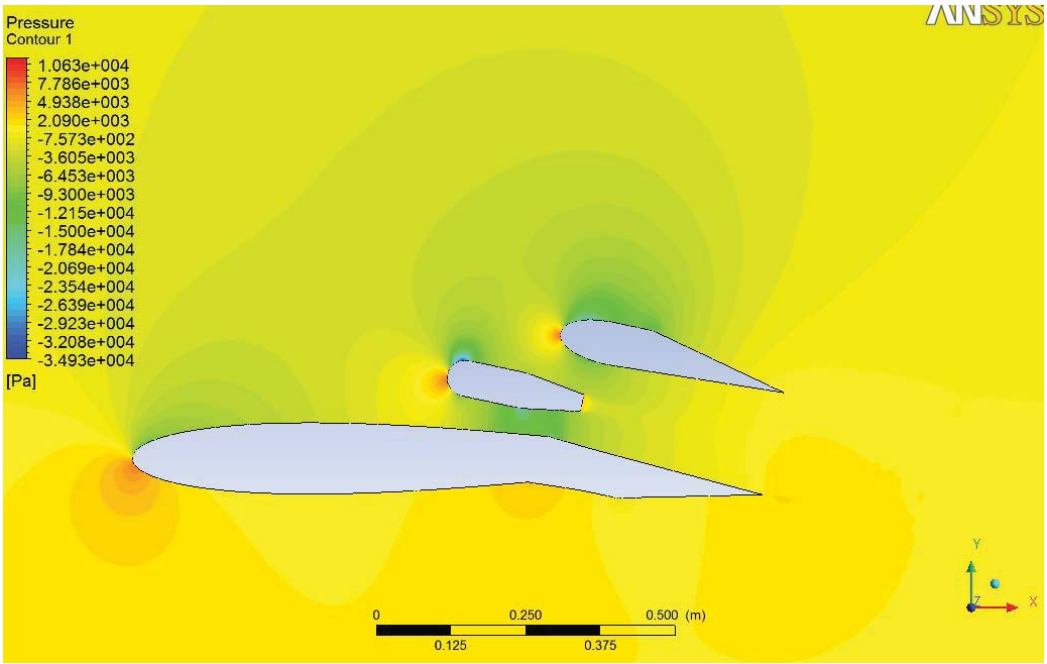

Pressure Contour: Angle 12 Mach =0.3

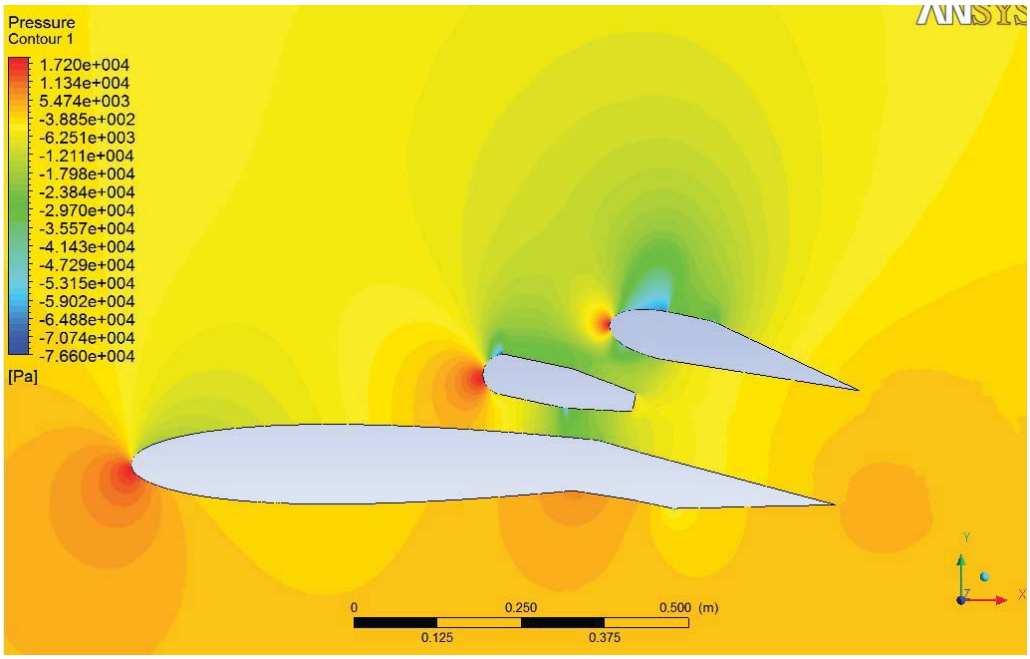

Pressure Contour: Angle 0 Mach =0.5

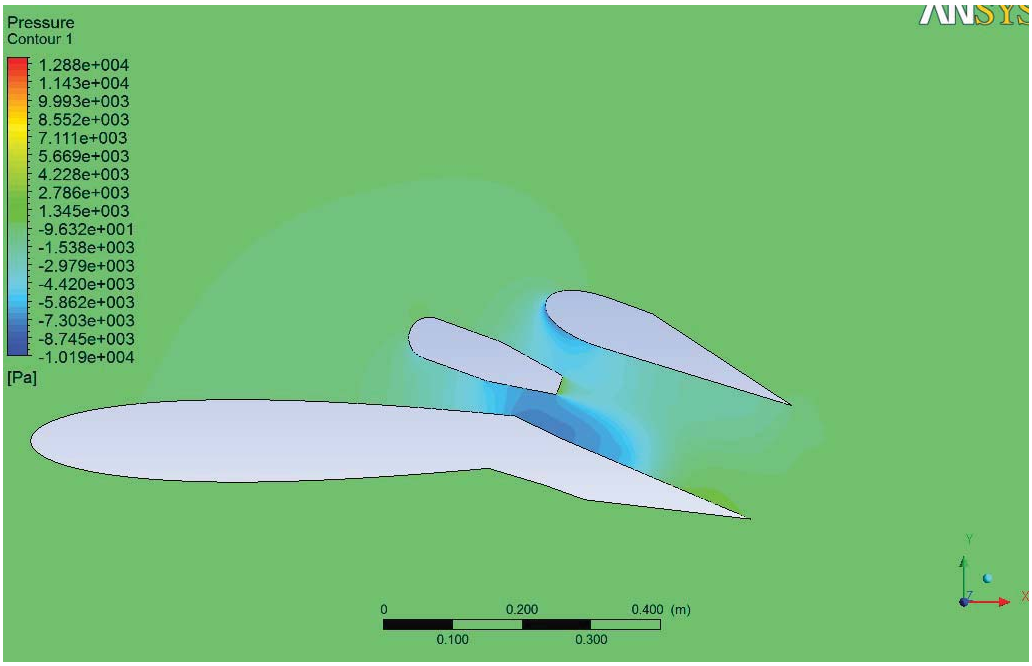

Pressure Contour: Angle 20 Mach =0.01

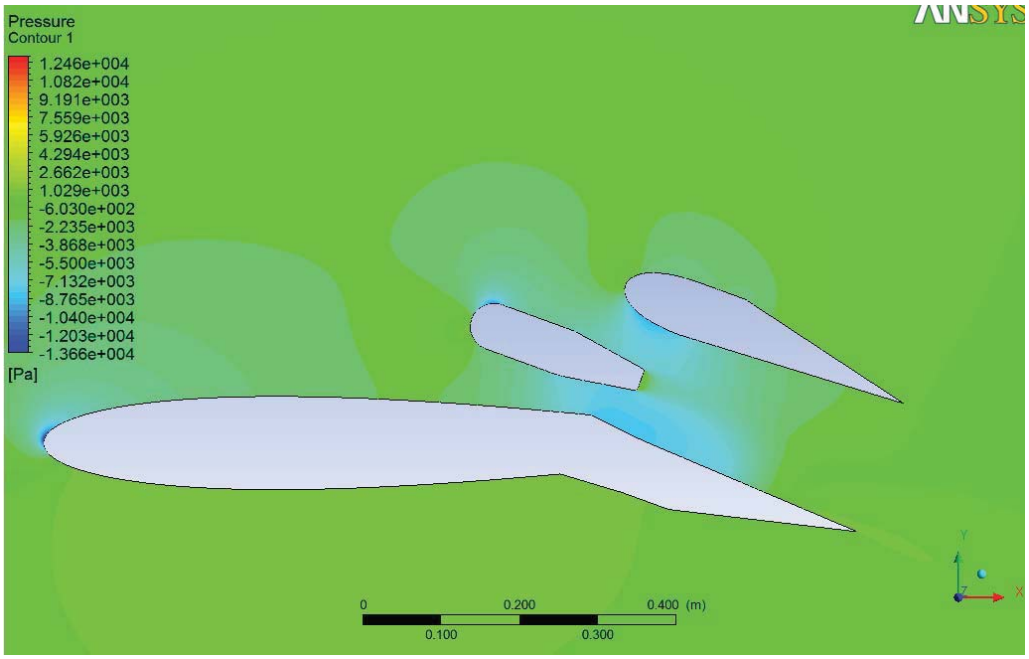

Pressure Contour: Angle 20 Mach =0.1

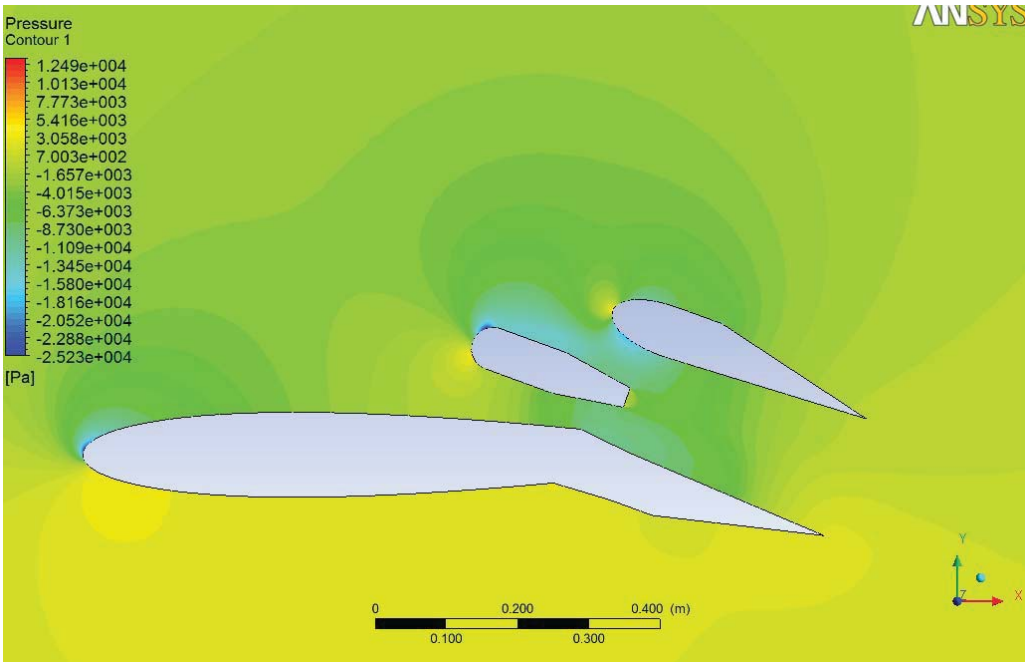

Pressure Contour: Angle 20 Mach =0.2

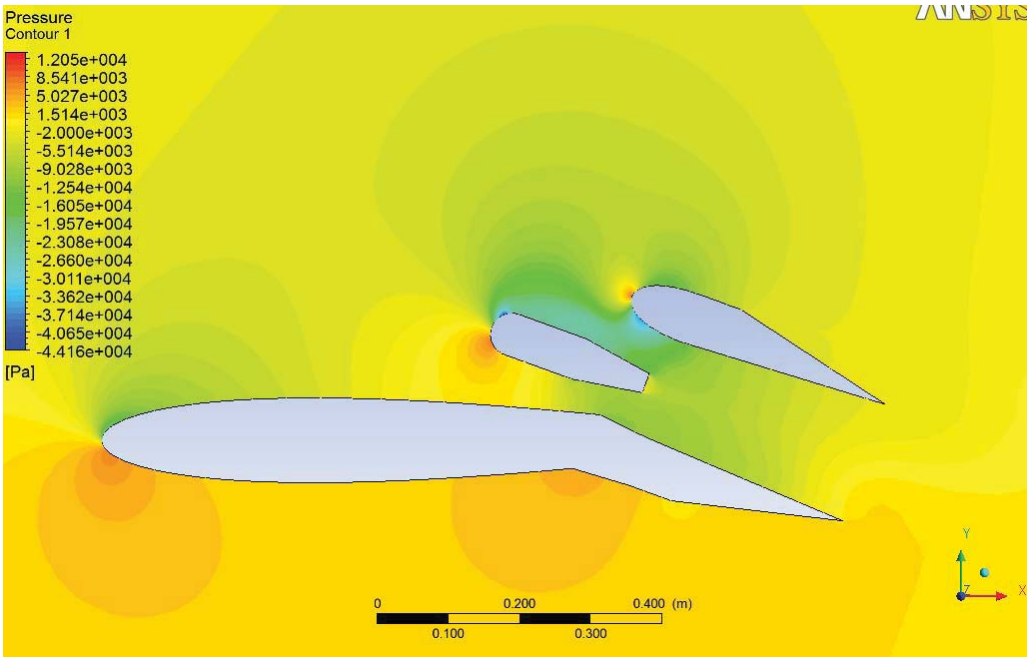

Pressure Contour: Angle 20 Mach =0.3

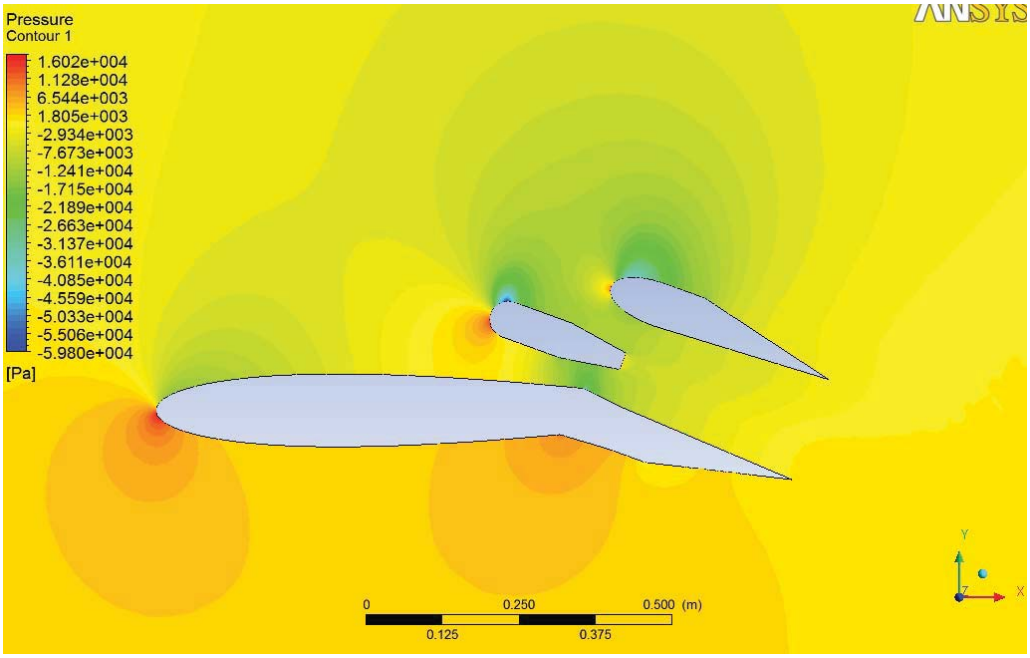

Pressure Contour: Angle 20 Mach =0.4

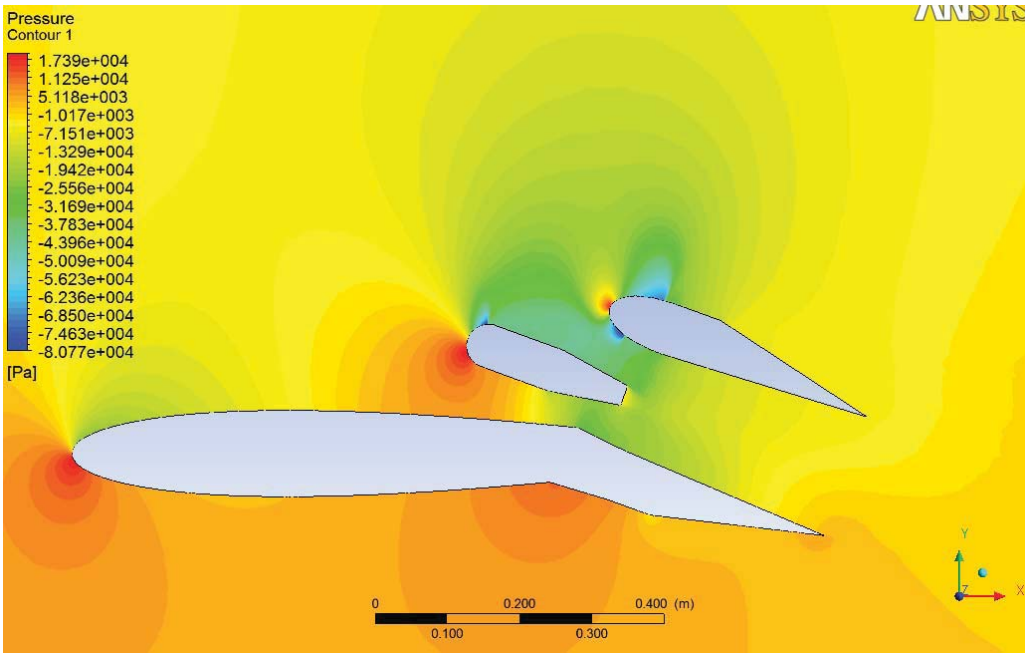

Pressure Contour: Angle 20 Mach =0.5

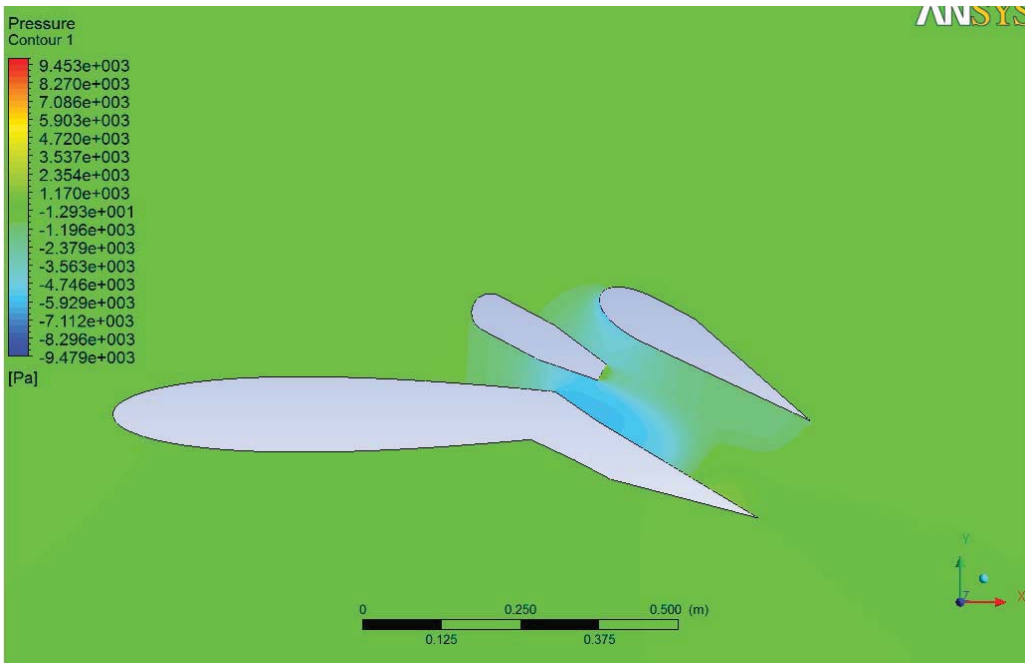

Pressure Contour: Angle 28 Mach =0.01

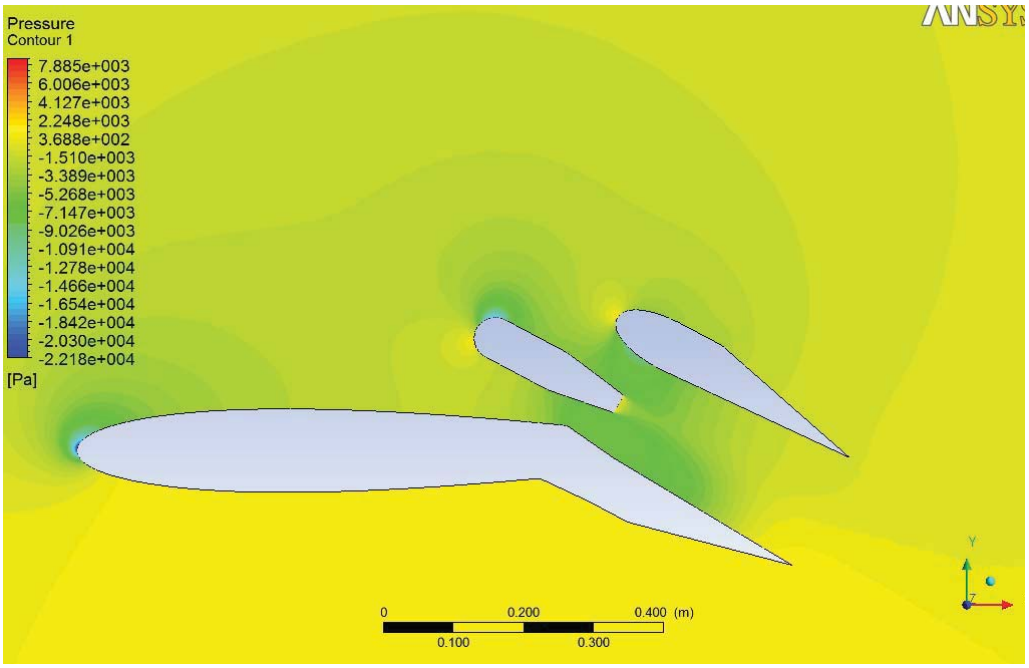

Pressure Contour: Angle 28 Mach =0.1

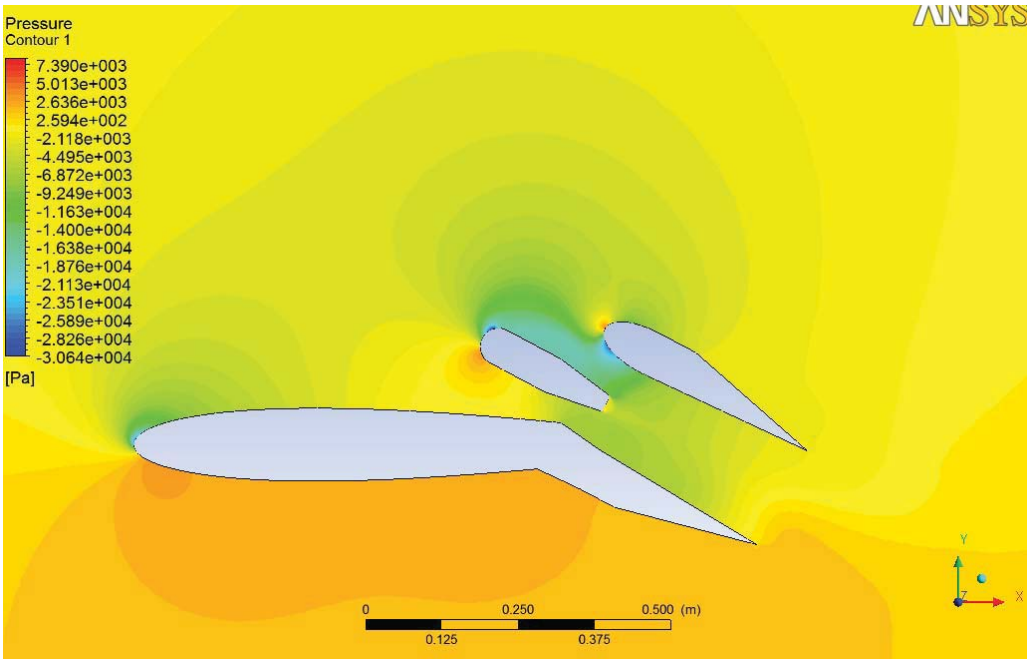

Pressure Contour: Angle 28 Mach =0.2

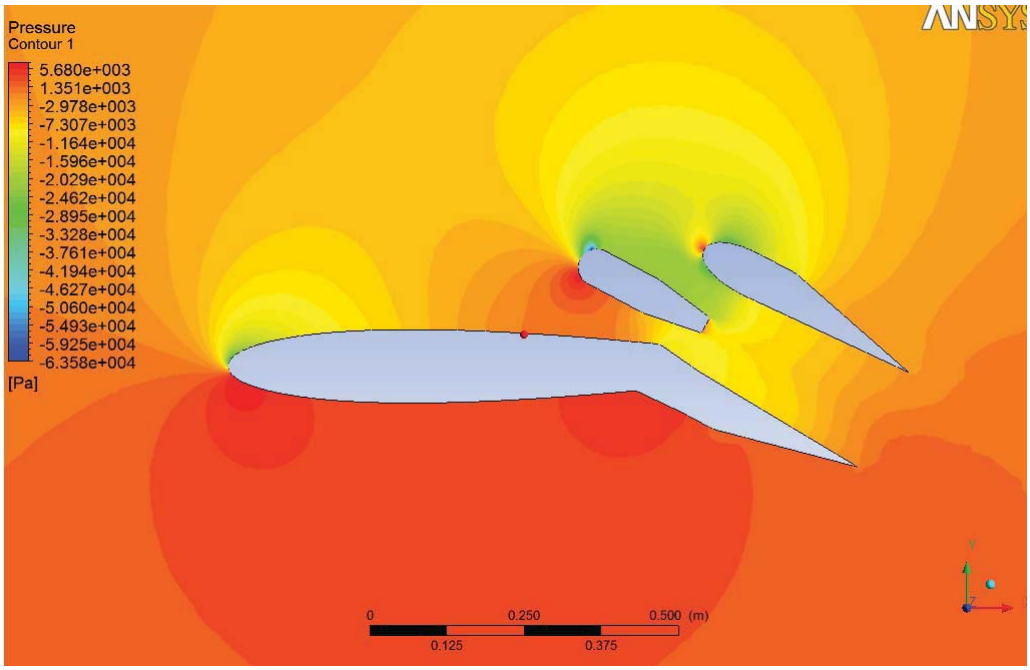

Pressure Contour: Angle 28 Mach =0.3

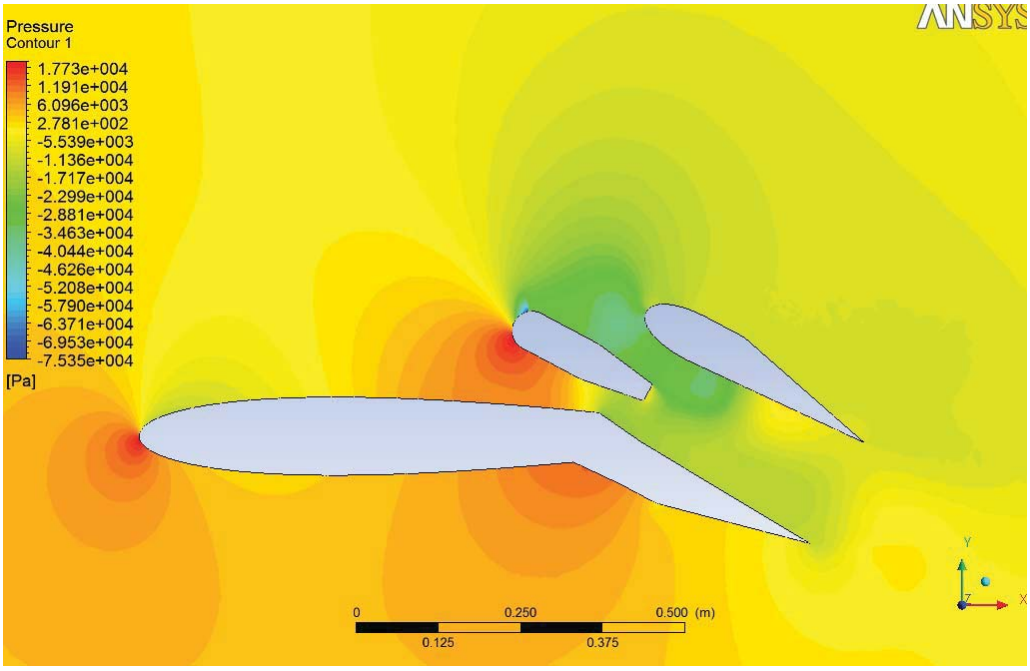

Pressure Contour: Angle 28 Mach =0.5

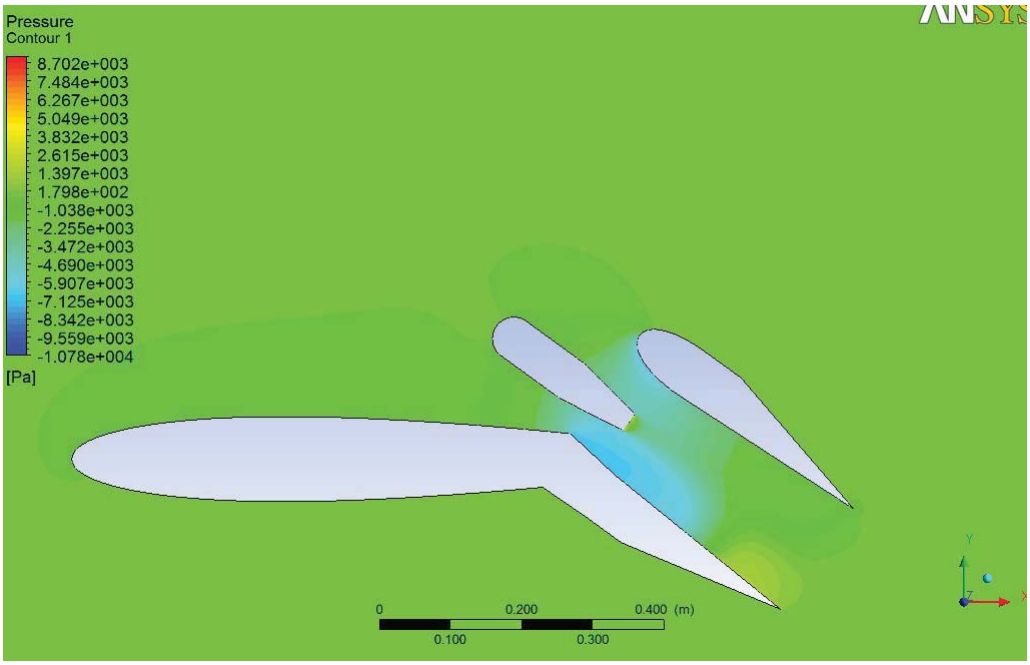

Pressure Contour: Angle 36 Mach =0.01

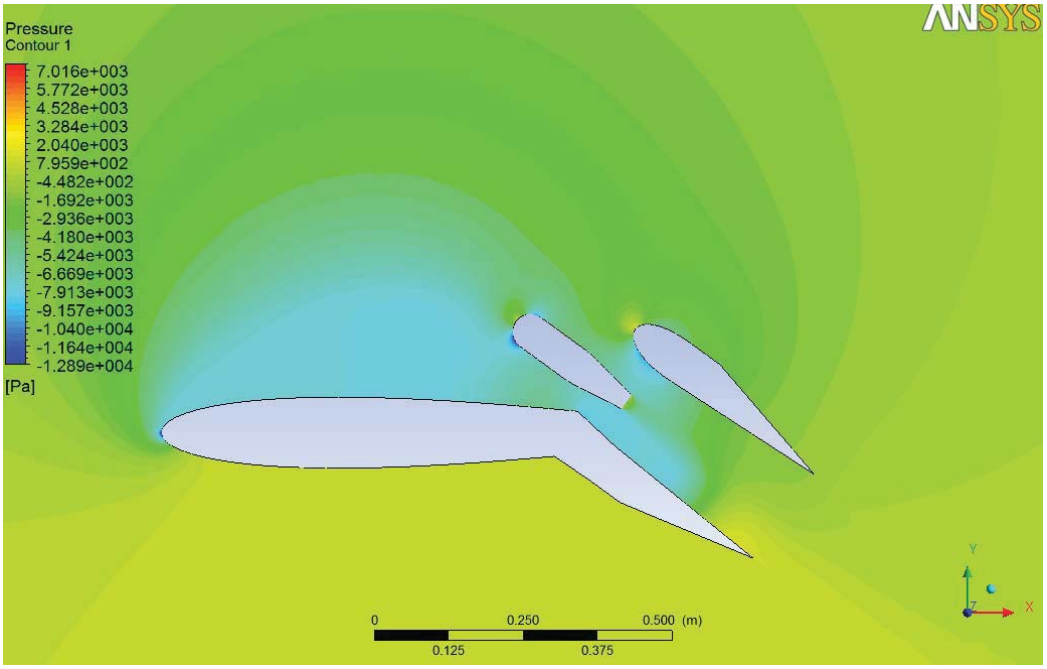

Pressure Contour: Angle 36 Mach =0.1

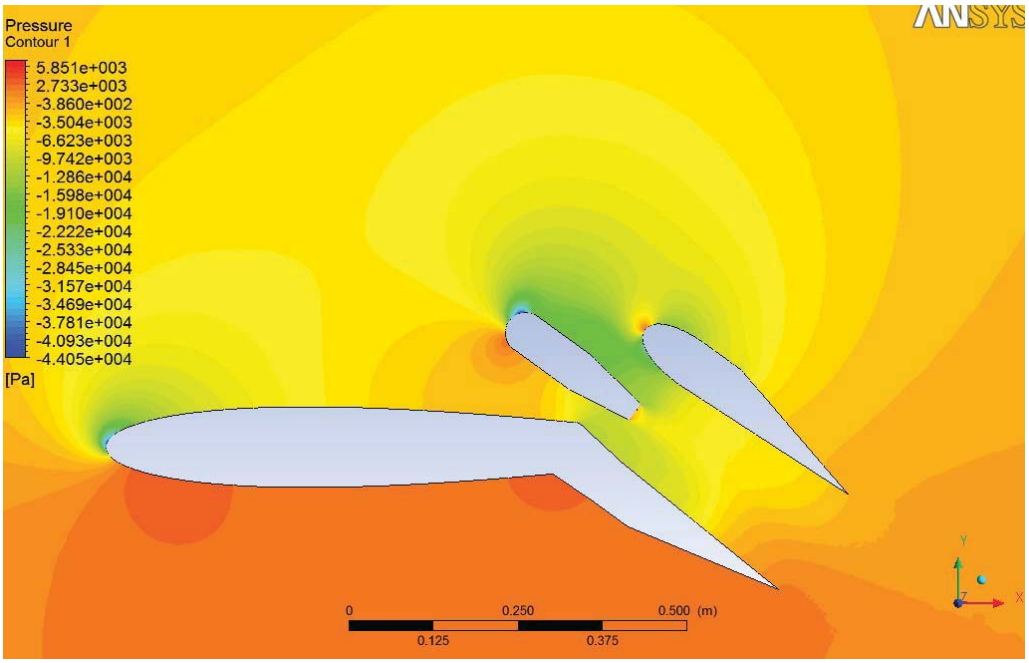

Pressure Contour: Angle 36 Mach =0.2

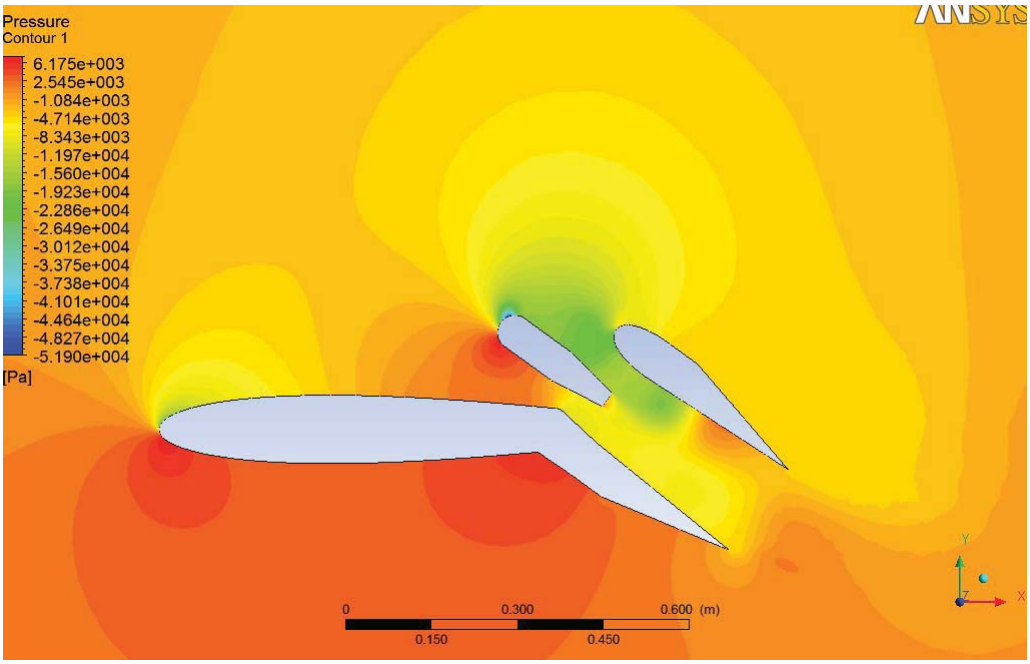

Pressure Contour: Angle 36 Mach =0.3

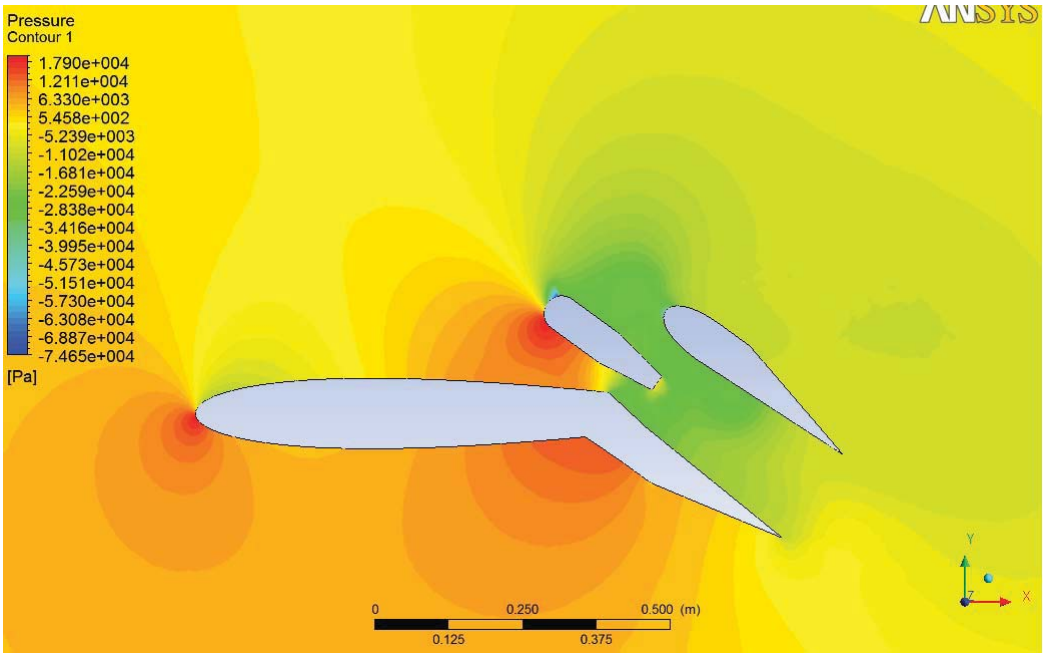

Pressure Contour: Angle 36 Mach =0.5

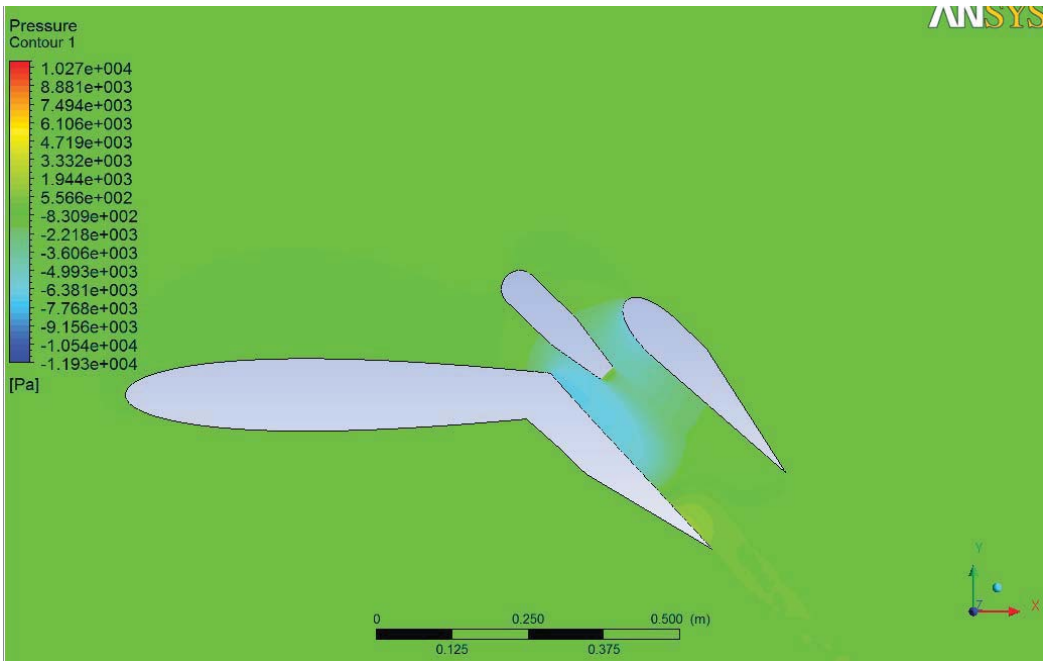

Pressure Contour: Angle 44 Mach =0.01

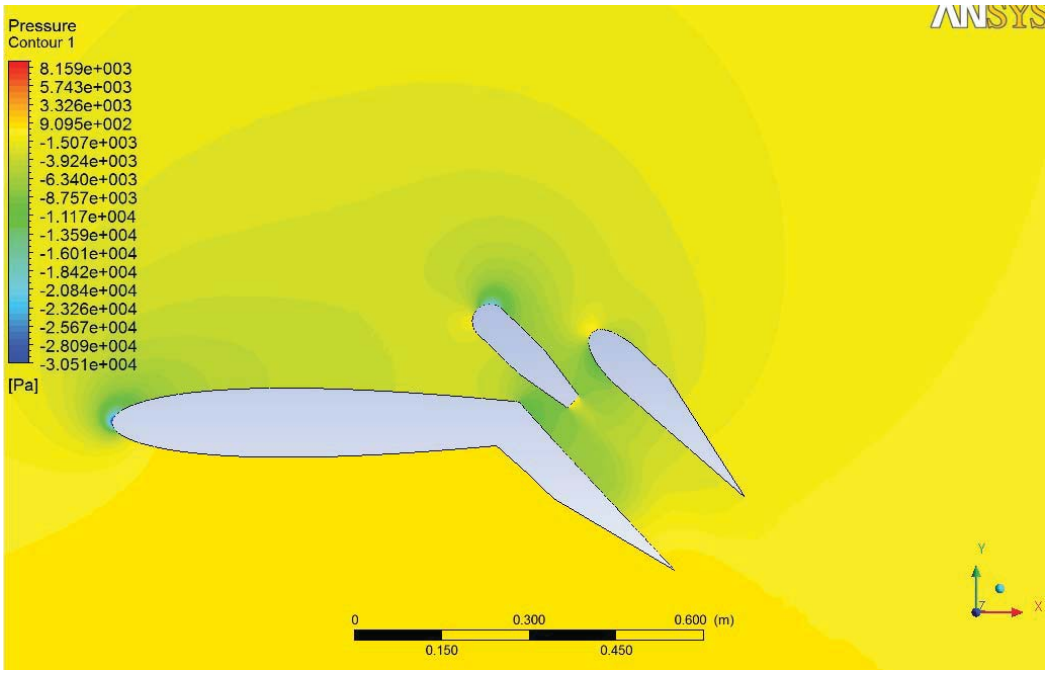

Pressure Contour: Angle 44 Mach =0.1

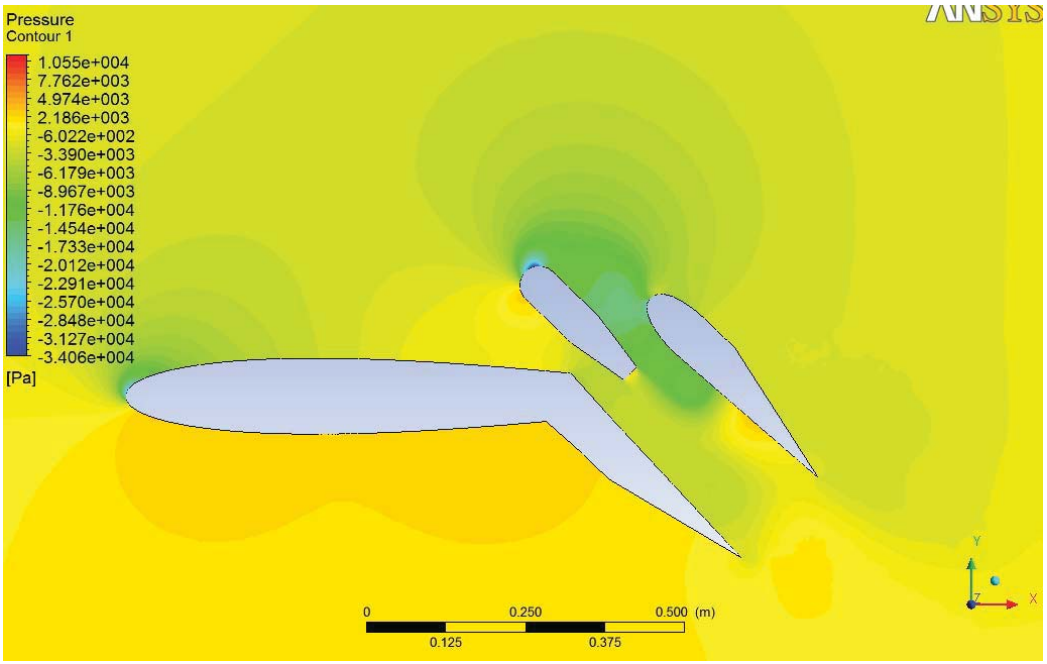

Pressure Contour: Angle 44 Mach =0.2

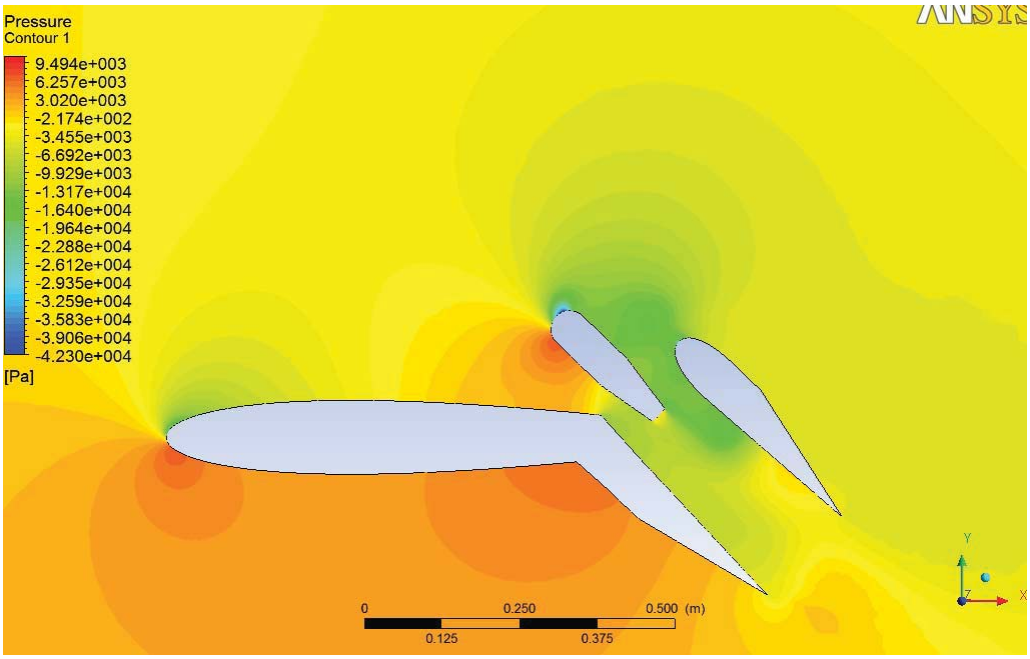

Pressure Contour: Angle 44 Mach =0.3

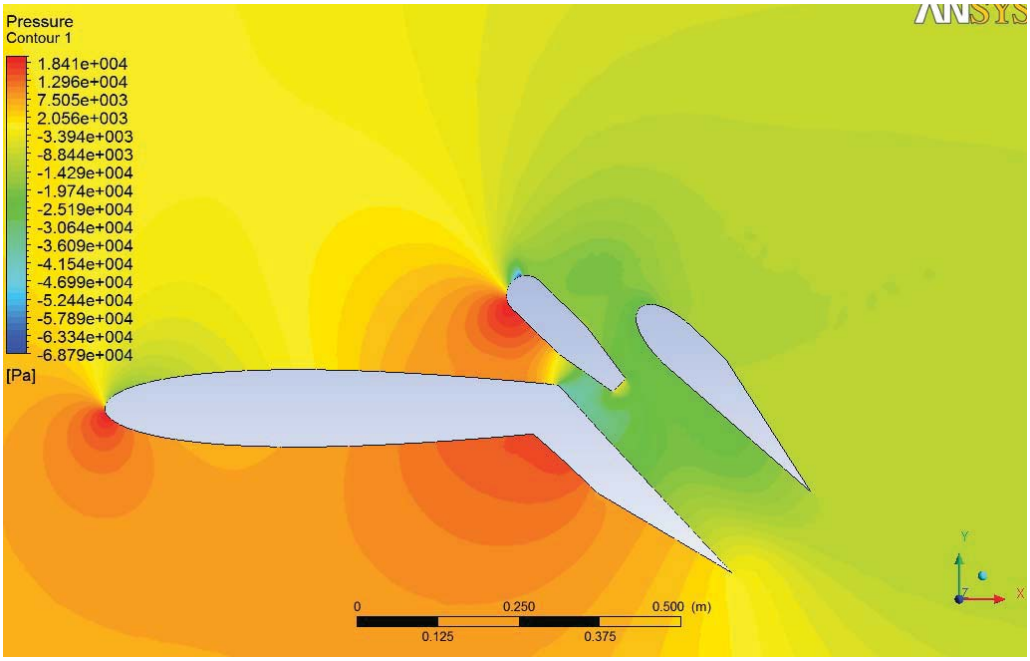

Pressure Contour: Angle 44 Mach =0.5

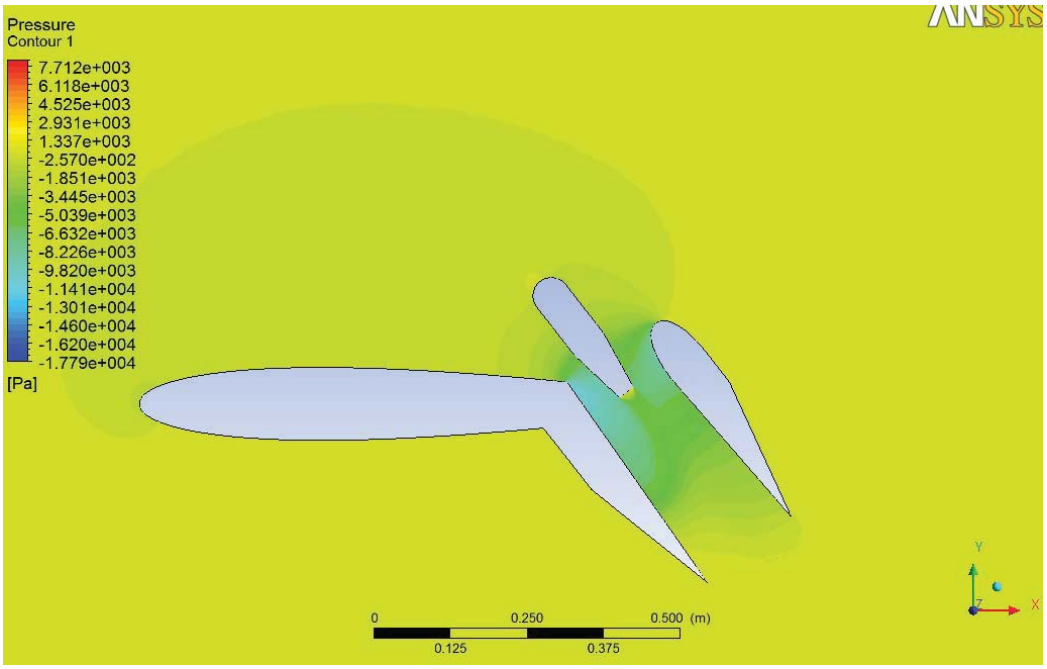

Pressure Contour: Angle 52 Mach =0.01

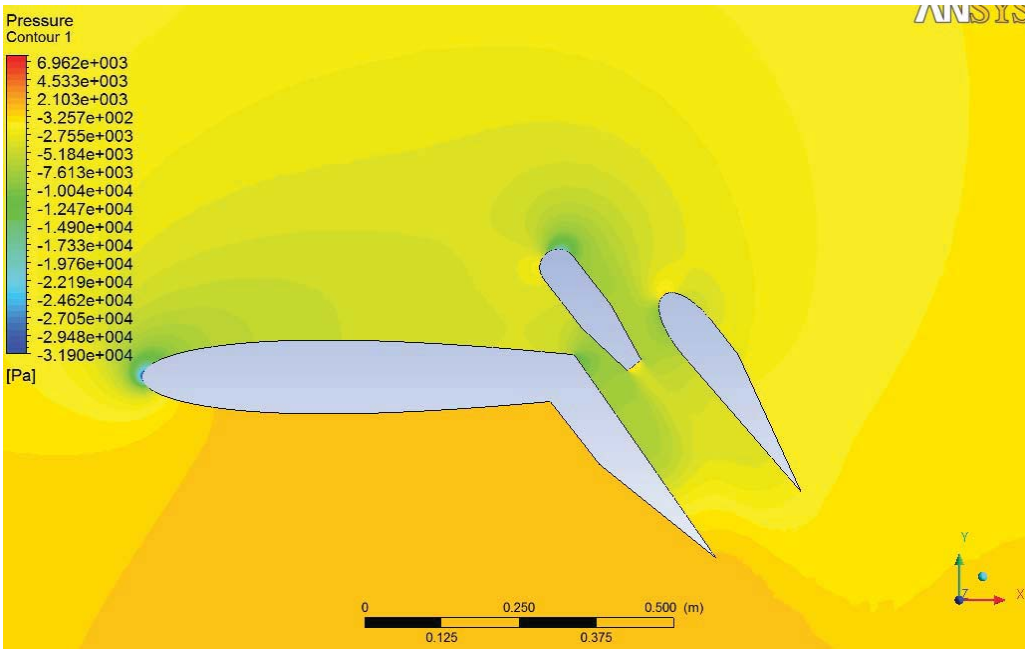

Pressure Contour: Angle 52 Mach =0.1

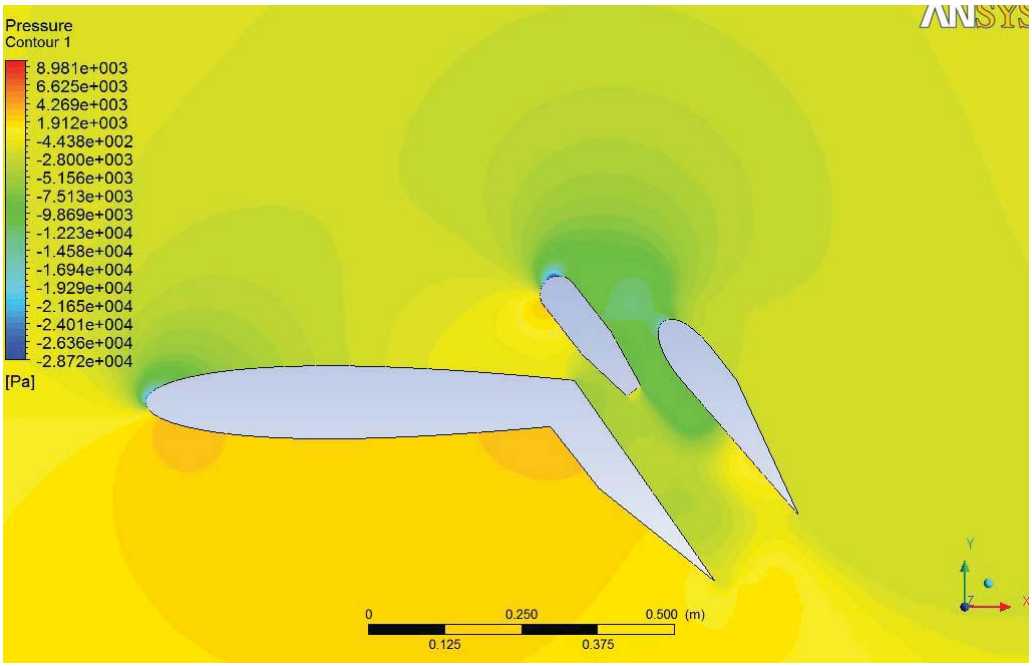

Pressure Contour: Angle 52 Mach =0.2

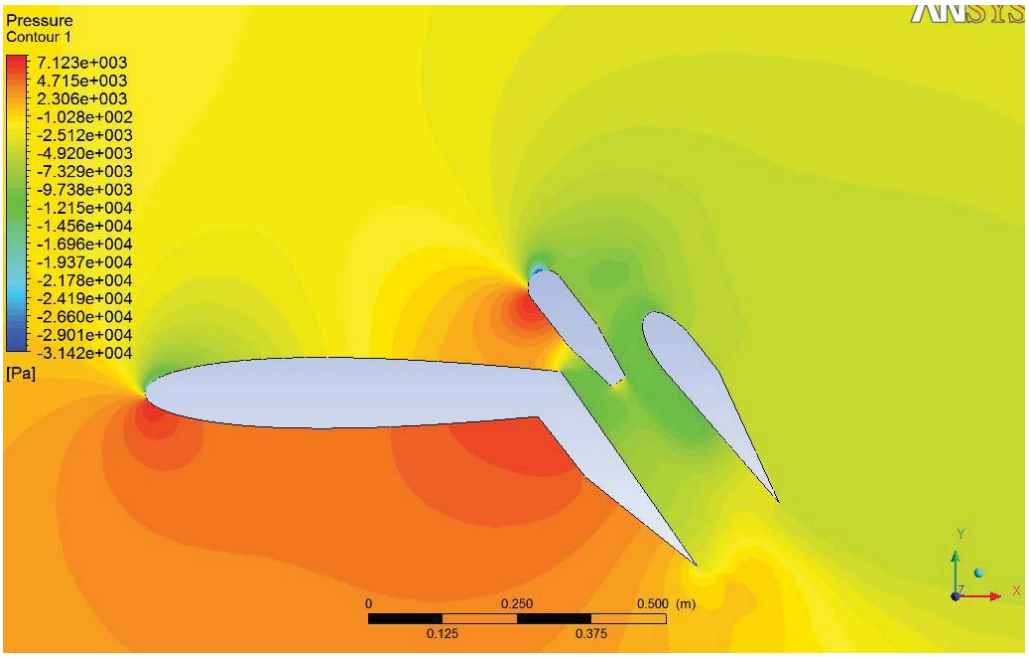

Pressure Contour: Angle 52 Mach =0.3

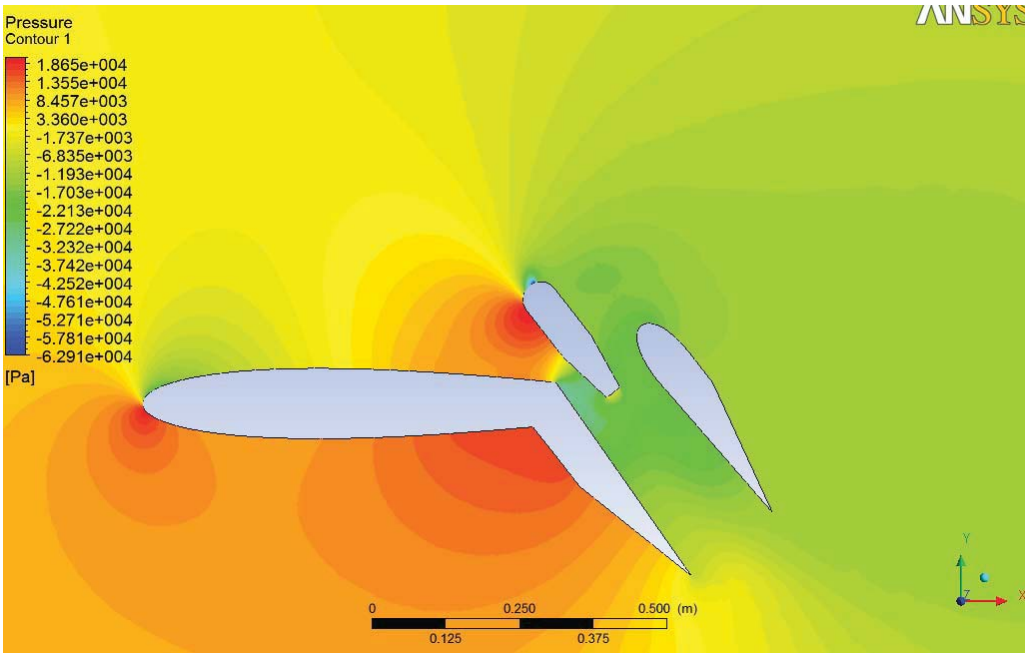

Pressure Contour: Angle 52 Mach =0.5

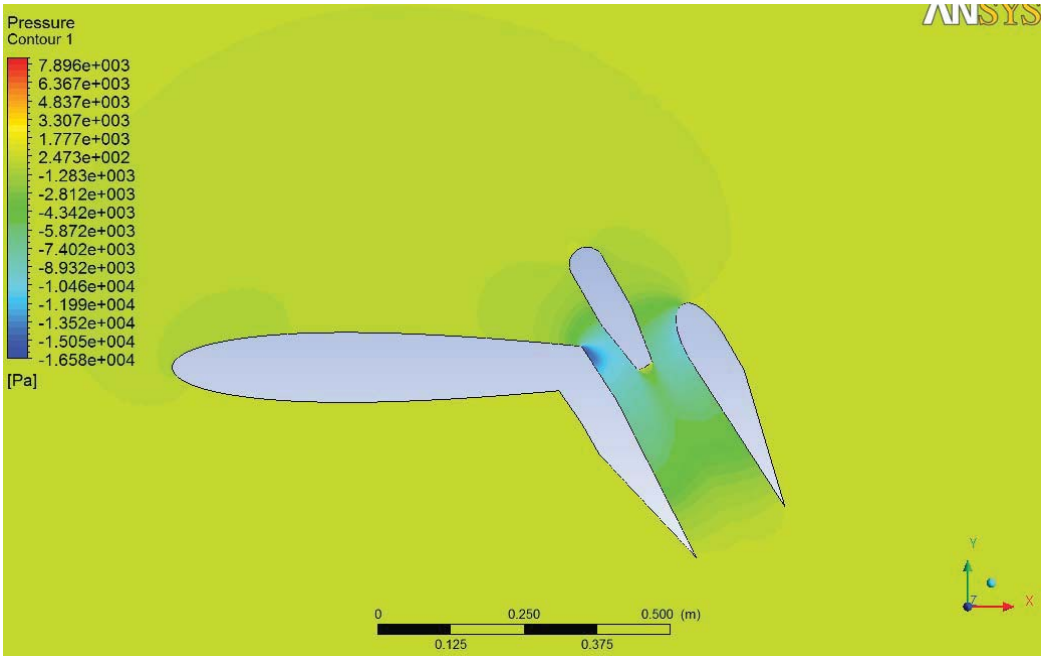

Pressure Contour: Angle 60 Mach =0.01

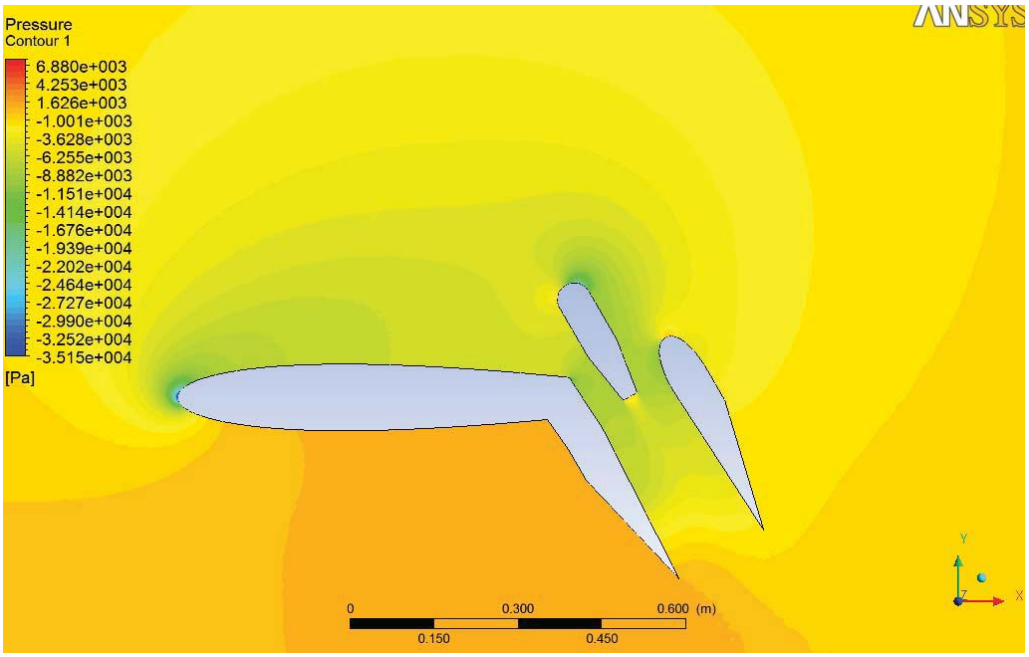

Pressure Contour: Angle 60 Mach =0.1

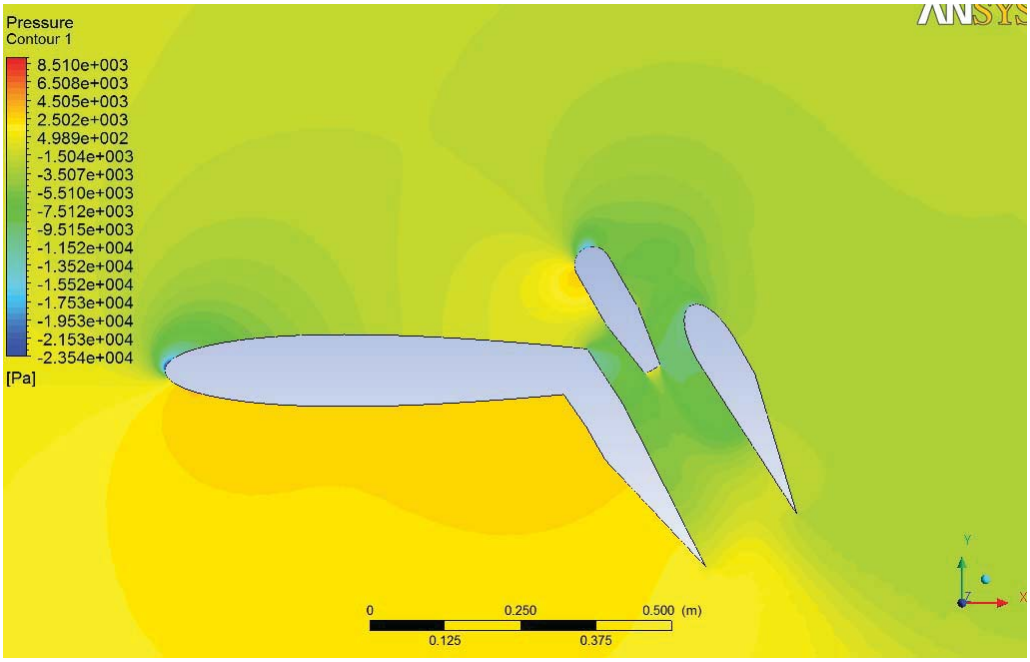

Pressure Contour: Angle 60 Mach =0.2

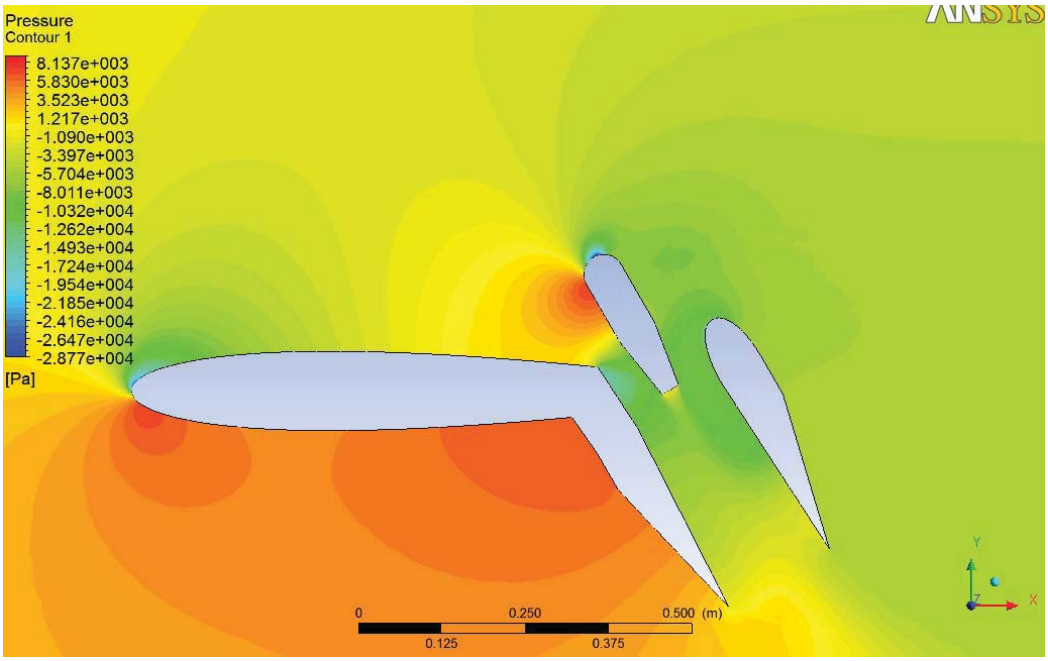

Pressure Contour: Angle 60 Mach =0.3

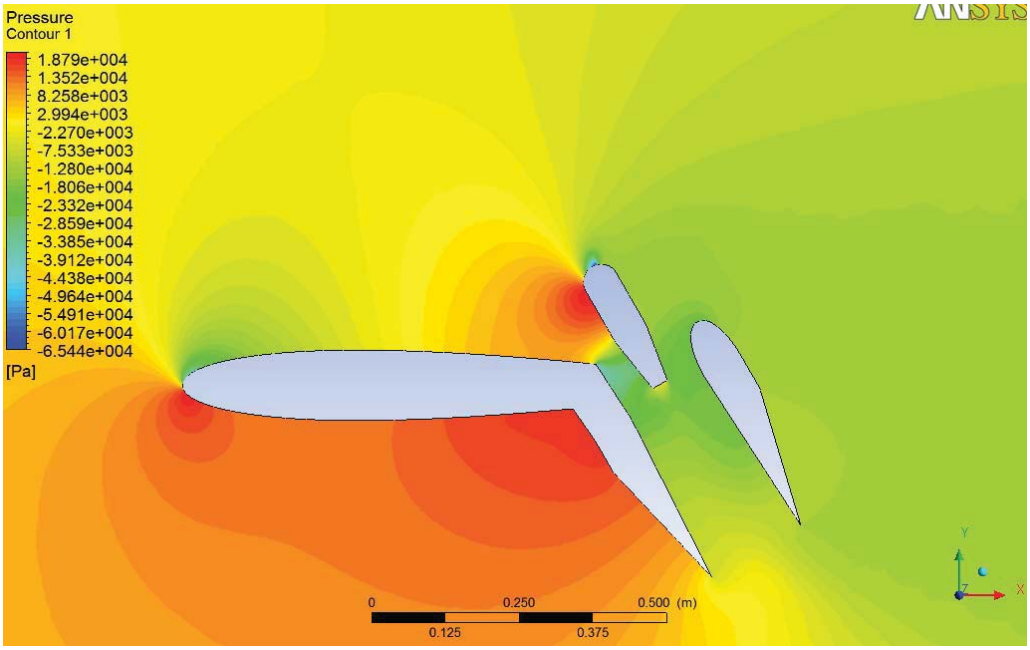

Pressure Contour: Angle 60 Mach =0.5

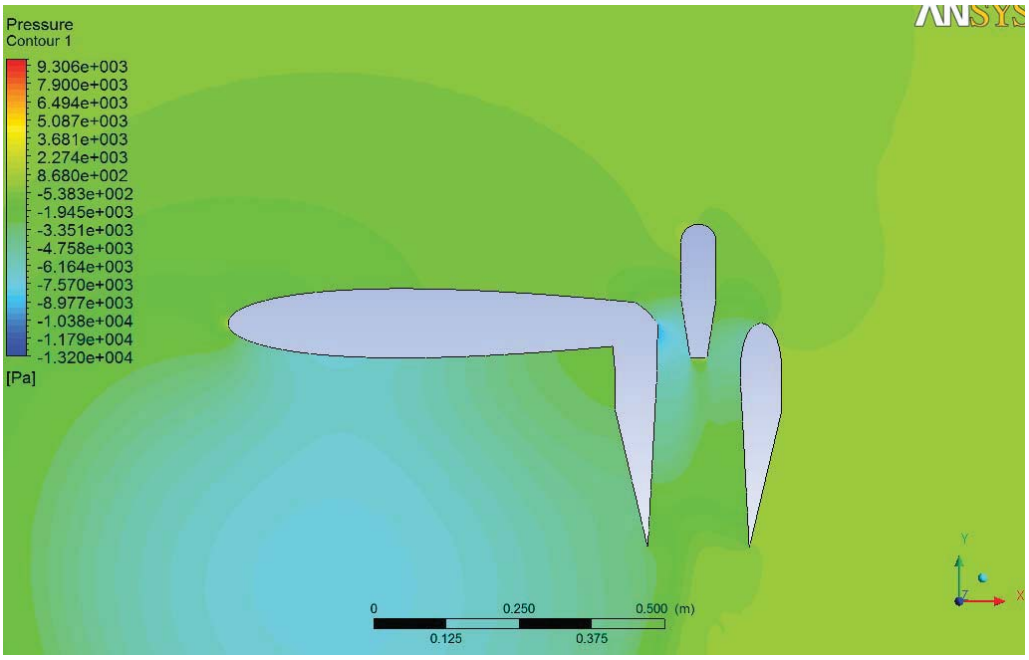

Pressure Contour: Angle 90 Mach =0.01

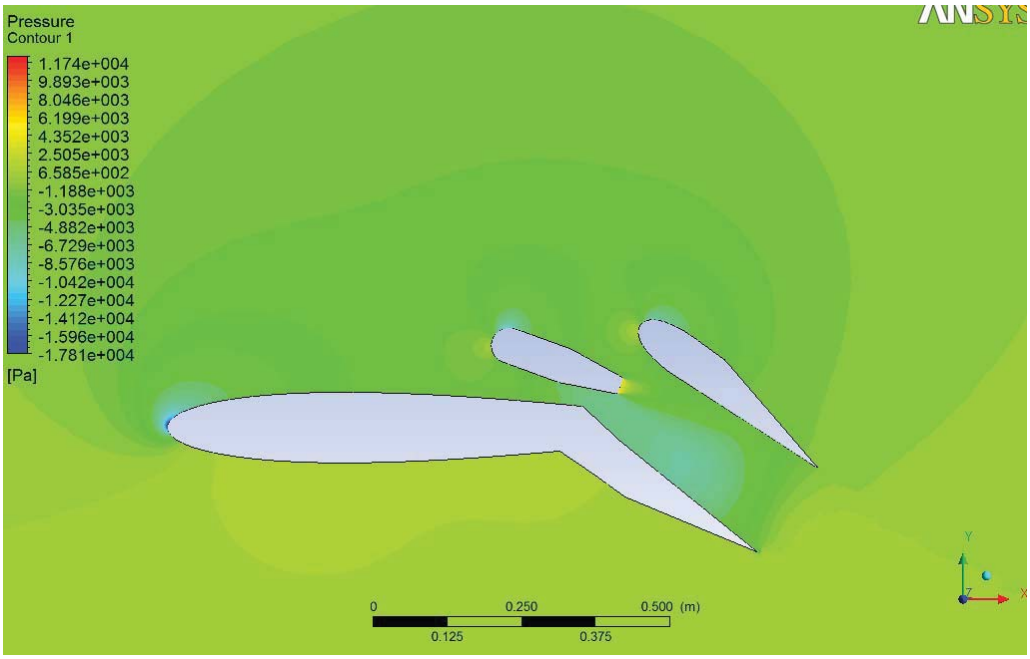

Pressure Contour: Angle 36 Mach =0.1 Deflected Nozzle Configuration

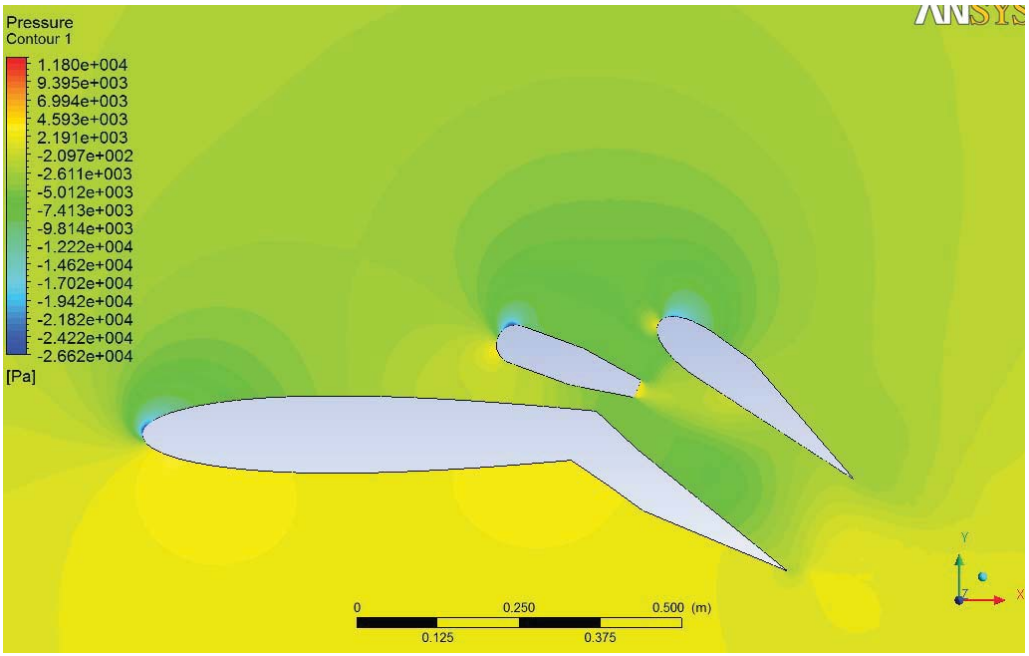

Pressure Contour: Angle 36 Mach =0.2 Deflected Nozzle Configuration

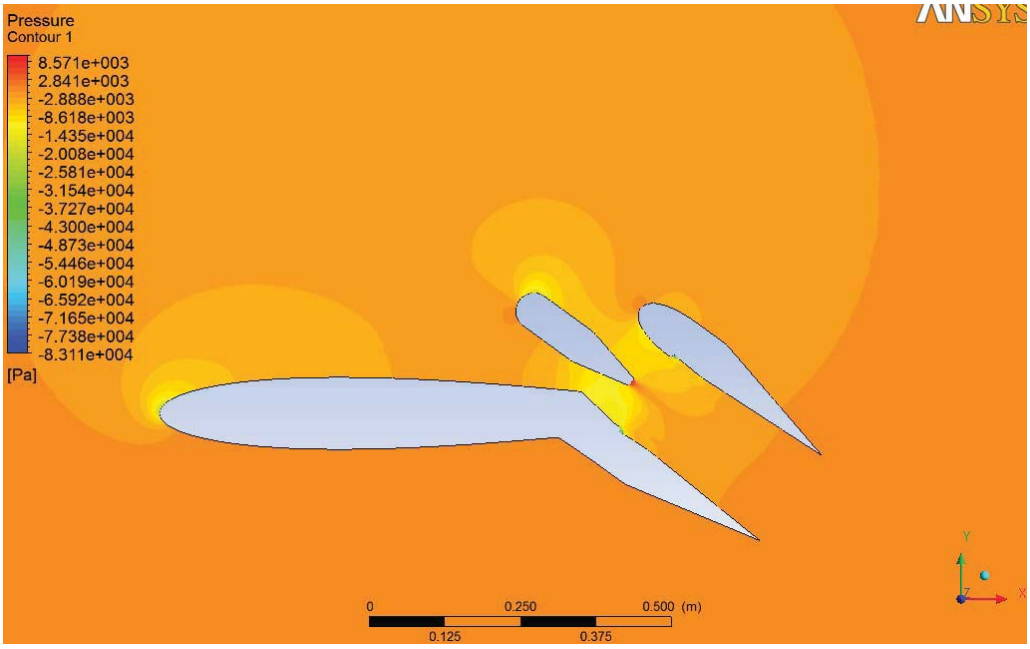

Pressure Contour: Angle 36 Mach =0.1 Wall Jets Configuration

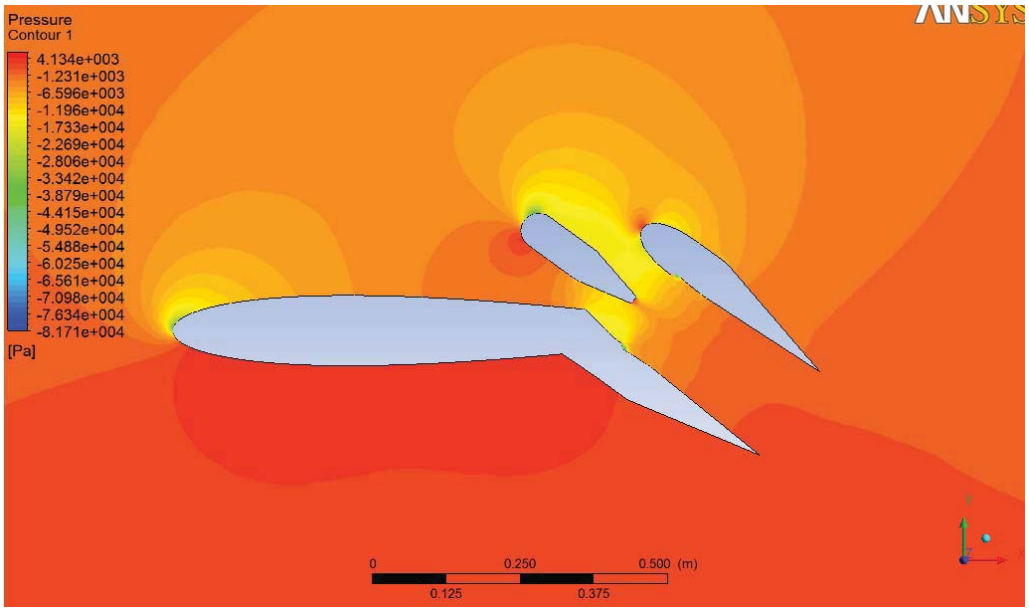

Pressure Contour: Angle 36 Mach =0.2 Wall Jets Configuration

Appendix B: Temperature Contours

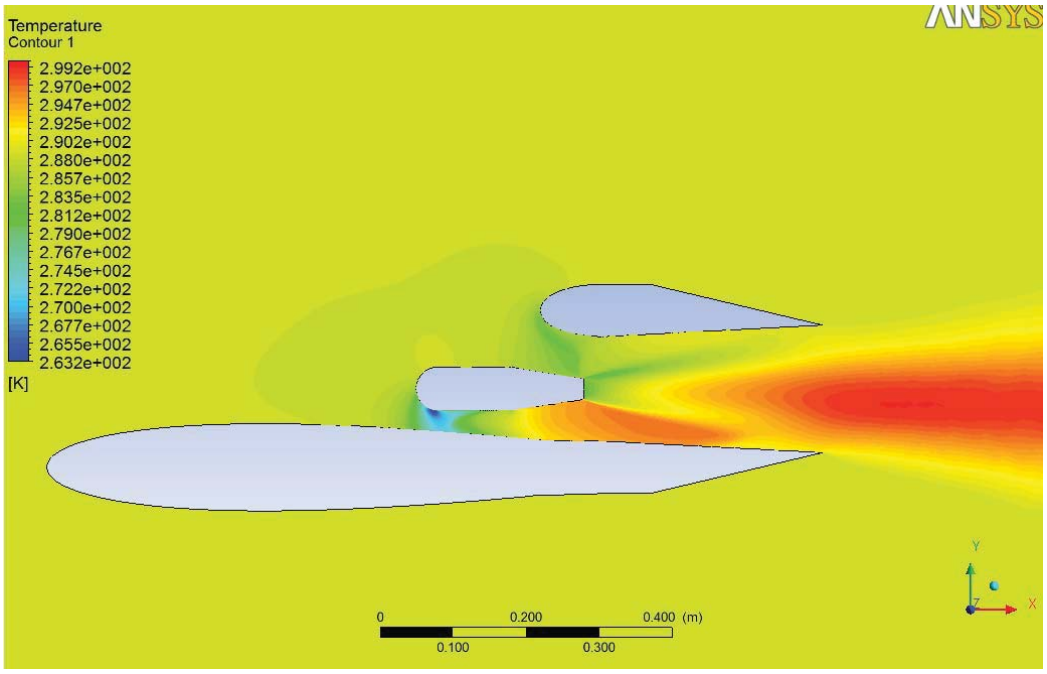

Temperature Contour: Angle 0 Mach =0.01

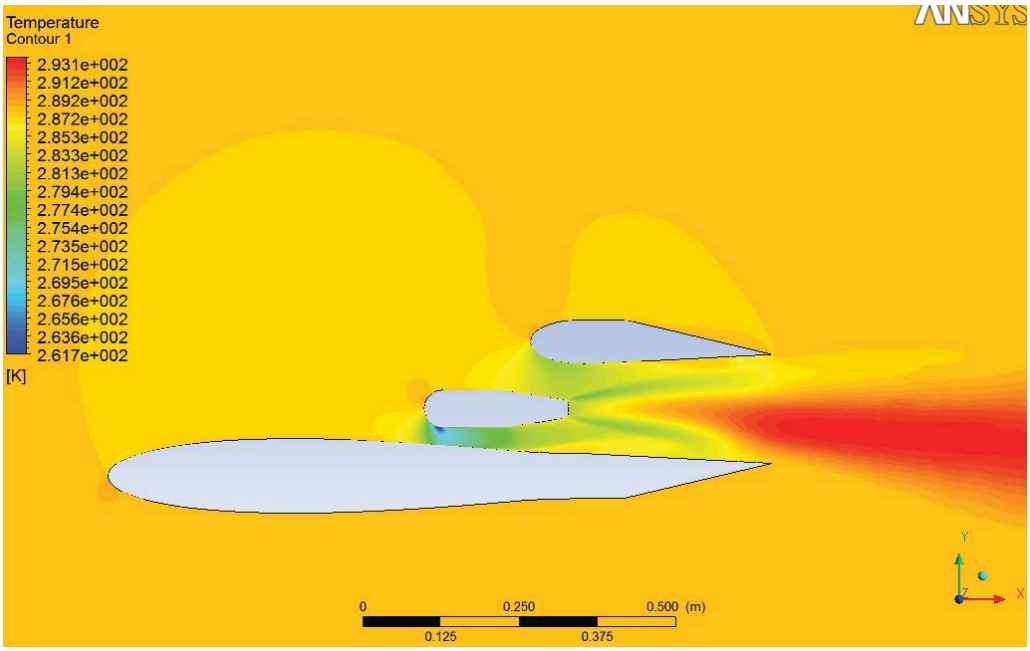

Temperature Contour: Angle 0 Mach =0.1

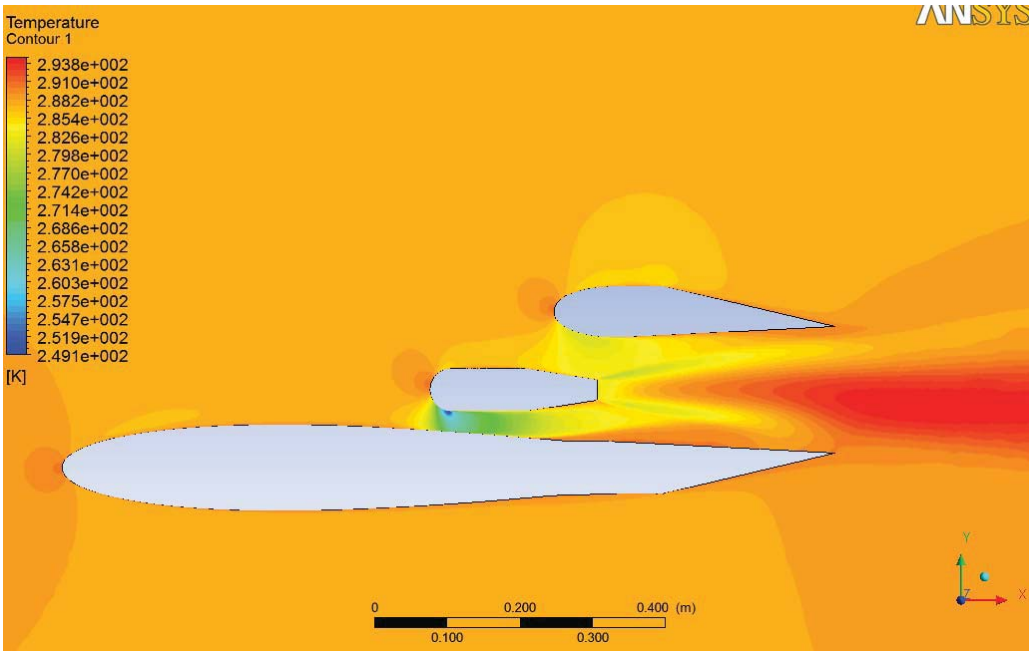

Temperature Contour: Angle 0 Mach =0.2

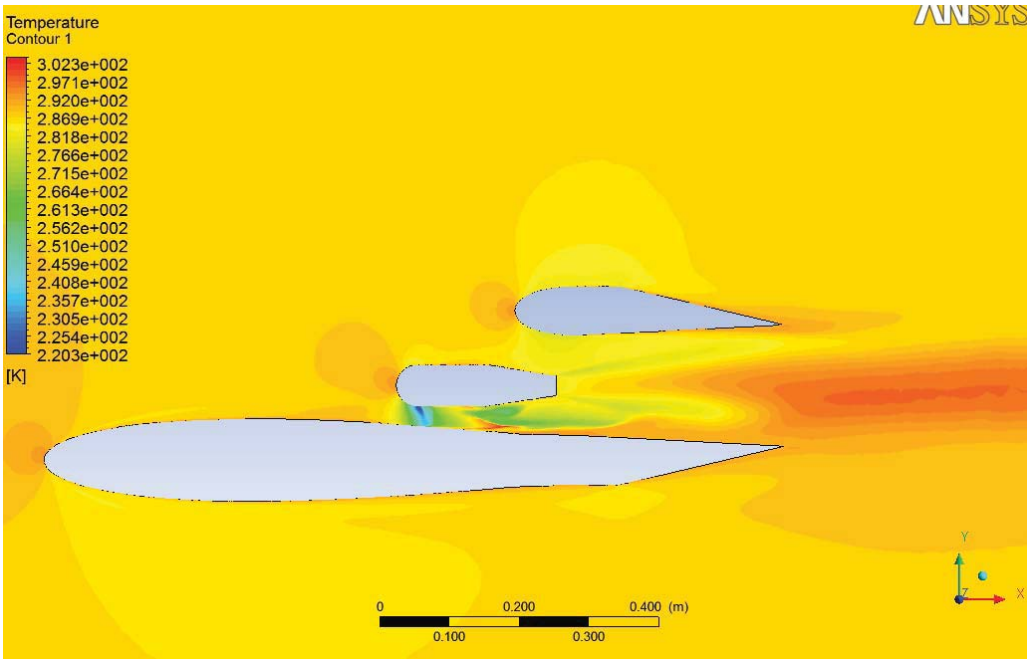

Temperature Contour: Angle 0 Mach =0.3

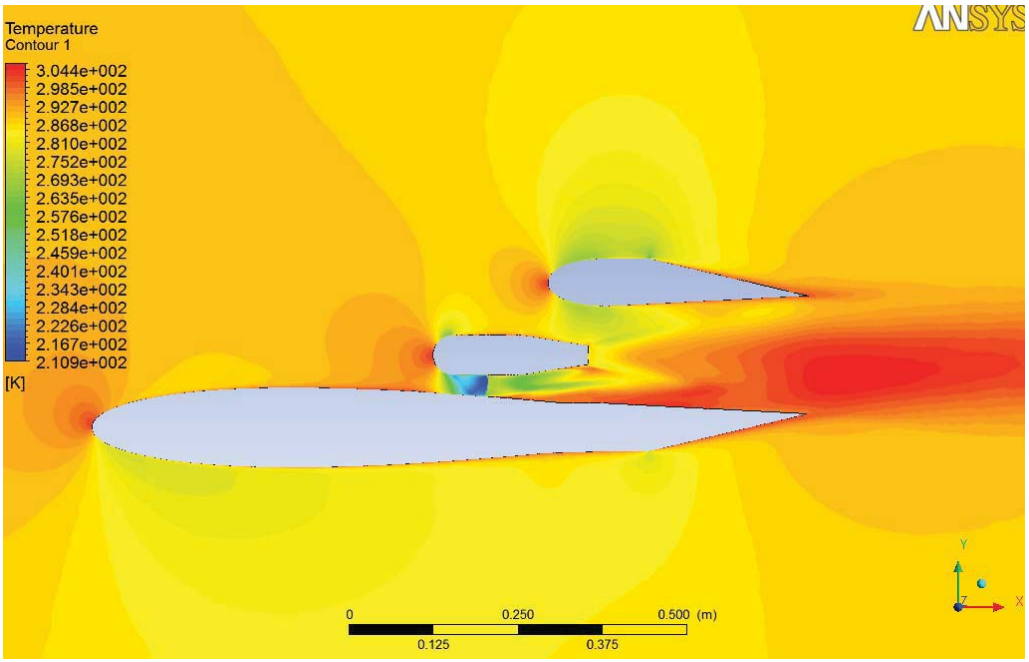

Temperature Contour: Angle 0 Mach =0.5

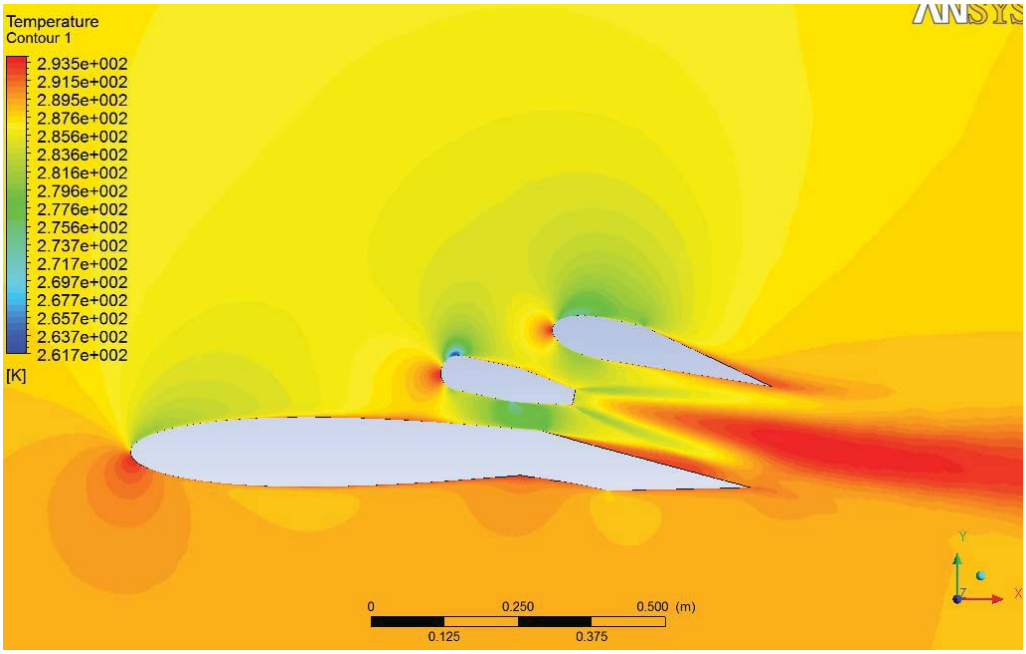

Temperature Contour: Angle 12 Mach =0.3

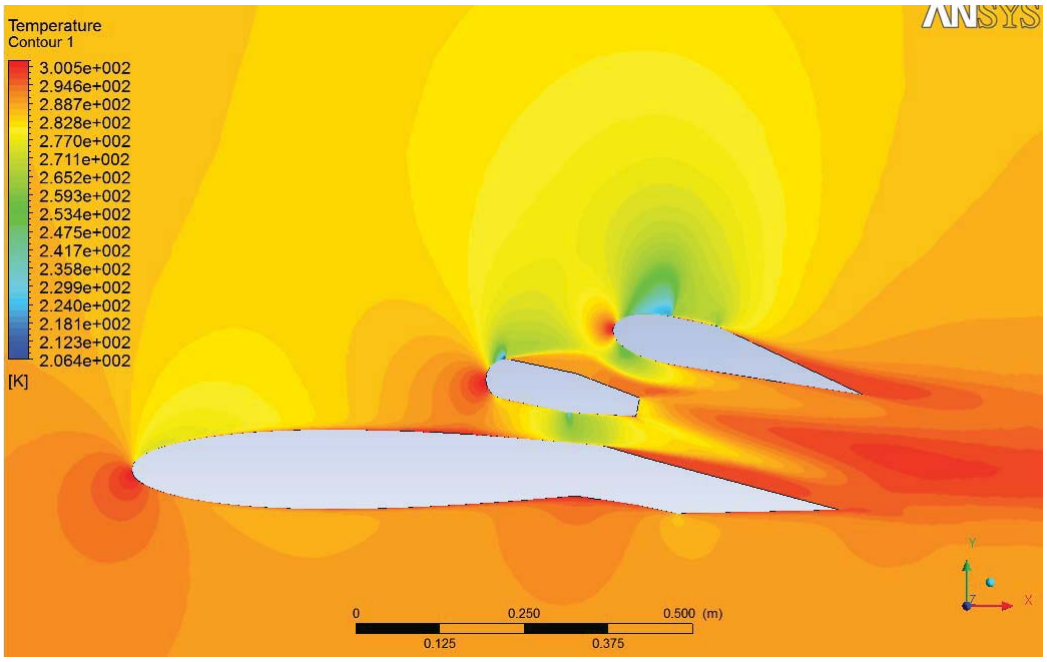

Temperature Contour: Angle 12 Mach =0.5

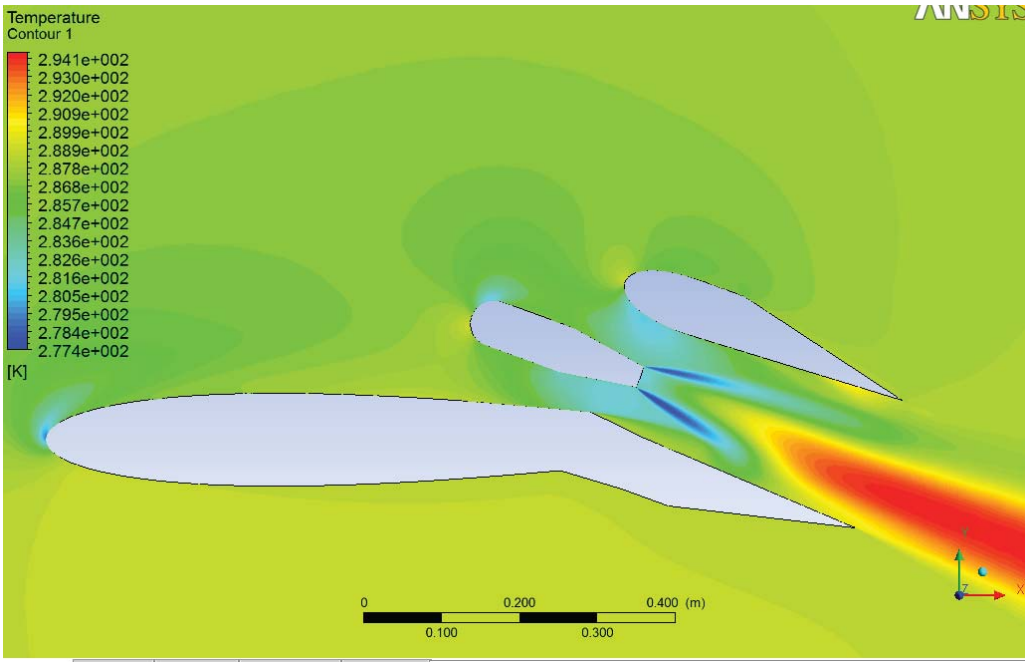

Temperature Contour: Angle 20 Mach =0.01

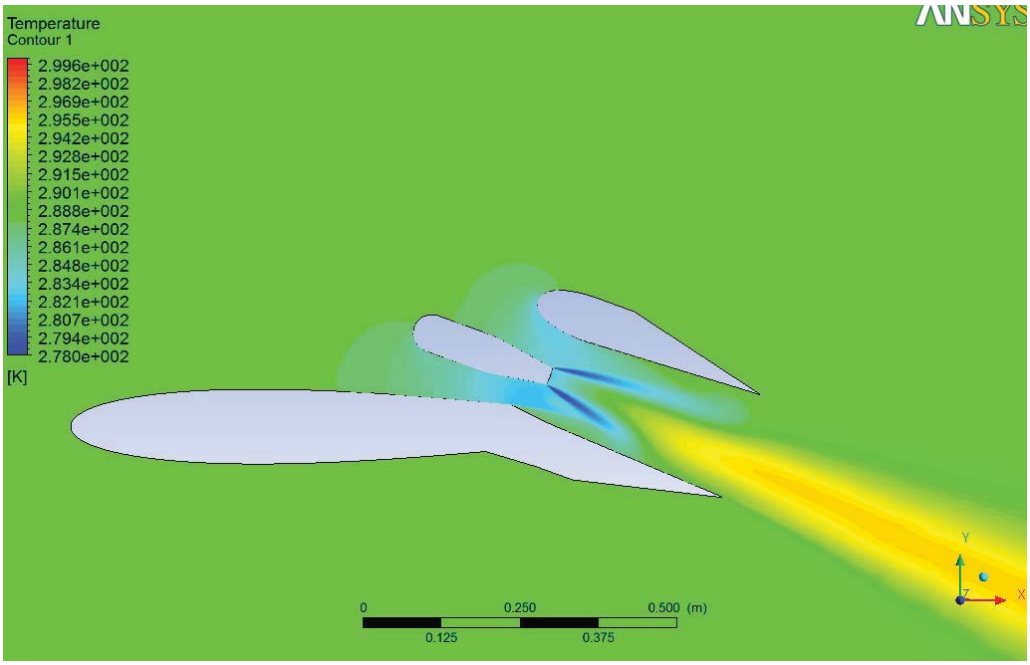

Temperature Contour: Angle 20 Mach =0.1

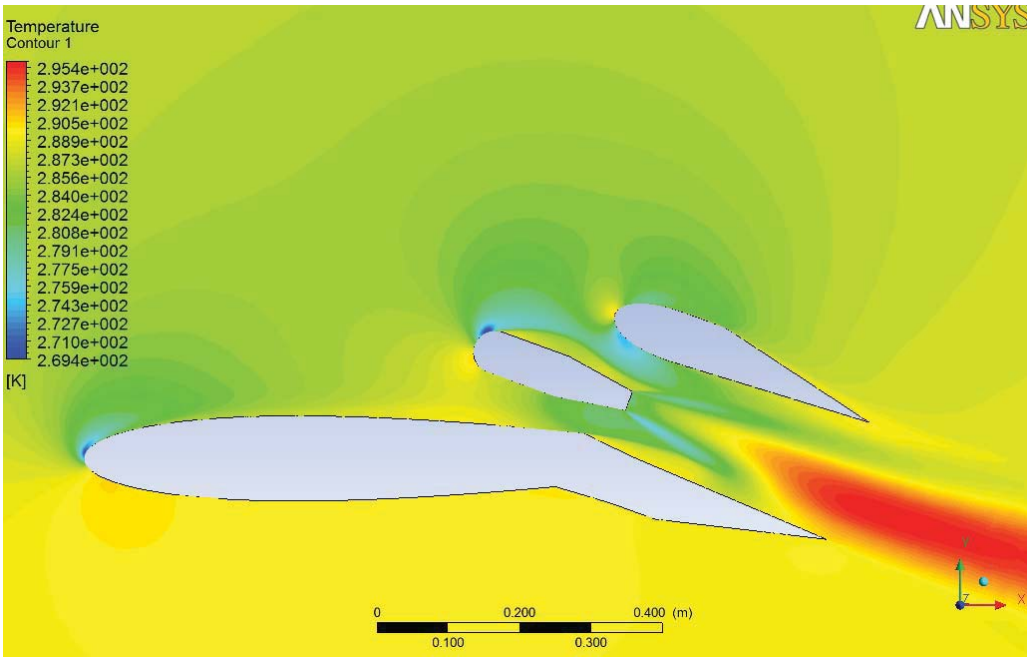

Temperature Contour: Angle 20 Mach =0.2

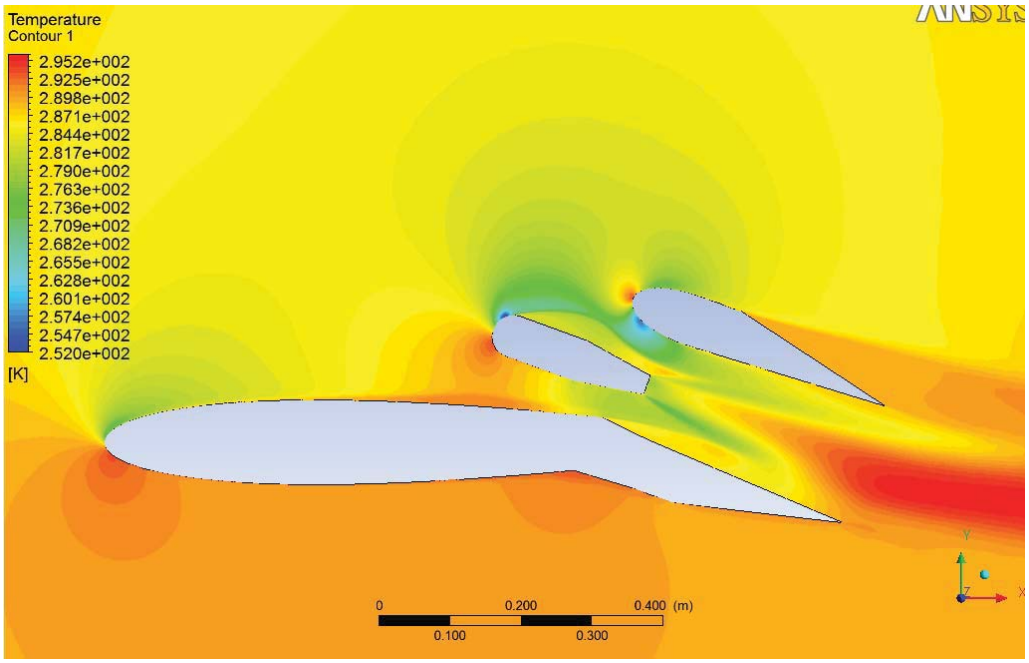

Temperature Contour: Angle 20 Mach =0.3

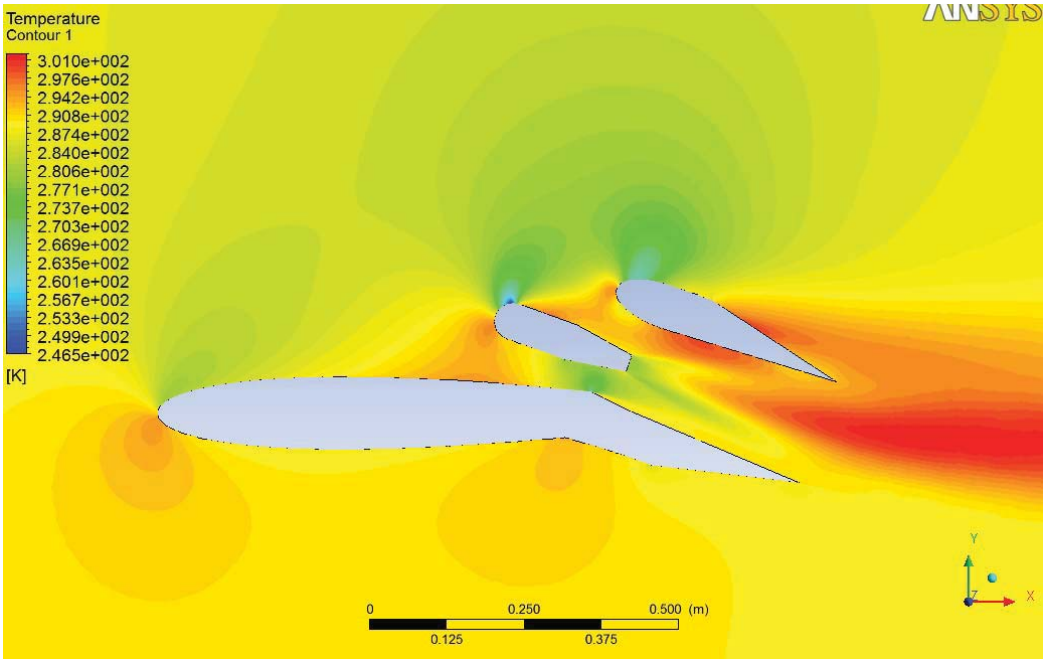

Temperature Contour: Angle 20 Mach =0.4

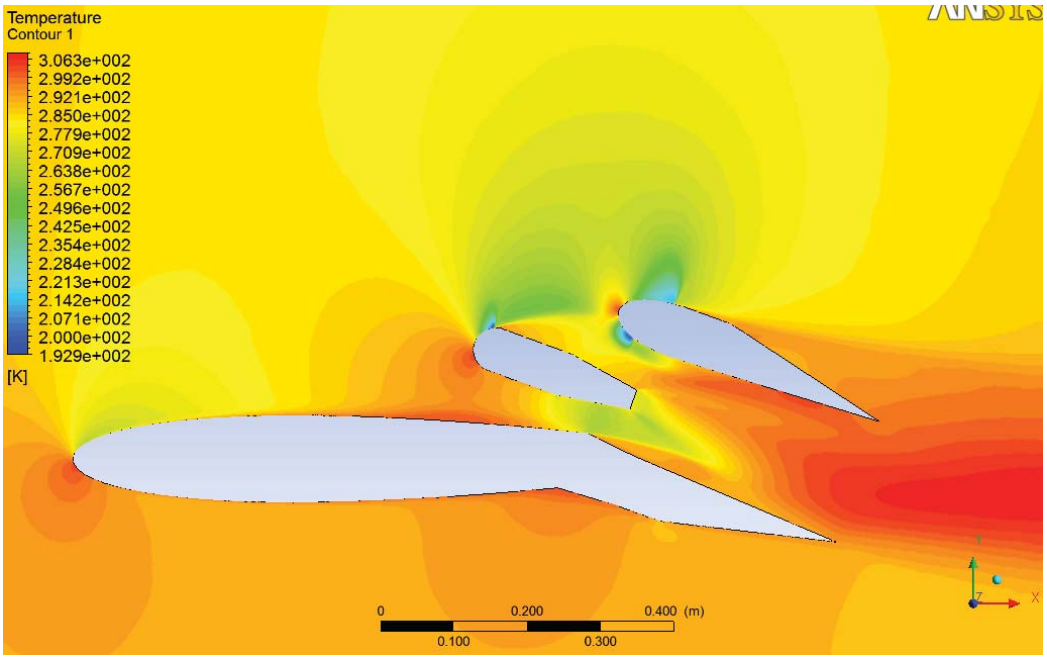

Temperature Contour: Angle 20 Mach =0.5

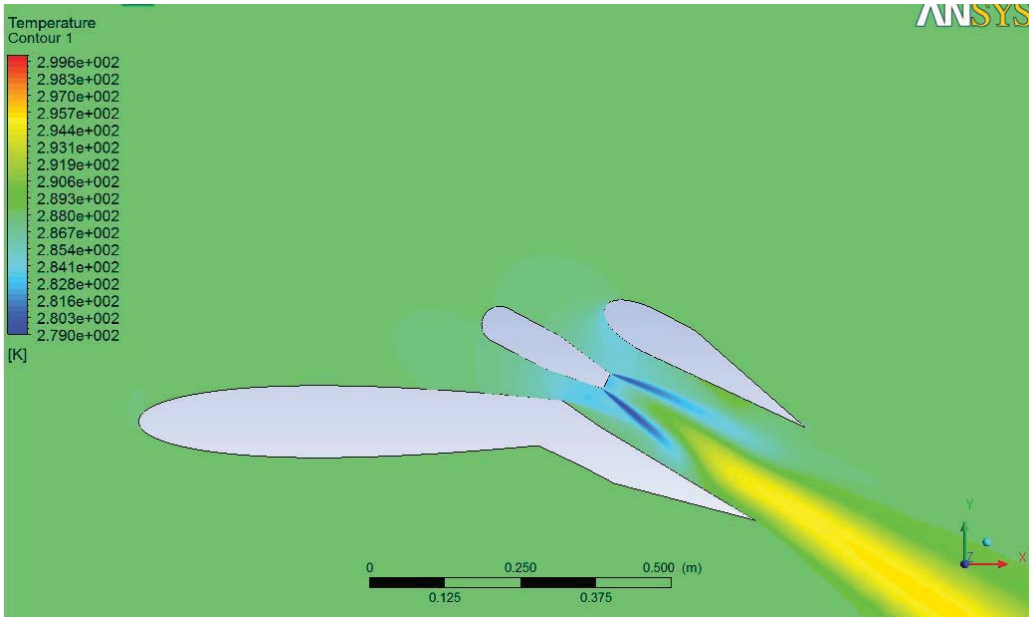

Temperature Contour: Angle 28 Mach =0.01

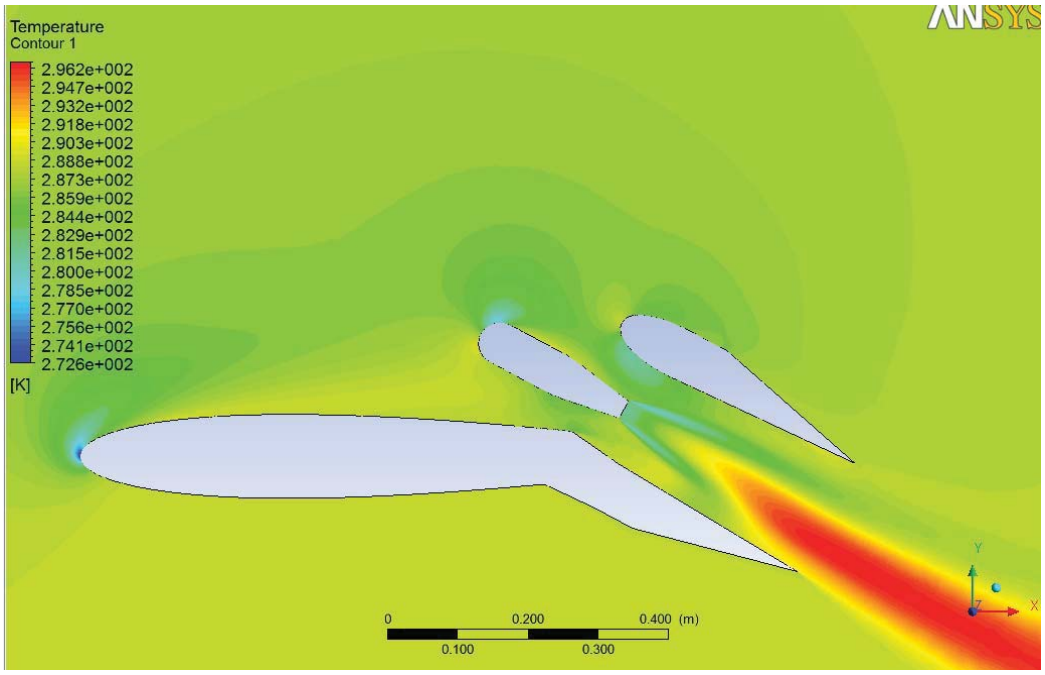

Temperature Contour: Angle 28 Mach =0.1

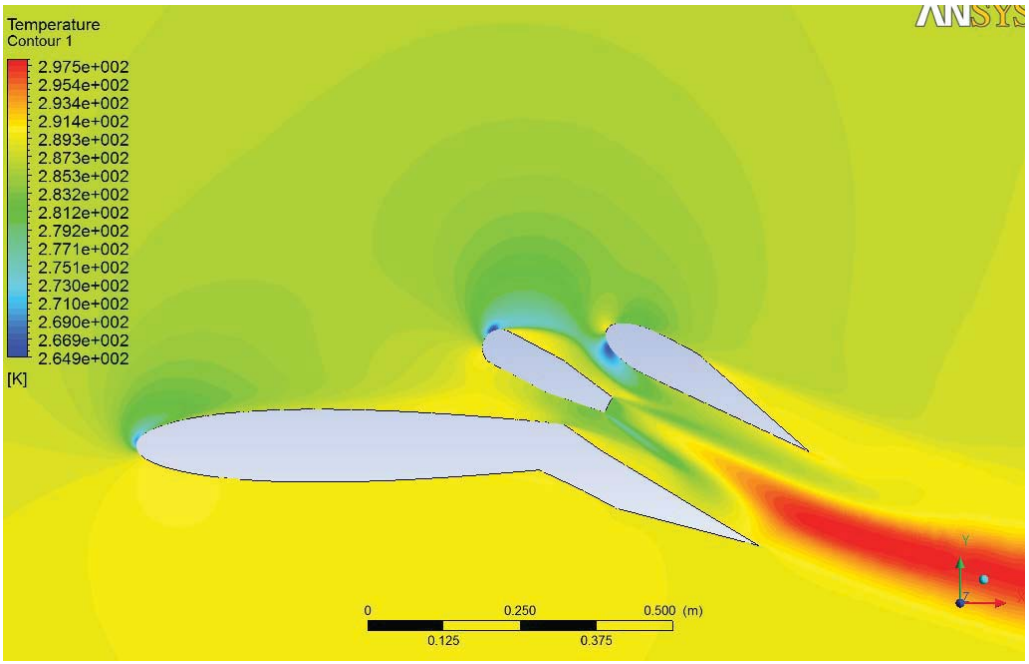

Temperature Contour: Angle 28 Mach =0.2

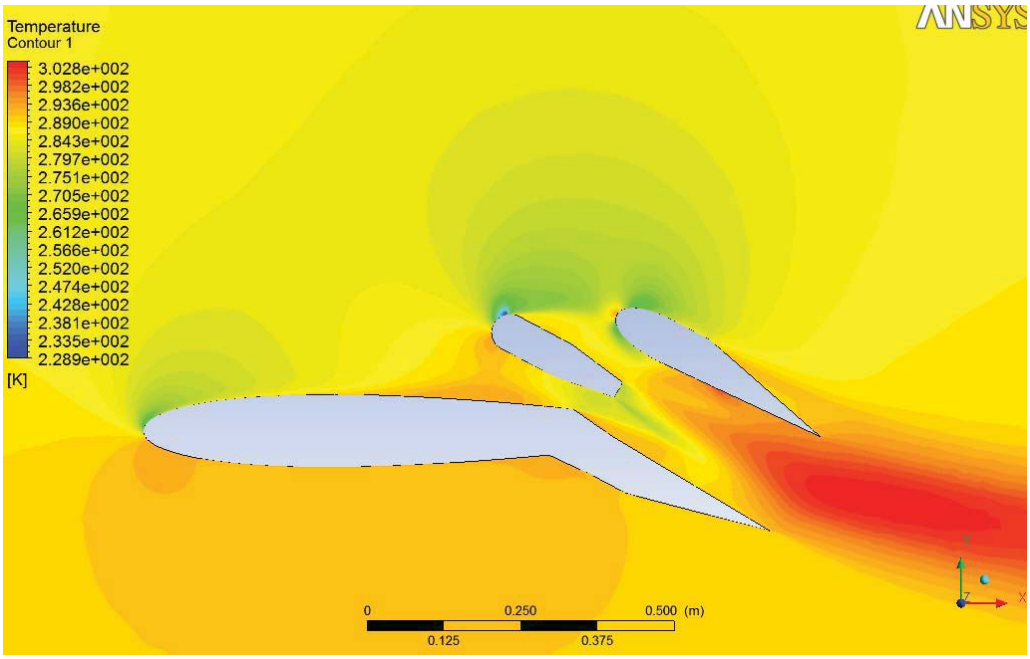

Temperature Contour: Angle 28 Mach =0.3

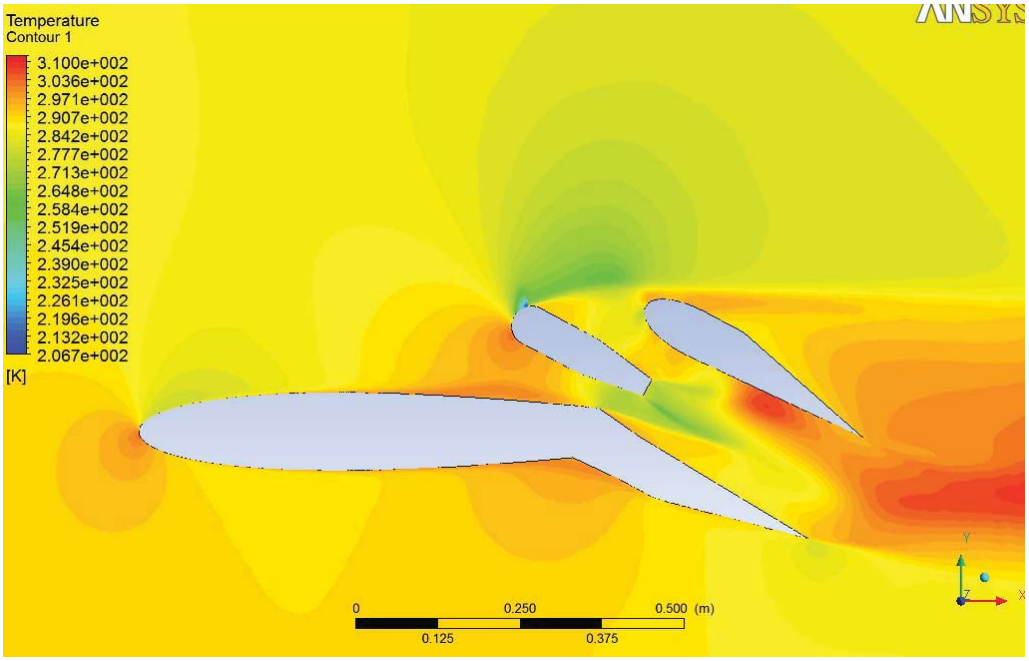

Temperature Contour: Angle 28 Mach =0.5

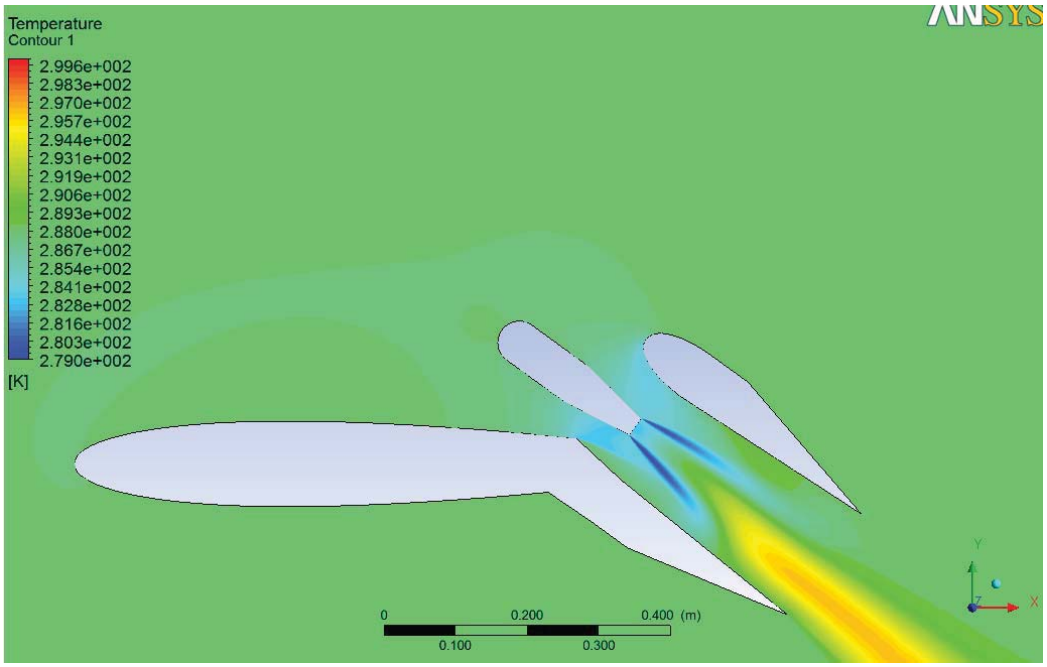

Temperature Contour: Angle 36 Mach =0.01

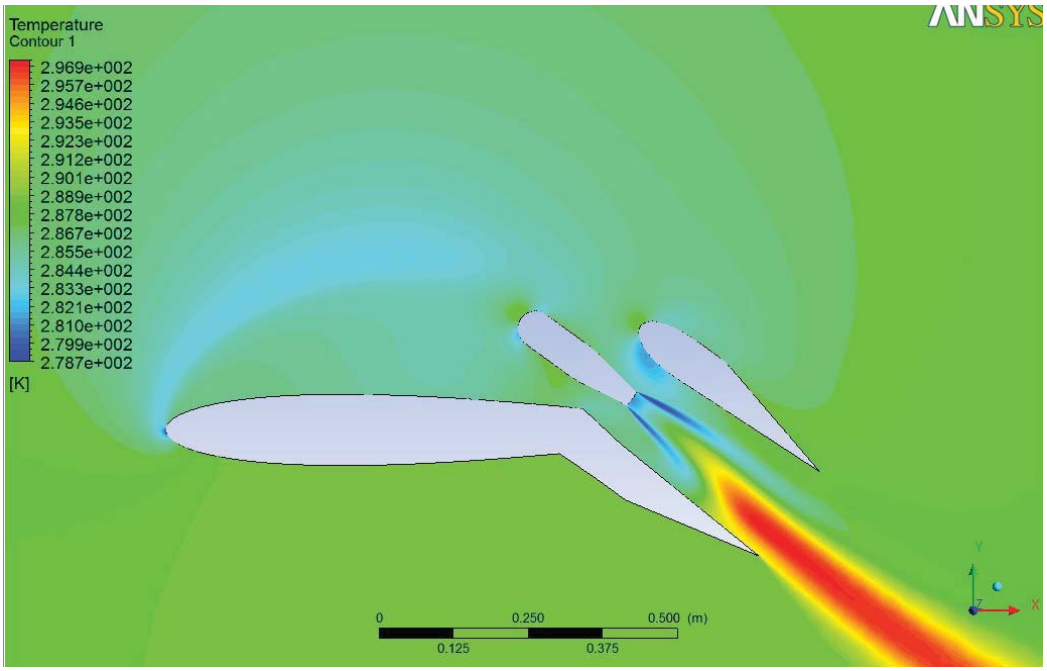

Temperature Contour: Angle 36 Mach =0.1

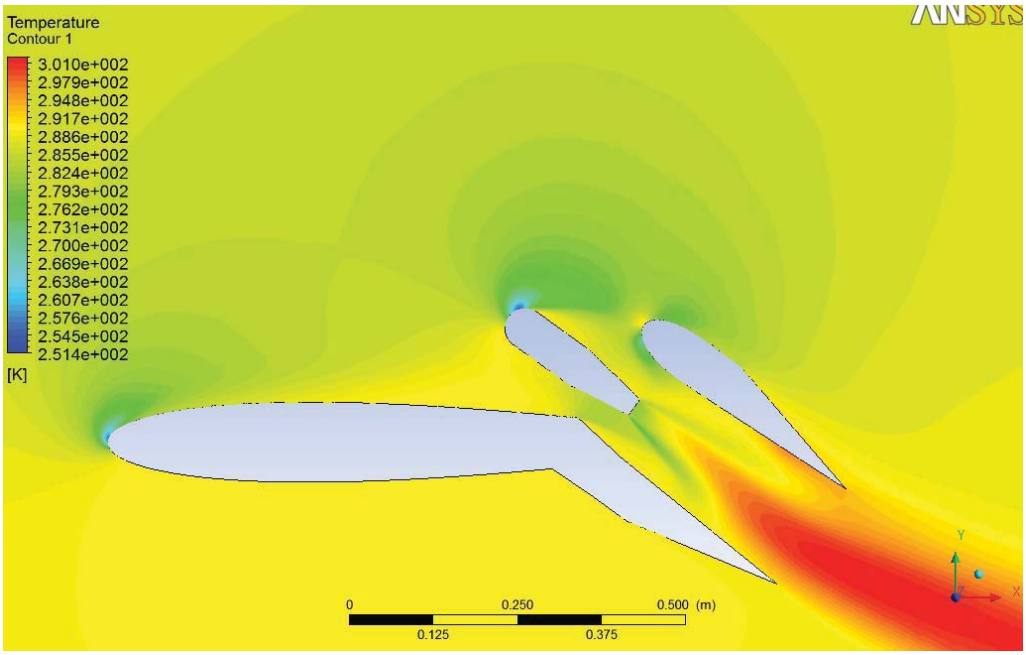

Temperature Contour: Angle 36 Mach =0.2

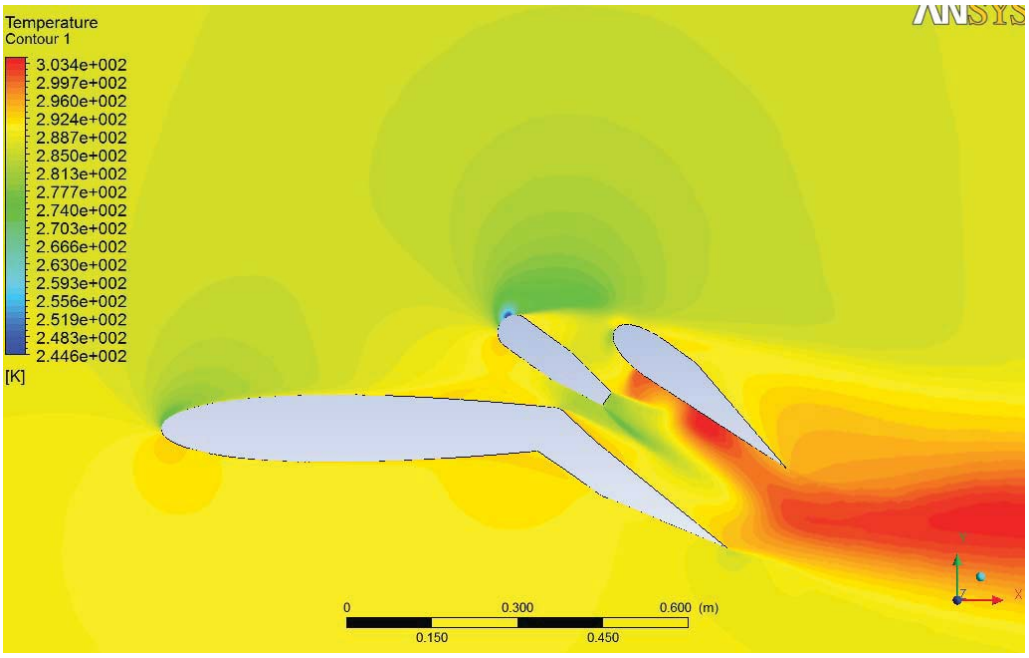

Temperature Contour: Angle 36 Mach =0.3

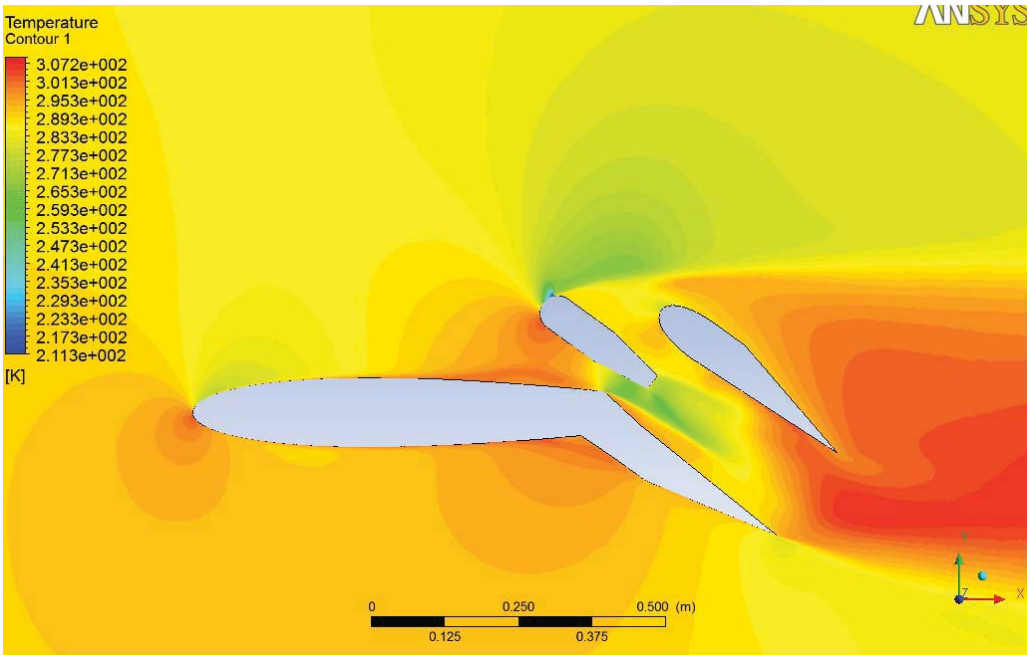

Temperature Contour: Angle 36 Mach =0.5

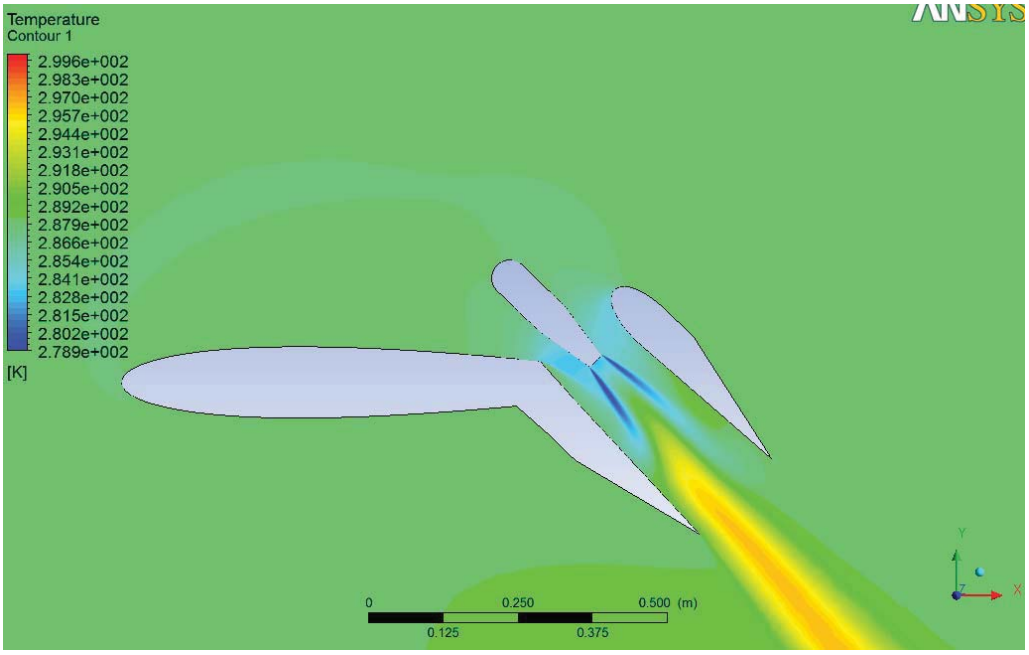

Temperature Contour: Angle 44 Mach =0.01

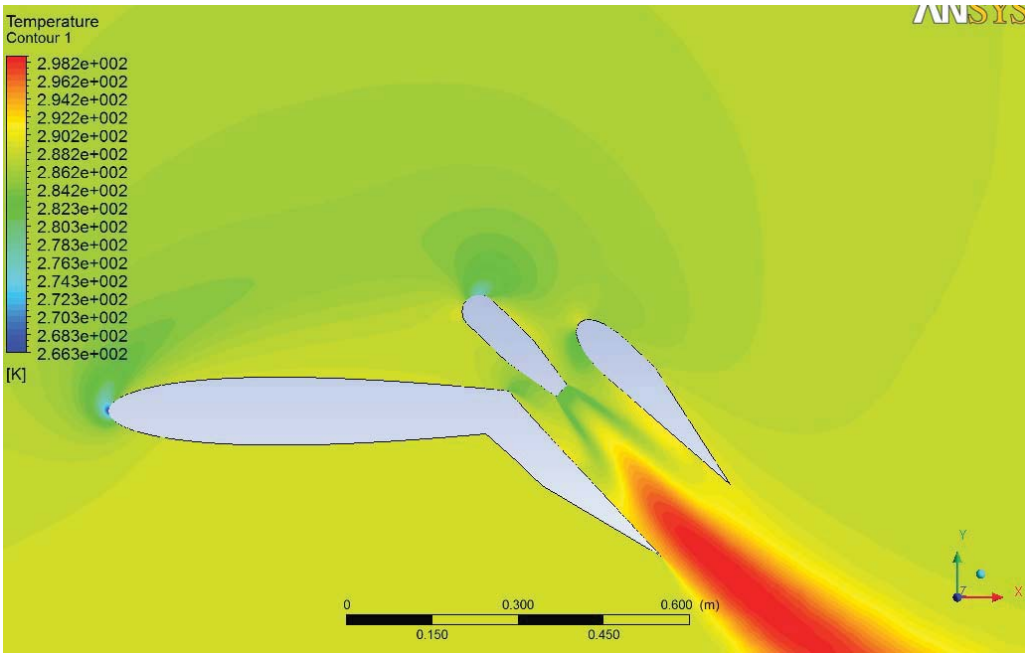

Temperature Contour: Angle 44 Mach =0.1

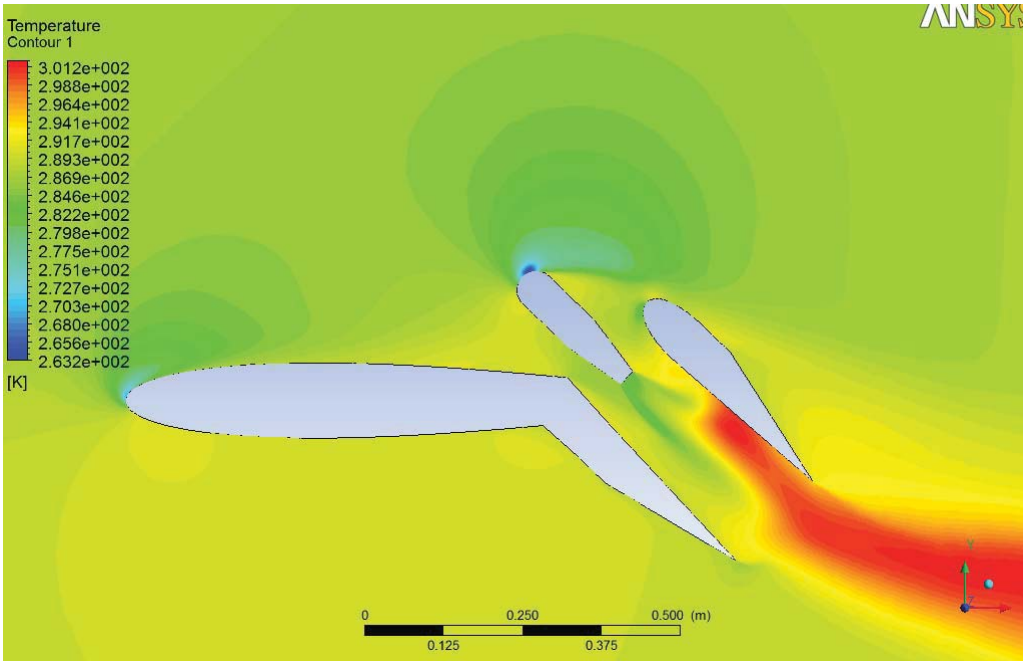

Temperature Contour: Angle 44 Mach =0.2

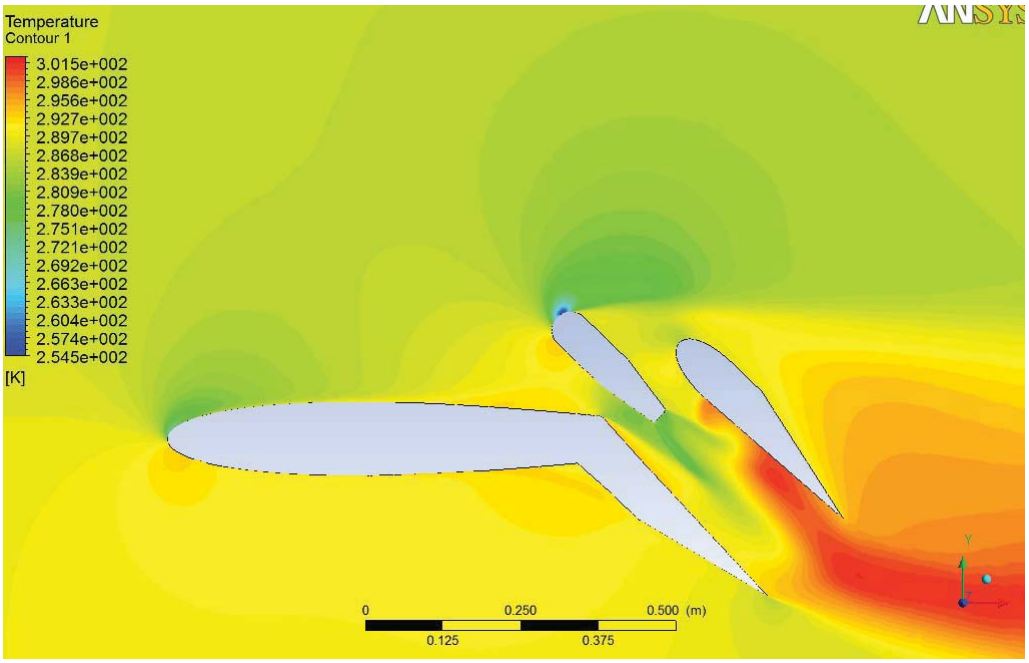

Temperature Contour: Angle 44 Mach =0.3

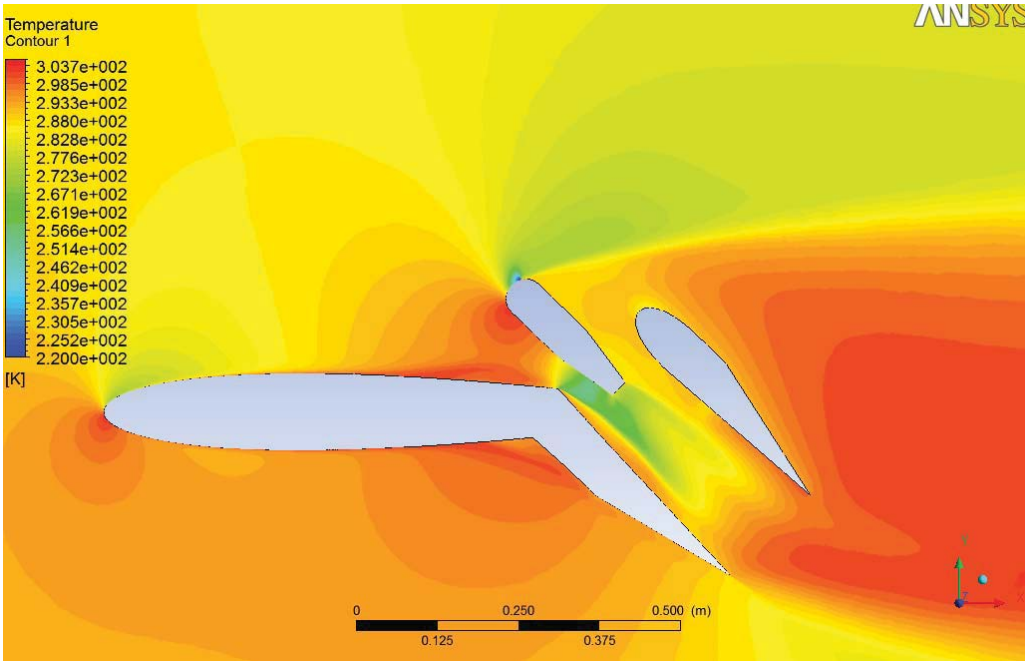

Temperature Contour: Angle 44 Mach =0.5

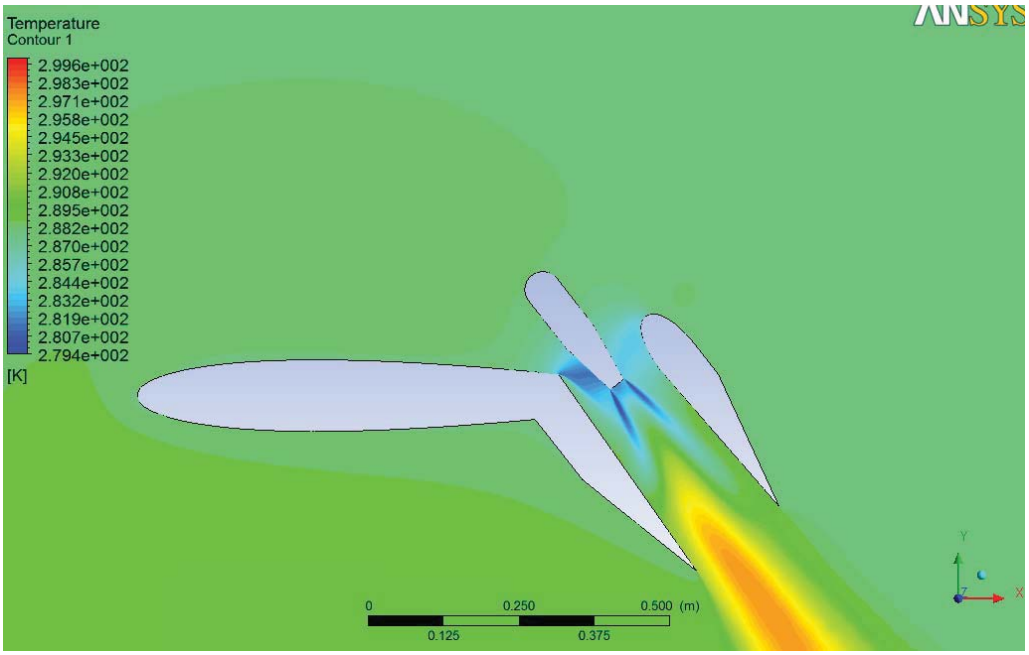

Temperature Contour: Angle 52 Mach =0.01

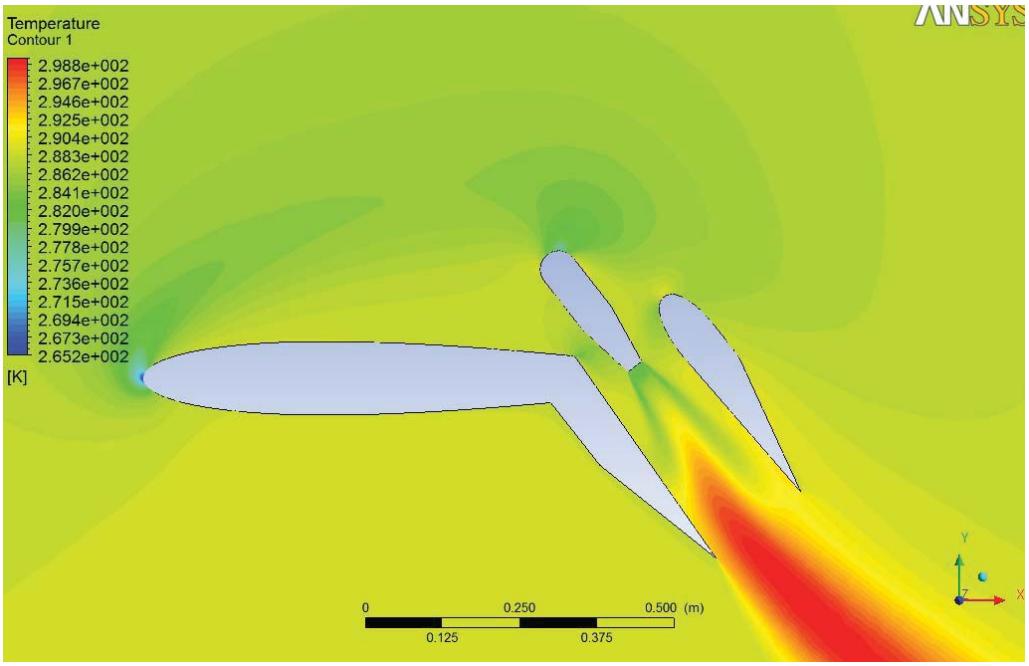

Temperature Contour: Angle 52 Mach =0.1

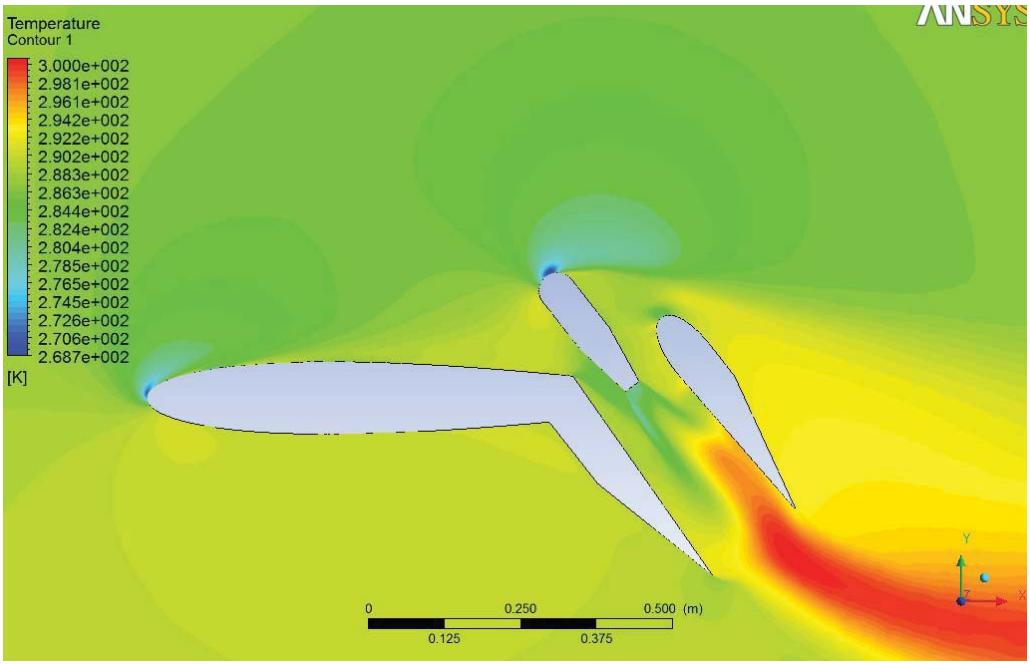

Temperature Contour: Angle 52 Mach =0.2

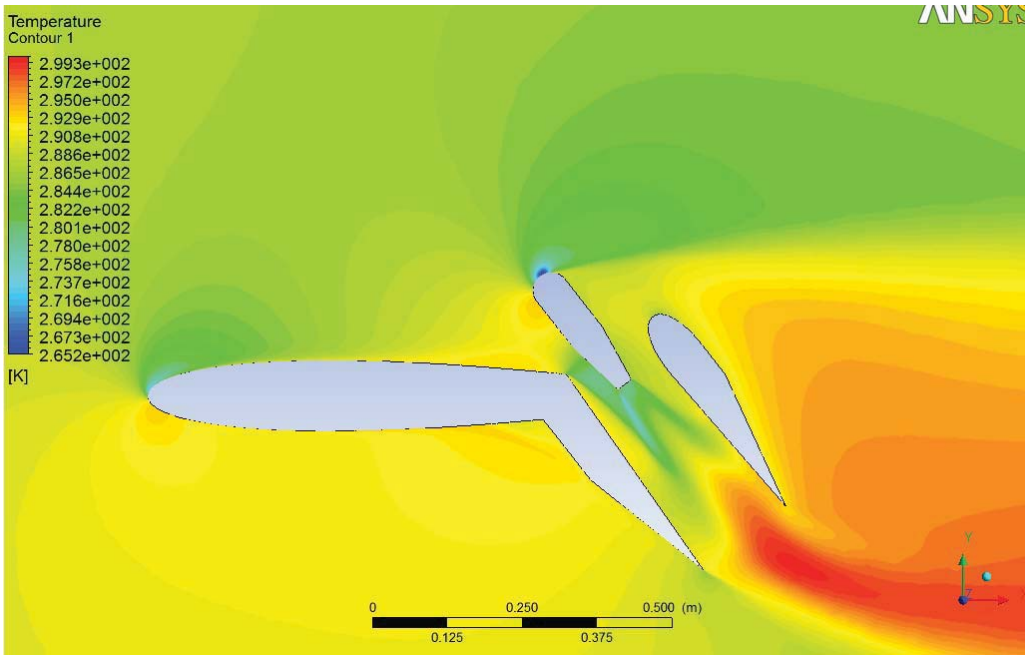

Temperature Contour: Angle 52 Mach =0.3

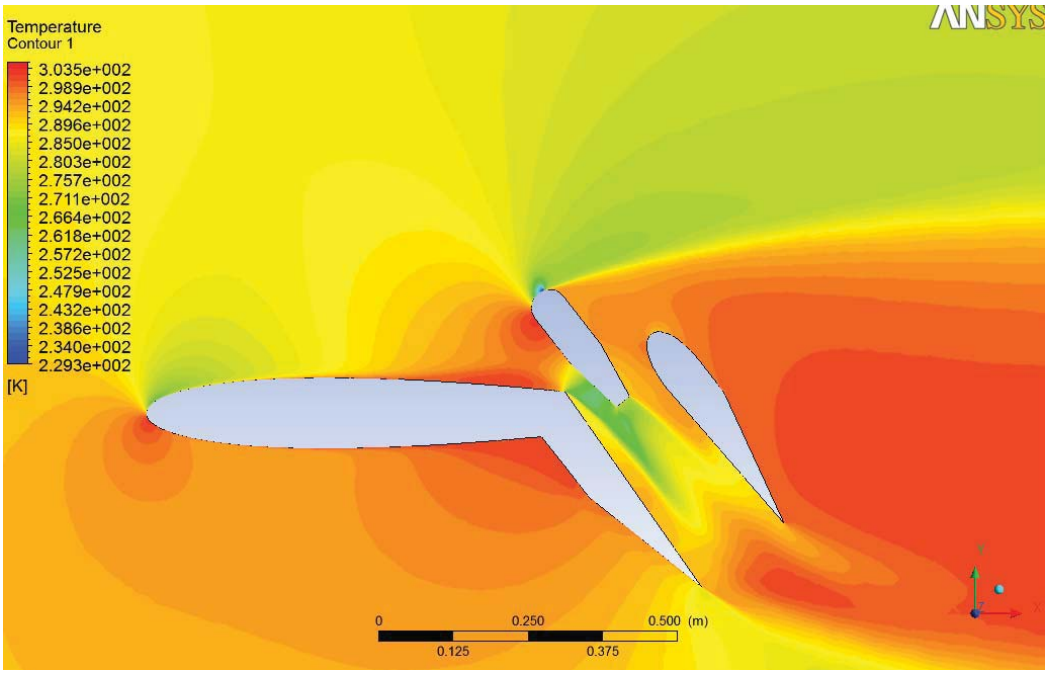

Temperature Contour: Angle 52 Mach =0.5

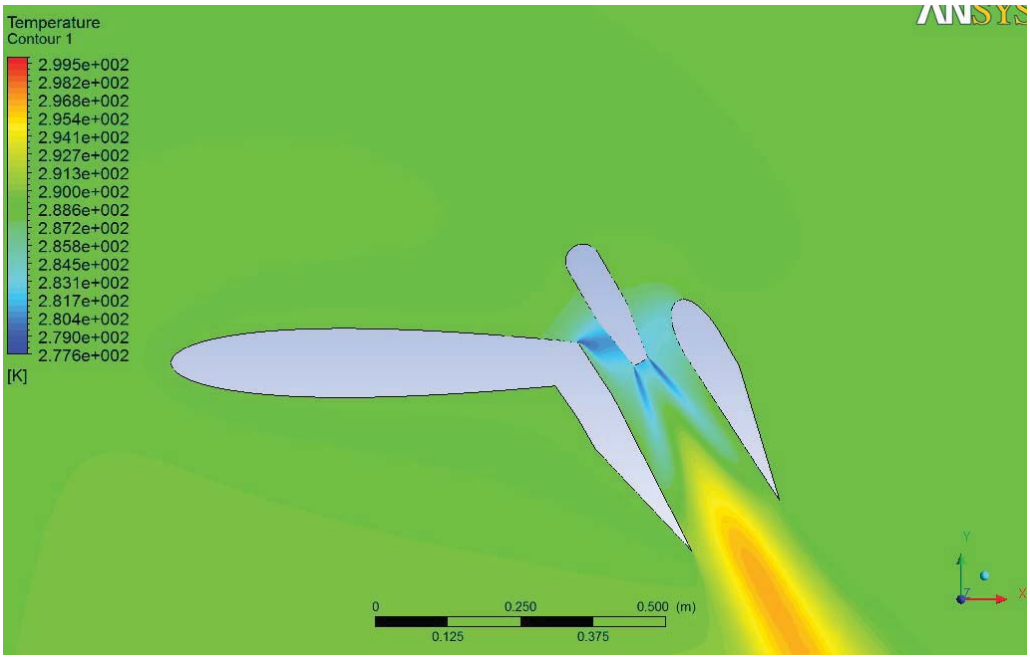

Temperature Contour: Angle 60 Mach =0.01

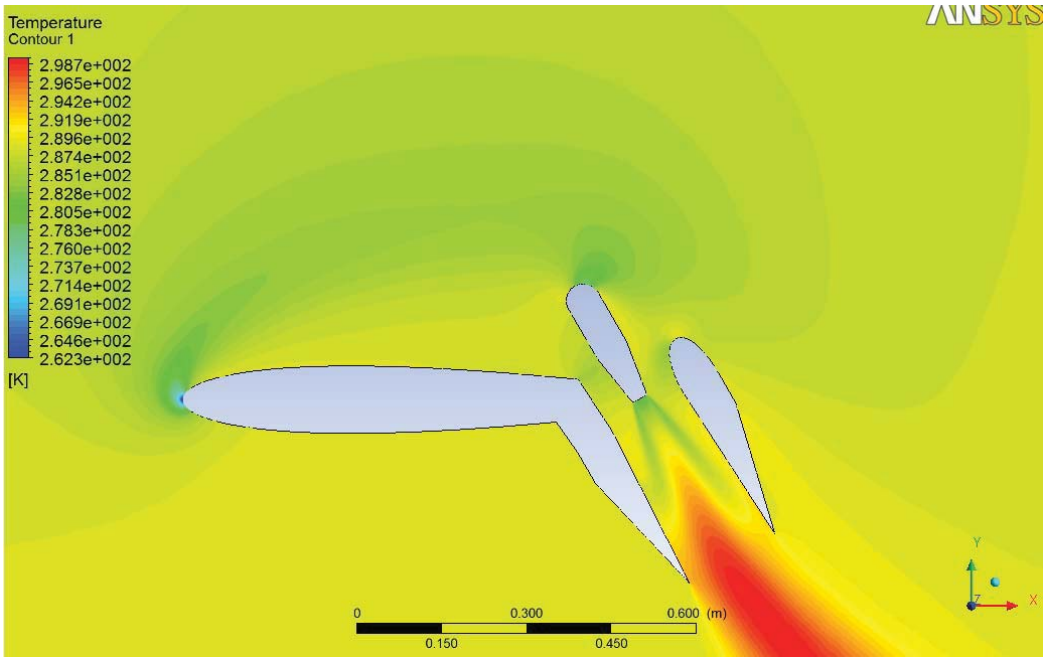

Temperature Contour: Angle 60 Mach =0.1

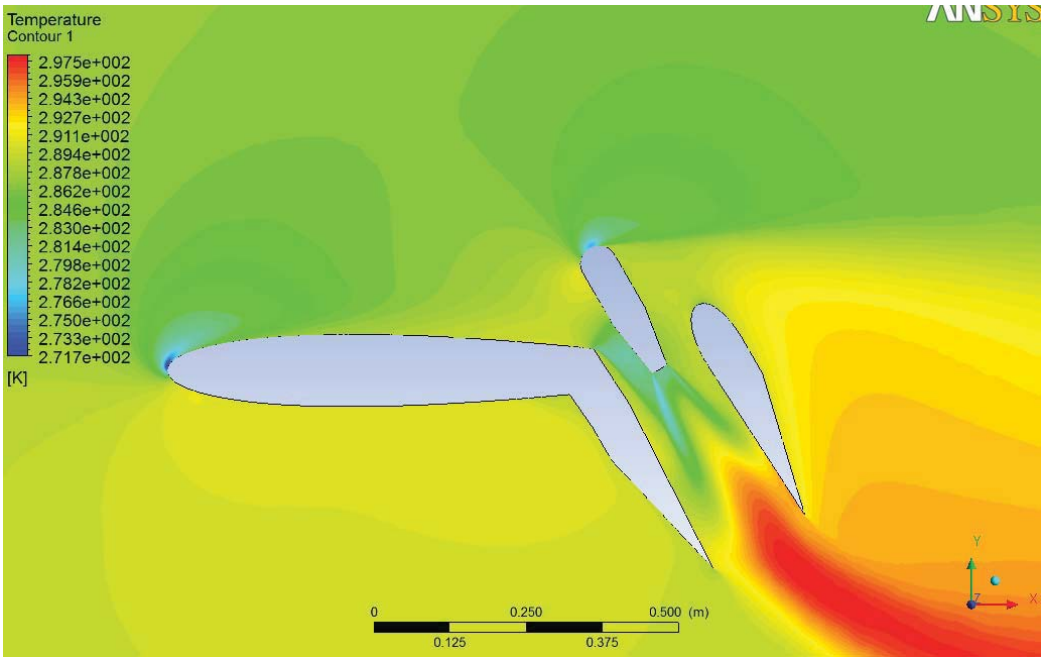

Temperature Contour: Angle 60 Mach =0.2

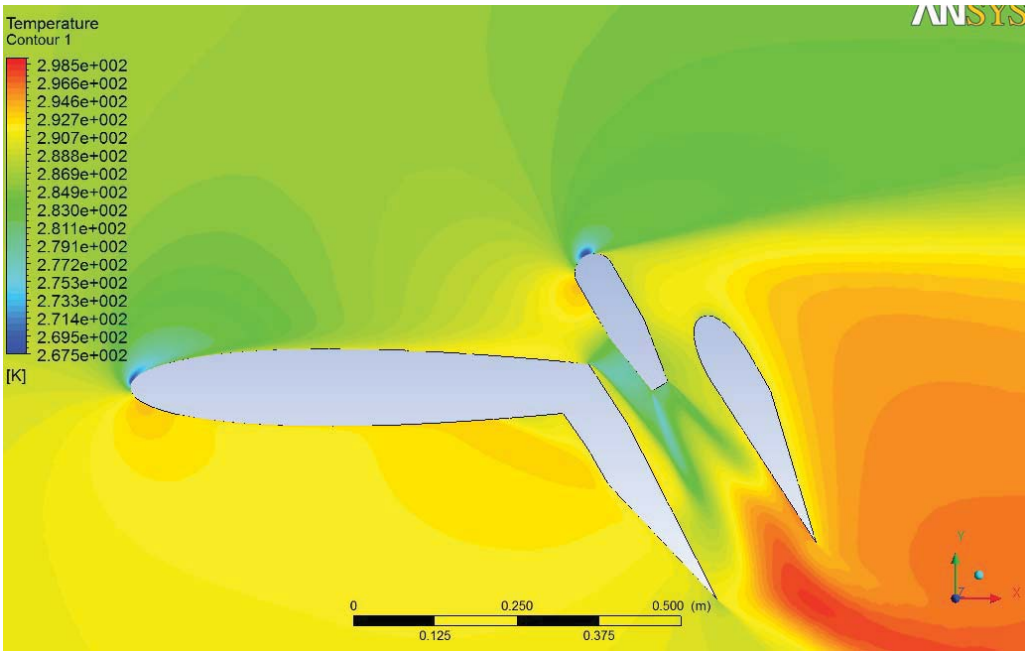

Temperature Contour: Angle 60 Mach =0.3

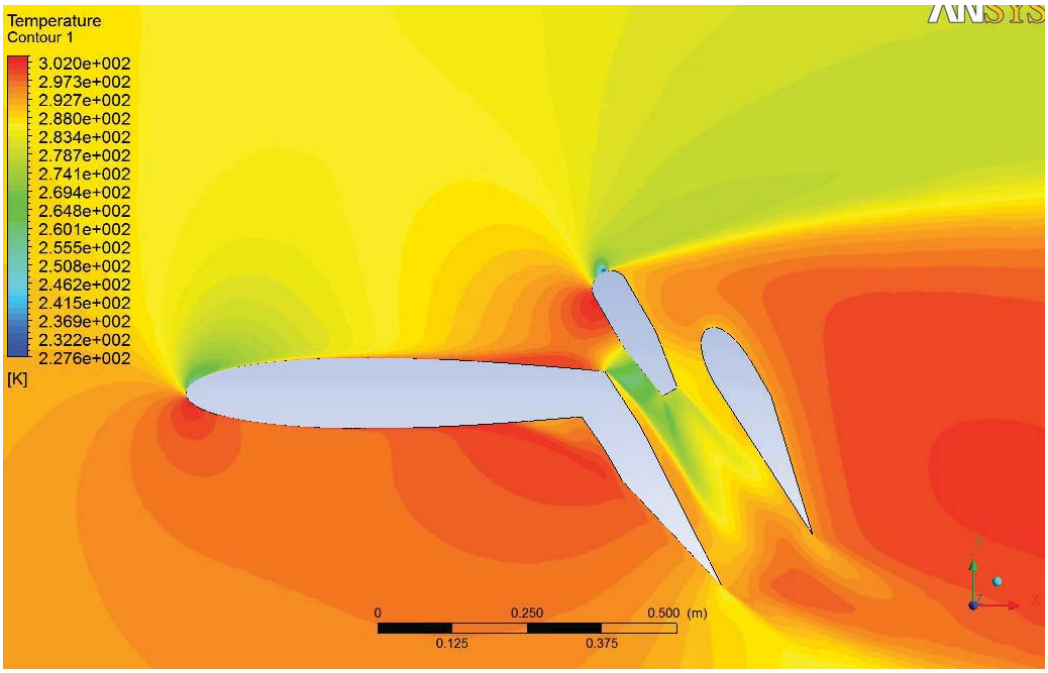

Temperature Contour: Angle 60 Mach =0.5

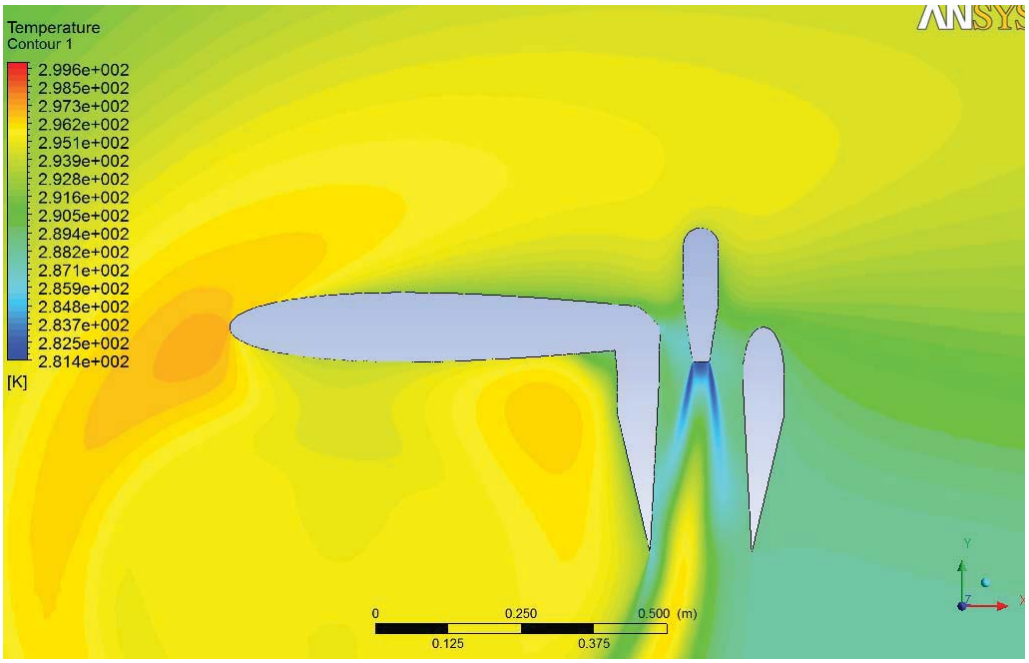

Temperature Contour: Angle 90 Mach =0.01

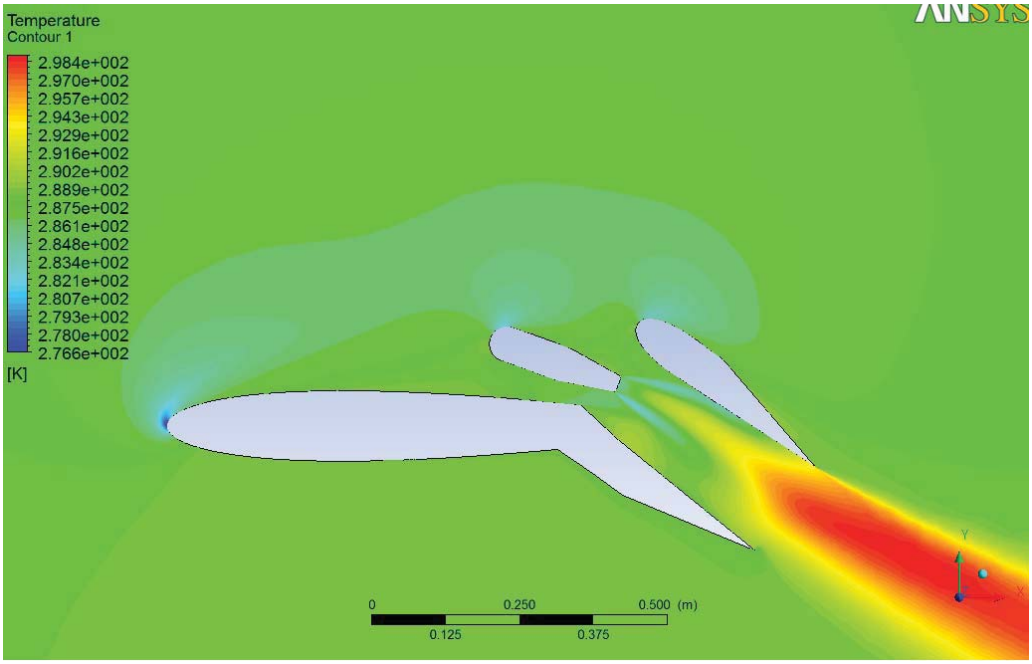

Temperature Contour: Angle 36 Mach =0.1 Deflected Nozzle Configuration

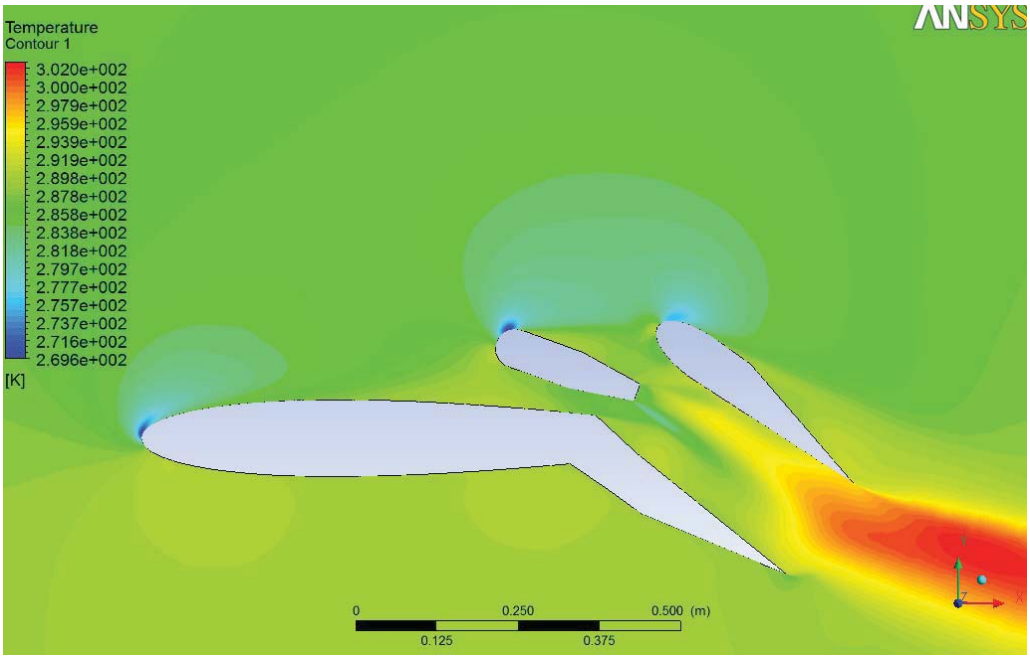

Temperature Contour: Angle 36 Mach =0.2 Deflected Nozzle Configuration

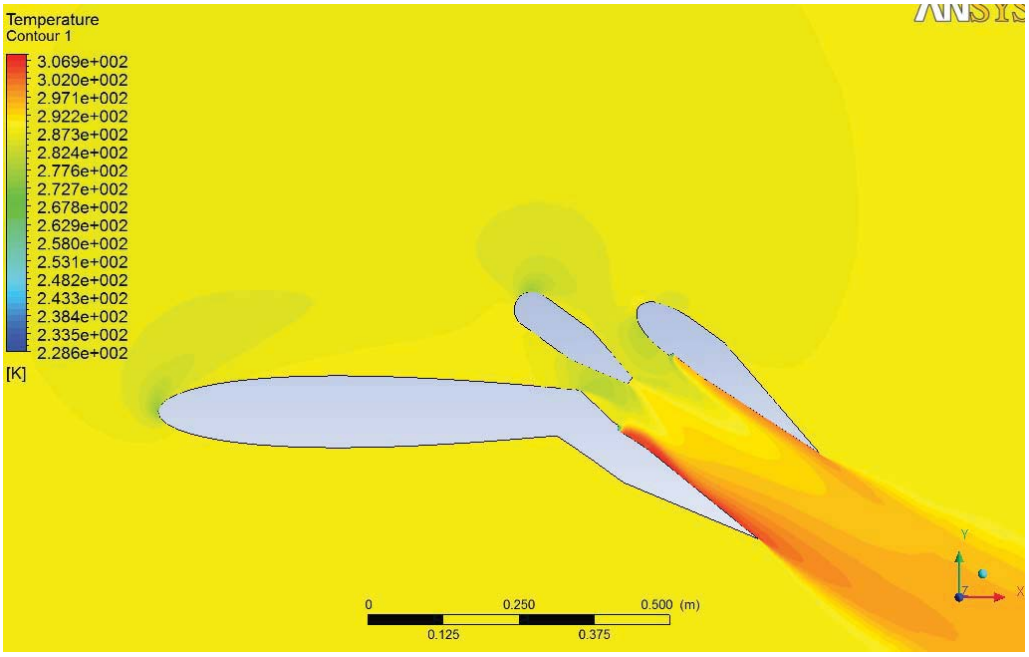

Temperature Contour: Angle 36 Mach =0.1 Wall Jets Configuration

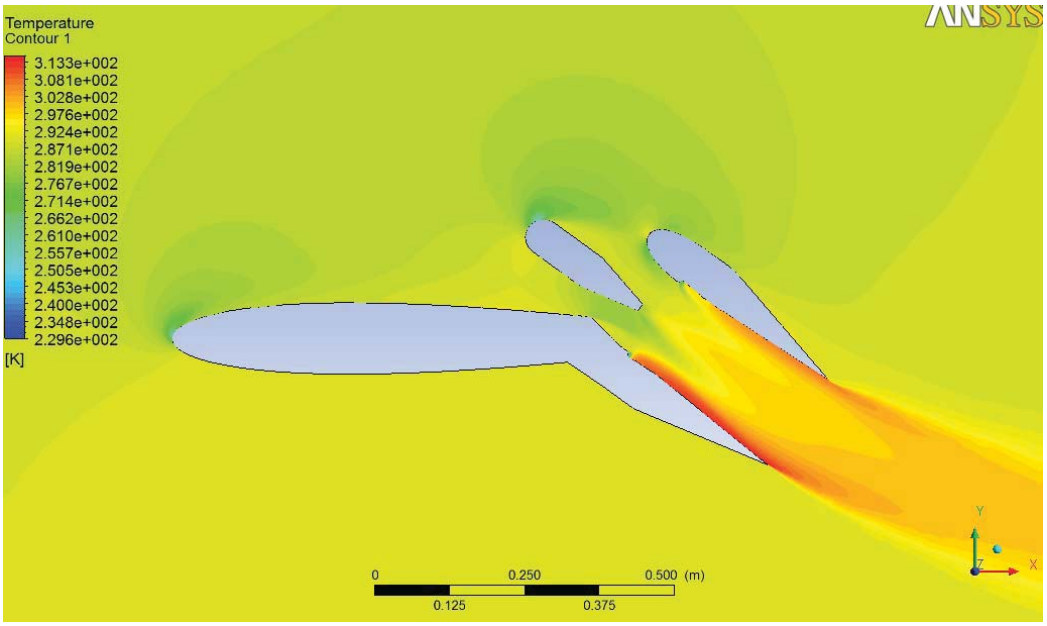

Temperature Contour: Angle 36 Mach =0.2 Wall Jets Configuration

Appendix C: Total Pressure Contours

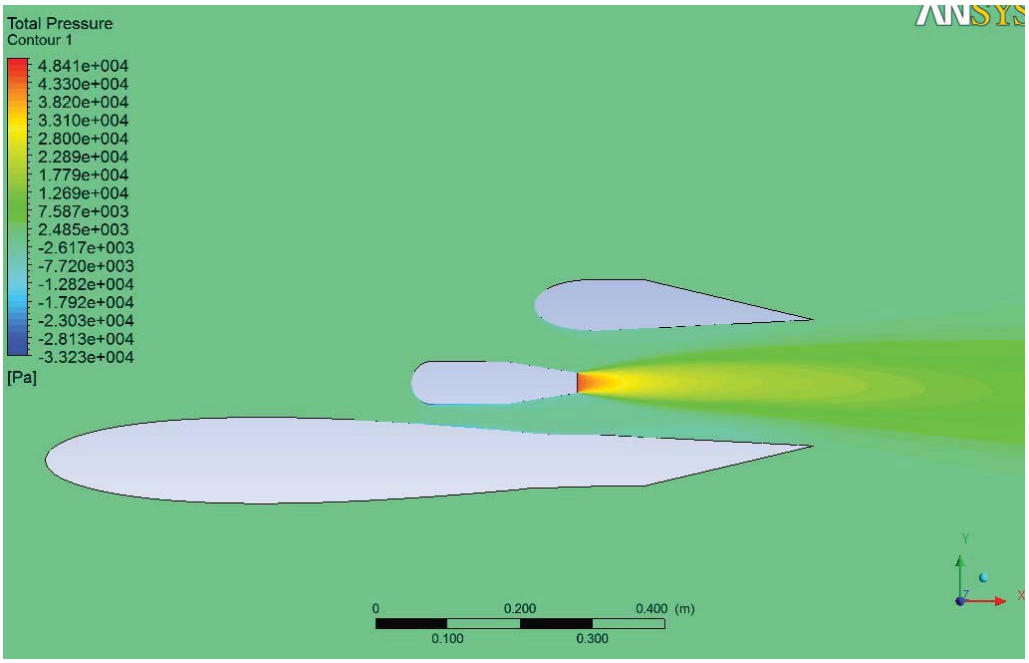

Total Pressure Contour: Angle 0 Mach =0.01

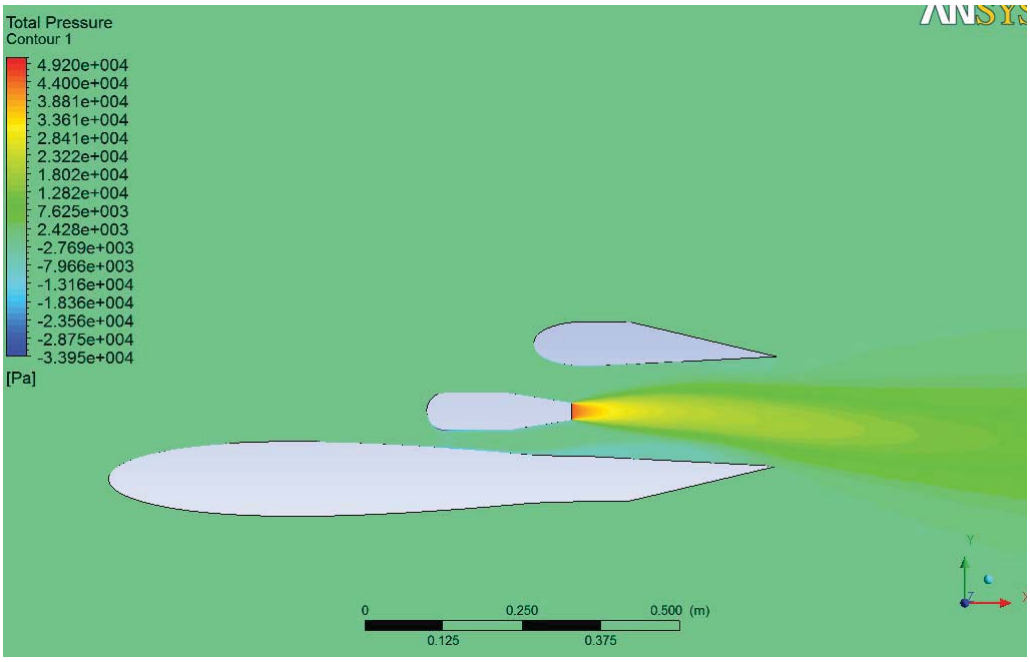

Total Pressure Contour: Angle 0 Mach =0.1

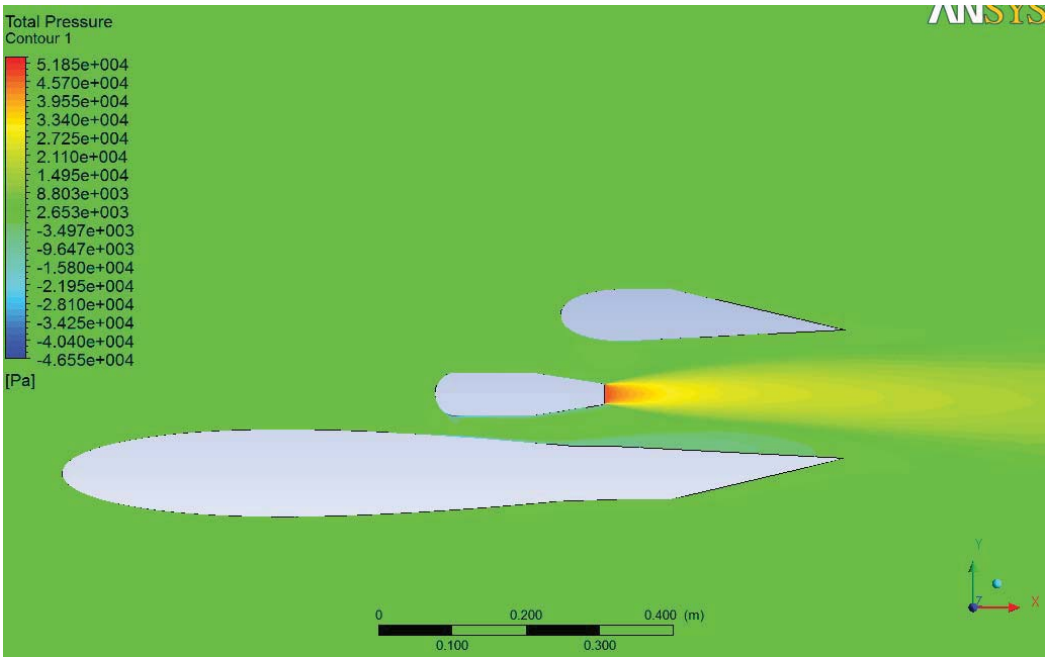

Total Pressure Contour: Angle 0 Mach =0.2

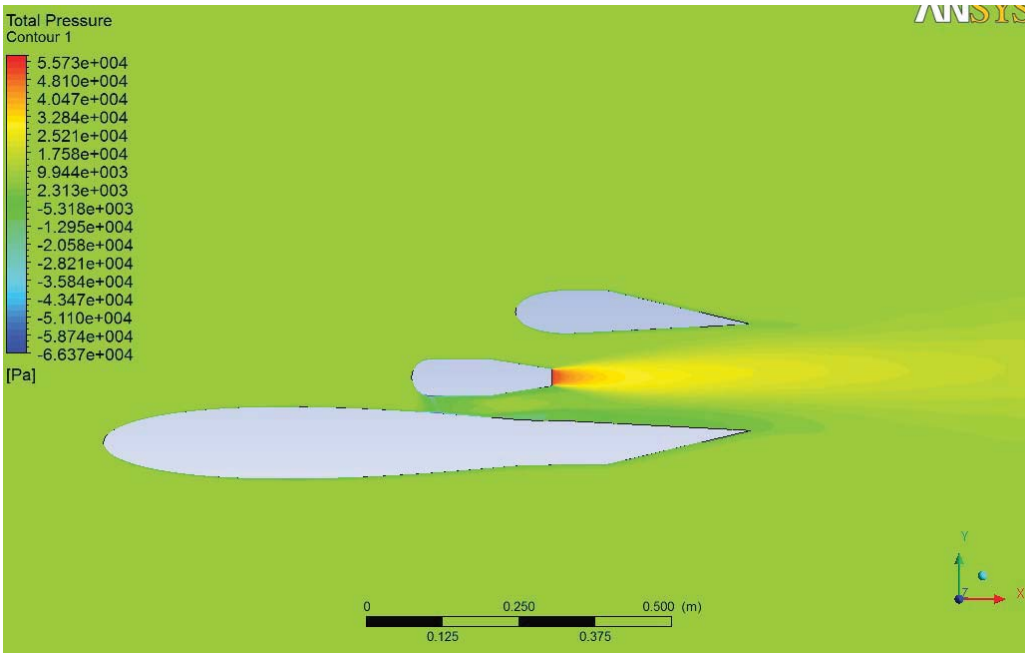

Total Pressure Contour: Angle 0 Mach =0.3

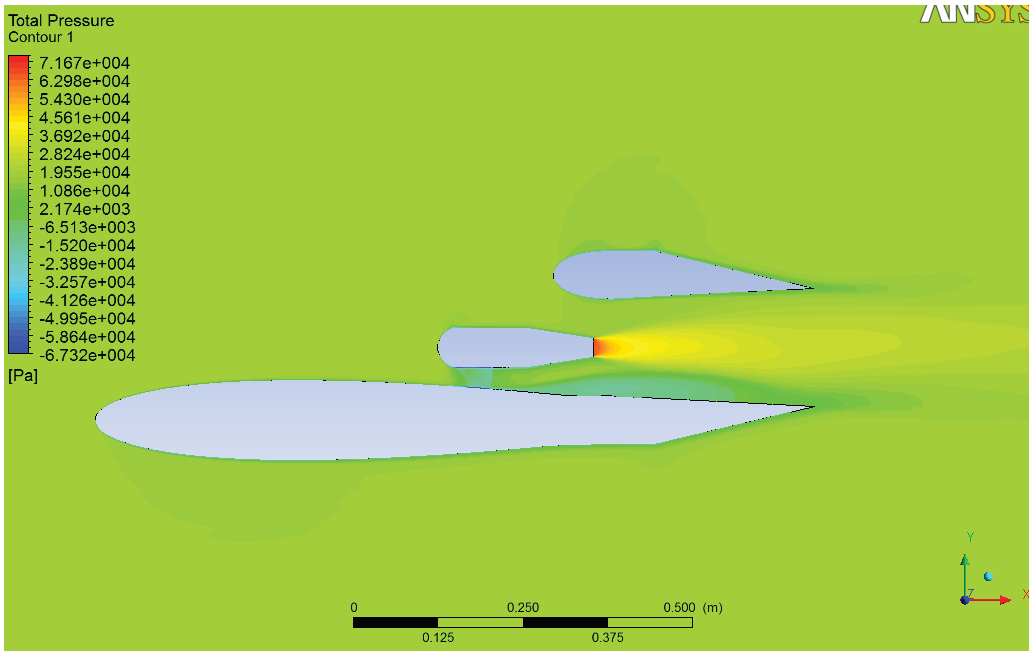

Total Pressure Contour: Angle 0 Mach =0.5

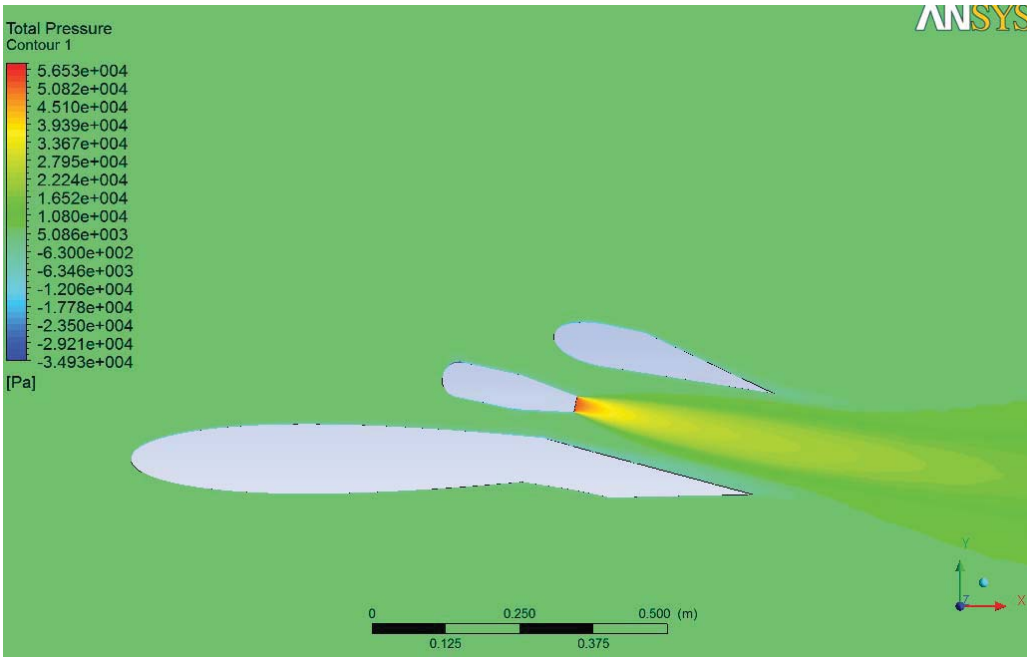

Total Pressure Contour: Angle 12 Mach =0.3

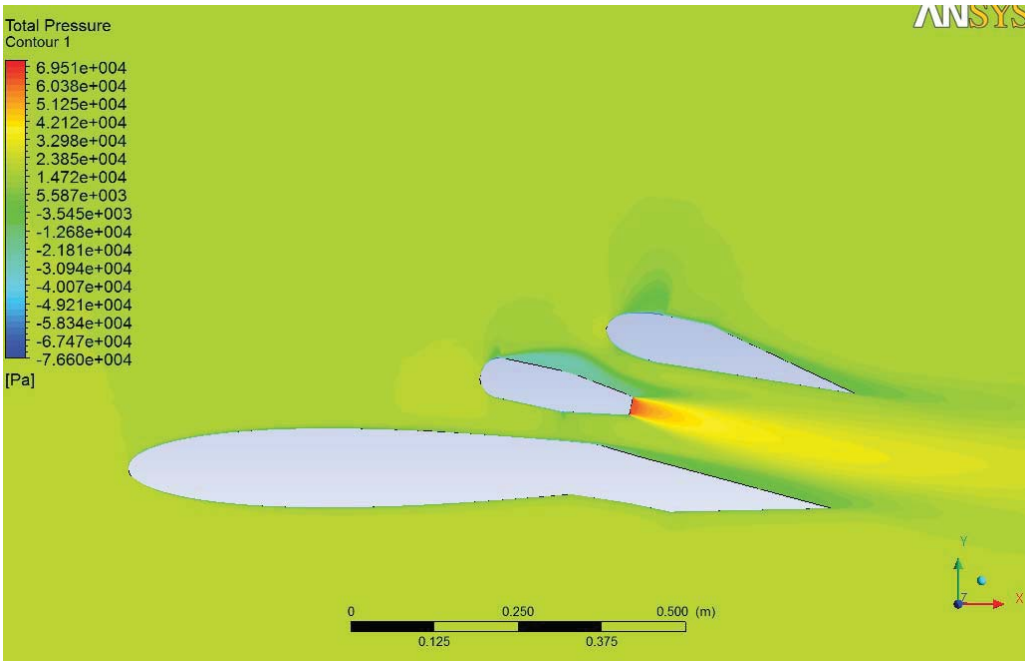

Total Pressure Contour: Angle 12 Mach =0.5

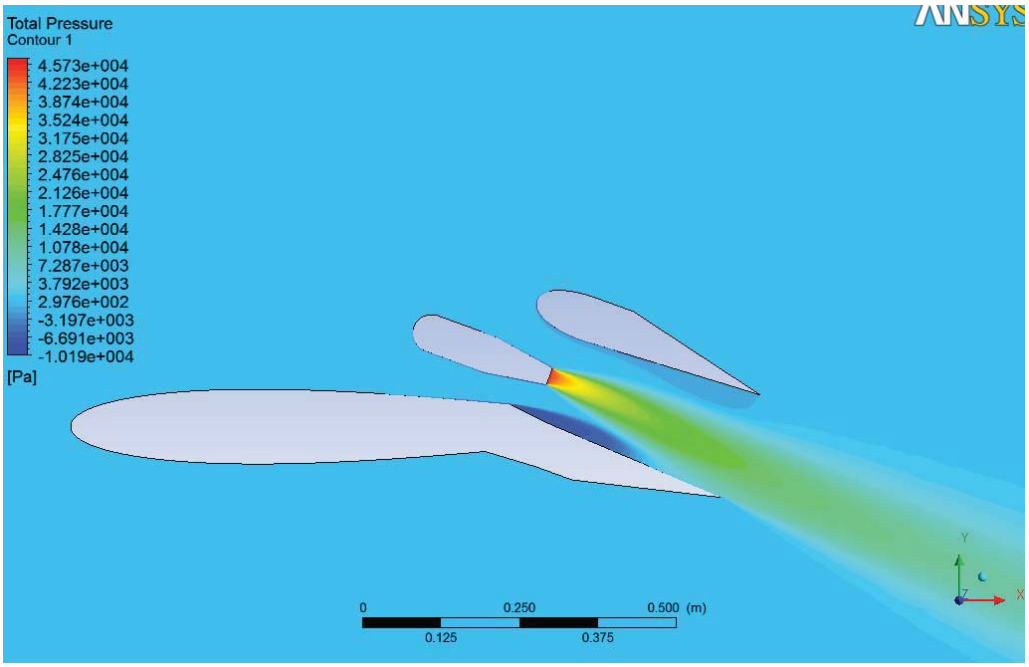

Total Pressure Contour: Angle 20 Mach =0.01

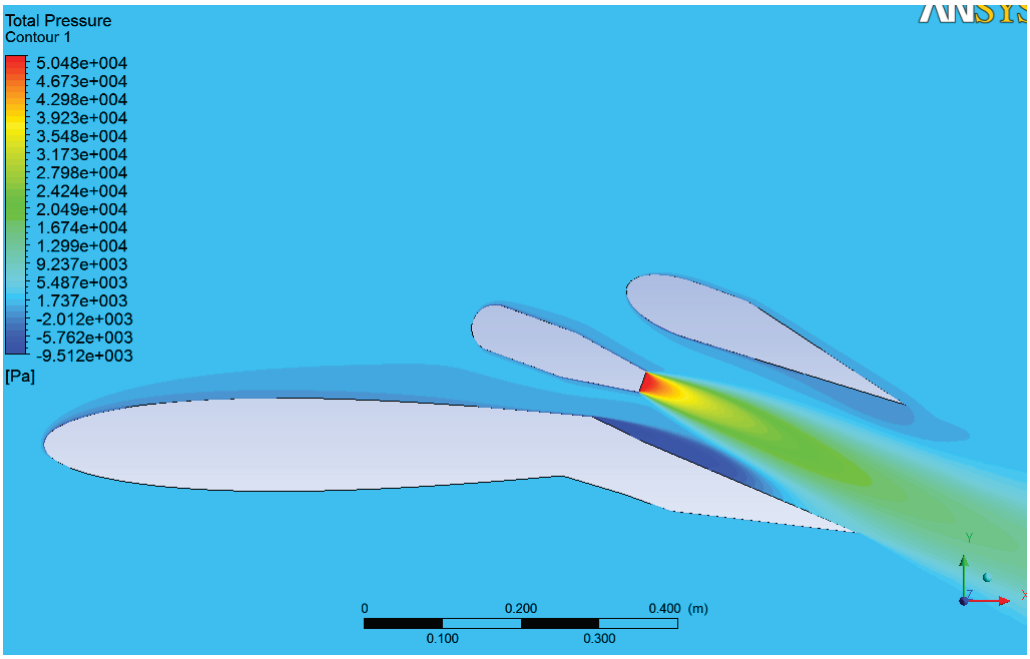

Total Pressure Contour: Angle 20 Mach =0.1

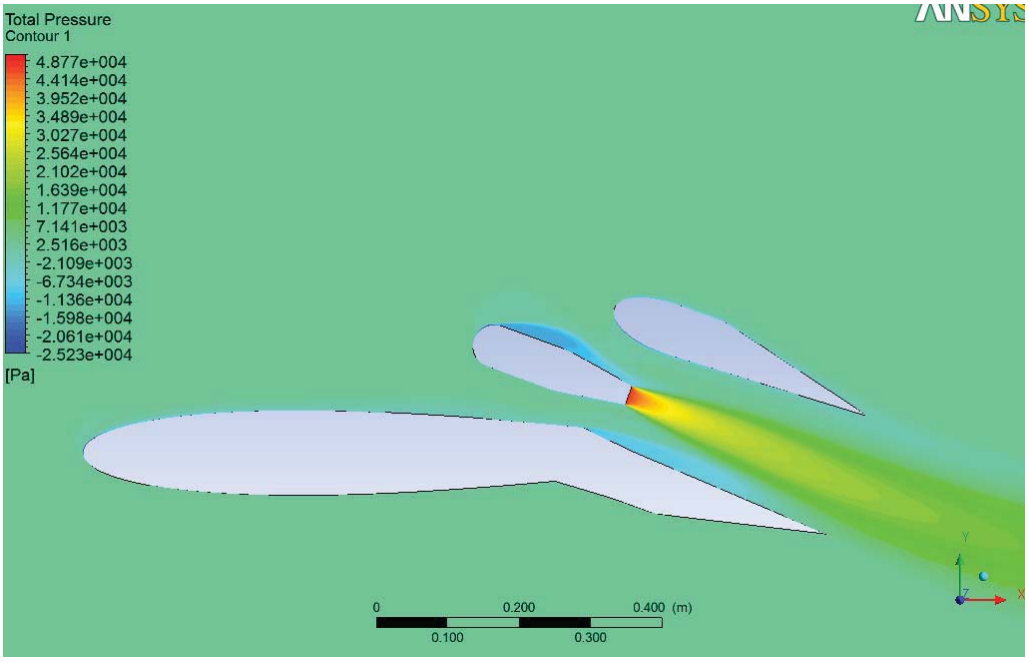

Total Pressure Contour: Angle 20 Mach =0.2

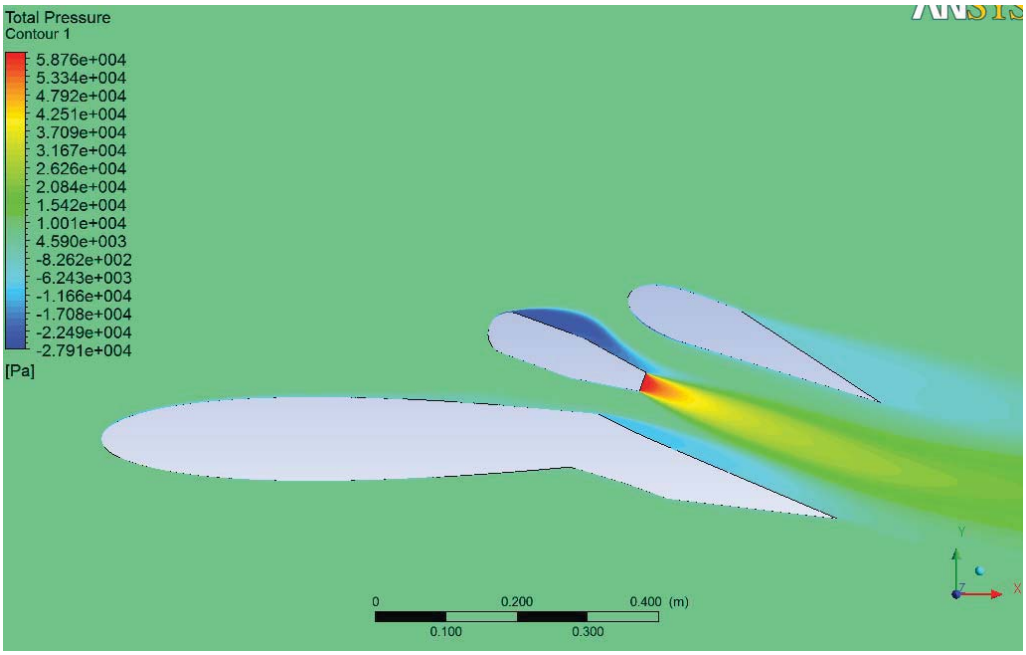

Total Pressure Contour: Angle 20 Mach =0.3

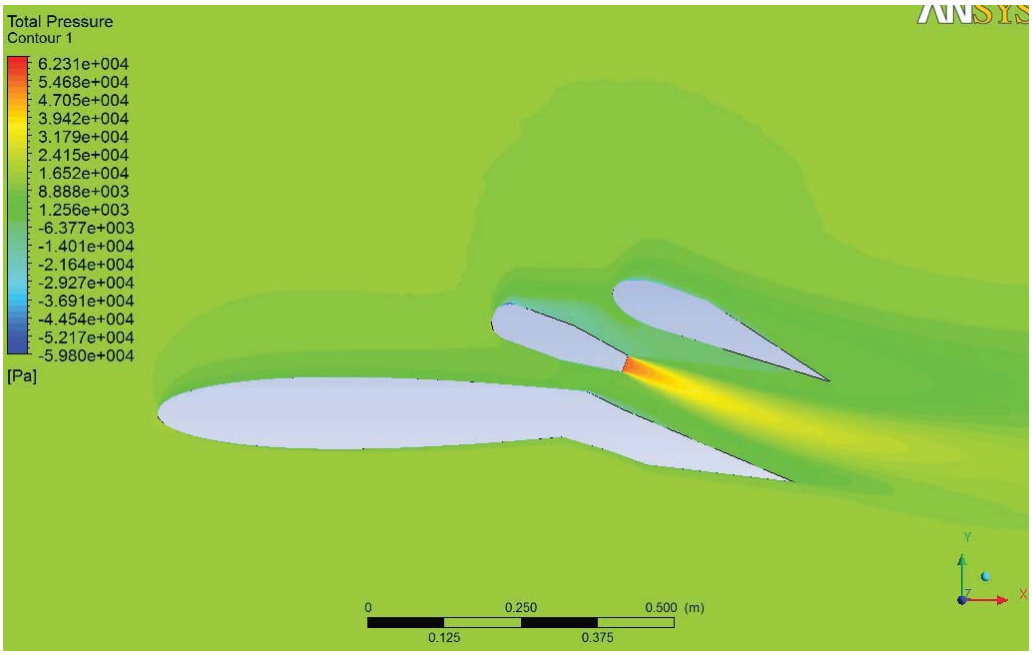

Total Pressure Contour: Angle 20 Mach =0.4

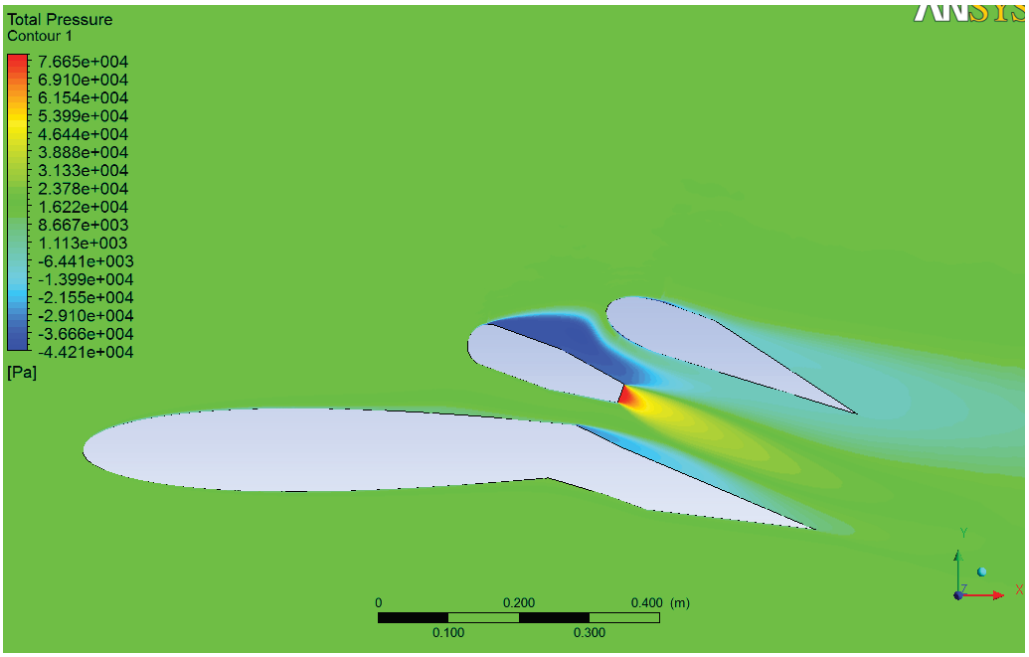

Total Pressure Contour: Angle 20 Mach =0.5

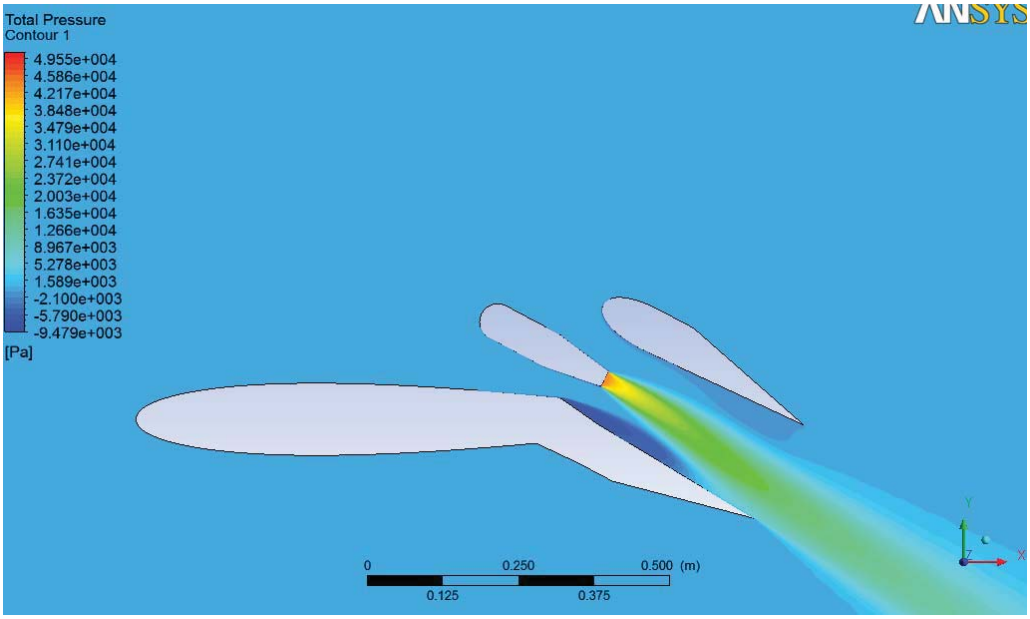

Total Pressure Contour: Angle 28 Mach =0.01

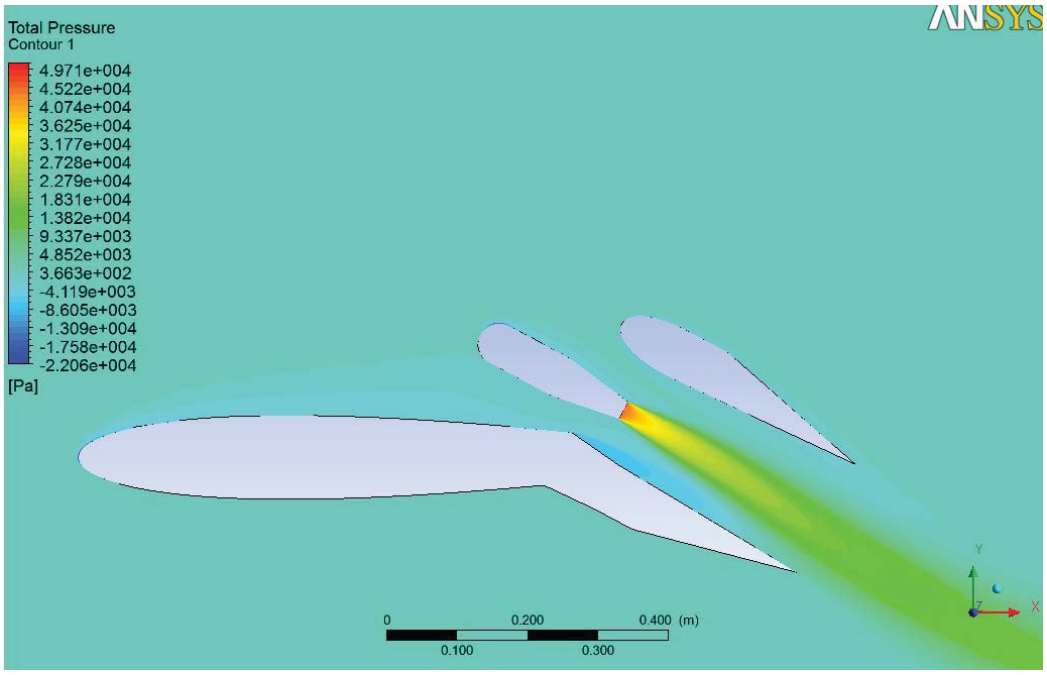

Total Pressure Contour: Angle 28 Mach =0.1

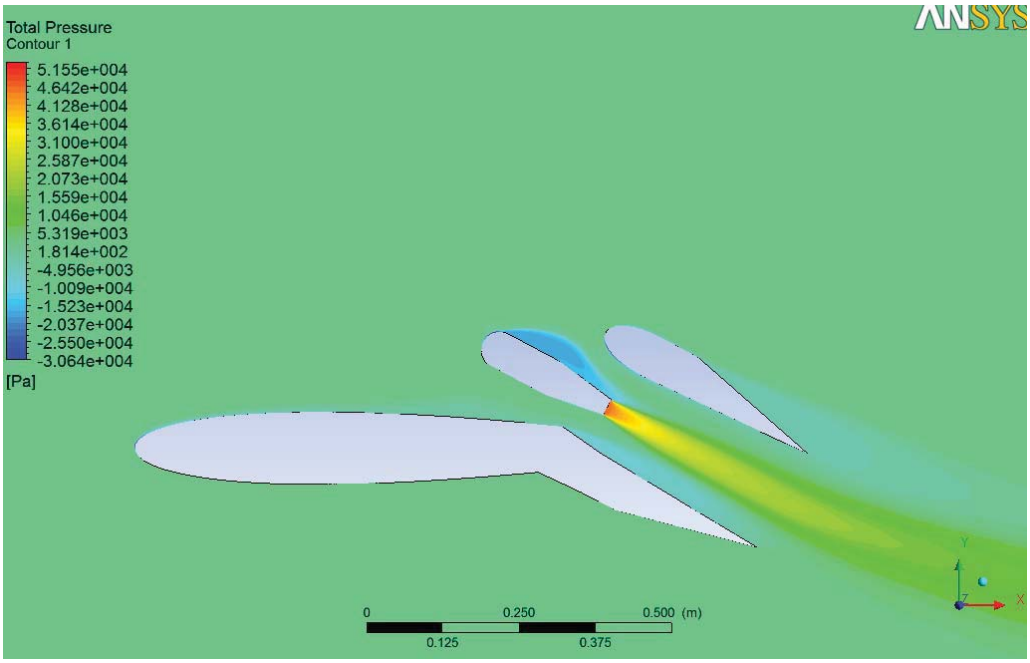

Total Pressure Contour: Angle 28 Mach =0.2

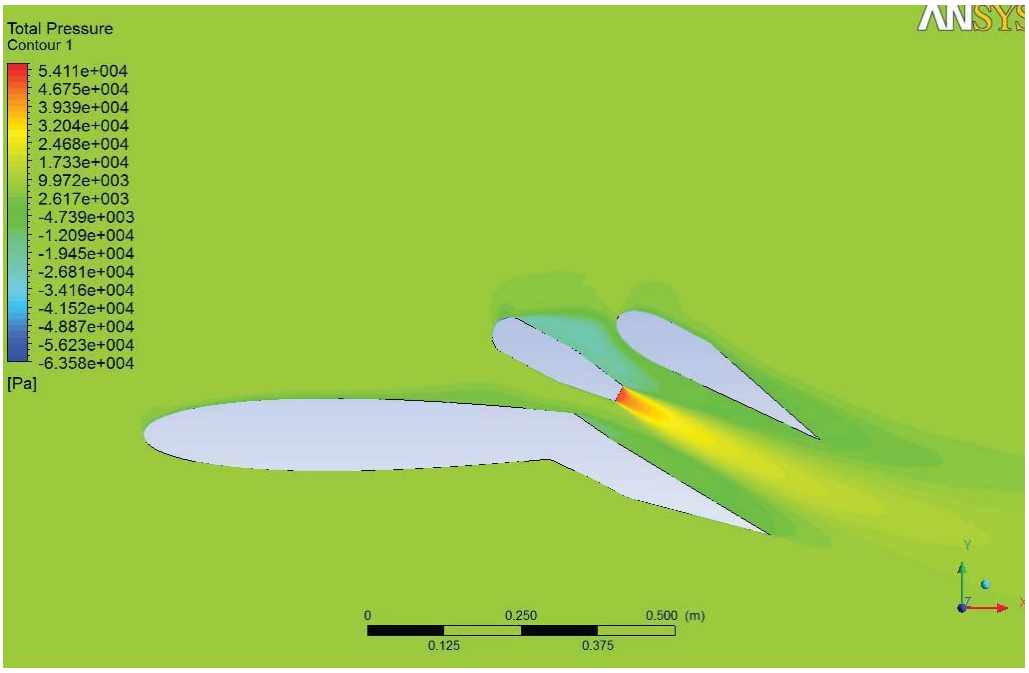

Total Pressure Contour: Angle 28 Mach =0.3

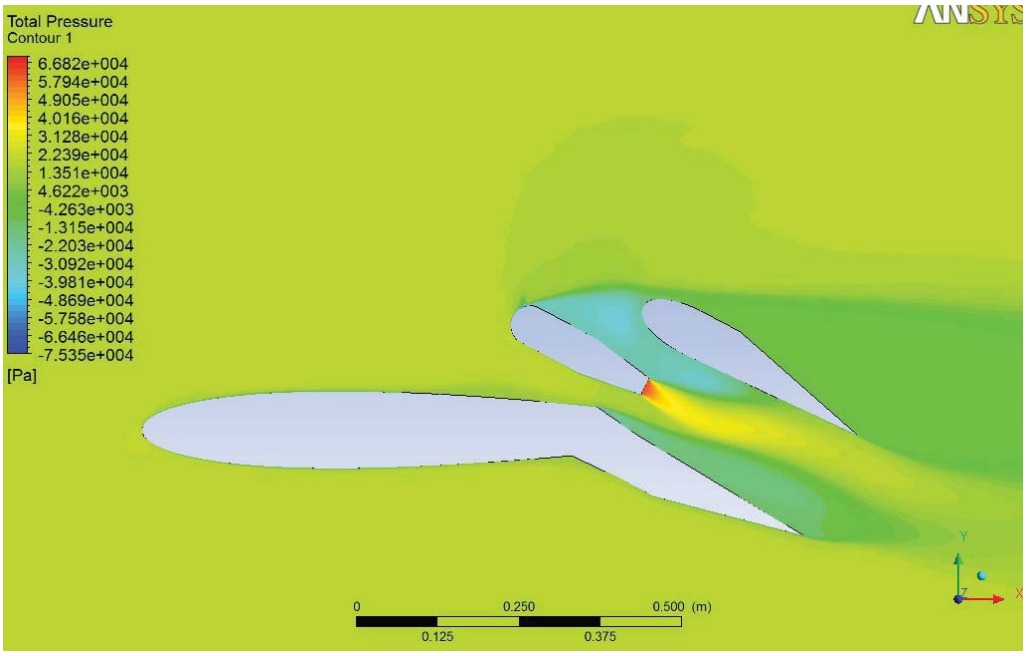

Total Pressure Contour: Angle 28 Mach =0.5

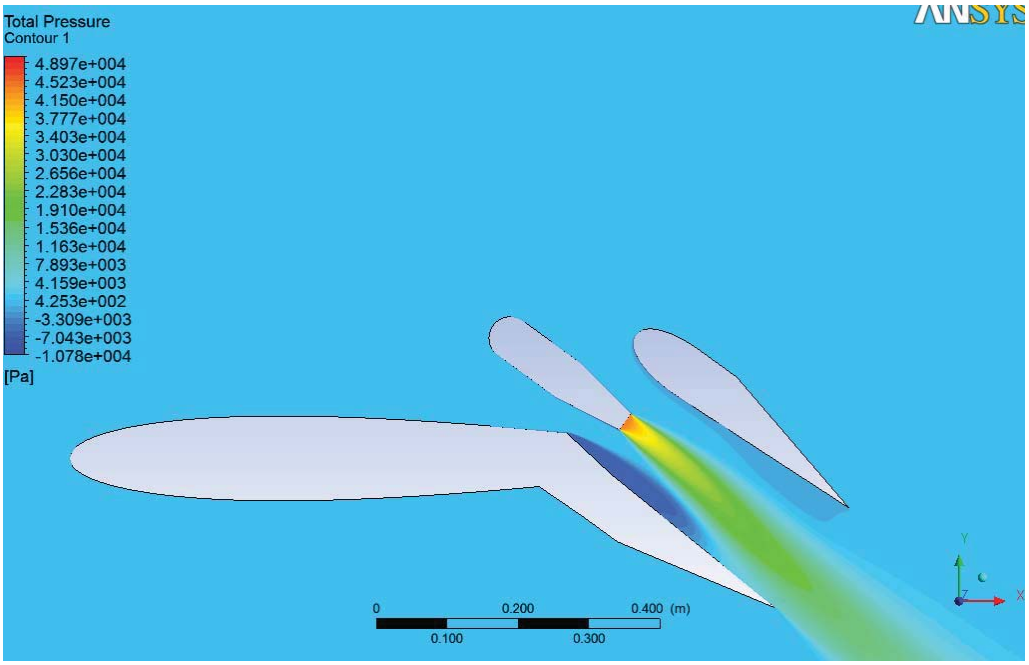

Total Pressure Contour: Angle 36 Mach =0.01

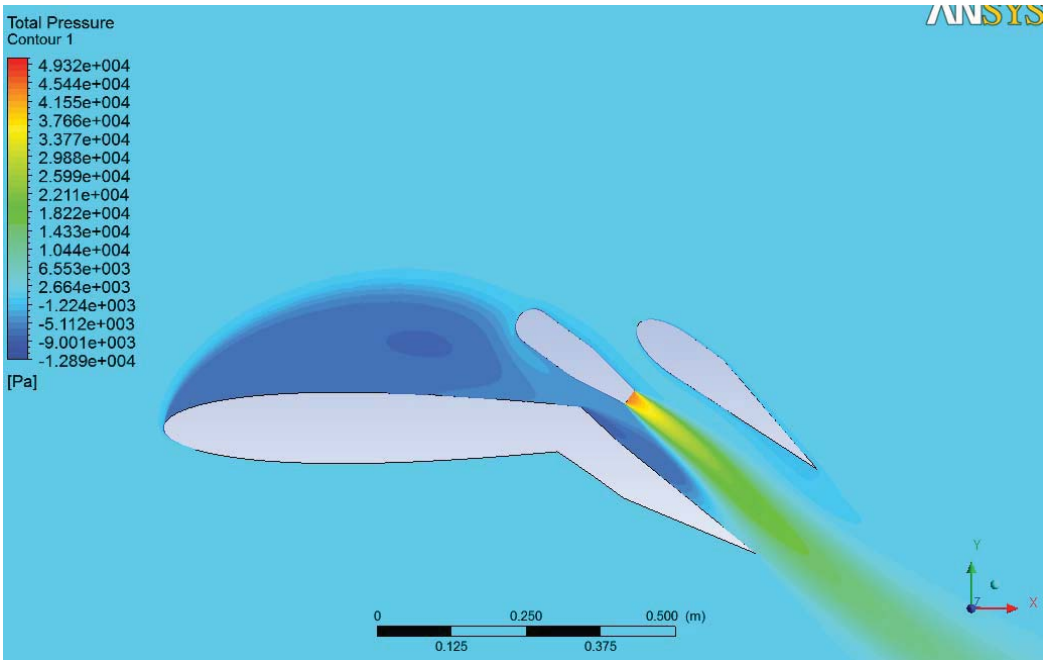

Total Pressure Contour: Angle 36 Mach =0.1

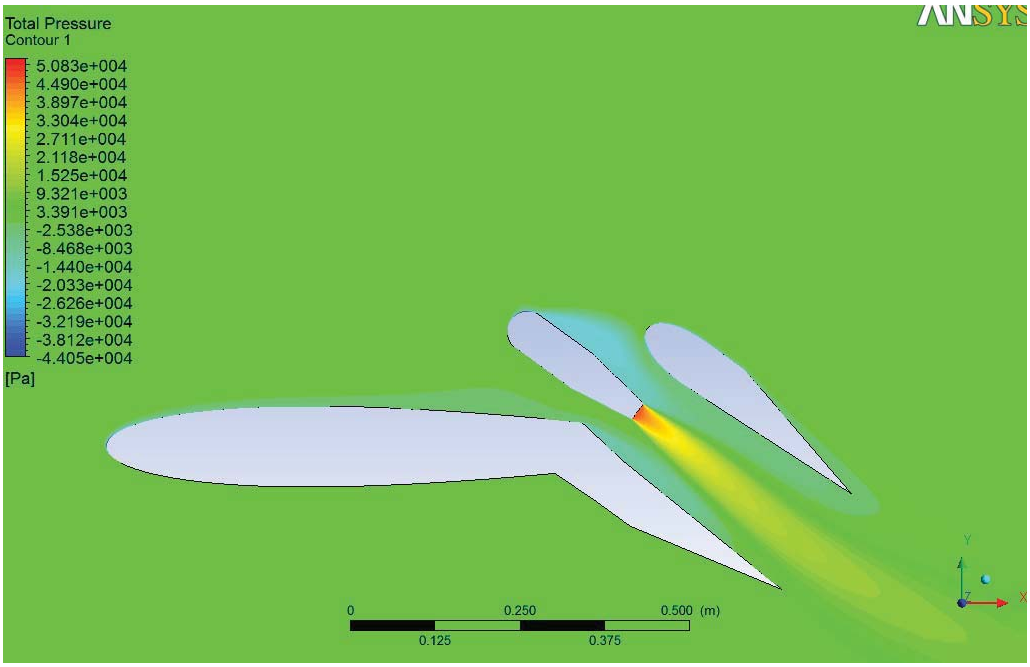

Total Pressure Contour: Angle 36Mach =0.2

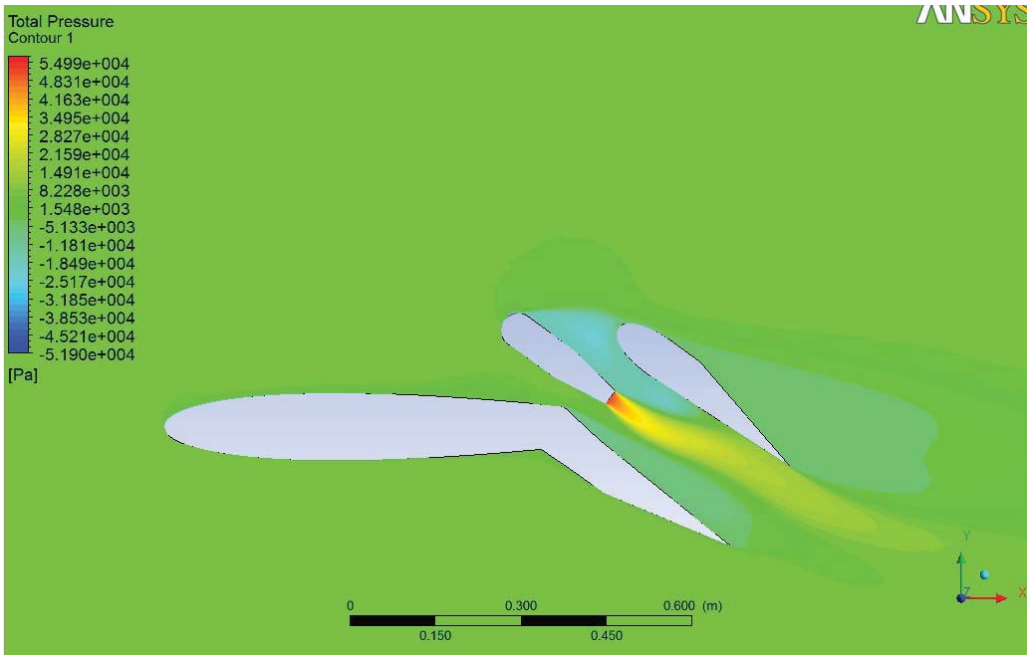

Total Pressure Contour: Angle 36 Mach =0.3

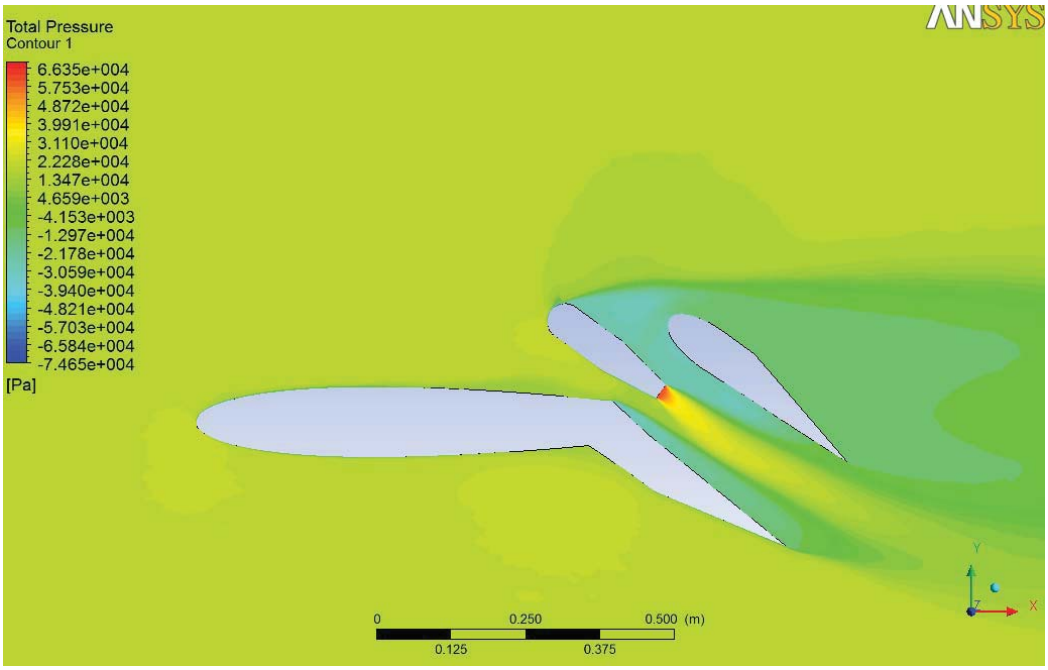

Total Pressure Contour: Angle 36 Mach =0.5

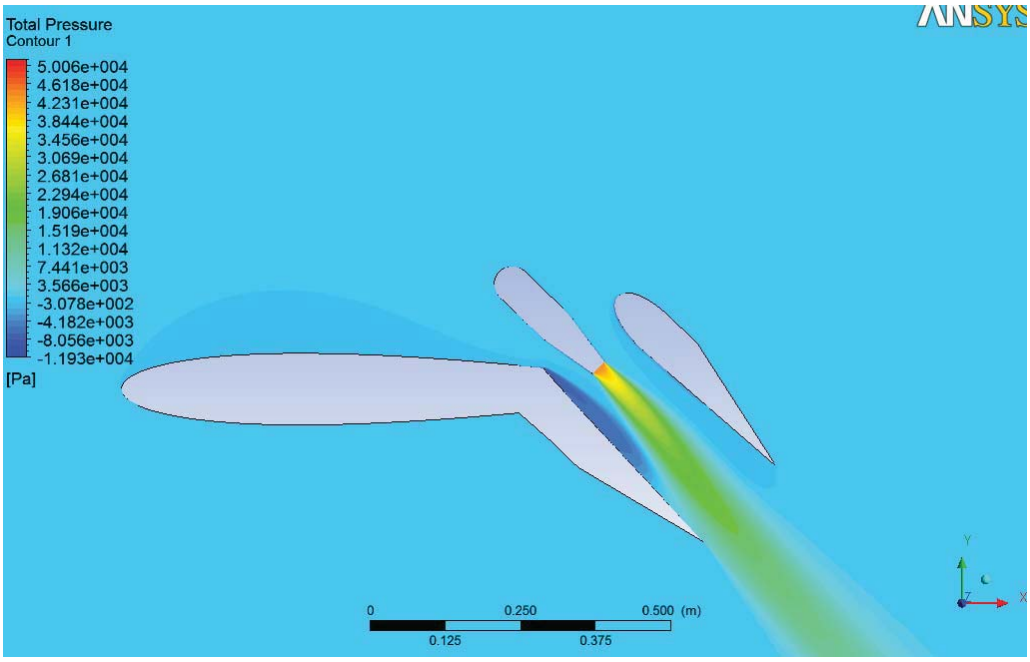

Total Pressure Contour: Angle 44 Mach =0.01

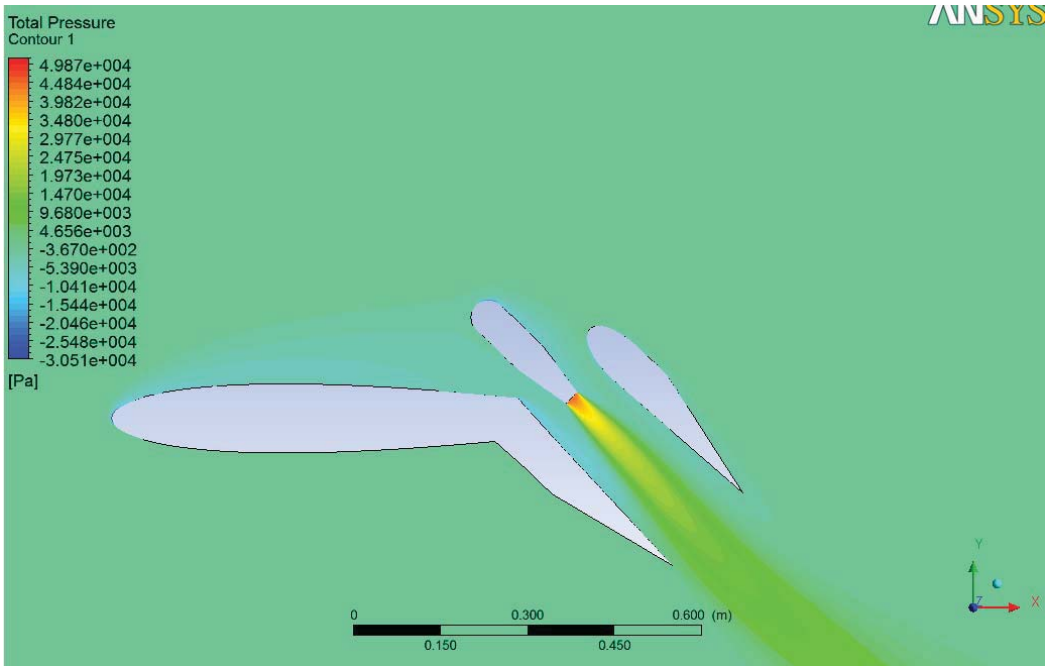

Total Pressure Contour: Angle 44 Mach =0.1

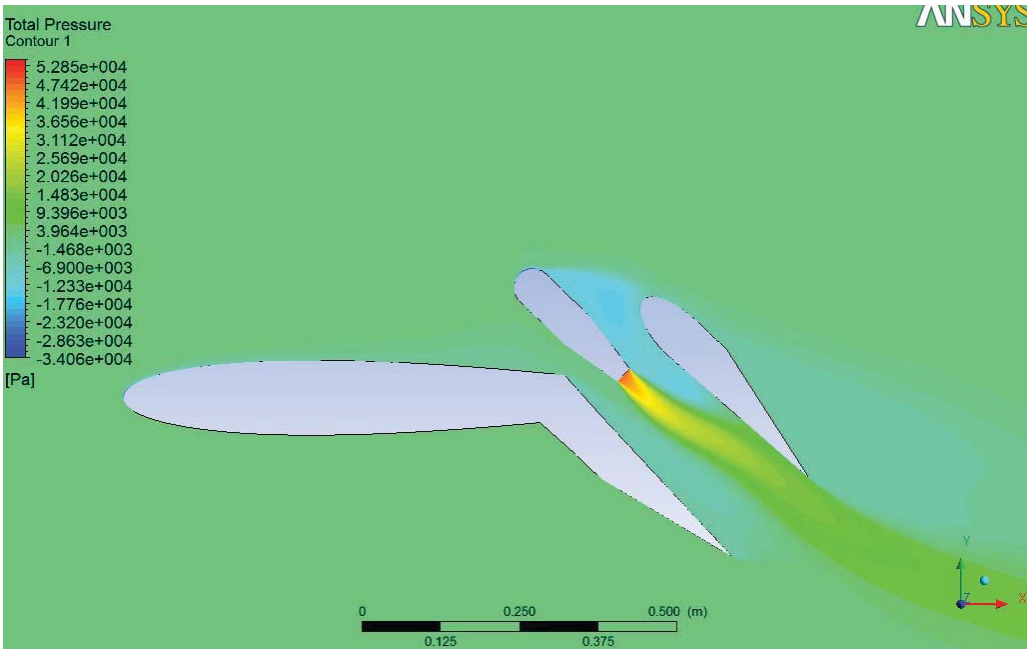

Total Pressure Contour: Angle 44 Mach =0.2

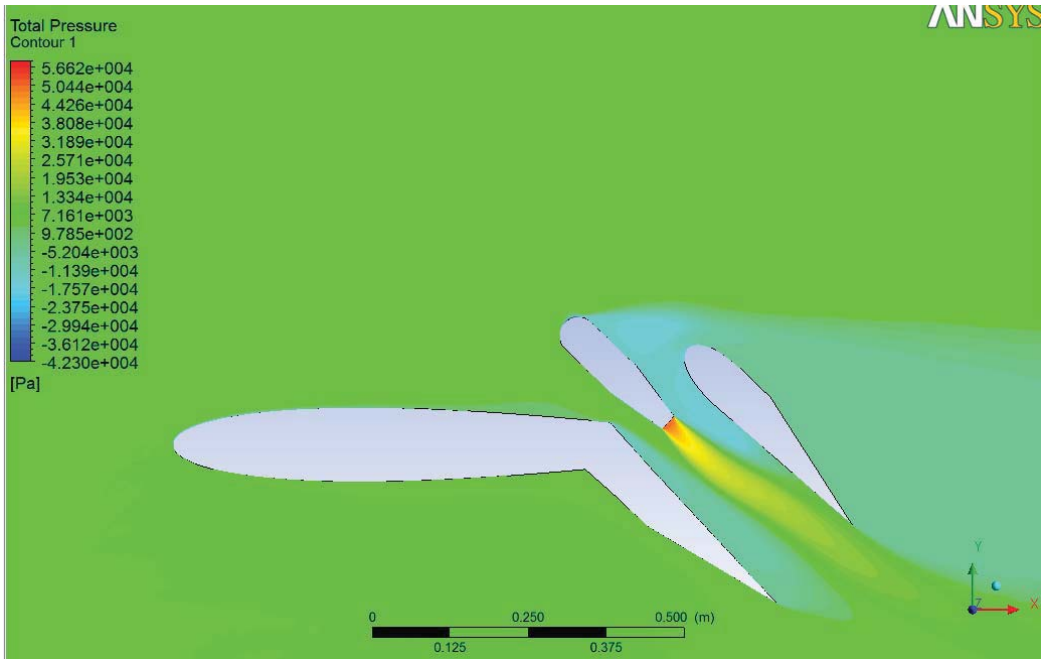

Total Pressure Contour: Angle 44 Mach =0.3

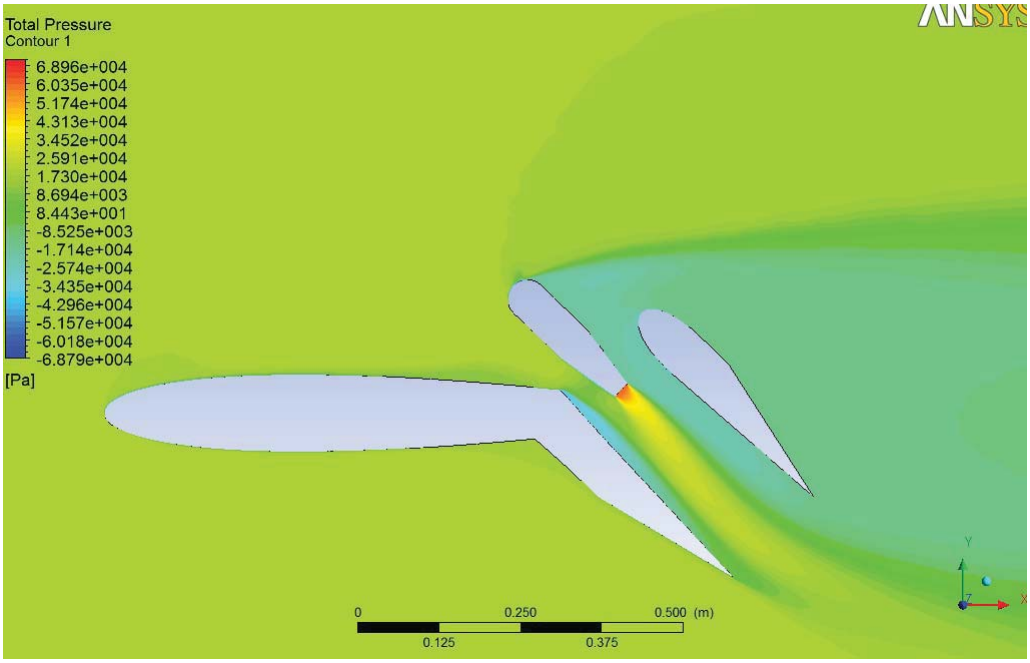

Total Pressure Contour: Angle 44 Mach =0.5

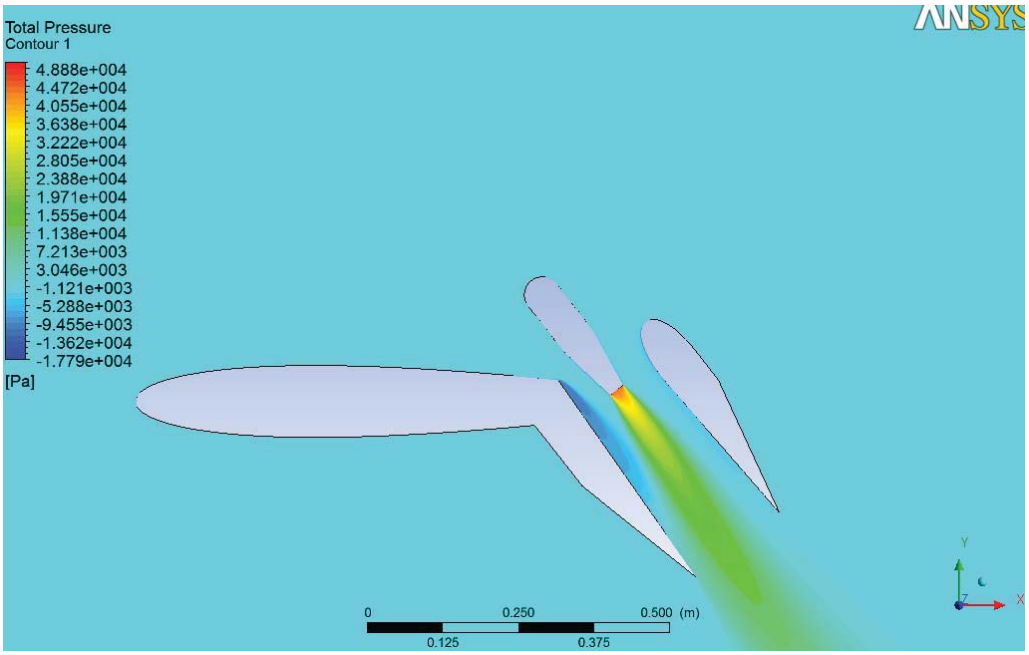

Total Pressure Contour: Angle 52 Mach =0.01

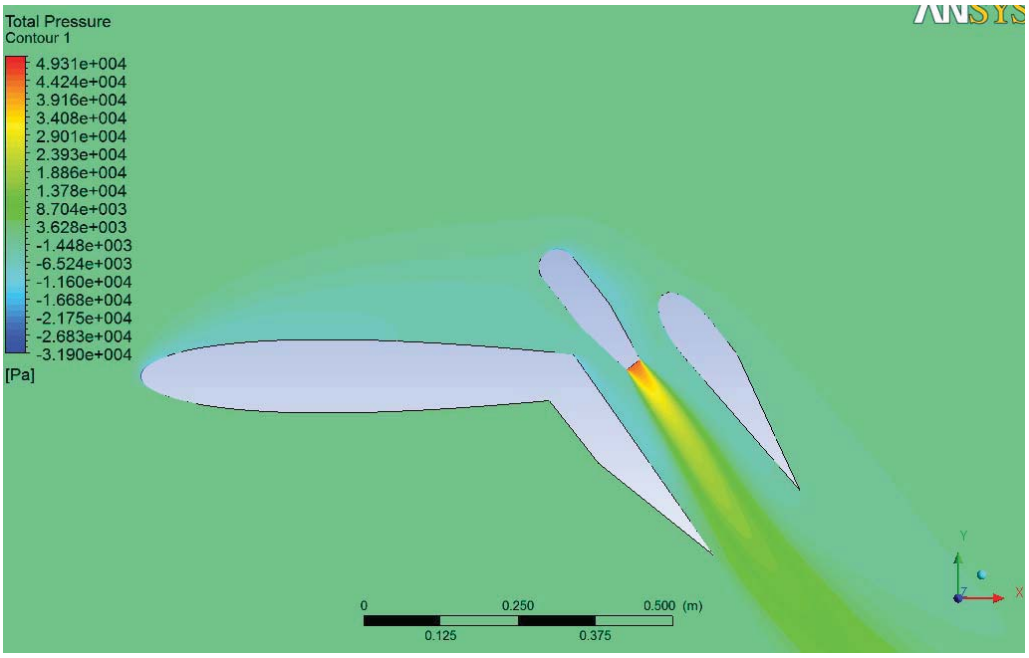

Total Pressure Contour: Angle 52 Mach =0.1

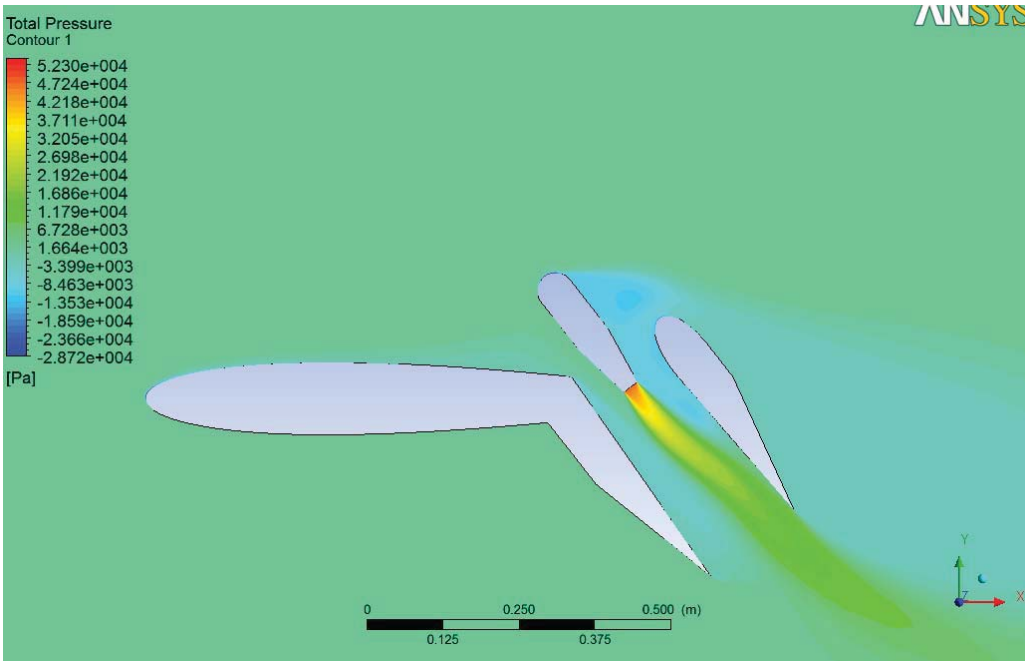

Total Pressure Contour: Angle 52 Mach =0.2

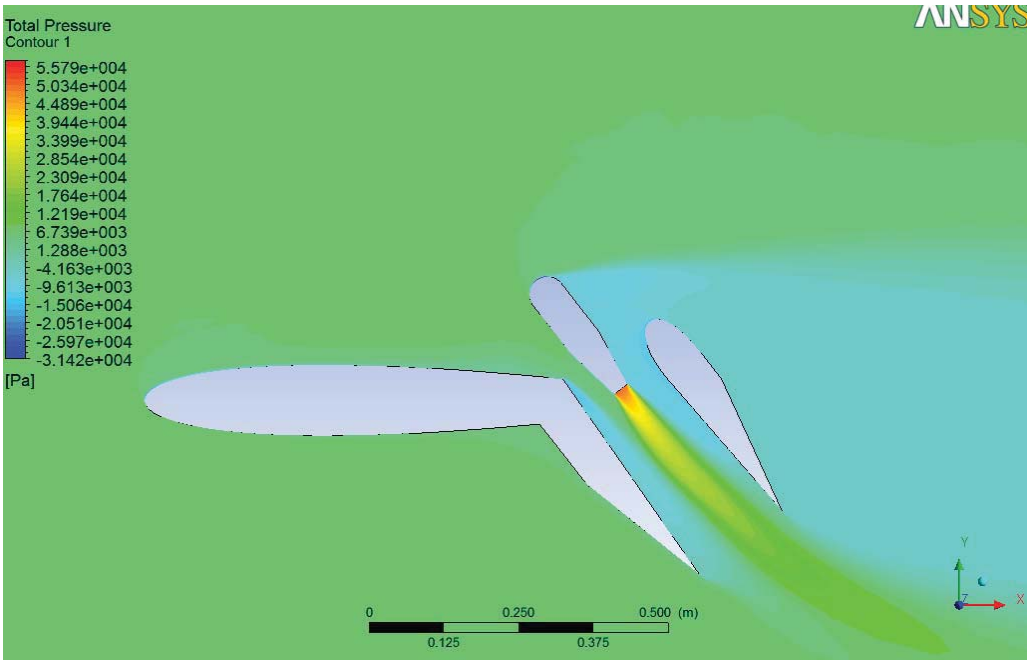

Total Pressure Contour: Angle 52 Mach =0.3

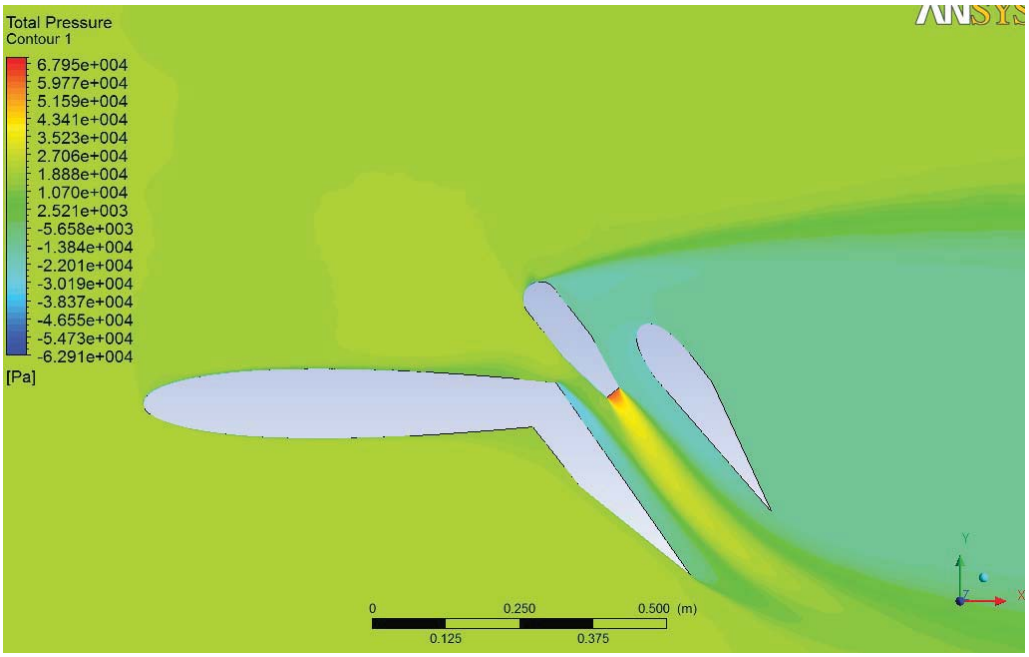

Total Pressure Contour: Angle 52 Mach =0.5

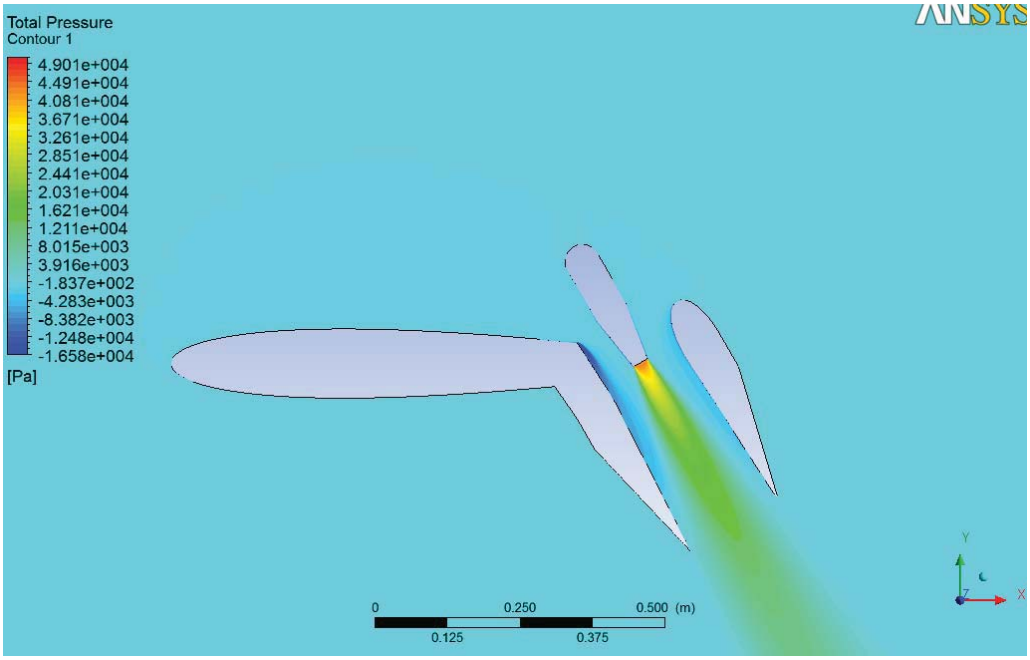

Total Pressure Contour: Angle 60 Mach =0.01

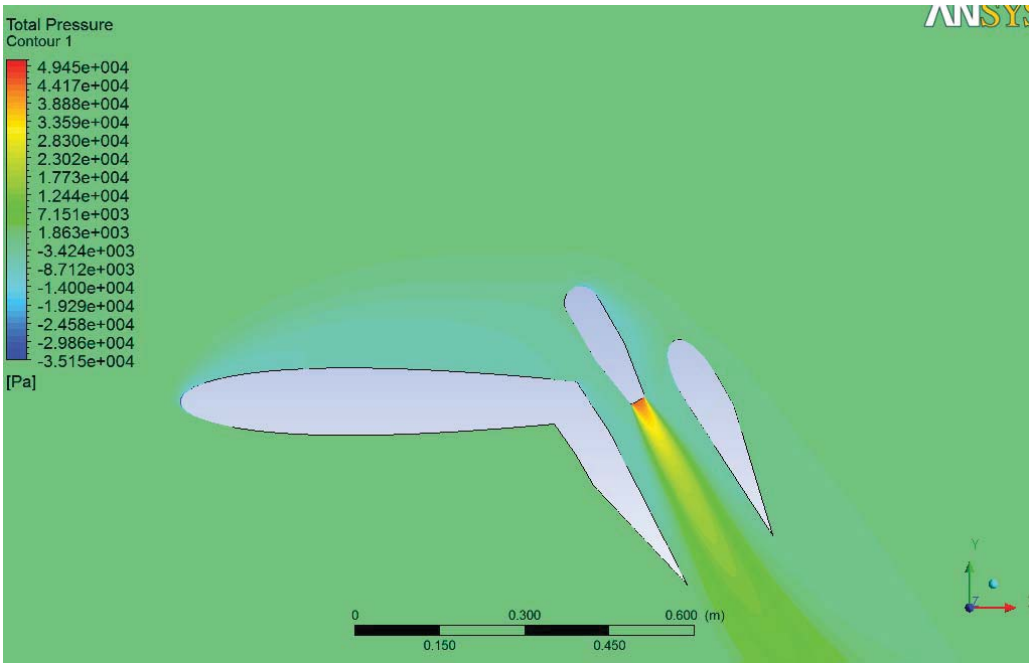

Total Pressure Contour: Angle 60 Mach =0.1

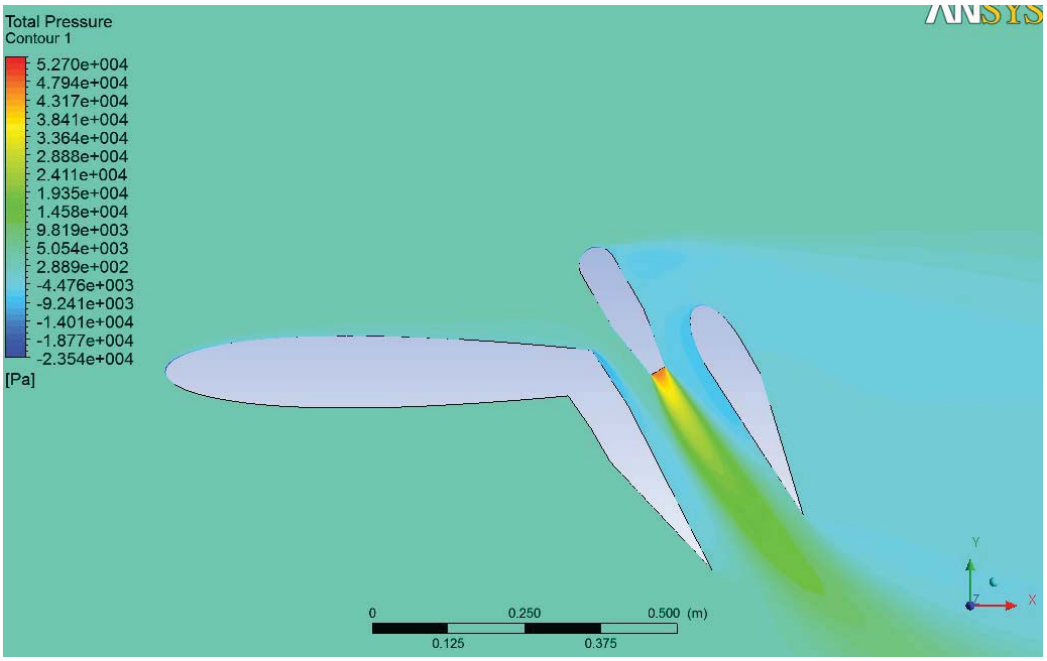

Total Pressure Contour: Angle 60 Mach =0.2

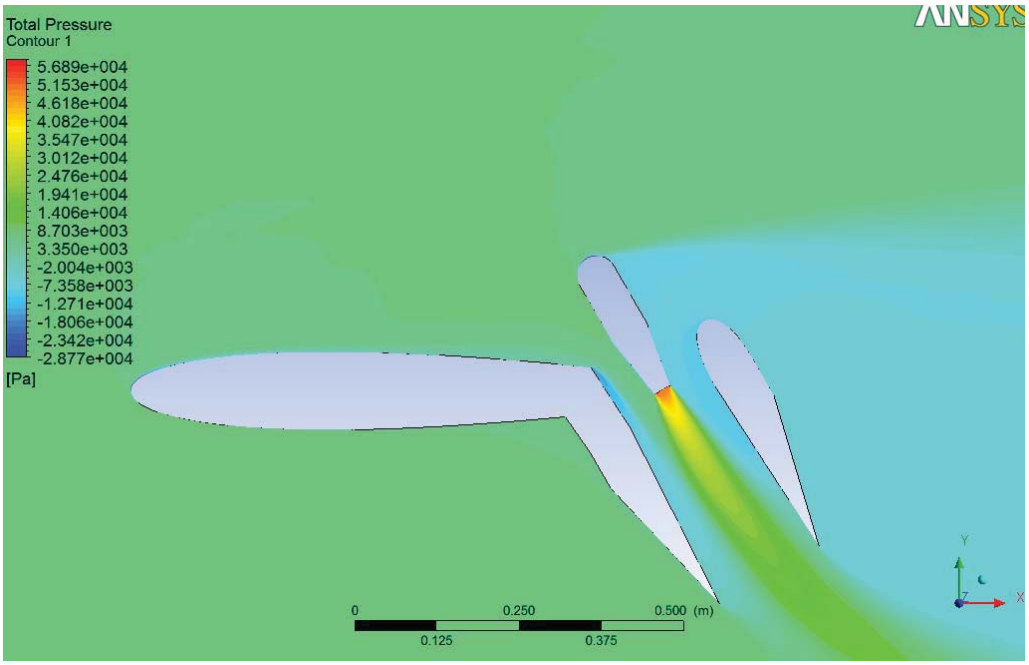

Total Pressure Contour: Angle 60 Mach =0.3

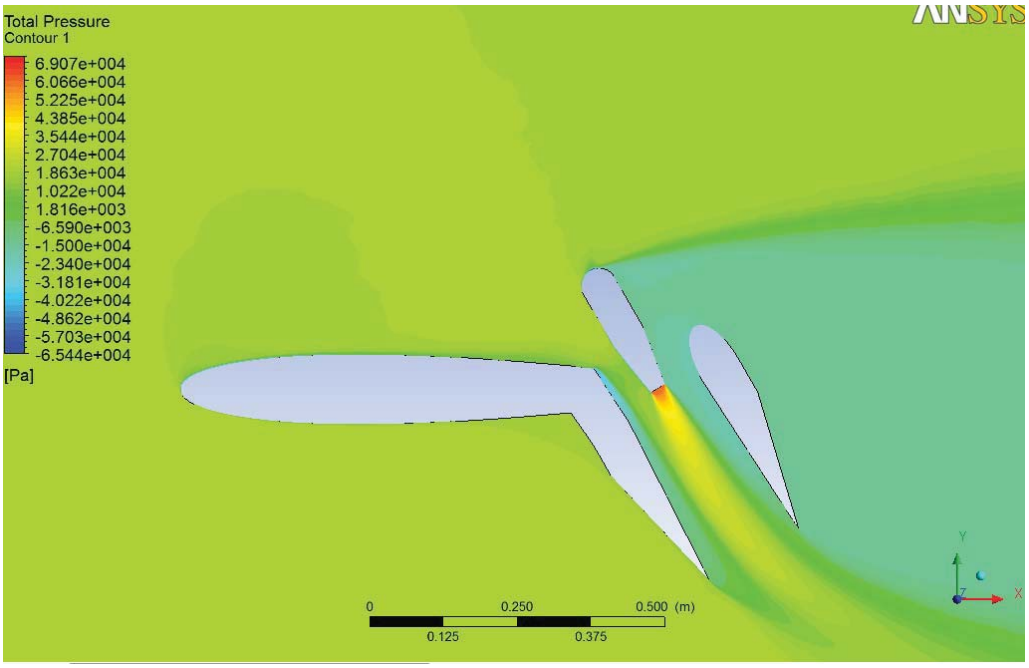

Total Pressure Contour: Angle 60 Mach =0.5

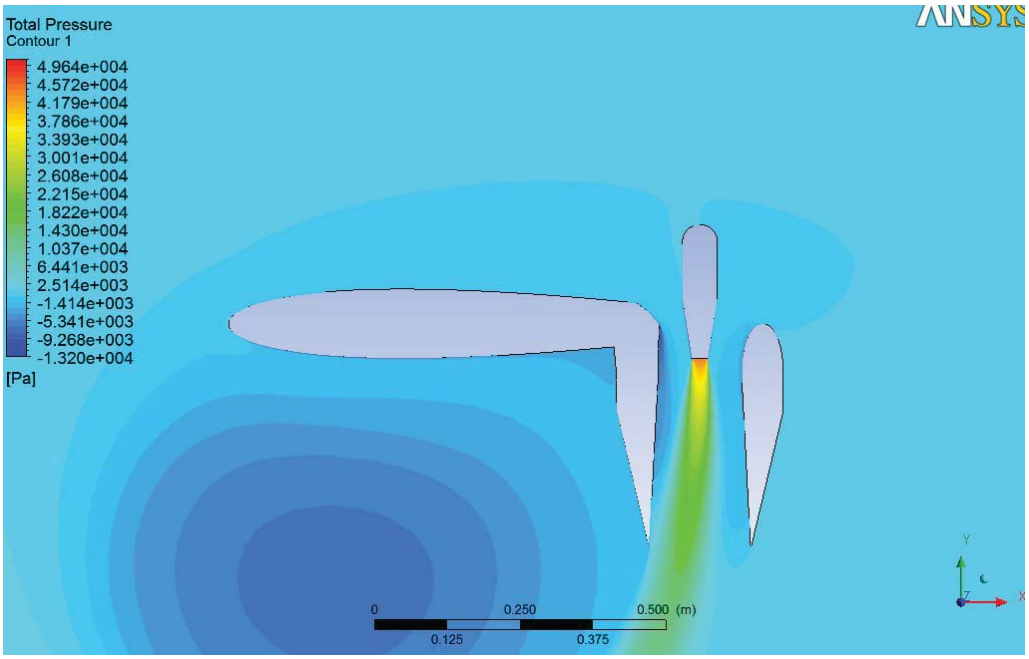

Total Pressure Contour: Angle 90 Mach =0.01

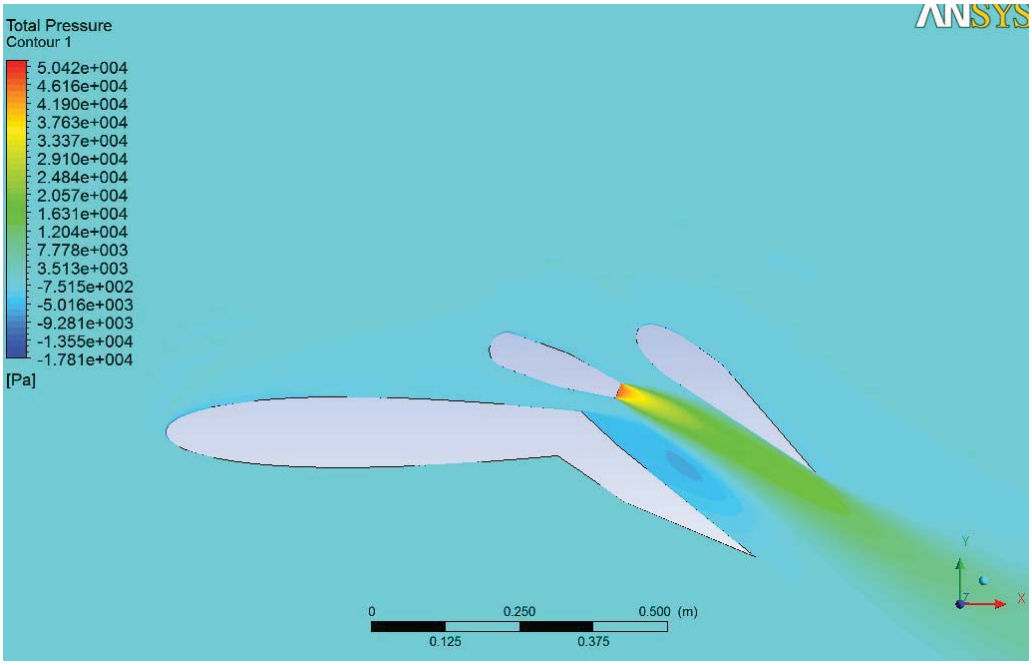

Total Pressure Contour: Angle 36 Mach =0.1 Deflected Nozzle Configuration

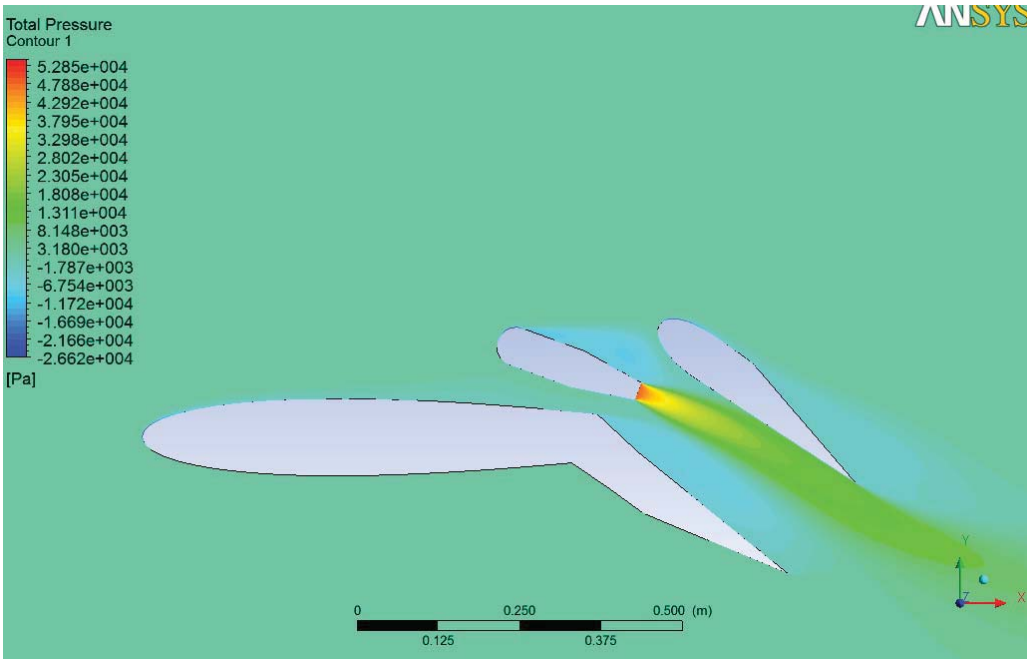

Total Pressure Contour: Angle 36 Mach =0.2 Deflected Nozzle Configuration

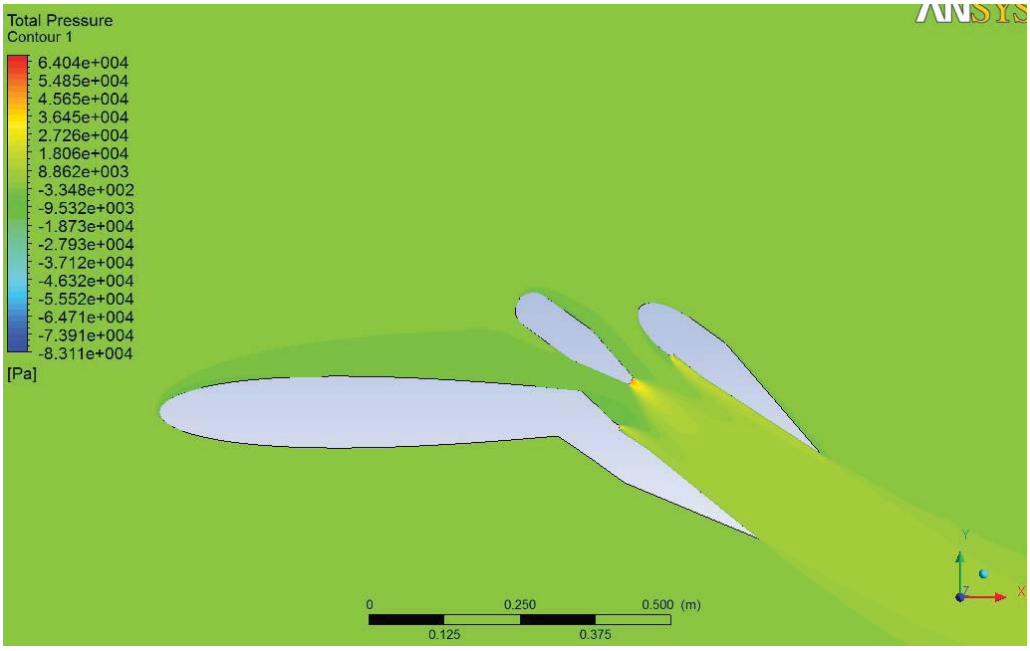

Total Pressure Contour: Angle 36 Mach =0.1 Wall Jets Configuration

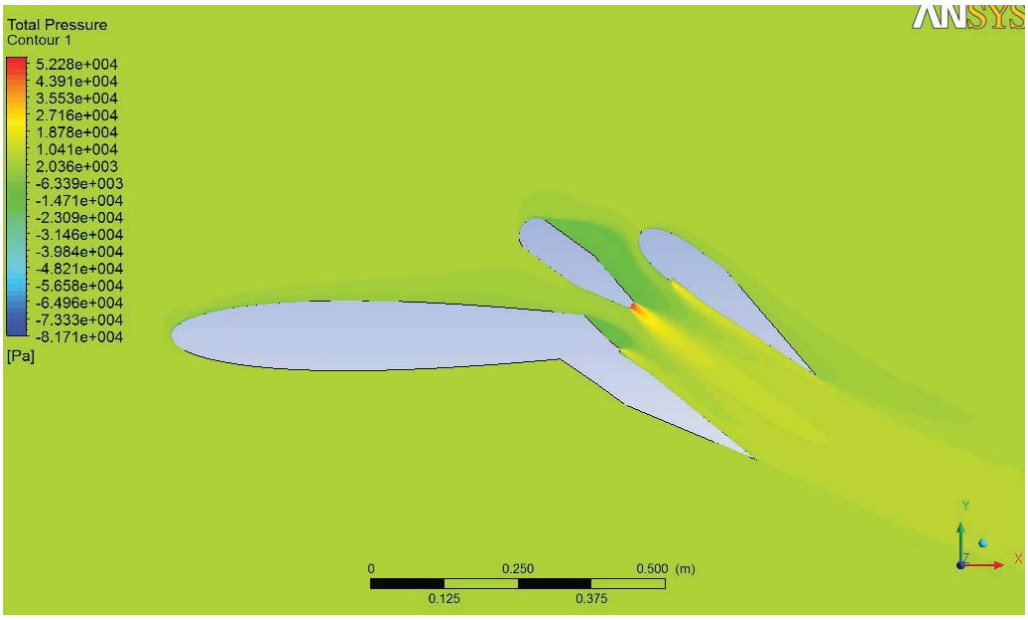

Total Pressure Contour: Angle 36 Mach =0.2 Wall Jets Configuration

Appendix D: Velocity Contours

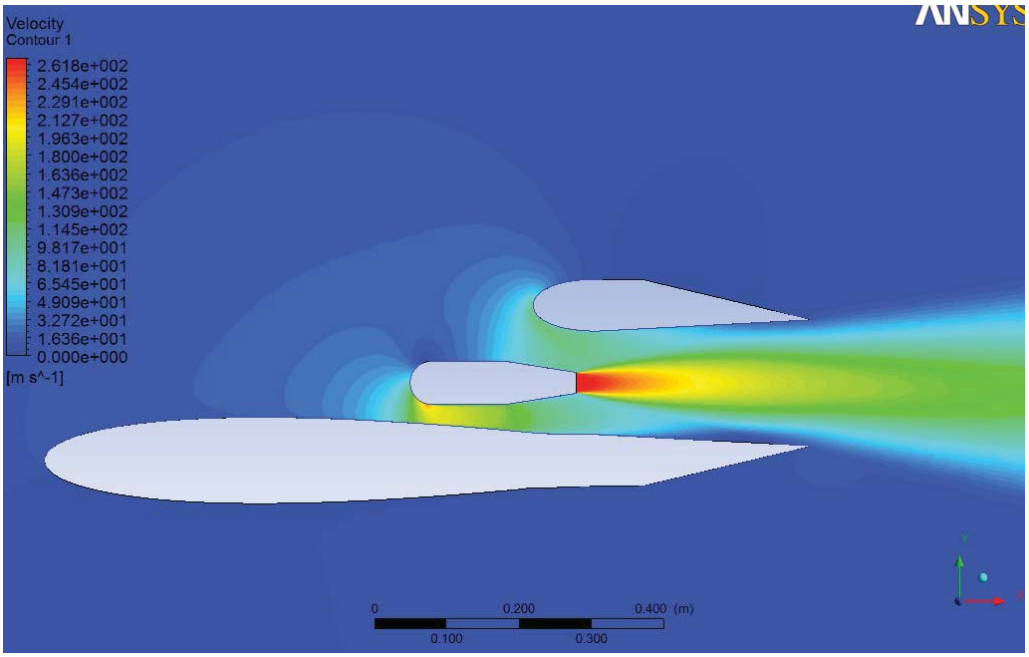

Velocity Contour: Angle 0 Mach=0.01

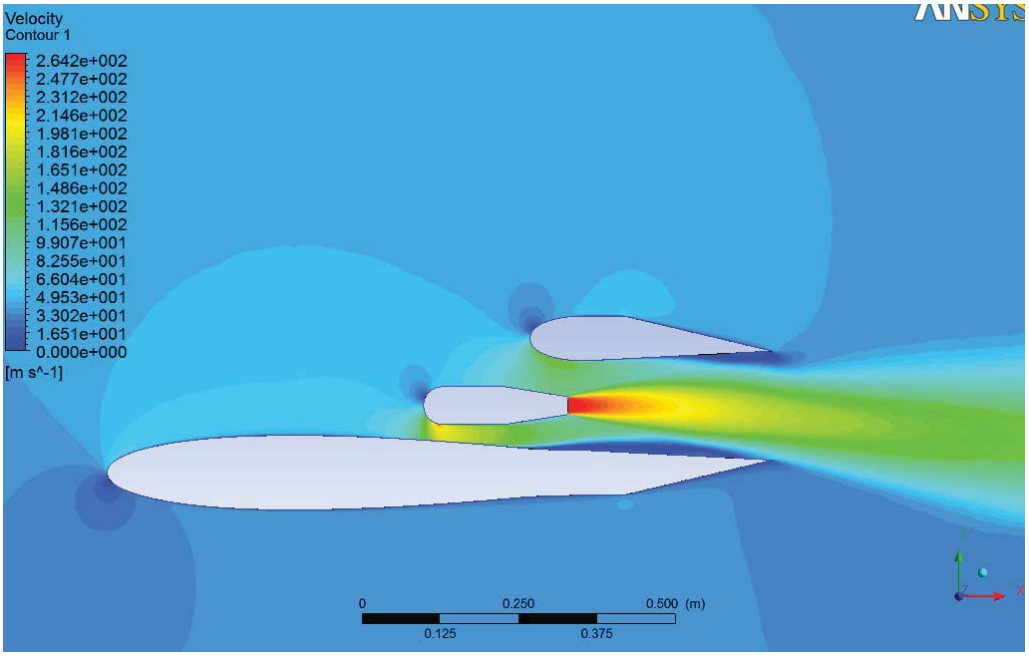

Velocity Contour: Angle 0 Mach=0.1

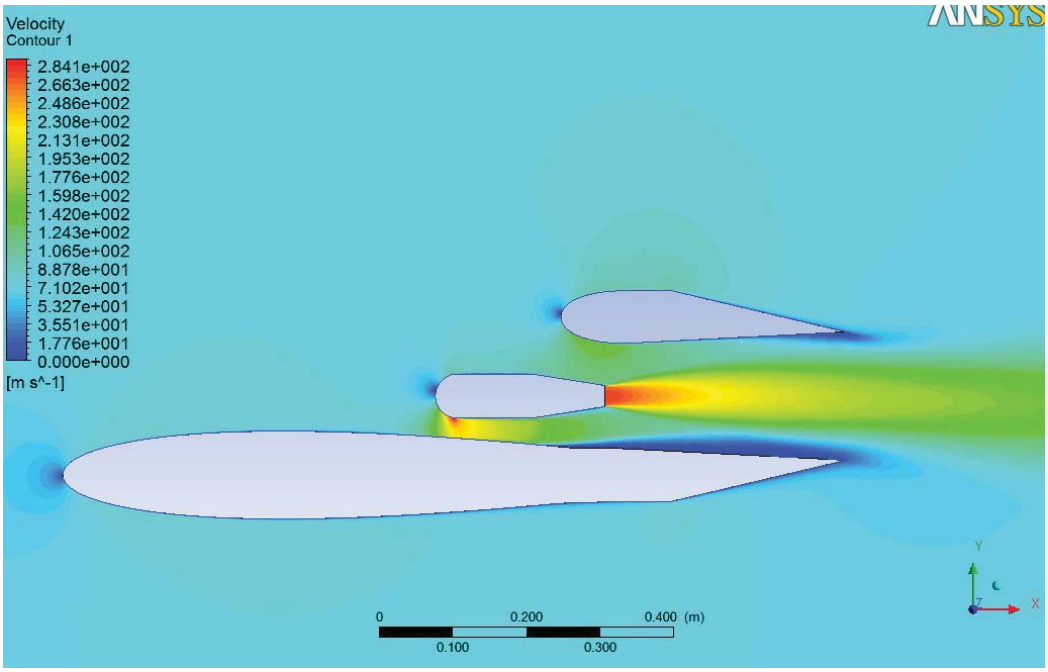

Velocity Contour: Angle 0 Mach=0.2

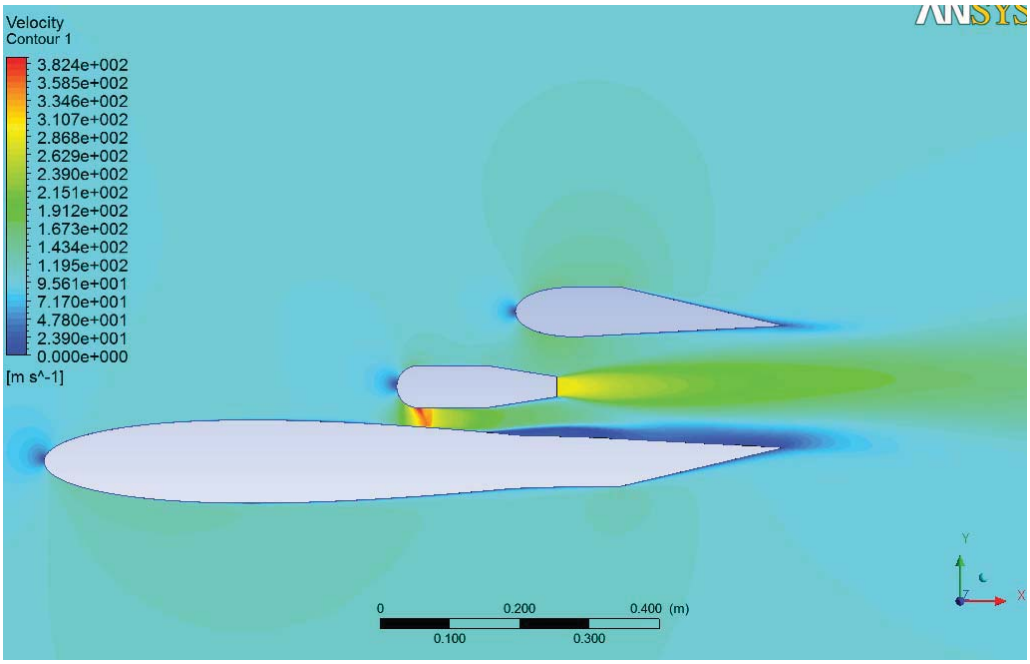

Velocity Contour: Angle 0 Mach=0.3

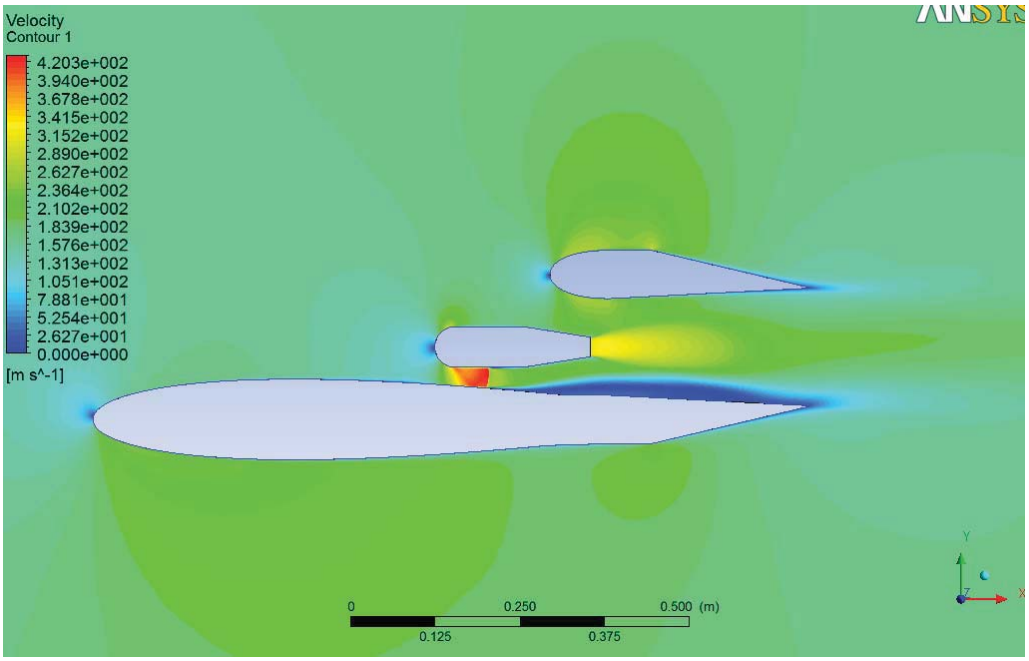

Velocity Contour: Angle 0 Mach=0.5

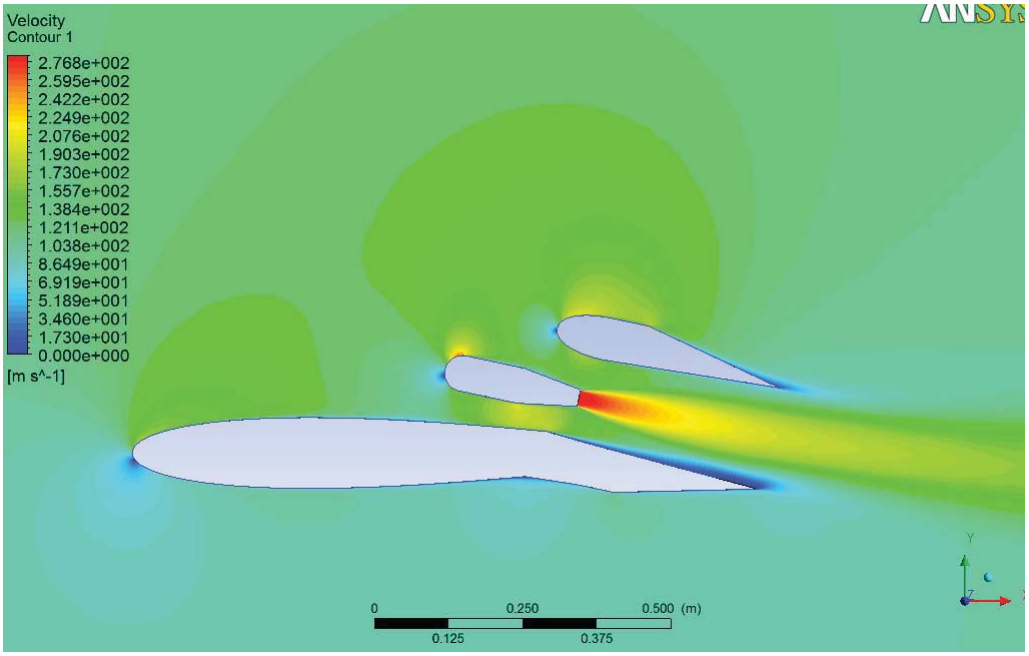

Velocity Contour: Angle 12 Mach=0.3

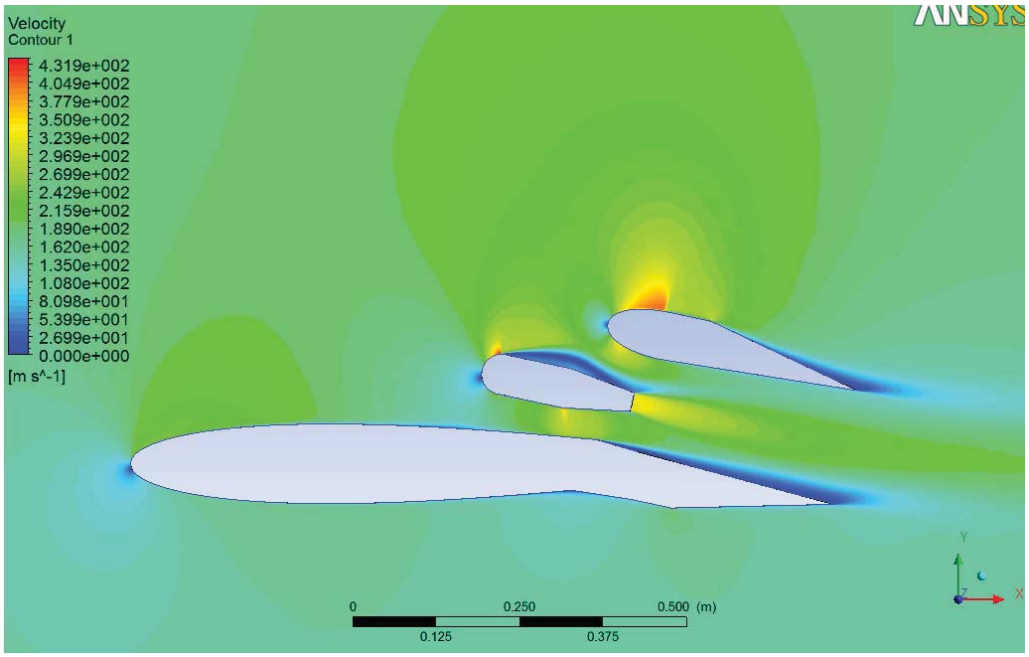

Velocity Contour: Angle 12 Mach=0.5

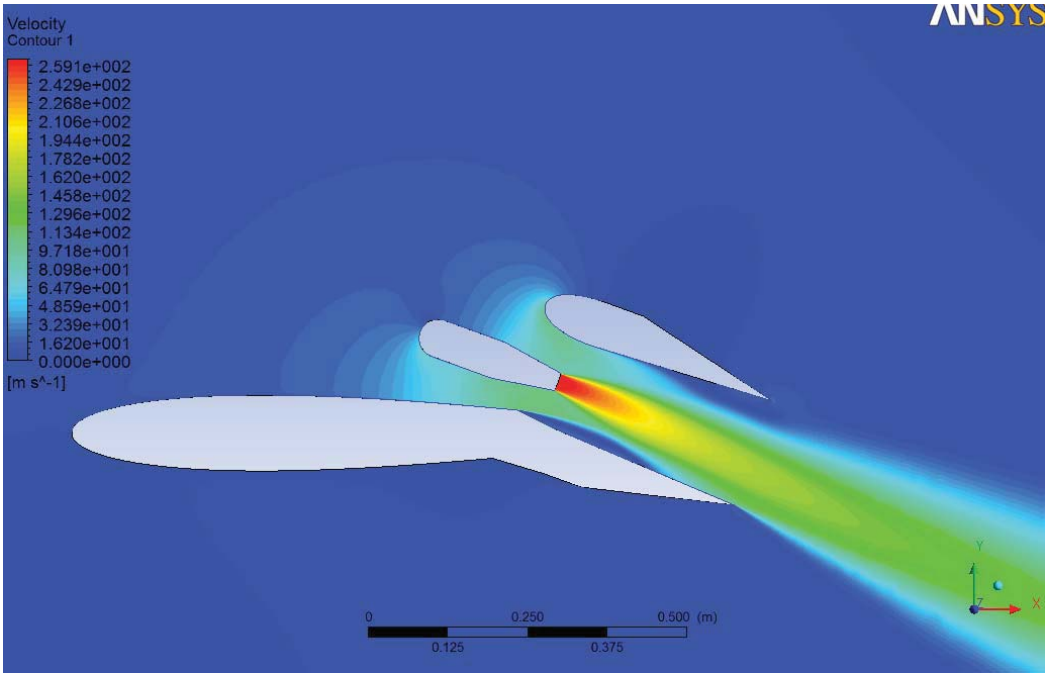

Velocity Contour: Angle 20 Mach=0.01

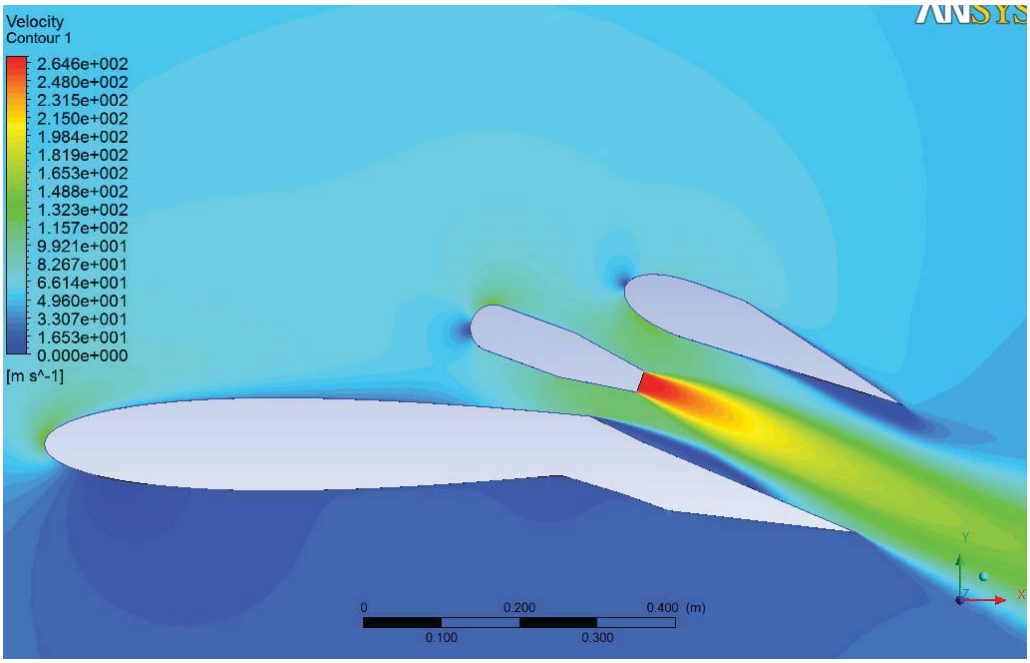

Velocity Contour: Angle 20 Mach=0.1

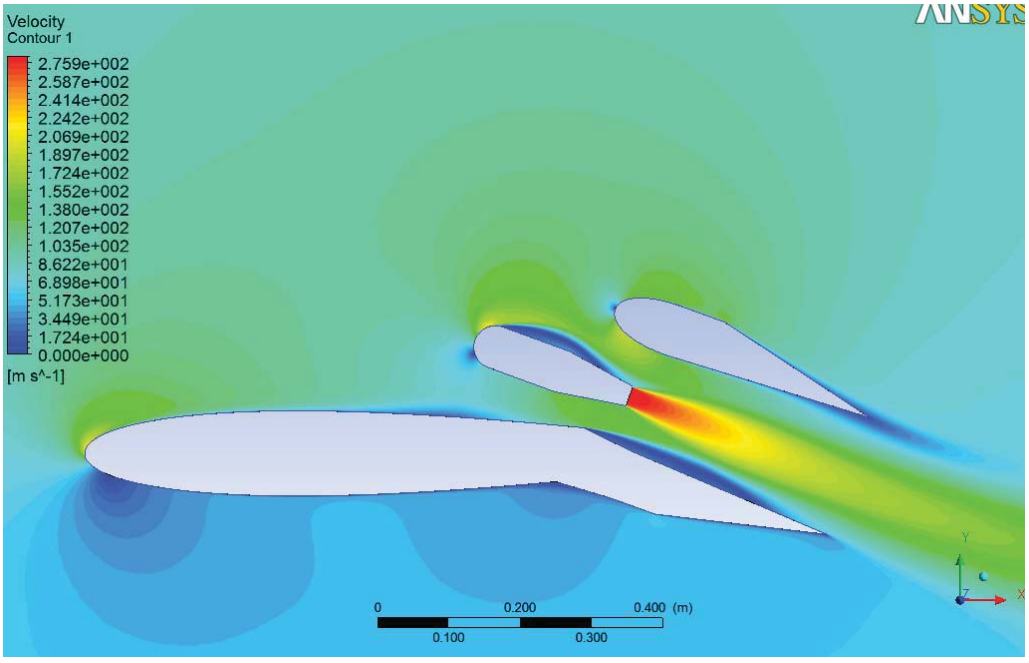

Velocity Contour: Angle 20 Mach=0.2

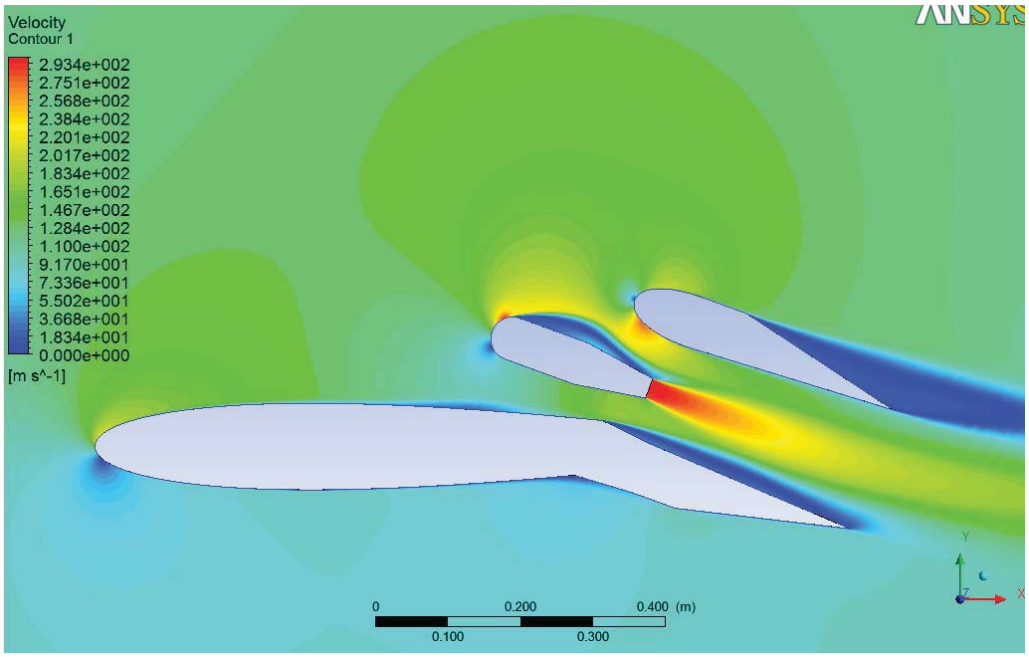

Velocity Contour: Angle 20 Mach=0.3

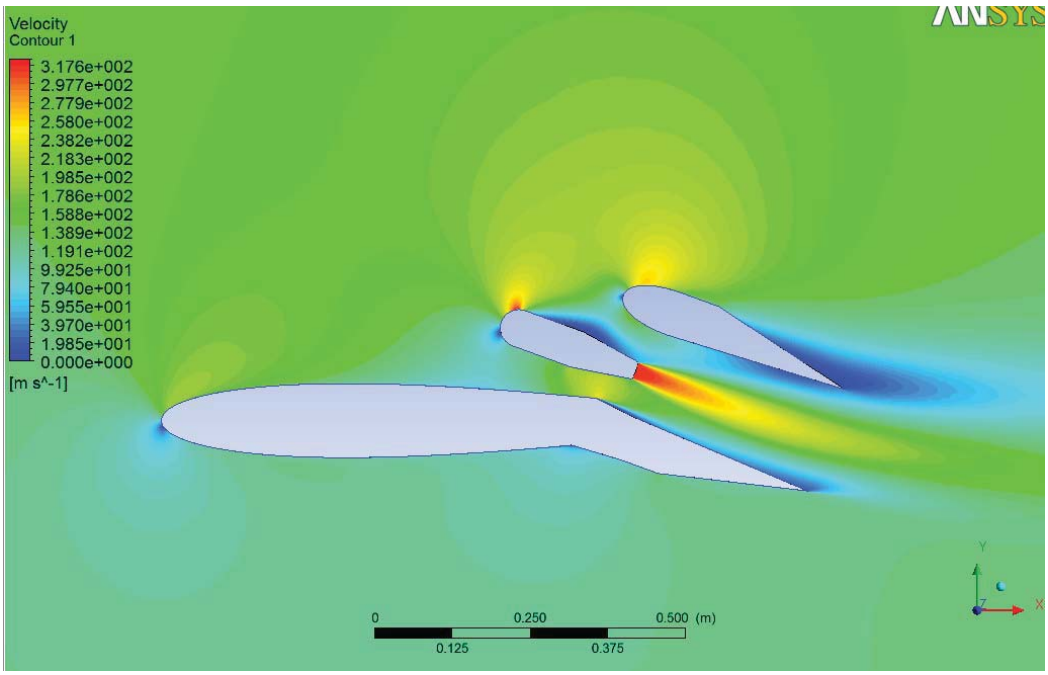

Velocity Contour: Angle 20 Mach=0.4

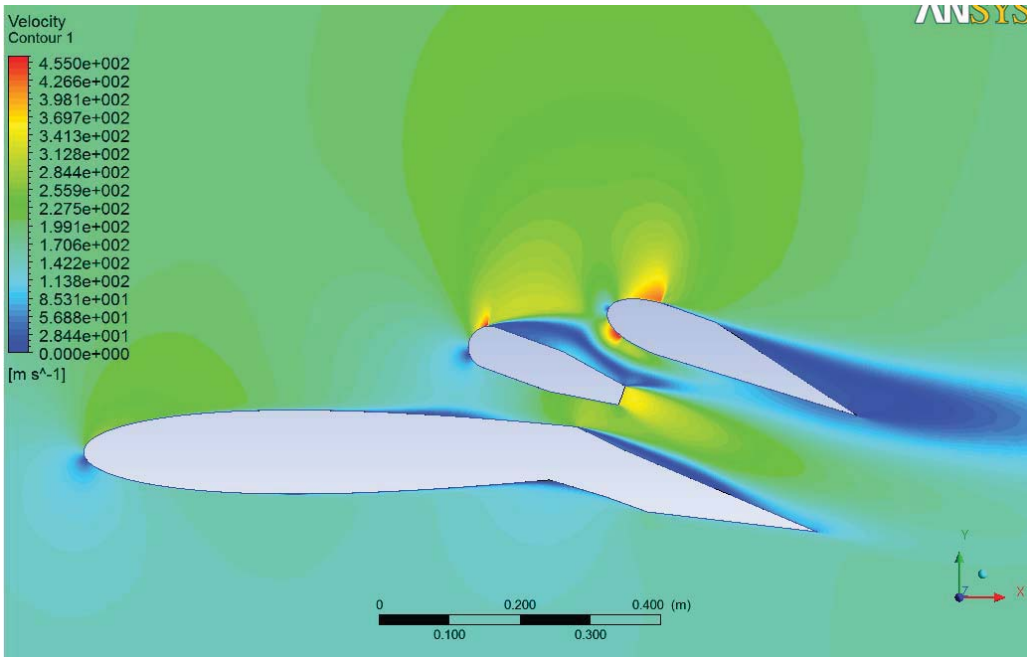

Velocity Contour: Angle 20 Mach=0.5

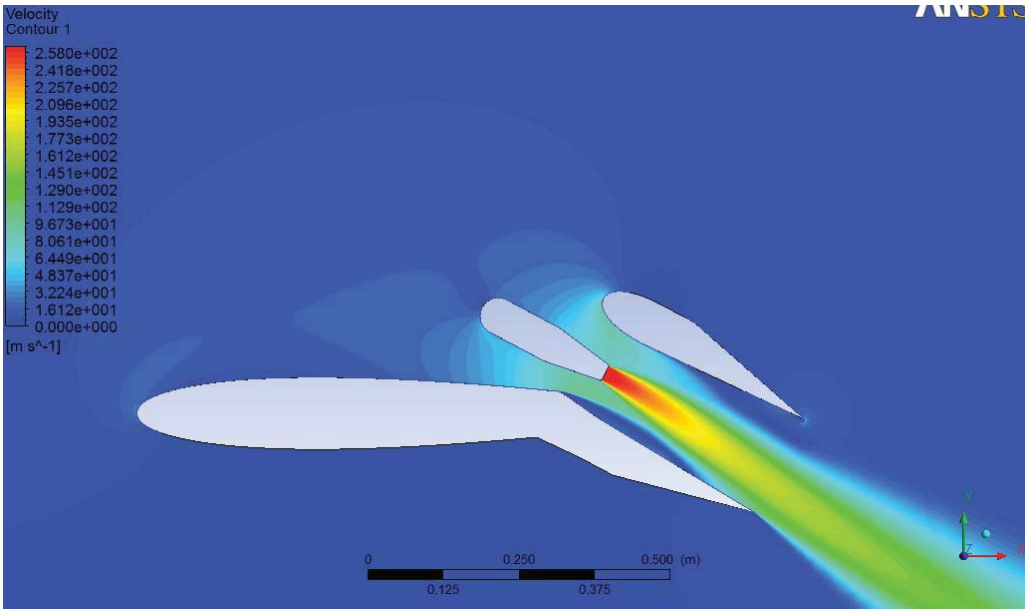

Velocity Contour: Angle 28 Mach=0.01

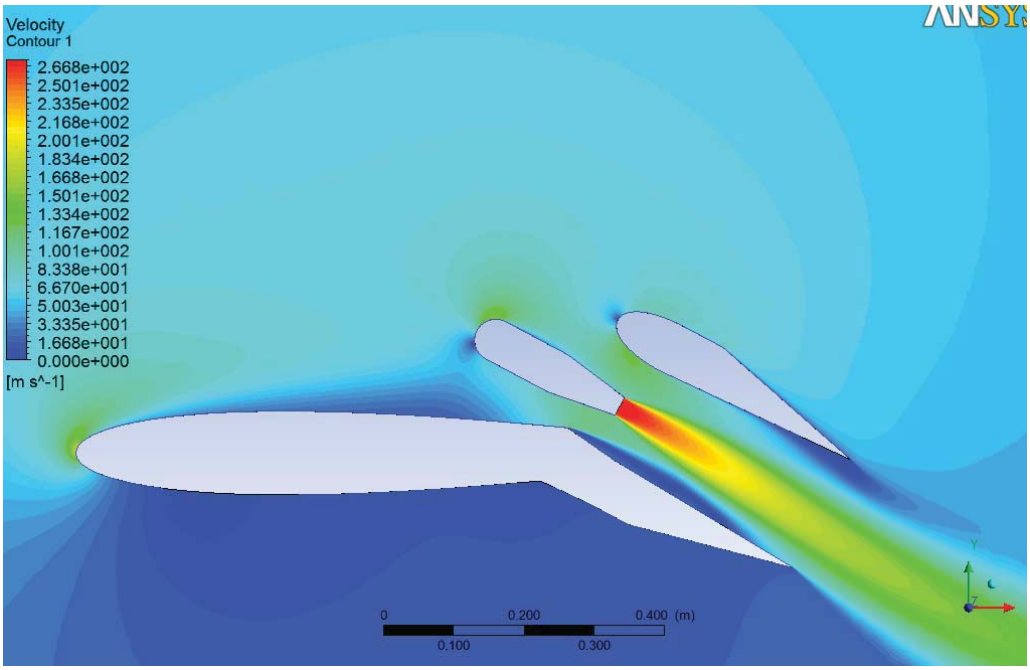

Velocity Contour: Angle 28 Mach=0.1

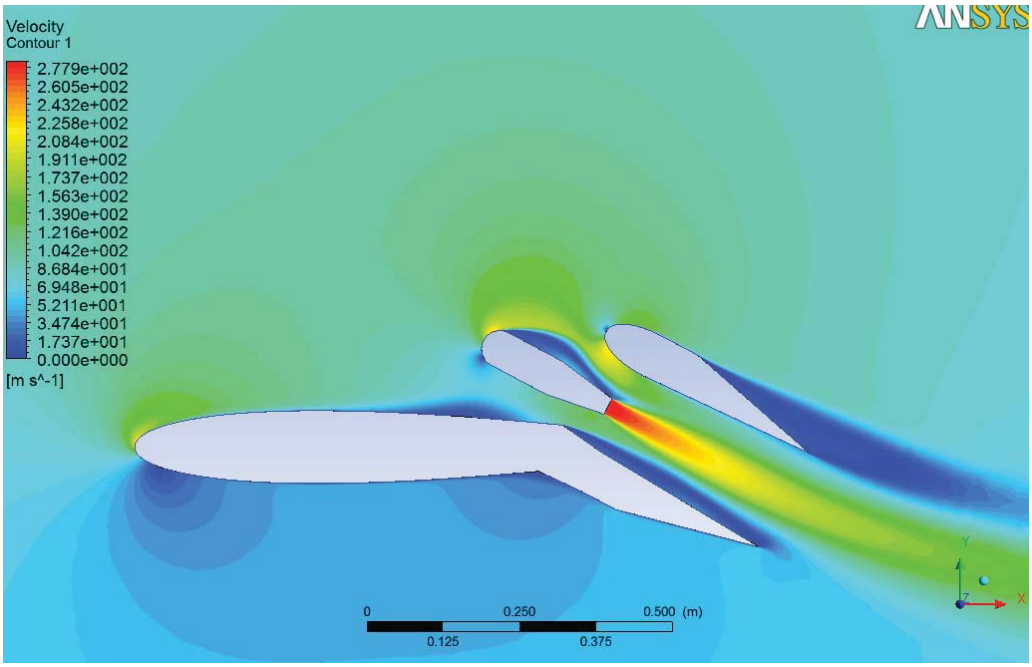

Velocity Contour: Angle 28 Mach=0.2

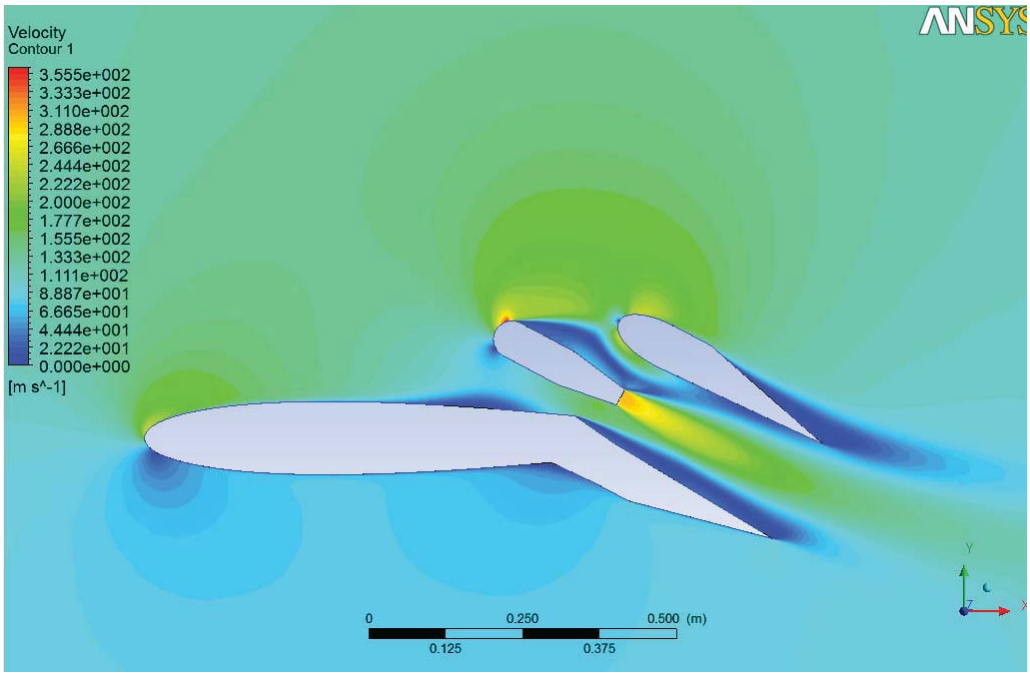

Velocity Contour: Angle 28 Mach=0.3

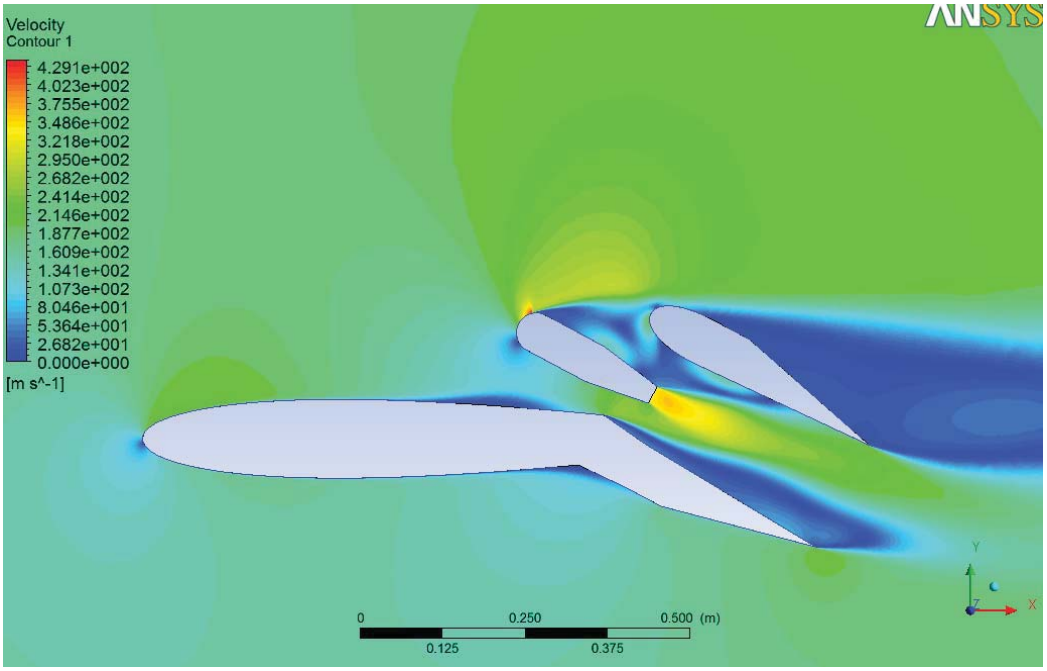

Velocity Contour: Angle 28 Mach=0.5

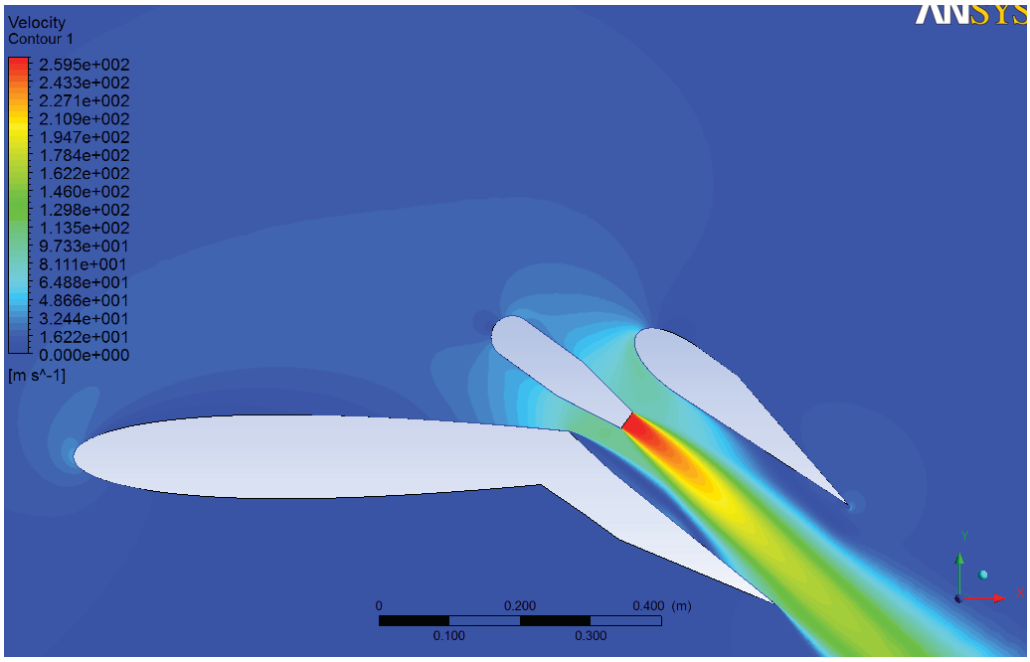

Velocity Contour: Angle 36 Mach=0.01

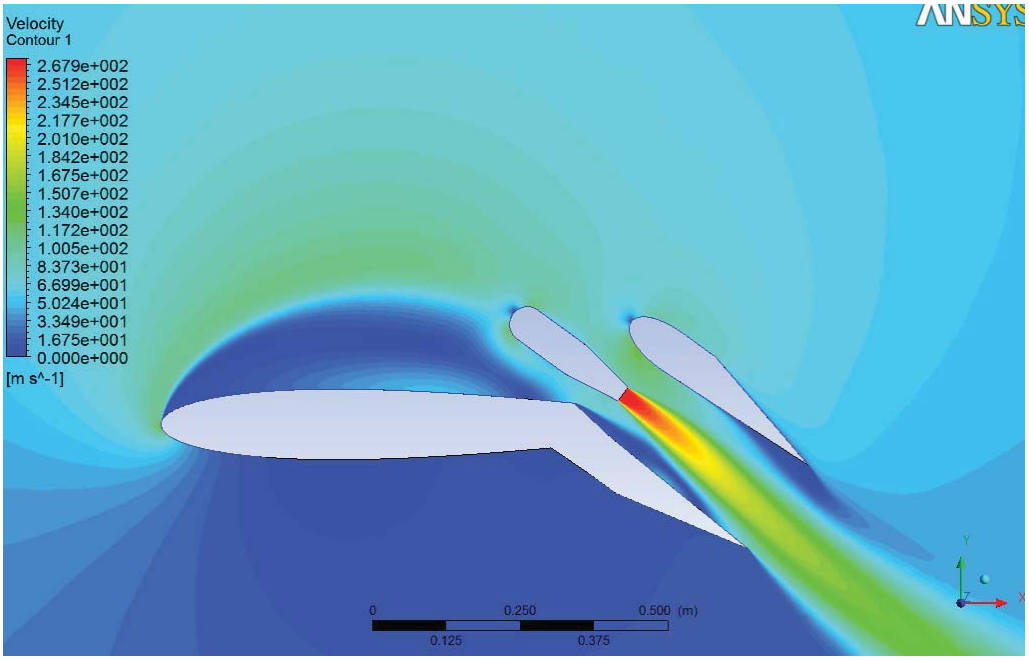

Velocity Contour: Angle 36 Mach=0.1

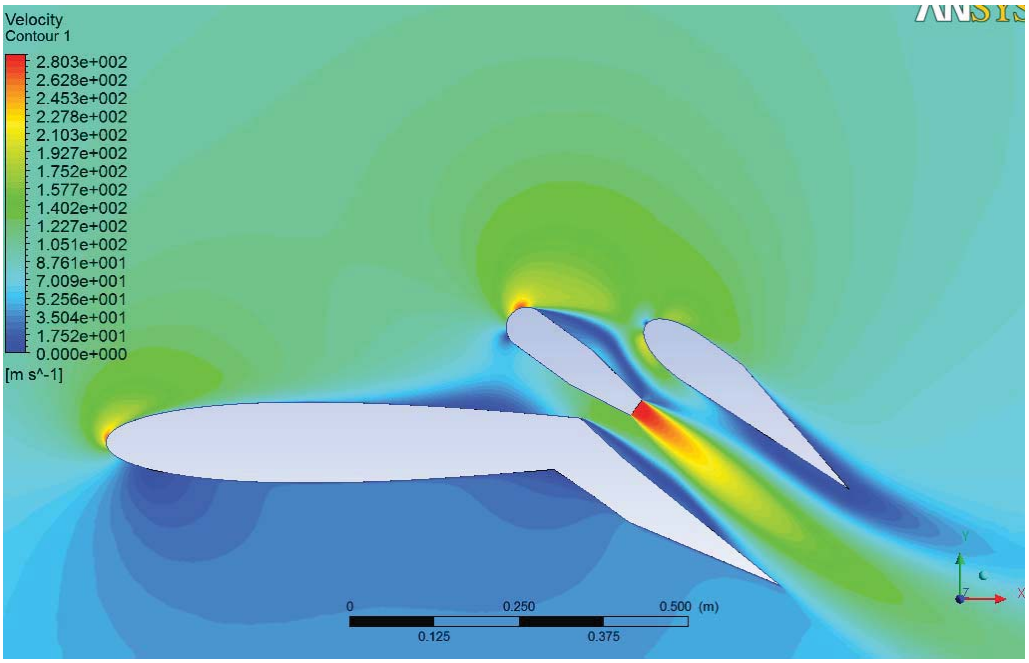

Velocity Contour: Angle 36 Mach=0.2

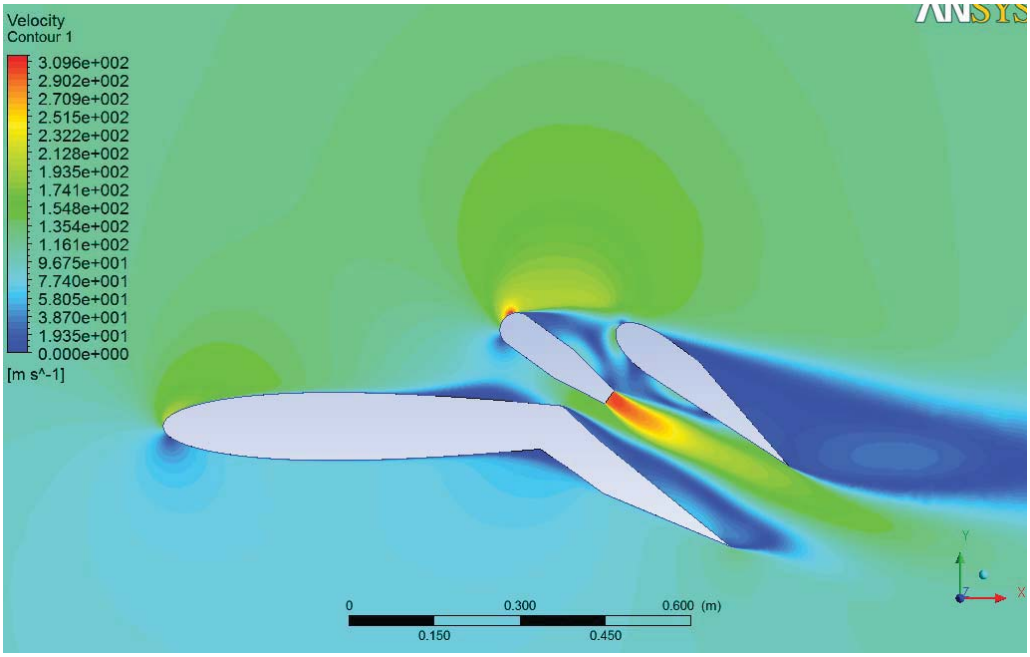

Velocity Contour: Angle 36 Mach=0.3

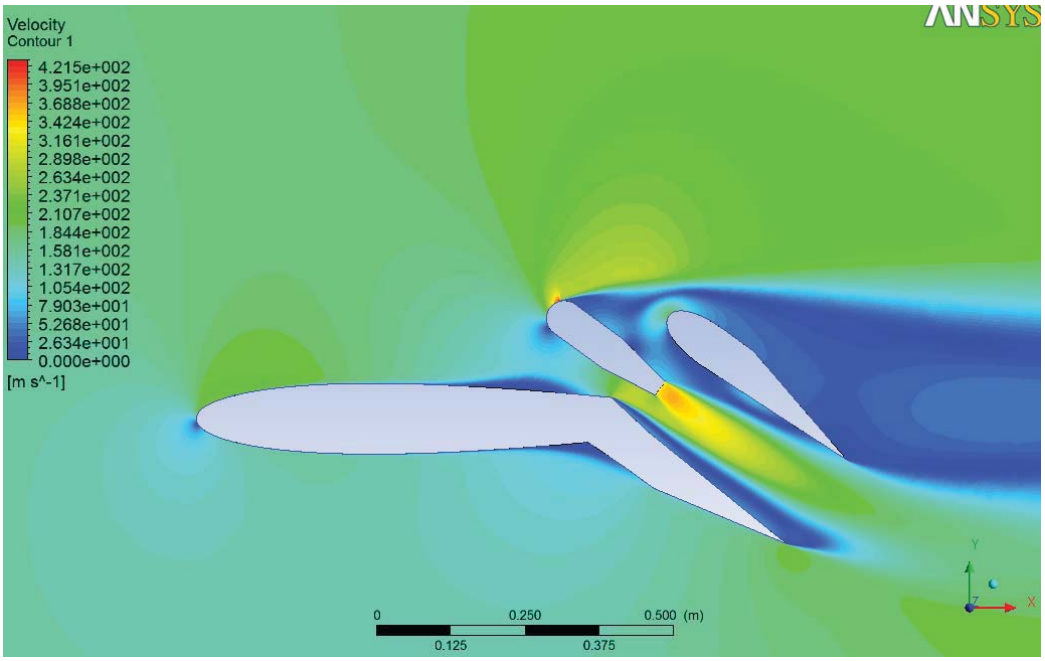

Velocity Contour: Angle 36 Mach=0.5

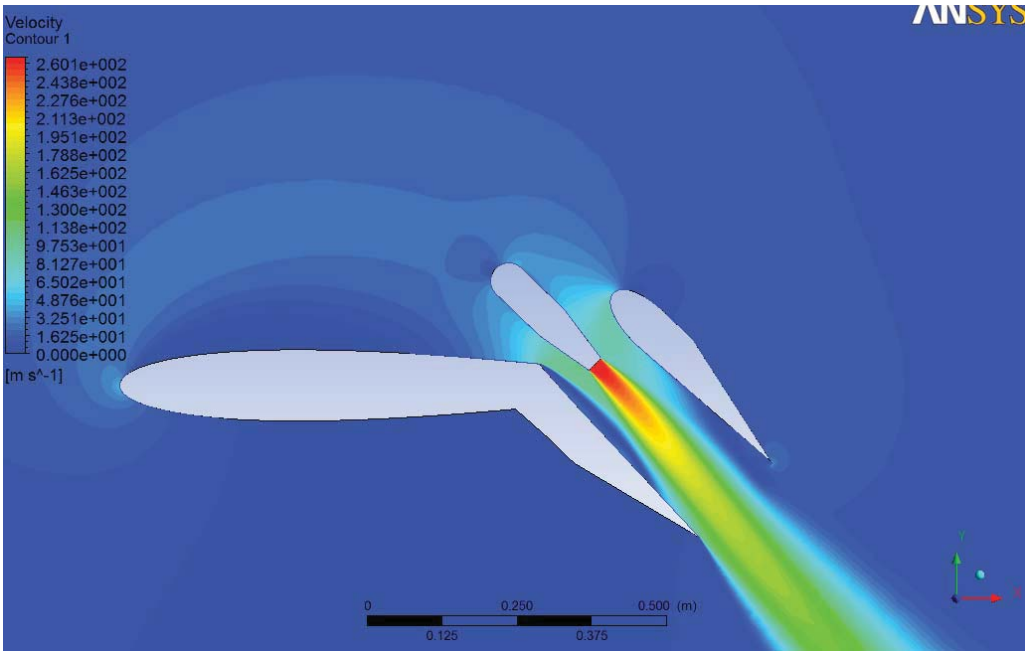

Velocity Contour: Angle 44 Mach=0.01

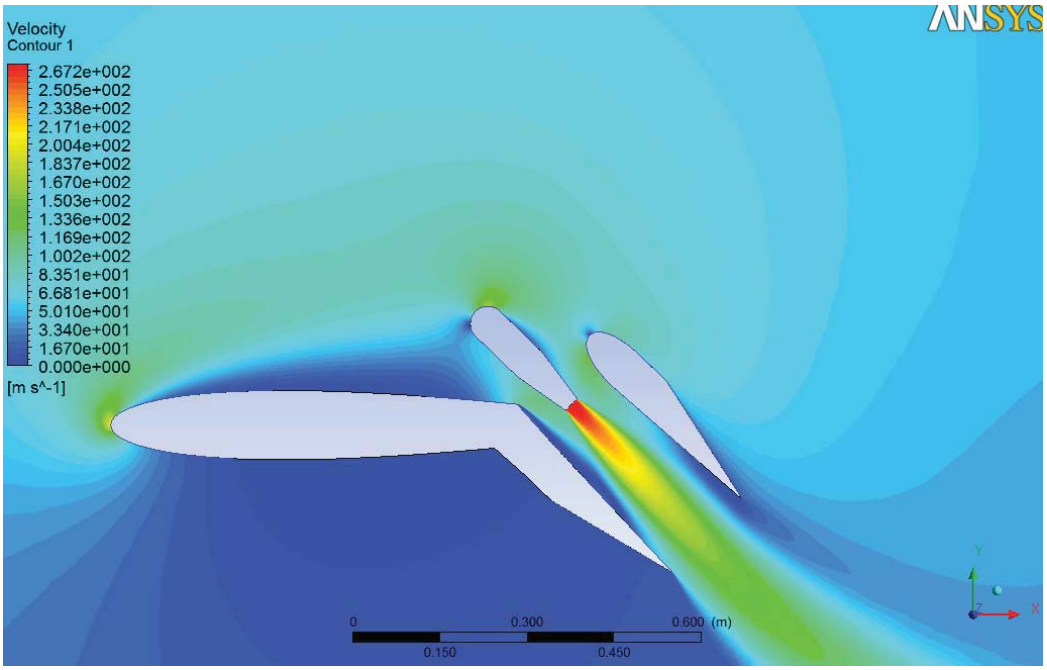

Velocity Contour: Angle 44 Mach=0.1

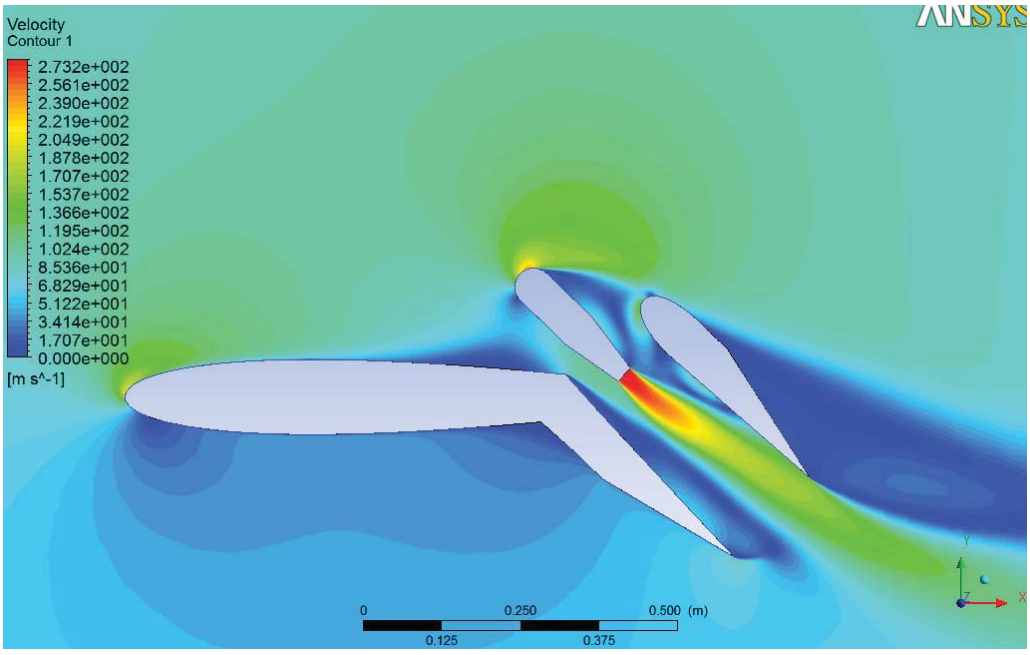

Velocity Contour: Angle 44 Mach=0.2

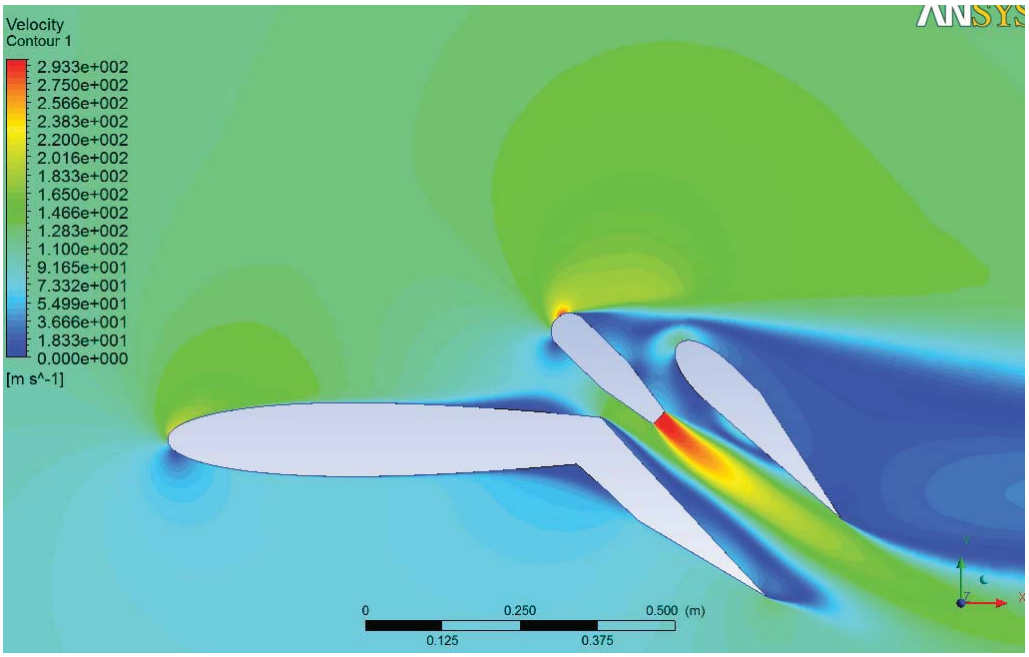

Velocity Contour: Angle 44 Mach=0.3

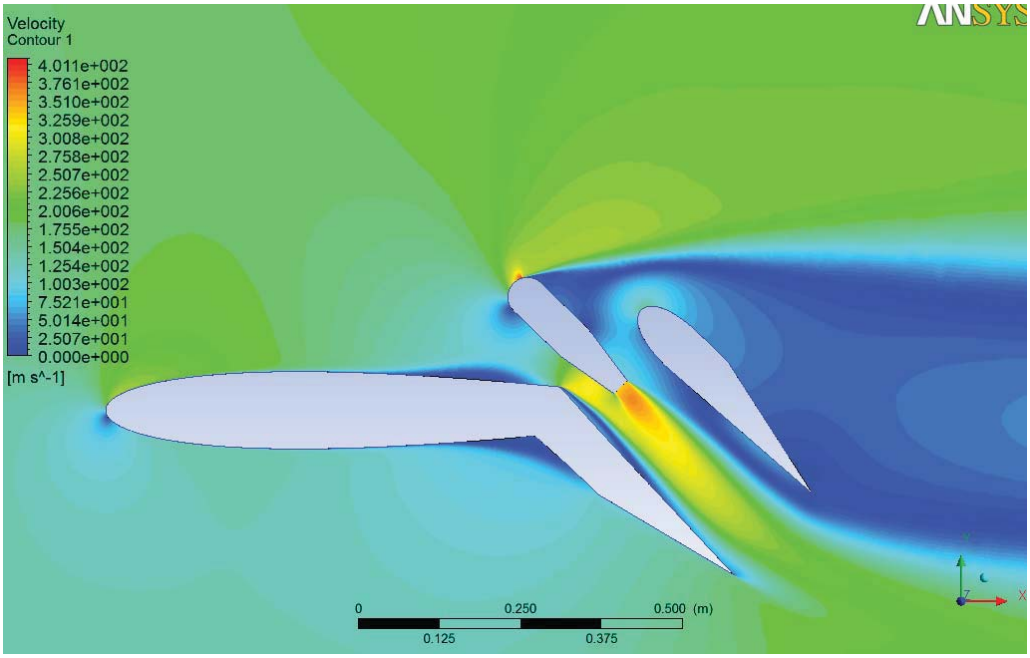

Velocity Contour: Angle 44 Mach=0.5

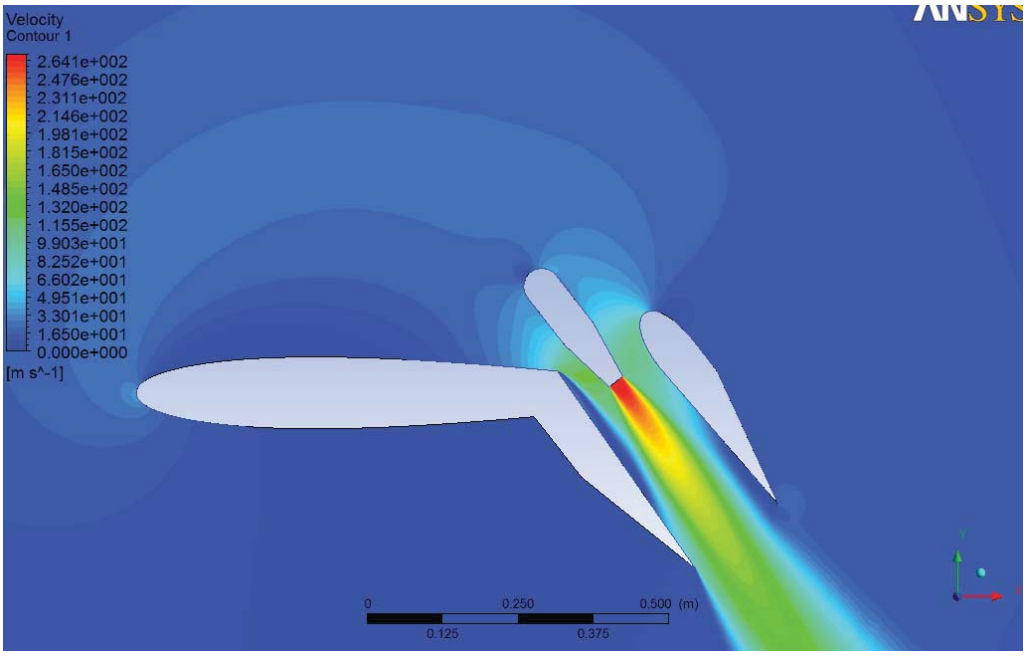

Velocity Contour: Angle 52 Mach=0.01

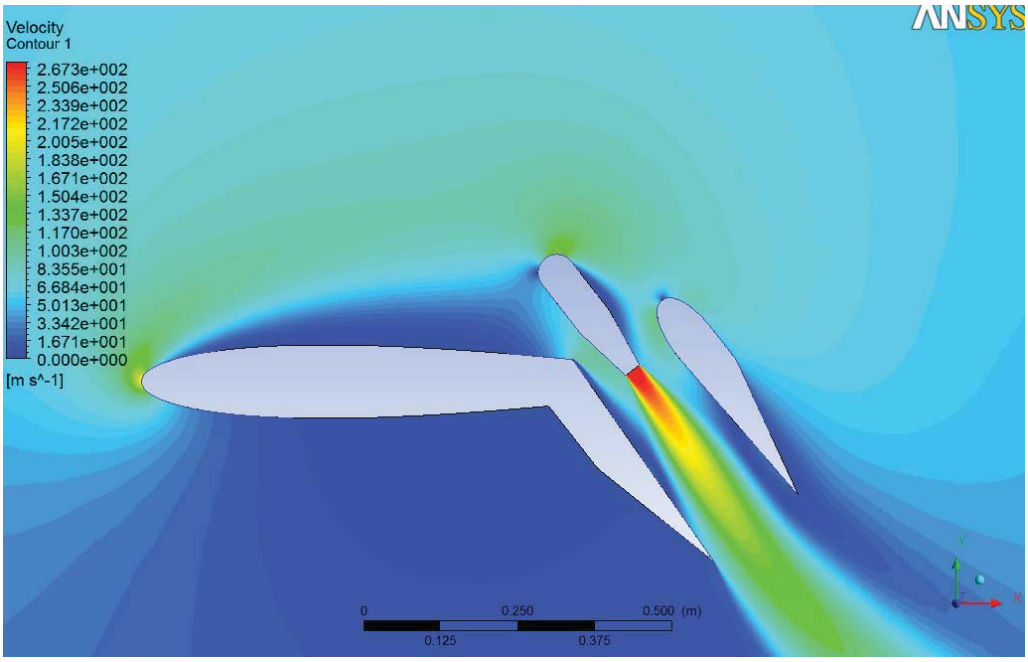

Velocity Contour: Angle 52 Mach=0.1

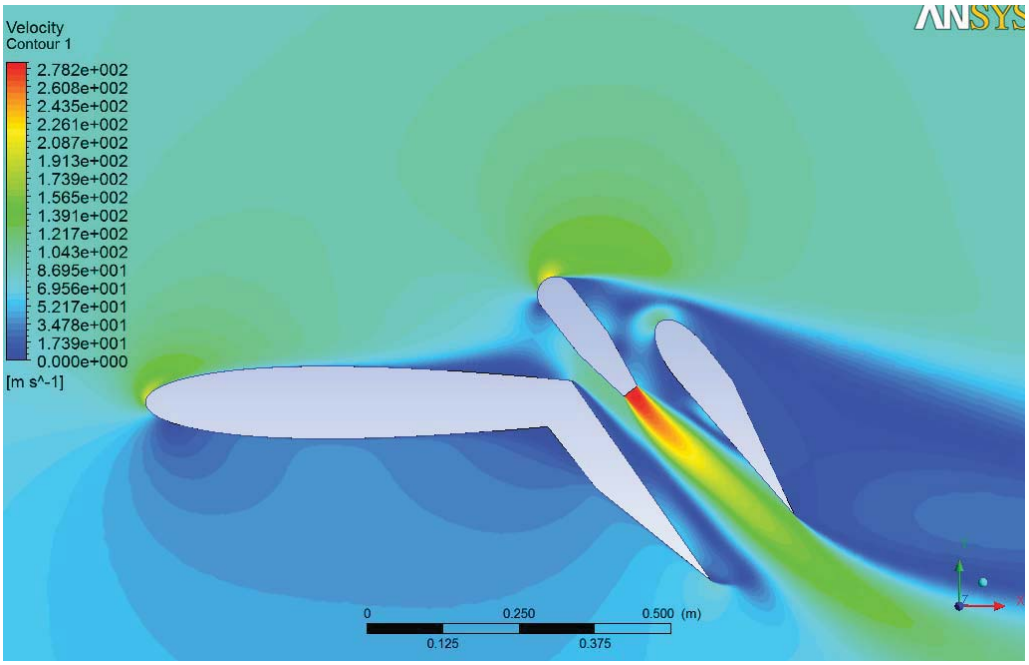

Velocity Contour: Angle 52 Mach=0.2

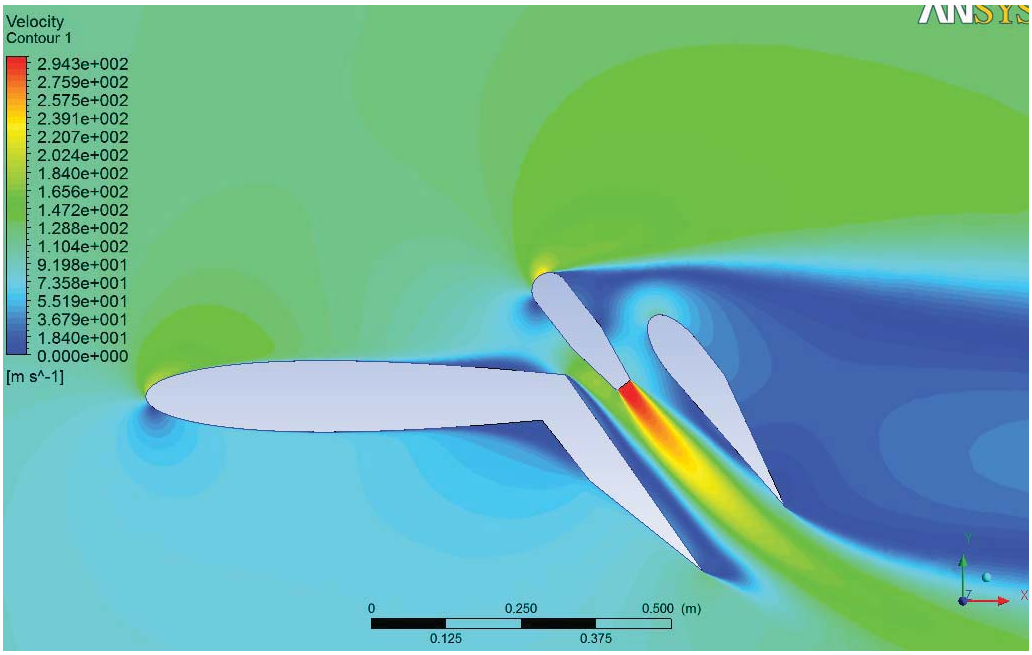

Velocity Contour: Angle 52 Mach=0.3

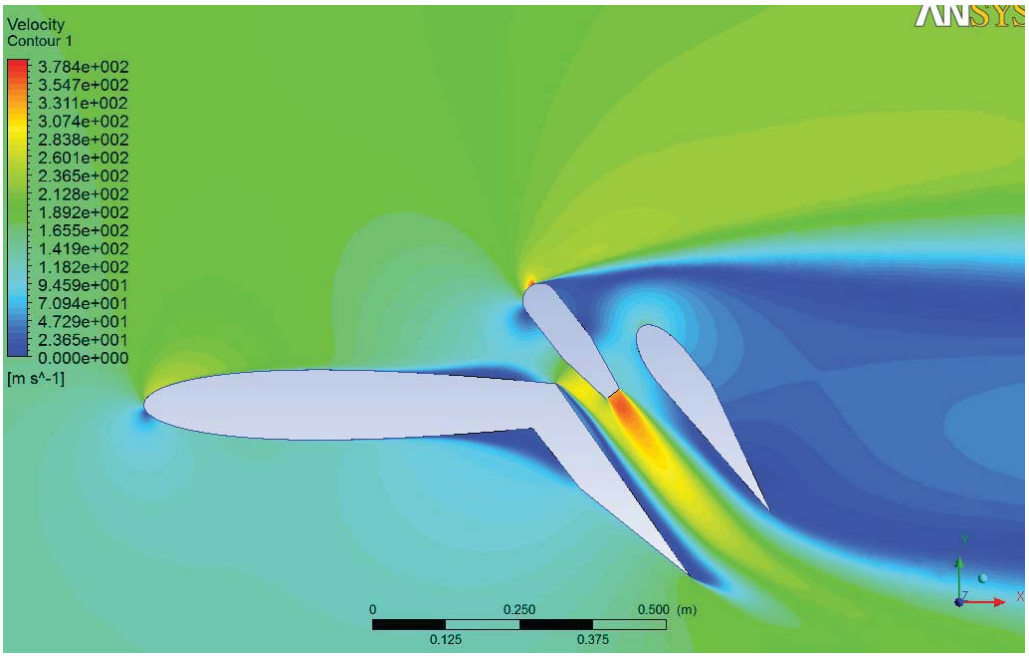

Velocity Contour: Angle 52 Mach=0.5

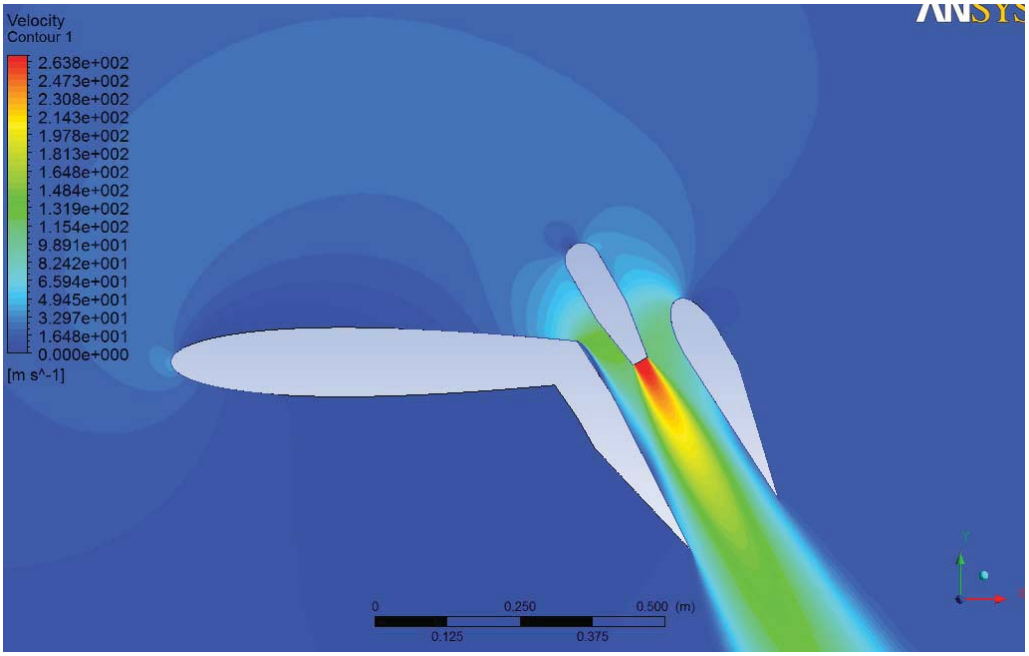

Velocity Contour: Angle 60 Mach=0.01

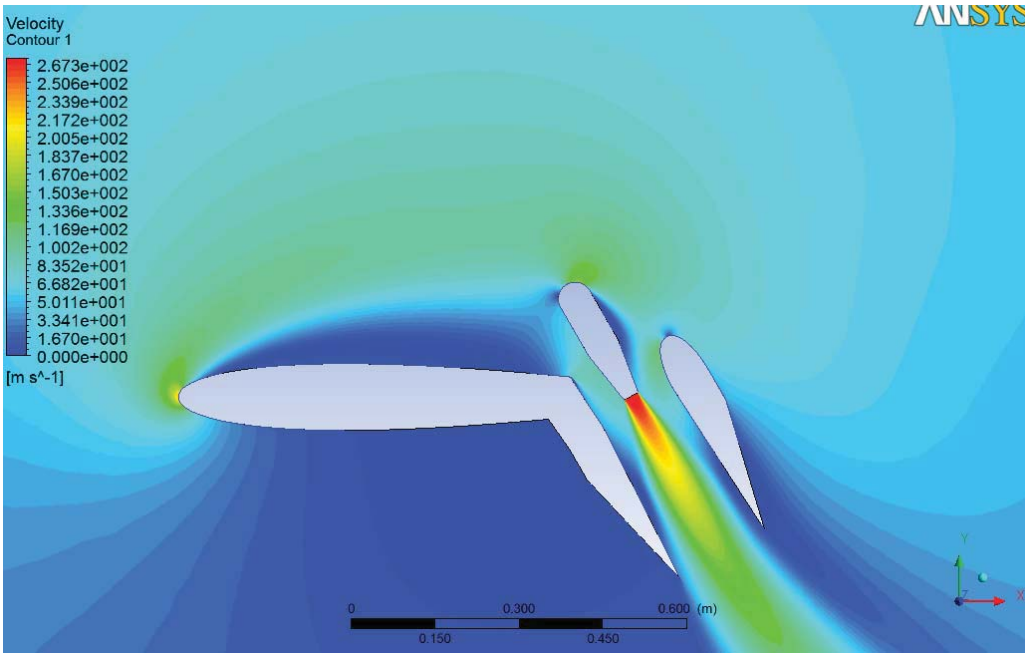

Velocity Contour: Angle 60 Mach=0.1

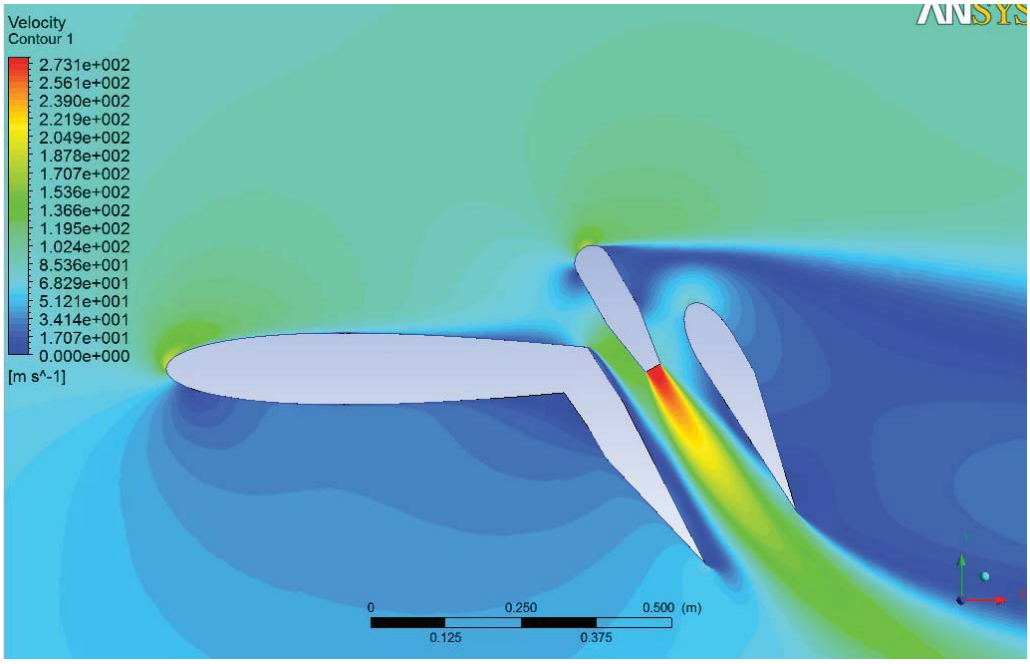

Velocity Contour: Angle 60 Mach=0.2

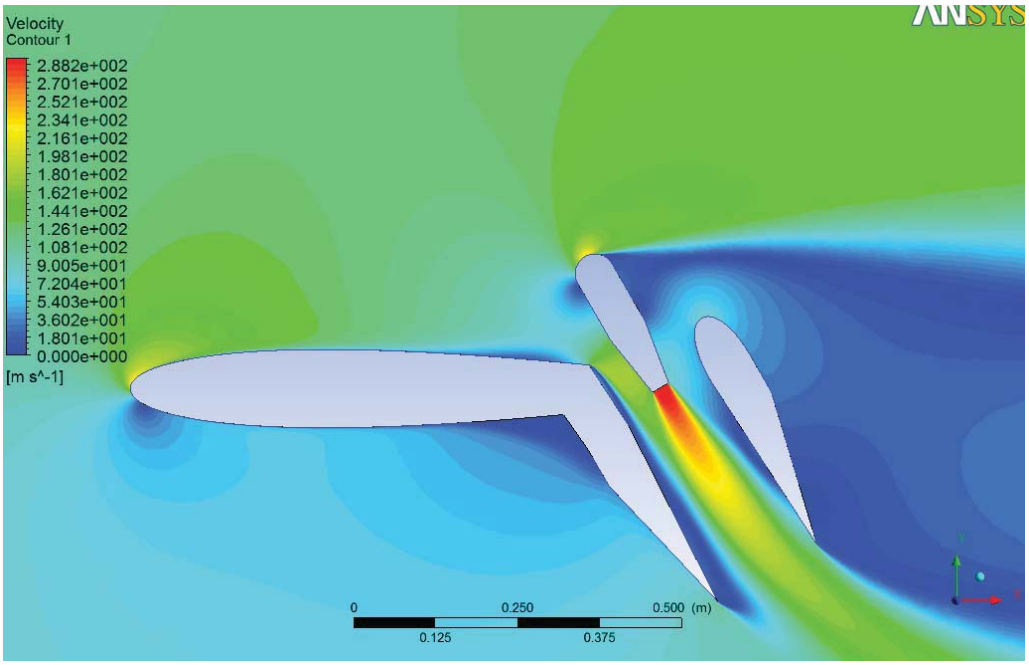

Velocity Contour: Angle 60 Mach=0.3

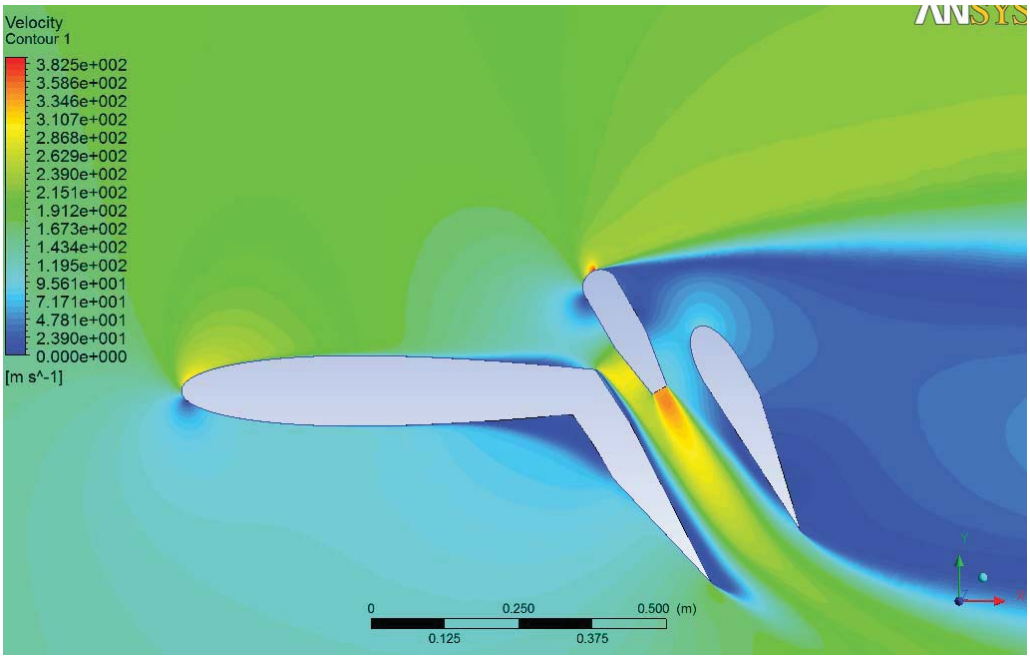

Velocity Contour: Angle 60 Mach=0.5

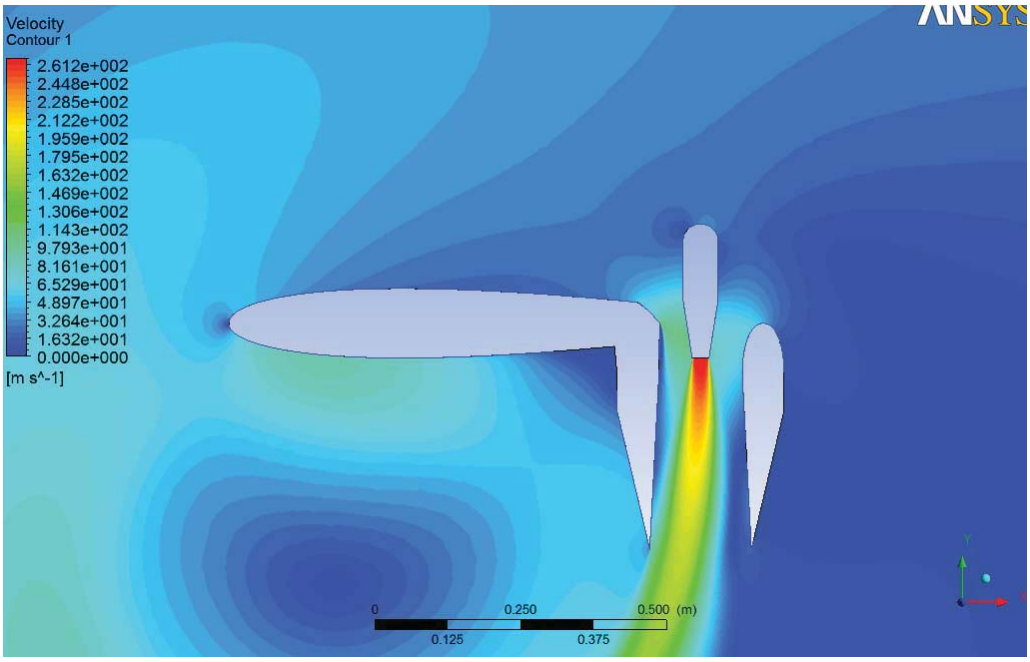

Velocity Contour: Angle 90 Mach=0.01

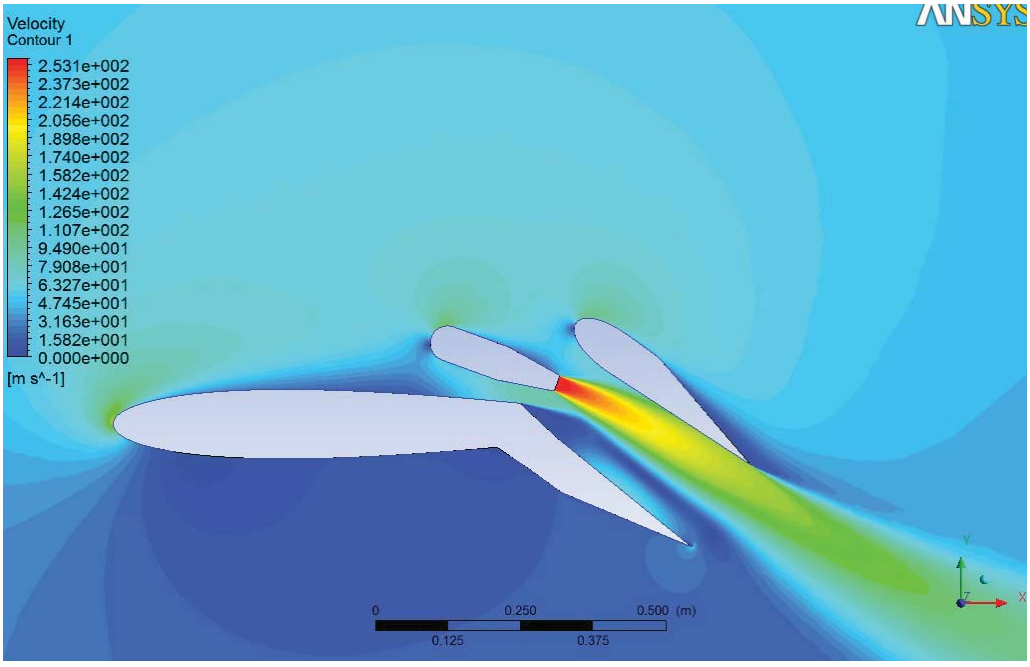

Velocity Contour: Angle 36 Mach=0.1 Deflected Nozzle Configuration

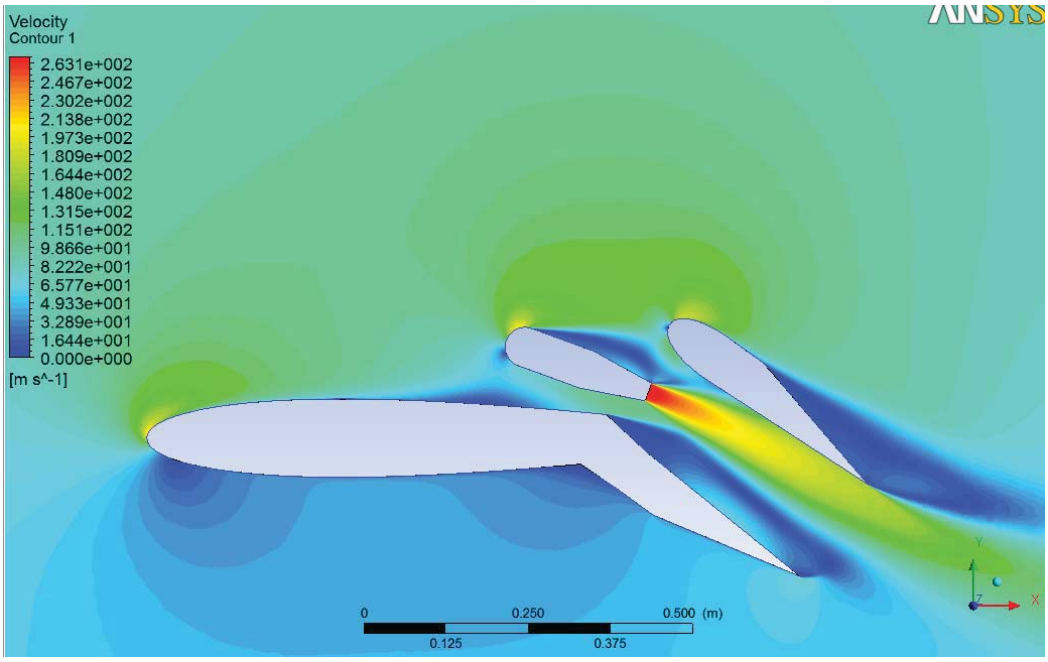

Velocity Contour: Angle 36 Mach=0.2 Deflected Nozzle Configuration

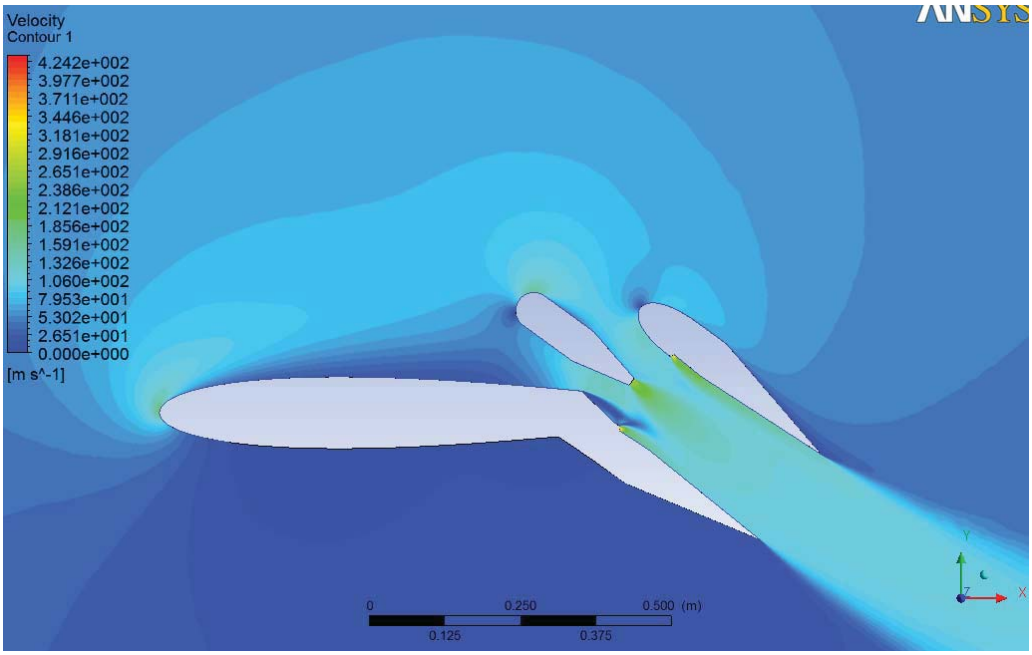

Velocity Contour: Angle 36 Mach=0.1 Wall Jets Configuration

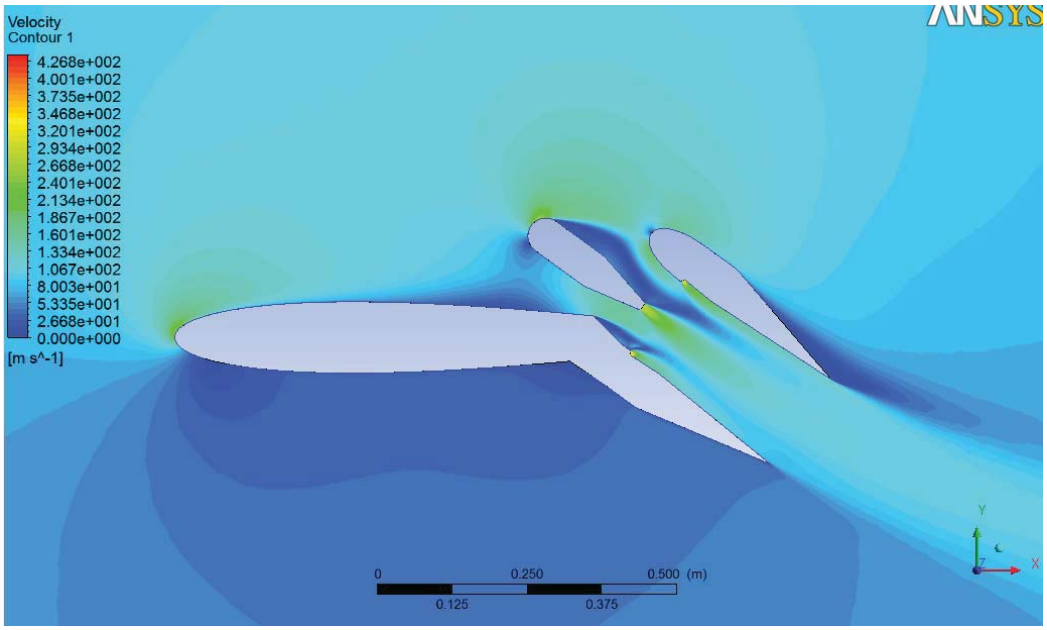

Velocity Contour: Angle 36 Mach=0.2 Wall Jets Configuration